THÈSE PRÉSENTÉE

POUR OBTENIR LE GRADE DE

DOCTEUR DE L'UNIVERSITÉ DE BORDEAUX

ÉCOLE DOCTORALE DES SCIENCES PHYSIQUES ET DE L'INGÉNIEUR

SPÉCIALITÉ : ÉLECTRONIQUE

Par Joan CAPDEVILA

Fabrication, caractérisation et modélisation de cellules photovoltaïques tandem organique/silicium en configuration 3 terminaux

Fabrication, characterization, and modeling of organic/silicon tandem photovoltaic cells in 3-terminal configuration

Soutenue le 16 octobre 2026

M. LEVI Timothée	Professeur, IMS, Talence	Président
Mme SCHNEIDER Nathanaëlle	Directrice de recherche, IPVF, Palaiseau	Rapporteure
M. DURAND Olivier	Professeur, INSA, Rennes	Rapporteur
M. CAMPOY-QUILES Mariano	Professeur, ICMAB-CSIC, Cerdanyola del Vallès	Examinateur
M. CROS Stéphane	Directeur de recherche, CEA-LITEN, Bourget du Lac	Examinateur
Mme GUEUNIER-FARRET Marie	Professeure, IMS, Talence	Directrice de thèse
M. CHAMBON Sylvain	Directeur de recherche, IMS, Talence	Co-directeur de thèse

Abstract

Photovoltaics is now a mature technology, largely dominated by crystalline silicon (c-Si), which accounts for more than 98 % of the global market. The performance of this technology is now approaching its theoretical Auger efficiency limit of 29.4 %, with the best devices achieving conversion efficiencies of 27.9 % (lab cells). Multijunction architectures currently represent the most promising route to surpass this limit by reducing thermalization losses through the combination of materials with complementary bandgaps. Among these, silicon-based tandem solar cells have attracted increasing interest for terrestrial applications. Combining a silicon bottom cell, using a well-established industrial process, with a wide-bandgap top cell (e.g., perovskite or CIGS) extends the efficiency limit of single-junction devices, with record efficiencies now exceeding 33 %. At the same time, recent advances in organic photovoltaics (OPV), with laboratory cells reaching efficiencies up to 20 %, together with the unique properties of organic semiconductors (including their wide range of available materials, tunable bandgaps, high optical absorption coefficients, and compatibility with low-cost fabrication processes), make this technology an attractive candidate for tandem integration with silicon. Within this context, and as part of the ANR ORGANIST project, this thesis aims to develop the key technological building blocks required to realize a tandem solar cell combining a wide-bandgap semi-transparent OPV top cell with an interdigitated back-contact (IBC) crystalline silicon bottom cell. A three-terminal (3T) architecture was selected because it eliminates the current-matching constraints and the need for tunnel junctions inherent to conventional two-terminal tandem devices. The first part of this work focuses on the development of the wide-bandgap organic top cell based on the PM6:GS-ISO bulk heterojunction. Optimization of the fabrication process, combining thermal treatments, solvent engineering, and conjugated solid additives, improved the crystallinity of the active layer, enhanced its optical properties, and reduced recombination losses, leading to power conversion efficiencies of 10 % with an open-circuit voltage (V_{OC}) of 1.20 V. The second part of the thesis addresses the development of a transparent top electrode based on indium tin oxide (ITO), deposited at room-temperature by magnetron sputtering and combined with a MoO_3 layer providing both protection of the organic layer and efficient hole transport. Optimization of the deposition parameters enabled the fabrication of semi-transparent organic solar cells with efficiencies close to 6 % and V_{OC} values exceeding 1.1 V. These developments enabled the first integration studies of a semi-transparent organic solar cell with an IBC silicon solar cell in a 3T architecture. Interface investigations demonstrated the potential of sputtered ITO as an interconnection layer owing to its high optical transparency, low electrical resistance, and compatibility with both organic and silicon photovoltaic technologies. Finally, a concept named RAINBOW, developed in collaboration with ICMAB-CSIC (Barcelona), was introduced to make the link between experimental results and modeling for the investigation of lateral organic/silicon multijunction architectures. Simulations predict

efficiencies of up to 18 % (for a silicon cell efficiency of approximately 16 %), confirming the potential of these hybrid structures and providing valuable guidance for the development of future generations of high-efficiency organic/silicon tandem solar cells.

Résumé

Le photovoltaïque est aujourd'hui une technologie mature, largement dominée par le silicium cristallin (c-Si), qui représente plus de 98 % du marché mondial. Les performances de cette technologie approchent désormais leur limite théorique Auger de 29,4 %, les meilleurs dispositifs atteignant des rendements de 27,9 % en laboratoire. Les architectures multijonctions constituent aujourd'hui la voie la plus prometteuse pour dépasser cette limite en réduisant les pertes par thermalisation grâce à l'association de matériaux de bandes interdites complémentaires. Parmi elles, les cellules tandem à base de silicium suscitent un intérêt croissant pour les applications terrestres. L'association d'une cellule silicium, dont la fabrication est mature industriellement, à une cellule à grand gap (pérovskite, CIGS...) permet de repousser la limite de rendement des cellules simples, avec des records dépassant 33 %. Les progrès récents du photovoltaïque organique (OPV), dont les cellules de laboratoire atteignent 20 % de rendement, ainsi que les propriétés des semi-conducteurs organiques (diversité des matériaux, largeur de bande interdite ajustable, forts coefficients d'absorption et procédés de fabrication à faible coût), rendent cette filière particulièrement attractive pour une association tandem avec le silicium. C'est dans ce contexte, et dans le cadre du projet ANR ORGANIST, que s'inscrit cette thèse. Son objectif est de développer les briques technologiques nécessaires à la réalisation d'une cellule tandem associant une cellule OPV semi-transparente à large bande interdite à une cellule en silicium cristallin à contacts interdigités en face arrière (IBC, Interdigitated Back Contacts). L'architecture trois terminaux (3T) a été retenue car elle s'affranchit des contraintes d'adaptation des courants et de l'utilisation de jonctions tunnel imposées par les configurations classiques à deux terminaux. Les premiers travaux ont porté sur le développement de la cellule organique à large bande interdite (« cellule top ») basée sur l'hétérojonction PM6:GS-ISO. L'optimisation des procédés de fabrication, combinant traitements thermiques, ingénierie des solvants et additifs solides conjugués, a permis d'améliorer la cristallinité de la couche active, ses propriétés optiques et de limiter les recombinaisons, conduisant à des rendements de 10 % pour une tension en circuit ouvert (V_{OC}) de 1,20 V. La seconde partie de la thèse est consacrée au développement d'une électrode transparente en oxyde d'indium-étain (ITO), déposée par pulvérisation cathodique à température ambiante et associée à une couche de MoO_3 assurant la protection des couches organiques et le transport des trous. L'optimisation des paramètres de dépôt a permis d'obtenir des cellules organiques semi-transparentes présentant des rendements proches de 6 % pour des V_{OC} supérieurs à 1,1 V. Ces développements ont conduit aux premières études d'intégration d'une cellule organique semi-transparente avec une cellule silicium IBC en architecture 3T. L'étude des interfaces a démontré le potentiel de l'ITO pulvérisé comme couche d'interconnexion grâce à sa forte transparence, sa faible résistance électrique et sa compatibilité avec les technologies organique et silicium. Enfin, un concept baptisé RAINBOW, développé en collaboration avec l'ICMAB-CSIC de Barcelone, a été proposé afin de relier

expérimentation et modélisation pour l'étude d'architectures multijonctions organique/silicium latérales. Les simulations prédisent des rendements pouvant atteindre 18 % (pour une cellule Si d'environ 16 %), confirmant le potentiel de ces associations et guidant le développement de futures générations de cellules tandem organique/silicium à haut rendement.

« Demandez, et l'on vous donnera ; cherchez, et vous trouverez ; frappez, et l'on vous ouvrira. »

Matthieu 7:7.

Acknowledgments

This manuscript marks the culmination of three years of work, for which I am officially the author. However, it would undoubtedly never have come to fruition without the support, guidance, trust, and invaluable assistance of the many people who accompanied me throughout this journey. It is with deep gratitude that I wish to express my most sincere thanks to them here.

My first and foremost thanks go to my two PhD supervisors, **Marie** and **Sylvain**. Nothing in my early years suggested that I would pursue higher education, let alone an academic career. If I find myself writing these lines today, it is partly thanks to a series of fortunate coincidences, but above all because you chose to place your trust in me. Despite my young age and sometimes unconventional personality, you offered me an exceptional opportunity, one that I have always done my very best to live up to. Over the past three years, I have learned an incredible amount from both of you. You found the perfect balance between guidance and independence. The freedom you gave me was invaluable: it allowed me to truly take ownership of this work, develop my critical thinking, and maintain the motivation needed to see this project through to the end. I am also deeply grateful to you for giving me the opportunity to take part in an international research stay and for encouraging me to present my work at conferences. You continually pushed me beyond my comfort zone and helped me grow in confidence. These experiences have played a major role in my development, both as a researcher and as a person. I sincerely hope that these past three years have made you as eager as I am to continue working together in a new capacity. I am truly excited to begin this new postdoctoral year alongside you.

Marie, it has been a true privilege to complete this PhD under your supervision. You always knew how to give me confidence whenever I doubted myself, while gently reminding me of the areas in which I still had room to grow. Your high standards, combined with your constant support, have helped me mature not only as a researcher but also as a person. I am convinced that I leave this PhD a very different person from the one who started it, with solid foundations on which to build the rest of my career. For that, I will always be grateful.

Sylvain, your calmness and composure were invaluable whenever stress or frustration threatened to take over. I truly appreciated your kindness, your availability, and the fact that your office door was almost always open whenever I had a question or needed advice. Thank you for your patience, your support, and the trust you placed in me throughout this journey. Finally, I sincerely hope that, in the years to come, supporting ASM Clermont will bring you more joy than disappointment... although, between us, I remain rather skeptical.

This work would never have been possible without the support, dedication, and contributions of many collaborators. First of all, I would like to thank all the members of the **ANR-ORGANIST** project, within which this PhD was carried out. The true strength of this

project lies in the close collaboration between the different research teams. I would especially like to thank both the teams at **LPICM** and **GeePs**. The many meetings, scientific discussions, travel, and collaborative efforts over the past three years have been instrumental in bringing the project to where it stands today.

I would also like to thank everyone who trained me and introduced me to experimental techniques that I am certain will remain invaluable throughout my career. In particular, I would like to thank the staff of the **ELORPrintTec** platform, as well as the **PLACAMAT** platform, for their patience, expertise, and willingness to share their knowledge.

I can never thank the people I met during my collaboration with the **ICMAB** in Barcelona enough. I am especially grateful to **Prof. Mariano Campoy-Quiles**, who is not only an outstanding scientist but also an exceptional person. A very special thank you also goes to **Xavi**. More than a collaborator, he has become a true friend, and I sincerely hope that our friendship will continue for many years to come. The few weeks I spent in Barcelona were an unforgettable experience. They gave me fresh perspectives, renewed motivation, and the momentum I needed to move my PhD forward with new enthusiasm. Without a doubt, this research stay will remain one of the highlights of my doctoral journey.

I would like to thank everyone I had the pleasure of meeting at **IMS**. I hope that, in return, I have left a positive impression on all of you. I would like to thank everyone I had the pleasure of working with in the corridor: **Lionel**, **Guillaume**, **Laurence**, **Farrah**, **Isabelle**, **Damien.T**, **Margot**, **Sara.B**, **Chélia**, **Matthieu**, **Ayoub** "*the president of Lebanon*", and **Getnet**. Thank you for your good humour, the countless conversations, and all those little moments that made everyday life in the lab so enjoyable.

A special thank you goes to everyone who shared an office with me over the past three years and somehow managed to put up with me. **Hugo**, thank you for your invaluable advice and, above all, for inspiring me to follow in your footsteps. I sincerely hope our paths will cross again. **Rebecca**, keep going, you'll soon be an amazing doctor. **Alejandro**, "*campeón del mundo, hermano...".* **Marius**, I hope I was a good internship supervisor, even though we were actually the same age...

To everyone else, all I can really say is that I now consider you much more than colleagues; you are true friends. **Finn**, your kindness and calmness are a true source of inspiration. I'm excited to bring you to more rugby games and turn you into a true fan of the sport. **Rémi**, never change. Keep being the person you are. **François**, better known as *the Parenthesis*, thank you for being the lab's official grumpy guy. Having you around made me feel a little less alone in that category. **Sara Z.**, thank you for all our wonderfully pointless conversations, your delicious tiramisu, and all the coffees I probably would never have drunk if you hadn't brought my mug to me. **Harmony**, "*my nitrogen*", thank you for being the wonderful person you are and for your support in the last few months of this journey. **Martial**, thank you for all the laughs and for getting me out of trouble time and time again thanks to your ingenuity and impressive engineering skills. **Damien.C**, "*picore".* **Darlane**, even though we were both a little wary of each other in the beginning, thank you for being the wonderful

person you are and for making the first year of my PhD such a memorable and enjoyable one. I hope we'll get to see each other much more often in the years ahead. **Chloé**, I don't think any acknowledgement could ever fully express how grateful I am for everything you've done for me. And since I would probably never manage to tell you all of this face to face without my pride getting in the way, these few lines will have to do. Even though our professional relationship has sometimes been eventful, I have always considered you a true friend. You were there through both the good times and the difficult ones. You never hesitated to take the time to talk, proofread my work, or simply support me, regardless of the day or the hour, often without expecting anything in return. My PhD would simply not have been the same without you. Thank you, truly. And finally... the GOAT, **Barth**. Thank you for everything, my brother. You are an incredible person, a friend anyone can rely on, and an extraordinary father. I feel incredibly lucky and grateful that our paths crossed. You can count on me until the very end of your PhD. I already can't wait to be part of it, and I'm sure it's going to be an amazing journey.

Pour continuer sur une touche amicale et sportive, je tiens à remercier toutes les personnes qui m'ont permis de m'évader et de partager de véritables moments de camaraderie tout au long de ces trois années.

À mes coéquipiers et à l'ensemble du **RC Cadaujacais**, merci de m'avoir rappelé qu'il y a bien plus dans la vie que la recherche. Je nous souhaite une excellente saison, remplie de victoires, de souvenirs inoubliables et de beaux moments de convivialité.

Un immense merci également à mes copains de **Los Pimientos**. Même si ce projet m'a coûté quelques heures de sommeil et a parfois pris une ampleur qui nous dépassait, je suis extrêmement fier de tout ce que nous avons construit ensemble. Plus encore, j'espère qu'il vous aura apporté autant de bonheur qu'il m'en a apporté. J'espère que cette aventure continuera encore de nombreuses années et qu'elle donnera naissance à bien d'autres souvenirs inoubliables.

Un merci tout particulier à la bande du **"R"** de m'avoir supporté toutes ces années. Le fait que vous ayez quitté le Pays basque sans bouteille d'oxygène pour venir assister à ma soutenance est, à mes yeux, la plus belle définition de l'amitié. Je vous dois bien plus que je ne pourrai jamais l'exprimer avec des mots, et j'espère sincèrement que de nombreux autres "13h12" nous attendent encore.

Merci aussi à mes copains éparpillés un peu partout entre la France et l'étranger et qui ont su entretenir ce lien avec moi tout au long de ma vie et plus particulièrement durant ces trois années : je pense notamment à **Loïc**, **Maxime** et **Adam**.

Pour finir, je tiens à remercier les personnes les plus importantes à mes yeux. Cette thèse vous appartient sans doute davantage qu'à moi. Sans votre amour, votre confiance et votre soutien, elle n'aurait tout simplement jamais existé.

Je souhaite d'abord remercier mes grands-parents, mes tantes et mes cousins, sans oublier ceux qui nous ont quittés au cours de ces trois dernières années. J'aime à croire que,

d'où vous êtes, vous avez suivi chacune de mes péripéties et partagé avec moi les joies comme les doutes de cette aventure.

À la personne qui partage ma vie depuis plusieurs années maintenant, merci. Tout n'a pas toujours été simple, mais tu as toujours su être présente lorsque j'en avais le plus besoin. Tu m'as soutenue sans jamais compter et je ne pourrai jamais te remercier à la hauteur de ce que tu m'as apporté. Je t'aime.

Merci à **Rémy**, mon frère, mon meilleur ami. Malgré toutes les bêtises que nous avons pu faire en vingt-deux ans, tu restes la personne la plus importante à mes yeux. Continue de me rendre fier comme tu le fais déjà si bien. Je te donne rendez-vous dans quelques années pour ta thèse de médecine, afin que nous puissions enfin nous appeler mutuellement « Docteur ».

Papa, malgré des années de relations parfois compliquées, tu es certainement la personne que j'ai le plus admirée au monde, sans jamais avoir su te le dire. Ces dernières années ne t'ont pas épargné, mais je suis profondément fier de la force avec laquelle tu affrontes tout cela. Continue de te battre comme tu l'as toujours fait. Quoi qu'il arrive, tu resteras toujours la même personne à mes yeux. Je suis fier de toi.

Maman, tu sais déjà tout. Merci d'avoir été mon modèle depuis le tout premier jour, le 27 avril 2001, jusqu'à aujourd'hui... et pour toujours. Malgré ta petite taille, tu es la personne la plus grande que je connaisse. Tu es, pour moi, un exemple de courage, de modestie et de résilience. Je ne t'ai jamais entendue te plaindre. Tu as toujours trouvé la force de regarder devant toi et de nous faire passer avant toute chose. Tu as cette capacité à relativiser chaque épreuve et à me rappeler l'essentiel lorsque la vie devient plus difficile. Je ne trouverai jamais de mots assez forts pour te remercier de tout ce que tu as fait pour moi. "*Maite zaitut, ama*".

Table of Contents

General Introduction **17**

Chapter 1 ..... **23**

Fundamentals and State-of-the-art of Silicon, Organic, and Silicon-based Tandem Photovoltaic Technologies **23**

1.1. Photovoltaic effect and semiconductor fundamentals 24

1.2. Silicon solar cells 25

1.2.1 Silicon materials 25

1.2.2 State-of-the-art silicon solar cell technologies 26

1.2.3 Interfacial defects and passivation strategies in silicon solar cells 27

1.3. Organic solar cells 29

1.3.1 Organic semiconductors: electronic structure and optical properties 29

1.3.2 Photoconversion mechanisms in organic solar cells 30

1.3.3 State-of-the-art of organic solar cells 34

1.3.4 Loss mechanisms in organic solar cells 35

1.4. Tandem solar cells 36

1.4.1 Motivation and operating principle 36

1.4.2 Tandem architectures: 2T, 3T, and 4T configurations 38

1.4.3 State-of-the-art of organic and hybrid tandem solar cells 40

Chapter 2 ..... **43**

Experimental Methods and Characterization Techniques **43**

2.1. Thin-film deposition techniques 44

2.1.1 Solution-processed deposition: spin-coating 44

2.1.2 Printing-based deposition: screen-printing 45

2.1.3 Vacuum deposition: thermal evaporation 46

2.1.4 Physical vapor deposition: RF magnetron sputtering 47

2.2. Laser scribing for thin-film electrode patterning 48

2.3. Characterization techniques 49

2.3.1 Electrical characterization of devices 49

a) Current-voltage (*J-V*) characteristics under AM1.5 G illumination 49

b) Current-voltage (*J-V*) characteristics under indoor illumination 53

c) Four-point probe conductivity measurements 53

d) Charge transport and mobility: SCLC method 54

e) Transient Photovoltage (TPV) measurements 56

f) Light-intensity dependence of J_{SC} and V_{OC} 57
g) Aging and operational stability measurements 58
2.3.2 Morphological characterization of thin films 59
a) Optical microscopy 59
b) Stylus profilometry 59
c) Scanning Electron Microscopy (SEM) 60
d) Atomic Force Microscopy (AFM) 61
e) Contact angle measurements 62
2.3.3 Optical and optoelectronic characterization 63
a) UV-Visible absorption spectroscopy 63
b) External Quantum Efficiency (EQE) 64
2.3.4 Structural characterization by Grazing-Incidence Wide-Angle X-ray Scattering (GIWAXS) 65
Chapter 3 67
Optimization of the Top Organic Solar Cell to be Integrated in an Organic/Silicon Tandem Cell 67
3.1. Material selection and device architecture of the wide bandgap top cell 68
3.1.1 Choice of the PM6:GS-ISO system 68
3.1.2 Device architecture: inverted structure 71
3.2. Device fabrication and sample preparation 73
3.3. Optimization of the PM6:GS-ISO active layer 73
3.3.1 Influence of solution concentration and film thickness 74
a) Solution concentration 74
b) Film thickness 75
3.3.2 Optimization of donor/acceptor ratio 77
3.3.3 Thermal annealing optimization 78
3.3.4 Solvent Additive Optimization 81
3.4. Solid Additive Engineering: F8T2 84
3.4.1 Motivation 84
3.4.2 Optimization of F8T2 Content and Impact on PV Performance 85
3.4.3 Optical Properties 86
3.4.4 Morphology and Structure 87
3.4.5 Charge Transport and Recombination 89
3.5. Indoor OPV: Development and application of the optimized top organic solar cell 96
3.5.1 Context, applications, and state-of-the-art 96
3.5.2 Spectral characteristics of indoor light sources 96
3.5.3 Relevance of wide-bandgap organic semiconductors for IOPV 99

3.5.4 IOPV performance of the optimized top cell under controlled illumination ... 100
3.6. Conclusion of Chapter 3 ... 104
Chapter 4 ... 107
Development, Optimization and Integration of Transparent Top Electrodes for Semi-Transparent Organic Solar Cells ... 107
4.1. Introduction ... 108
4.2. Comparative development of transparent top electrodes ... 109
4.2.1 Thermally evaporated oxide-metal-oxide electrodes ... 109
a) State-of-the-art and motivation ... 109
b) Physical principles ... 110
c) Optimization of the Ag interlayer ... 112
d) Optimization of the MoO_3 upper layer ... 113
4.2.2 Screen-printed silver-nanowires electrodes ... 115
a) State-of-the-art and motivation ... 115
b) Electrode fabrication and characterization ... 116
4.2.3 Spin-coated silver nanowires electrodes ... 117
a) State-of-the-art and motivation ... 117
b) Optimization of the Ag-NWs network ... 118
c) Laser patterning of Ag-NWs electrodes ... 121
4.2.4 Room-temperature sputtered ITO electrodes ... 127
a) State-of-the-art and motivation ... 127
b) Optimization of sputtering conditions ... 129
4.2.5 Selection of the transparent electrode ... 134
a) Figures of merit for transparent electrodes ... 134
b) Comparative assessment and electrode selection ... 135
4.3. Integration of the selected transparent electrode into semi-transparent organic solar cells 136
4.3.1 Integration into PM6:GS-ISO semi-transparent organic solar cells ... 137
a) Device architecture and transparent electrode integration ... 137
b) Photovoltaic performance ... 140
c) Electrical limitations and current collection optimization ... 144
4.3.2 Operational stability ... 147
4.3.3 Transferability toward emerging photoactive systems ... 150
a) Opaque reference devices ... 151
b) Semi-transparent devices ... 153
4.4. Conclusion of Chapter 4 ... 158

Chapter 5 ..... **161**
Organic/Silicon Tandem Solar Cells **161**
5.1. Introduction 162
5.2. IBC silicon bottom cells for hybrid OPV/Si tandem integration 163
5.2.1 Motivation for using IBC silicon solar cells 163
5.2.2 Evolution of the IBC architecture: from Generation 1 to Generation 2 163
5.2.3 Front-side engineering and electrical validation of the IBC bottom cells 166
a) Development and validation of the front-side treatment 166
b) Validation of the received IBC-Gen2 silicon bottom cells 167
5.3. Development and integration of the interfacial architecture for monolithic OPV/Si tandem cells 170
5.3.1 Requirements and selection of the interfacial layer 170
5.3.2 Compatibility with the organic photovoltaic stack 171
5.3.3 Scale-up toward IBC dimensions 176
5.4. Experimental implementation of the monolithic 3-terminal OPV/Si tandem cell 177
5.4.1 Fabrication of the monolithic tandem device 177
5.4.2 Electrical validation of the Si bottom cell after OPV deposition 181
5.4.3 Principle of the three-terminal electrical characterization 183
5.4.4 Electrical validation of the OPV top cell and limitations 183
5.5. Lateral multijunction OPV/Si solar cells based on the RAINBOW concept 186
5.5.1 Concept and motivation 186
5.5.2 Modeling and performance prediction of RAINBOW architectures 188
a) Modeling principles and assumptions 188
b) Simulation of OPV/Si RAINBOW lateral multijunction devices 190
5.5.3 Experimental validation of the RAINBOW concept 193
a) Experimental principle and Spectrum-on-Demand setup 193
b) Applications to OPV/Si RAINBOW lateral multijunction devices 194
5.6. Conclusion of Chapter 5 200
Chapter 6 ..... **203**
Conclusion and Outlook **203**
6.1. Conclusion 204
6.2. Outlook 208
Glossary **215**
References **223**
Publications and Presentations **243**

General Introduction

Since the onset of the Industrial Revolution in the 18th century, the unprecedented expansion of human activities has been paralleled by a significant increase in energy demand, particularly in the requirement for electricity, which is the most adaptable form of energy. By 2025, several centuries later, over 80 % of our primary energy supply and nearly 60 % of global electricity production continue to rely on fossil fuels (**Figure GI-1** and **Figure GI-2**), which substantially contribute to atmospheric CO_2 pollution.[1,2]

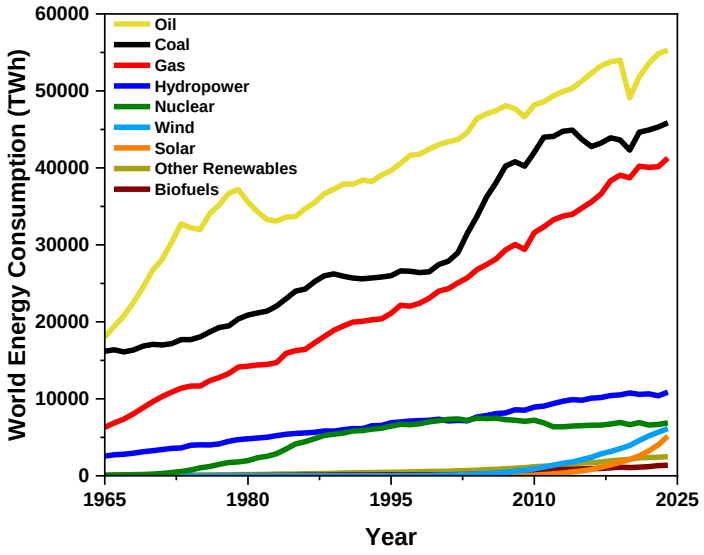

Figure GI-1: *World energy consumption by source, measured in terms of primary energy.*[1]

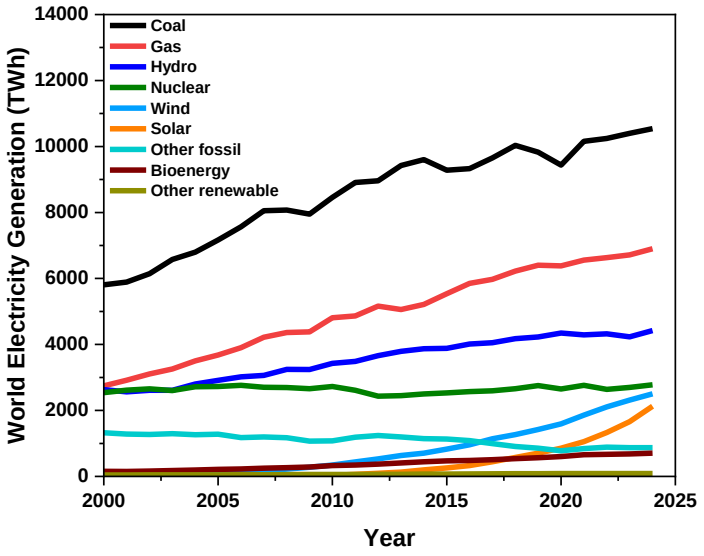

Figure GI-2: *World electricity generation by source.*[2]

The phenomenon known as the "greenhouse effect" is a primary driver of global warming, a critical issue in the 21st-century societal discourse. To mitigate greenhouse gas

emissions, international political agreements, such as the Paris Agreement (2015), have been established. These agreements aim to significantly advance the development of cleaner energy sources, commonly referred to as "renewable" energies. These include hydroelectric, wind, solar, and bioenergy. Although solar energy currently accounts for a relatively small portion of global electricity production, it is the most rapidly expanding renewable energy source worldwide, with its installed capacity continuously increasing (**Figure GI-3**).[2]

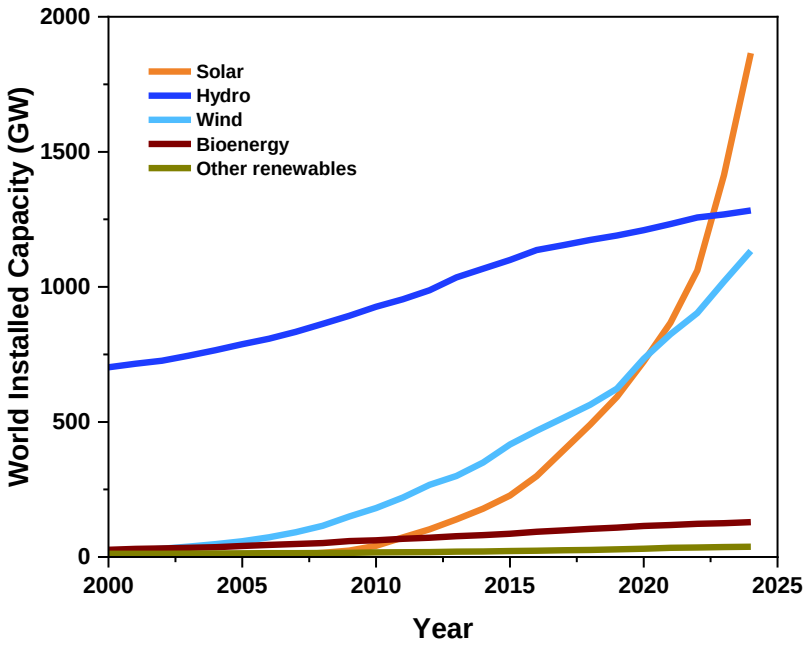

Figure GI-3: *World installed electricity capacity from renewables.*[2]

The primary appeal of solar energy is twofold. Firstly, the sun delivers more energy to the Earth in a single hour than the global consumption in an entire year, rendering it the most abundant energy source.[1] Secondly, it is an energy source that can be harnessed locally in residential settings as well as on a large scale in industrial facilities. These factors position photovoltaics (PV) as a pivotal technology in the transition toward sustainable energy. PV technologies are typically categorized into three generations, and the progression of their best research-cell efficiency, as documented by National Renewable Energy Laboratory (NREL), is illustrated in **Figure GI-4**.[3]

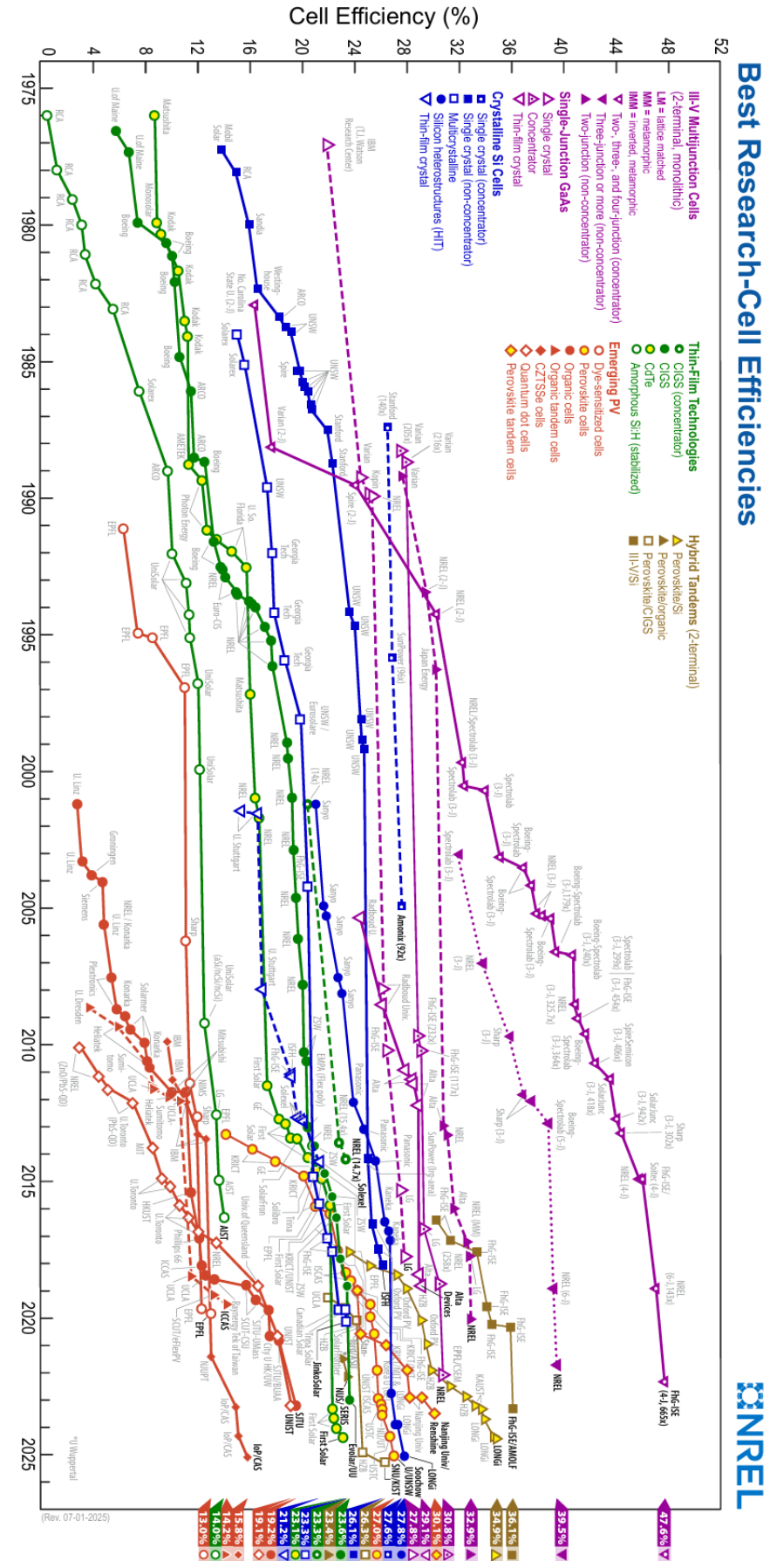

Figure GI-4: *Best research-cell efficiency chart provided by NREL in 2025.*[3]

First-generation: the first PV generation includes the technologies based on mono-crystalline (c-Si) and multi-crystalline (mc-Si) silicon, as well as III-V materials such as gallium arsenide (GaAs). These technologies are characterized by high efficiencies (27.9, 23.3 and 27.8 % for c-Si, mc-Si and III/V solar cells, respectively) and reliability, along with an extended service life.[3] However, they are notably rigid and heavy, and their manufacturing process involves a significant energy footprint with standard panels whose value today varies between 700 and 800 $kgCO_2eq/kWp$.[4]

Second-generation: the second PV generation describes the inorganic thin-film technologies, which include copper indium gallium diselenide (CIGS), cadmium telluride and sulphide (CdTe and CdS) and hydrogenated amorphous silicon (a-Si:H). This technology generally requires less raw material, with the active layer being approximately 100 times thinner than that of crystalline Si cells (a few µm compared to 200 µm). These technologies are also lighter, sometimes flexible, and can be produced at lower temperatures.[5] In addition, these thin-film layers are typically deposited using vapor-phase techniques, often involving plasma-assisted processes such as Plasma-Enhanced Chemical Vapor Deposition (PECVD) or Chemical Vapor Deposition (CVD), which enable precise control over thickness and material properties. Nevertheless, inorganic thin-film technology is less efficient than large-scale crystalline Si (23.6 % for CIGS compared to 27.9 % for c-Si).

Third-generation: the third PV generation includes the emerging thin-films technologies that utilize novel materials or innovative architectures. These include organic solar cells (OSC), perovskite solar cells (PSC), quantum dots (QD) solar cells and dye-sensitized solar cells (DSSC). The primary advantage of this technology lies in its wide variety of materials and architectures, and its very high potential for the future (efficiency, flexibility, transparency, low cost).[6] However, certain challenges persist, particularly concerning stability, durability and industrialization.[7]

Among all the commercial PV technologies, c-Si solar cells have achieved impressive progress over the past decades. Their high stability, mature fabrication ecosystem, and excellent power conversion efficiency (PCE), now exceeding 27.9 % in laboratory conditions, have made them the backbone of today's solar industry.[8] However, Si solar cells are now approaching their theoretical efficiency limit, known as the Shockley–Queisser (SQ) limit**,** estimated at around 29.4 % for single-junction devices under standard illumination (AM1.5G).[9] As a result, novel device architectures are required to sustain efficiency gains and reduce the levelized cost of electricity (LCOE). To overcome these fundamental limitations, the PV community is turning toward multijunctions, and notably tandem architecture. This combination integrates two sub-cells with complementary spectral absorption, as a promising solution to enhance overall device efficiency and then surpass the SQ limit.[10] In this context, combining an adapted technology as top cell with a bottom Si cell is attracting increasing interest.

Within emerging PV technologies, organic photovoltaic (OPV) represent a particularly attractive candidate for integration in Si-based tandem solar cells. Indeed, OPV has been the subject of particularly intense research and development over the last few decades, and is

now on the verge of widespread adoption by industry. This growing interest is largely due to the ability of OPV to produce lightweight and transparent solar cells with tunable optical absorption (a key point in spectral complementarity requirement for a tandem association) while maintaining low manufacturing costs.[11,12] Moreover, the predominantly carbon-based nature of organic semiconductors and the potential use of low-toxicity solvents may offer environmental advantages compared to lead-containing technologies such as PSC.[13] The manufacturing techniques associated with OPV also contribute significantly to cost reduction. For example, some layers of an OPV device can be manufactured using solution-based methods, which are compatible with scalable, high-yield production techniques such as roll-to-roll processing.[12] However, despite these advantages, their integration into hybrid organic/silicon (OPV/Si) tandem devices introduces specific challenges which remain insufficiently explored. In this context, this thesis aims to investigate, fabricate and characterize OPV/Si tandem solar cells in a three-terminal (3T) configuration. This work is carried out within the framework of the ORGANIST ANR project (ANR-22-CE05-0025).

The first chapter of this thesis will cover the fundamentals of PV, from the operating principle to the various technologies used in this study (Si, OPV, tandem architectures). The second chapter will focus on the manufacturing and characterization methods used throughout the thesis. The third chapter will focus on the optimization of the top cell of the tandem device, i.e. the organic solar cell (OSC). The fourth chapter will focus on the optimization of the top transparent electrode and its integration into the top OSC. The fifth chapter will deal with the integration of the semi-transparent OSC (ST-OSC) and the Si bottom cell, taking into account the study carried out on the interfacial layer. Finally, the last chapter will offer a conclusion and an outlook to bring this study to a close.

Chapter 1
Fundamentals and State-of-the-art of Silicon, Organic, and Silicon-based Tandem Photovoltaic Technologies

1.1. Photovoltaic effect and semiconductor fundamentals

The origins of the PV effect can be traced back to 1839 when French physicist Antoine César Becquerel and his son Alexandre Edmond Becquerel discovered that light could influence the electrical behavior of electrodes immersed in an electrolyte solution.[14] Several decades later, in 1887, Heinrich Rudolf Hertz provided a detailed description of this phenomenon in the renowned journal Annalen der Physik.[15] He demonstrated that when a metal surface is exposed to incident light, it emits electrons, a phenomenon now recognized as the photoelectric (PE) effect. Albert Einstein, building upon Max Planck's quantum theory of energy quanta, later proposed a theoretical model to explain this effect, earning him the Nobel Prize in Physics in 1921.[16] His work clarified that light can be understood as discrete packets of energy (photons), which can transfer their energy to electrons in a material. The PV effect, while conceptually similar to the PE effect, differs fundamentally in its physical manifestation. When light interacts with a metal and causes electron emission, the phenomenon is termed PE. In contrast, in the PV effect, light absorption in a semiconductor generates charge carriers that remain inside the material and are separated and collected by an internal electric field, typically created by a junction or built-in potential.

In quantum mechanics, materials are characterized by their electronic band structures, which determine how electrons behave within them. These energy levels, expressed in electron volts (eV), define the valence band (with an energy E_v, occupied by electrons) and the conduction band (with an energy E_c, where electrons can move freely). The distinction between metals and semiconductors lies in the relationship between these bands. In metals, valence and conduction bands overlap, enabling electrons to move freely and making them excellent conductors (**Figure 1-1**). By contrast, semiconductors exhibit a band gap, a forbidden energy range between E_v and E_c, where no electrons can exist. This gap energy (E_g) typically ranges from approximately 0.1 to 5 eV, depending on the material.

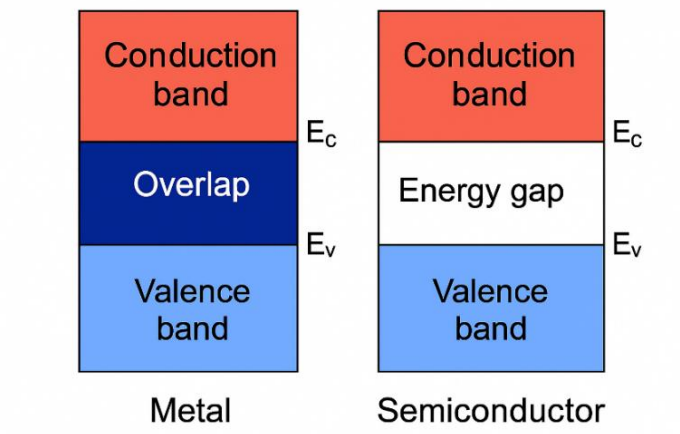

Figure 1-1: *Energy band diagram of a metal (overlapping bands) vs a semiconductor (distinct bandgap).*

Depending on the band structure of a material, light exposure can lead to different outcomes. In metals, sufficiently energetic photons can eject electrons entirely from the material (**Figure 1-2**). These electrons can then be accelerated, focused, and controlled using electromagnetic fields, forming electron beams that are widely used in imaging technologies such as electron microscopy.[17] In semiconductors, the situation differs. When a photon with energy greater than the band gap strikes a semiconductor, it can excite an electron from the valence band into the conduction band, leaving behind a positively charged "hole" (**Figure 1-2**). This process results in the generation of an electron-hole pair.

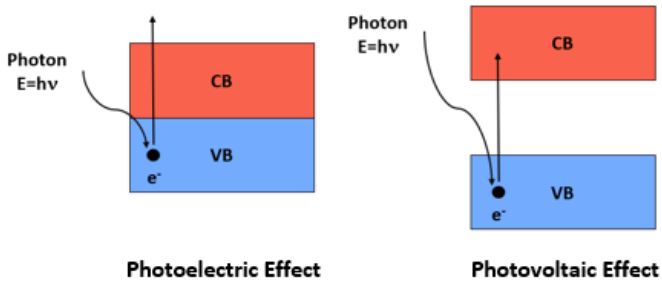

Figure 1-2: *Schematic comparison between PE and PV effects.*

By integrating appropriate semiconductor materials or electrodes and an internal electric field into the device, these charge carriers can be separated and collected, generating an electric current. This is the foundational operating principle behind PV devices, commonly referred to as solar cells.[18]

On the basis of these fundamental principles of light-matter interaction and charge carrier generation in semiconductors, a wide range of PV technologies has been developed.

1.2. Silicon solar cells

1.2.1 Silicon materials

Silicon solar cells currently represent the backbone of the PV industry and serve as the benchmark technology in terms of efficiency, reliability and industrial scalability. This technology dominates the global solar market, representing over 95 % of commercial solar panels.[19] This success stems from silicon's favorable optoelectronic properties: a bandgap of approximately 1.1 eV, high abundance, non-toxicity, and mature processing infrastructure. Over the years, both c-Si and mc-Si have been widely used as absorber materials for solar cells.

Monocrystalline silicon (c-Si) wafers are typically produced from single-crystal ingots grown using the Czochralski method (CZ). In this process, a seed crystal is slowly pulled from molten silicon, enabling the formation of a continuous and highly ordered crystal lattice. The absence of grain boundaries results in a low defect density, which reduces carrier recombination and enables high open-circuit voltages (V_{OC}) and long carrier lifetimes. Consequently, c-Si remains the material of choice for high-performance PV applications.[20,21] However, the CZ process is energy-intensive, with an energy demand for ingot growth typically reported in the range of 13-30 kWh·kg^{-1} of silicon produced.[22] This high energy consumption

arises from the need to maintain silicon above its melting point (1414 °C) for extended periods, typically 24 to 36 hours per ingot, combined with a slow crystal pulling rate and the precise thermal control required to ensure single-crystal growth.

Multicrystalline silicon (mc-Si) wafers are typically produced by directional solidification (casting), in which molten silicon is poured into a crucible and slowly cooled to form a solid ingot composed of multiple grains with different crystallographic orientations. In contrast to the CZ method used for c-Si, this process does not involve pulling a single crystal but rather relies on bulk solidification of the melt, which is less demanding in terms of process control and duration, with production cycles typically completed in 20-30 hours. The energy consumption at the ingot growth step is estimated at 4-8 $kWh \cdot kg^{-1}$, roughly 2-5 times lower than CZ growth.[23] As a result, the overall energy consumption of casting is generally lower than that of CZ growth. Furthermore, the casting process enables more efficient use of the silicon material due to the near-square geometry of the ingots. However, the presence of grain boundaries introduces recombination-active defects, which reduce carrier lifetime and limit device performance, typically resulting in efficiencies that are 2-3% (absolute) lower than those of c-Si cells.[3] Compared to c-Si, mc-Si technologies historically offered lower production costs due to simpler growth processes and higher throughput. However, this advantage has largely diminished with the industrial optimization of c-Si technologies. As of the early 2020s, the PV industry has largely transitioned toward c-Si, particularly for advanced high-efficiency architectures, which benefit from its superior material quality.

1.2.2 State-of-the-art silicon solar cell technologies

As shown in **Figure 1-3**, numerous Si-based solar cells architectures have been developed over time, such as Passivated Emitter and Rear Cell (PERC)[24], Tunnel Oxide Passivated Contact (TOPCon)[25], and Silicon Heterojunction with Intrinsic Thin Layer (SHJ).[26] Among these single-junction Si-based cells, a recent technology stands out for its efficiency and unusual architecture called **Interdigitated Back Contact (IBC).**[27] These cells feature both n^+ and p^+ contacts on the rear side of the cell, eliminating front-side shading entirely. Light enters through the bare front surface, allowing maximized optical absorption. Complex photolithography or laser doping techniques are used to define interdigitated contact regions (**Figure 1-3d**). The absence of front-side shading primarily enhances short-circuit current (J_{SC}), while the optimized rear-side passivation and contact design reduce recombination losses, leading to high V_{OC}, Fill Factor (FF), and overall PCE. The laboratory efficiencies recorded with such a technology are around 26.7 %.[28]

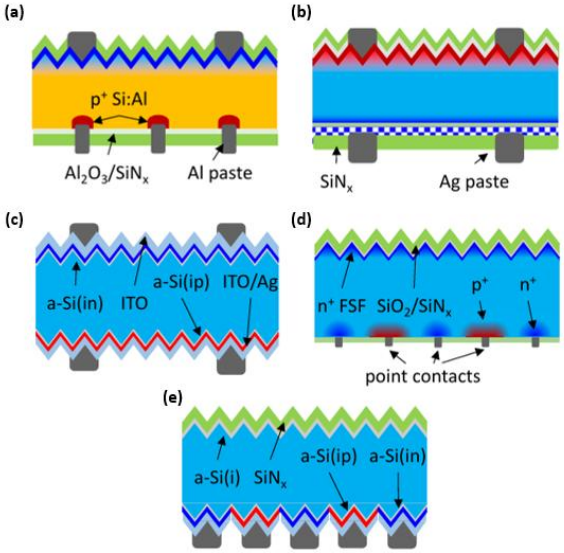

Figure 1-3: *Schematic representation of (a) PERC, (b) TOPCon, (c) SHJ, (d) IBC and (e) SHJ-IBC technologies.*[29]

Nowadays, the state-of-the-art silicon-based solar cells include **Silicon Heterojunction IBC (SHJ-IBC)** architectures, which combine the advantages of SHJ and IBC design. In such devices, a c-Si wafer acts as the light-absorbing layer, while ultra-thin a-Si:H layers are deposited on its surfaces to form the junctions. Typically, intrinsic a-Si:H (i-layer) is first deposited as a passivation buffer layer, followed by thin doped p^+ and n^+ a-Si:H layers that enable carrier-selective contacts. The IBC configuration places both contacts on the rear side of the device in an interdigitated pattern, eliminating front-side metallization and thus reducing optical shading losses. This architecture leverages the excellent surface passivation and low-temperature processing of SHJ, together with the zero-shading advantage of the IBC layout (**Figure 1-3e**).[29,30] Recent advances have optimized the rear contact design using doped a-Si and transparent conductive oxides (TCO)-free metallization. This architecture has achieved a record PCE of 27.81 % (LONGi, 2025).[31] As device architectures have evolved toward increasingly sophisticated contact and rear-side designs, the role of interfaces has become a central performance-limiting factor. In high-efficiency Si solar cells, interfacial recombination must be decreased to extremely low levels. This makes interface engineering and surface passivation key technological pillars.

1.2.3 Interfacial defects and passivation strategies in silicon solar cells

In high-efficiency c-Si based solar cells, the device performance is strongly dependent on the quality of the interfaces between the Si substrate and the dielectric or contact layers.[32] These interfaces govern carrier separation, collection, and recombination of photogenerated charges. Interface defects such as dangling bonds, lattice discontinuities, or impurities create electronic states within the Si bandgap that act as non-radiative recombination centers (via Shockley-Read-Hall processes).[33] The density of these defects (D_{it}) directly determines the effective carrier lifetime and limits the V_{OC} of the cell.[34] To mitigate these losses, surface

passivation is an essential step in the design of Si solar cells. It relies on two fundamental mechanisms: chemical passivation, which consists of saturating silicon dangling bonds (often via hydrogenation), and field-effect passivation, originating from the presence of fixed charges in dielectric layers that repel minority carriers.[35] These two effects are often combined to achieve an interface with minimal recombination activity.

IBC solar cells exhibit a specific configuration in which all the metallization and the selective n^+/p^+ regions are located on the rear side, while the front surface is entirely exposed to light to maximize absorption. This geometry imposes distinct requirements in terms of surface passivation. The front-side passivation must be optically transparent, thermally stable, and exhibit low surface recombination velocity (SRV), since no electrical contact is present on that side. It also serves as an antireflective coating (ARC) to minimize optical losses.[36] In contrast, the rear-side passivation must combine excellent chemical passivation on the non-contacted areas with effective carrier selectivity in the contacted regions, where conductive and doped materials ensure carrier transport while minimizing recombination.[37] Consequently, the materials and stacks employed differ according to their position within the cell and the desired function. Currently, the most commonly used layers include intrinsic hydrogenated amorphous silicon (a-Si:H(i))[38] and aluminum oxide (Al_2O_3)[39] for chemical and field-effect passivation of the c-Si surface prior to the deposition of the upper layers, ultrathin silicon oxide (SiO_x)[39] or silicon nitride (SiN_x) films as dielectric barriers and optical tuning layers.

Thermal SiO_2 is primarily used for front-side passivation on non-contacted surfaces. It remains the benchmark material for chemical passivation, offering an extremely low D_{it}. SiO_2 is particularly effective on the front surface of IBC cells, where no conduction path is required, owing to its excellent transparency and chemical stability. On the rear side, however, its insulating nature and the high temperatures required for growth (> 900°C) make it poorly compatible with selective back contacts (poly-Si, a-Si:H, metals, etc.), as it would hinder carrier transport and degrade temperature-sensitive layers during annealing.[39]

SiN_x:H is widely used on the front surface as both a capping and ARC, often combined with SiO_2 in a SiO_2/SiN_x stack. This stack provides field-effect passivation due to fixed charges (typically positive in SiN_x:H, depending on the substrate and stack configuration) and releases hydrogen during post-deposition annealing, improving the chemical passivation of the underlying SiO_2. Its tunable refractive index (approximately 1.9-2.1) makes it an effective ARC, crucial for maximizing the J_{SC}. On the rear side, SiN_x:H can be employed as a protective or diffusion-barrier layer, but not as a direct contact material with Si, since it does not allow selective carrier transport. It is often deposited over SiO_2 or poly-Si layers to stabilize the surface and enhance mechanical robustness.

Al_2O_3 can also be deposited for front-side passivation, although this remains less common than SiO_2/SiN_x stacks. While it provides excellent passivation on p-type Si, its relatively high optical absorption and unsuitable refractive index make it less attractive for front-side optical management. Conversely, it has become the reference material for rear-side passivation of non-contacted areas in IBC architectures, particularly on n-type substrates. Its high density of negative fixed charges induces a strong field-effect repulsion for minority

holes, thereby suppressing recombination. When combined with SiN_x (in Al_2O_3/SiN_x stacks), it offers enhanced thermal stability and mechanical protection while remaining compatible with moderate annealing temperatures.

a-Si:H is widely employed on the front surface of SHJ architectures. Intrinsic layers (a-Si:H(i)) effectively saturate interface defects while maintaining optical transparency, whereas doped layers (a-Si:H(n/p)) provide carrier selectivity when required. On the rear side, a-Si:H is used in SHJ-IBC or hybrid designs to form selective n^+ or p^+ contacts while preserving excellent passivation through low-temperature processes (< 200°C).[38]

Poly-Si/SiO_x structures are not used on the front surface due to their high optical absorption, which would significantly reduce the transmitted photon flux. On the rear side, however, poly-Si/SiO_x stacks are currently among the most effective passivation and contact schemes for IBC cells. The ultrathin tunnel oxide (1-2 nm) ensures outstanding chemical passivation, while the doped poly-Si layer provides selective carrier conduction through tunneling. These structures combine low recombination, low contact resistance, and excellent thermal stability, establishing them as the state-of-the-art for high-efficiency IBC devices.

In multijunction architectures incorporating a Si bottom cell, surface and interfacial passivation become even more critical. Here, the role of passivation extends beyond simple recombination suppression, it must also ensure chemical and energetic compatibility between two materials of distinct natures (inorganic, organic, or hybrid). On the Si sub-cell, passivation must maintain a minimal SRV to preserve the tandem V_{OC}, remain optically transparent to allow maximum light transmission to the lower cell, and be thermally stable during the deposition of the upper sub-cell, often performed at low temperatures (< 200°C for organic materials). It must also act as a diffusion barrier against solvents, metal ions, or halides originating from the upper layer, particularly in PSC/Si tandems. In OPV/Si tandems, which are the focus of this work, these interfacial layers have to ensure energy-level alignment between the organic absorber and the Si, while preventing chemical degradation of the c-Si surface caused by solvent exposure. They may also serve to enhance the mechanical and chemical compatibility between the two junctions, thereby improving both device stability and overall performance.

1.3. Organic solar cells

1.3.1 Organic semiconductors: electronic structure and optical properties

Organic semiconductors, also known as π-conjugated materials, are based on carbon-rich molecules or polymers in which alternating single and double bonds enable the delocalization of π-electrons along a conjugated backbone. This delocalization plays a key role in their optoelectronic properties. To understand how these materials work, it is essential to consider the electronic configuration and bonding characteristics of carbon atoms. In its ground state, a carbon atom has the configuration $1s^2\ 2s^2\ 2px^1\ 2py^1\ 2pz^0$. Upon promotion of one 2s electron to the empty 2pz orbital, the carbon can form four covalent bonds. In molecules like ethane, carbon atoms undergo sp^3 hybridization, forming four σ-bonds.

However, in systems such as ethene, only three sp^2 hybrid orbitals are formed: two bond with hydrogen atoms and one with another carbon. The remaining unhybridized 2pz orbital contributes to the formation of a π-bond through side-to-side overlap with an adjacent carbon's 2pz orbital, resulting in a π and π* molecular orbital. In more extended π-conjugated systems, common in organic semiconductors, this bonding pattern repeats, allowing the π-electrons to delocalize across the molecule or polymer chain. This delocalization facilitates charge transport, a fundamental requirement for semiconducting behavior.

From a molecular orbital perspective, the π-orbitals across the conjugated system combine to form energy states. The bonding π-orbitals form a lower-energy π-state (analogous to a valence band), while the anti-bonding π* orbitals create a higher-energy π*-state (similar to a conduction band). The energy difference between the highest occupied molecular orbital (HOMO) and the lowest unoccupied molecular orbital (LUMO) defines the electronic bandgap (E_g) of the material.[40] This gap typically ranges from approximately 1 to 3 eV in organic semiconductors, enabling them to absorb light in the visible range. An electron can be excited from the HOMO to the LUMO through the absorption of a photon, leading to the formation of an excited state. This photoexcitation process is at the heart of applications such as OPV.

1.3.2 Photoconversion mechanisms in organic solar cells

The conversion of photons from the light source into electricity in an OSC can be divided into four steps, as illustrated in **Figure 1-4**.

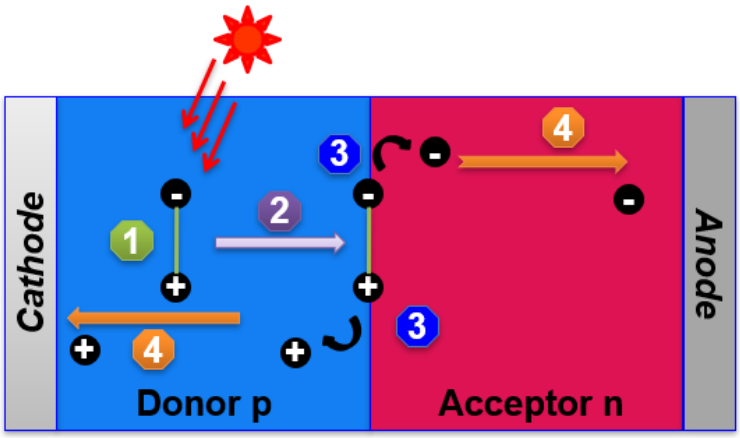

Figure 1-4: *Schematic representation of the mechanisms for converting photons into electricity in an OSC with (1) the absorption of photons and the generation of excitons, (2) the transport of excitons by diffusion, (3) the dissociation of excitons into free charges and (4) the transport and collection of the charges.*

The first step of the conversion is the **absorption of photons and the generation of excitons**. When an organic semiconductor absorbs a photon, an electron is promoted from its ground state in the HOMO to an excited state in the LUMO, using the energy provided by the photon. This electronic transition leaves behind a positively charged "hole" in the HOMO. Due to the Coulombic attraction between the negatively charged excited electron in the LUMO

and the positively charged hole in the HOMO, the two remain bound together, forming a neutral quasi-particle known as an exciton. The energy difference between the bound electron-hole pair is referred to as the optical bandgap ($E_{g,opt}$), which is generally smaller than the electronic bandgap. This is because the electron is promoted to a level slightly below the LUMO and the hole remains at a level slightly above the HOMO due to their mutual attraction. The optical bandgap can be estimated from the onset of the material's absorption spectrum (λ_{Edge}) using **Equation 1-1**.

$$E_{g,opt} = \frac{hc}{\lambda_{Edge}} \quad \textbf{(1-1)}$$

where *h* is Planck's constant and *c* the speed of light.

In organic semiconductors, which are typically disordered and possess low dielectric constants, the excitons formed are tightly bound and spatially localized. These are known as Frenkel excitons, characterized by a small radius (typically < 10 Å) and a relatively high binding energy (E_b) ranging from 0.1 to 1 eV.[41] Unlike Mott-Wannier excitons, common in inorganic semiconductors with high dielectric constants and large exciton radii, Frenkel excitons cannot be thermally dissociated at room temperature due to their strong Coulombic binding. Therefore, in organic semiconductors, thermal energy alone is insufficient to separate the exciton into free charge carriers. Efficient exciton dissociation requires the presence of a second organic semiconductor material with appropriately offset energy levels.

The second and third steps of the process are the **transport of excitons by diffusion and the dissociation of excitons into free charges**.

Once a Frenkel exciton is generated within an organic semiconductor, it is capable of diffusing through the material. However, its lifetime is extremely short (on the order of a few hundred picoseconds) which limits its diffusion length to approximately 10-30 nm. This short lifetime is primarily related to strong electron-phonon coupling and efficient non-radiative relaxation pathways, while the strong Coulomb binding energy prevents spontaneous exciton dissociation into free charge carriers. If the exciton does not reach a donor-acceptor interface within this diffusion length, it undergoes recombination through radiative (fluorescence) or non-radiative (vibrational) relaxation processes, in which the excited electron returns to its ground state. This process is known as geminate recombination, as it involves recombination of an electron and a hole originating from the same excitonic event.[42] To mitigate geminate recombination and enhance exciton dissociation, the active layer of OSC typically adopts a bulk heterojunction (BHJ), a finely intermixed blend of two organic semiconductors: an electron donor and an electron acceptor (**Figure 1-5**).[43] In this architecture, excitons generated within the donor or acceptor phases have a high probability of reaching a donor-acceptor interface before recombining.

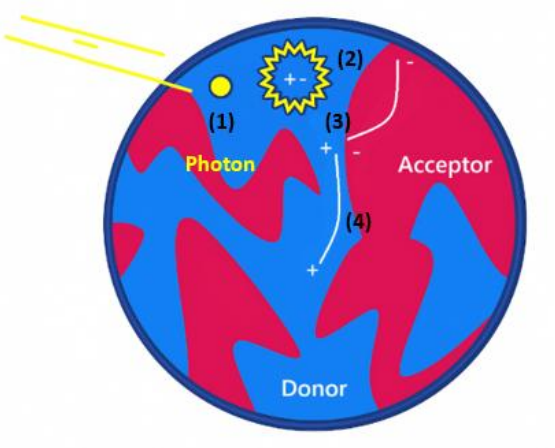

Figure 1-5: *Photogeneration processes in the BHJ active layer.*

At the donor-acceptor interface, the energetic offset between the LUMO levels of the two materials provides the driving force for charge transfer. Specifically, the electron transitions from the LUMO of the donor to the lower-energy LUMO of the acceptor. This charge transfer results in the formation of a charge-transfer (CT) state, comprising a spatially separated electron and hole. Although the electron and hole remain coulombically bound in this state, the increased distance between them reduces their interaction strength. If the separation between the two charges exceeds the Coulomb capture radius, also referred to as the Onsager radius, defined as the distance at which the Coulomb binding energy equals the thermal energy k_BT, the electron and hole can escape their mutual attraction and become free charge carriers capable of contributing to photocurrent. A similar process occurs when the exciton is formed in the acceptor phase: the hole can transfer from the HOMO of the acceptor to the higher-energy HOMO of the donor, again driven by a favorable energy level offset. This cascade alignment of energy levels is critical for efficient charge separation.

The last part of the conversion process is the **transport and collection of the charges**. Once the exciton is dissociated at the donor-acceptor interface, the resulting free charges (electrons and holes) must be transported to their respective electrodes. The efficiency of this charge transport process is strongly influenced by the morphology of the BHJ. Charge transport occurs via two primary mechanisms. The first is intrachain transport, where charges move along a single conjugated polymer chain. The second is interchain transport, which involves hopping from one π-orbital to another across adjacent chains.[44] In this context, electrons typically hop between acceptor domains, while holes move across donor domains. The ability of the active layer to support efficient transport of both types of charge carriers is quantified by their mobility, denoted as μ_e for electrons and μ_h for holes, with units of $cm^2.V^{-1}.s^{-1}$. These mobilities are determined by both the intrinsic properties of the organic semiconductors and the nanoscale morphology of the BHJ.

For optimal performance in OSC, the active layer must exhibit ambipolar transport behavior, meaning that both charge carriers possess sufficiently high and balanced mobilities. A mismatch in mobilities can lead to space-charge accumulation, which in turn creates a counteracting electric field that impedes further charge separation and extraction.[45] Charge

carrier mobility can be measured in two directions. First of all vertical mobility (along the direction of current flow in the device) and then lateral mobility (in-plane). Once charges reach the interfaces with the electrodes, they are extracted by conductive materials. The difference in the Fermi levels of the electrodes creates an internal electric potential that drives the charges toward their respective collecting electrodes. However, not all metals efficiently collect both types of charges. For example, calcium cannot effectively collect holes due to its shallow Fermi level, while gold is ineffective at collecting electrons due to its deep Fermi level. This misalignment creates energetic barriers for charge extraction. To overcome these barriers, interfacial transport layers are introduced. The hole transport layer (HTL) is designed with a HOMO level close to that of the donor, facilitating efficient hole extraction, whereas the electron transport layer (ETL) features a LUMO level close to that of the acceptor, enabling efficient electron extraction. In addition to lowering energy barriers, these layers act as selective contacts as the HTL blocks electrons (via a deep LUMO) while the ETL blocks holes (via a deep HOMO). Thus, both HTL and ETL enhance charge selectivity and reduce recombination at the electrodes. These intermediate layers often combine both charge transport and charge selection functionalities.

Two different architectures, direct and inverted, are possible for single junction OSC (**Figure 1-6**). In both cases, the substrate consists of glass and the bottom electrode is a transparent conductive layer (TCL) to allow light to reach the active layer.[46] The conventional (direct) architecture has been widely used due to its well-established charge extraction layers. However, it typically suffers from poor environmental stability, mainly due to the use of low work function metals that are sensitive to oxygen and moisture. In contrast, the inverted architecture offers significantly improved device stability, as it relies on more stable electrode materials and interfaces, making it more suitable for long-term operation and large-scale fabrication.[47,48] In this work, the inverted architecture is used, and the corresponding fabrication details are presented in **Chapter 2**.

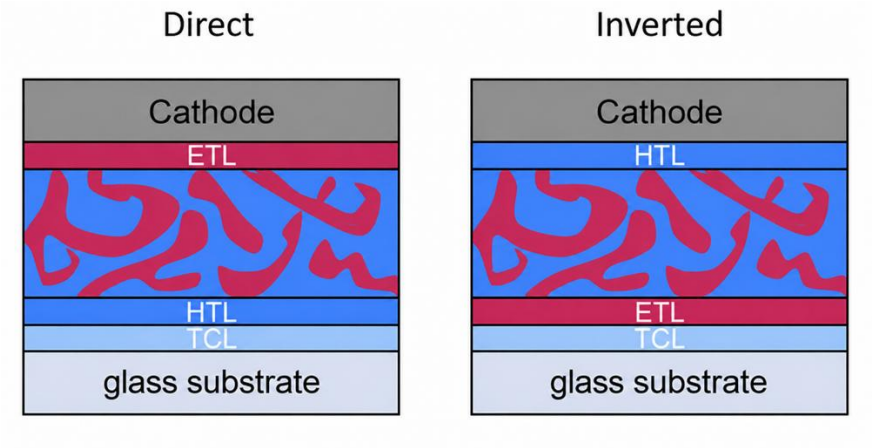

Figure 1-6: *Direct and inverted architectures for single-junction OSC.*

Once extracted, the charges are directed into the external circuit by the built-in electric field of the device, completing the PV process.

1.3.3 State-of-the-art of organic solar cells

OSC have undergone rapid and transformative evolution since their first demonstration in the 1980s. Initially, the field was largely exploratory, with the first OSC based on a bilayer heterojunction using copper phthalocyanine and perylene derivatives showing a PCE below 1 % (Tang, 1986).[49] These early architectures suffered from limited exciton dissociation and poor charge transport, primarily due to their low dielectric constants and short exciton diffusion lengths.

A major leap came with the development of the BHJ concept in the mid-1990s, which involves blending donor and acceptor materials into a single photoactive layer (PAL).[50] This interpenetrated network drastically improved the PCE to about 2.9 % by increasing the donor-acceptor interfacial area, enhancing exciton dissociation and improving charge extraction.[50]
Fullerene derivatives, such as [6,6]-phenyl-C_{61}-butyric acid methyl ester (PCBM), are cage-like carbon molecules that have been extensively used as electron acceptors in organic solar cells due to their high electron affinity, efficient electron transport properties, and favorable nanoscale phase separation with donor materials. However, fullerene acceptors exhibit several intrinsic limitations: weak light absorption in the visible range, restricted tunability of energy levels, and morphological instability, which limited record PCE to around 12 %.[51]

These drawbacks paved the way for the emergence of non-fullerene acceptors (NFAs), a class of π-conjugated organic semiconductors specifically engineered to overcome the intrinsic limitations of fullerene derivatives by offering tunable energy levels, strong and broad optical absorption, and improved control over intermolecular interactions through molecular design.[52] NFAs are a class of π-conjugated organic semiconductors specifically engineered to overcome the intrinsic limitations of fullerene derivatives, offering tunable energy levels, strong and broad optical absorption, and improved control over intermolecular interactions through molecular design. NFAs, such as the Y-series (e.g., Y6, Y5), offer strong and broad absorption profiles, adjustable energy levels, and enhanced thermal and morphological stability. The adoption of NFAs resulted in an unprecedented surge in OSC efficiency, with certified single-junction devices reaching PCE values above 18.6 % (in 2021) in laboratory conditions.[53]
Concurrently, significant effort was made to design donor polymers with finely tuned HOMO/LUMO levels to optimize charge transfer and minimize energy losses.[54] The synergy between low-bandgap (LBG) NFA and high-performance donor polymers enabled near-optimal absorption of the solar spectrum and suppressed voltage losses, thus pushing the limits of device efficiency and stability.

More recently, the field has moved beyond binary blends toward ternary[55] and even quaternary or higher-order multicomponent systems.[56] In these architectures, additional donors or acceptors are incorporated into the binary BHJ to enhance light harvesting, improve charge transport, or optimize morphology. Ternary OSC, for example, can leverage complementary absorption spectra and cascade energy level alignments to facilitate exciton dissociation and charge collection. These blends also offer better control over domain purity

and size within the active layer, which is crucial for maintaining efficient charge separation and suppressing recombination. Nowadays, record efficiencies for OSC are moving toward the theoretical limits of single-junction devices, with certified values exceeding 20.8 %.[57] This progress has been supported not only by molecular design but also by improved device engineering, including interfacial layers, optimized electrode work functions, and advanced fabrication techniques such as sequential deposition and post-processing treatments (e.g., solvent additives, thermal annealing).[58] Despite these remarkable advances in materials design and device engineering, the performance of OSC remains limited by a variety of intrinsic and extrinsic loss mechanisms.

1.3.4 Loss mechanisms in organic solar cells

In an ideal OSC, each photon absorbed within the PAL would result in the generation of one free electron-hole pair, with the electron and hole subsequently collected at their respective electrodes. However, in real systems, several loss mechanisms occur at different stages of the PV process, limiting the overall device efficiency. Understanding these mechanisms is key to improving the performance of OSC.

The first category of losses corresponds to geminate recombination, which occurs when the electron and hole, generated from the same photon, recombine before being fully separated into free charge carriers.[59,60] This process can occur during exciton diffusion, as each exciton has a finite diffusion length (typically ranging from 10 to 30 nm) depending on the material. Since this length is often shorter than the PAL thickness, many excitons fail to reach the donor–acceptor interface and instead decay back to the ground state. This process is generally radiative and can be detected using photoluminescence (PL) measurements. Geminate recombination can also take place at the donor-acceptor interface. Once an exciton reaches the interface and forms a CT state, the electron and hole remain coulombically bound. Recombination may then occur directly from the CT state, either radiatively or via a transition through a molecular triplet state. Radiative CT-state recombination typically manifests as a red-shifted PL or electroluminescence (EL) signal, while non-radiative CT recombination, which occurs on the sub-nanosecond timescale, requires time-resolved techniques such as transient absorption spectroscopy (TAS) for proper investigation.

Once the electron and hole are fully separated, losses can still occur via non-geminate recombination pathways, involving charges that originate from different photon absorption events.[61] These mechanisms include first Langevin (bimolecular) recombination, which occurs when free electrons and holes encounter one another and recombine. In organic semiconductors, this recombination process is often significant due to the combination of relatively high charge carrier densities and morphological disorder. Within the Langevin framework, the recombination rate scales with the sum of the electron and hole mobilities and with the product of the charge carrier densities. The Langevin model therefore provides a useful phenomenological description of bimolecular recombination in disordered organic semiconductors. Another important pathway is trap-assisted recombination, when charge carriers become trapped in defect or impurity states located within the bandgap.[62] If a trapped

carrier encounters an opposite free carrier, recombination can occur. Depending on the trap energy relative to the bandgap, carriers may also be thermally released. This form of recombination is often linked to morphological disorder and the presence of energetic inhomogeneities within the PAL. Unlike geminate recombination, which is fast (on the sub-nanosecond timescale), non-geminate recombination typically occurs over longer timescales (ns to μs). A variety of electrical and optical techniques are employed to characterize these processes and quantify their impact on device performance.

1.4. Tandem solar cells

1.4.1 Motivation and operating principle

In a conventional single-junction solar cell, incident photons with energy greater than the material's bandgap can excite electrons from the valence band to the conduction band, generating electron-hole pairs that contribute to an electric current under the influence of an internal electric field. However, single-junction architectures suffer from fundamental limitations. The most well-known is the SQ limit, which sets the theoretical maximum PCE of an ideal single-junction cell under AM1.5G illumination to approximately 33.16 %, for a material with an optimal bandgap of around 1.34 eV (**Figure 1-7**).[63]

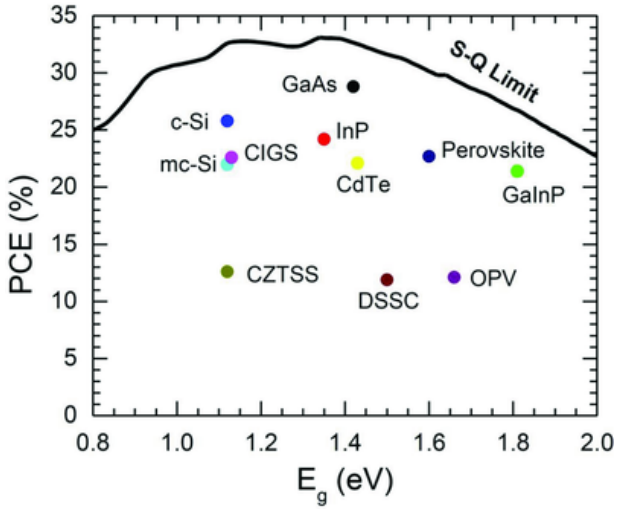

Figure 1-7: *Shockley-Queisser limit depending on the bandgap and the technology of the semiconductor material (2018).*[64]

In practice, this limit is reduced due to various intrinsic loss mechanisms. First, low-energy photons (below the bandgap) are not absorbed. Second, high-energy photons lose their excess energy as heat through thermalization. Finally, additional losses occur due to carrier recombination, contact resistance, and parasitic absorption.[65] To overcome these fundamental limitations, tandem solar cells have emerged as a powerful strategy, particularly by reducing thermalization losses through spectral splitting. In such architectures, two photovoltaic materials with decreasing bandgaps are combined to better match the solar spectrum. As shown in **Figure 1-8**, the key concept is to have a wide bandgap (WBG) top cell

absorbing high-energy photons (e.g., in the blue region), while lower-energy photons pass through and are absorbed by a low-bandgap bottom cell (e.g., in the red region). [66–68]

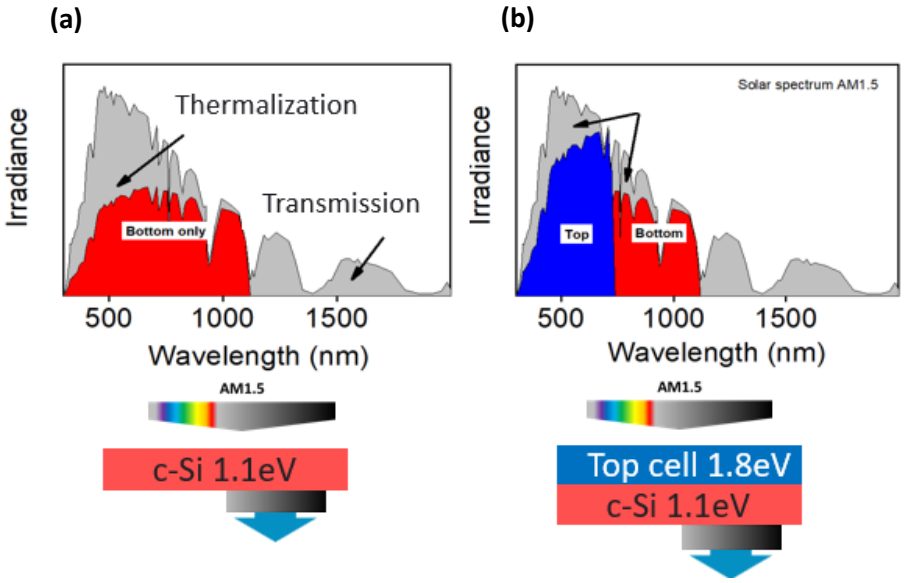

Figure 1-8: *Illustration of thermalization and transmission losses: (a) in a single junction c-Si cell (red) and (b) in a tandem cell involving OPV as the top cell (blue) and c-Si as the bottom cell (red).*

This spectral splitting reduces thermalization losses by more efficiently matching the photon energy to the absorber bandgap, thereby limiting excess energy dissipation as heat. As a result, tandem architectures can surpass the SQ limit. The theoretical efficiency of tandem cells can exceed 40 %, depending on the specific configuration and materials used (**Figure 1-9**).[69]

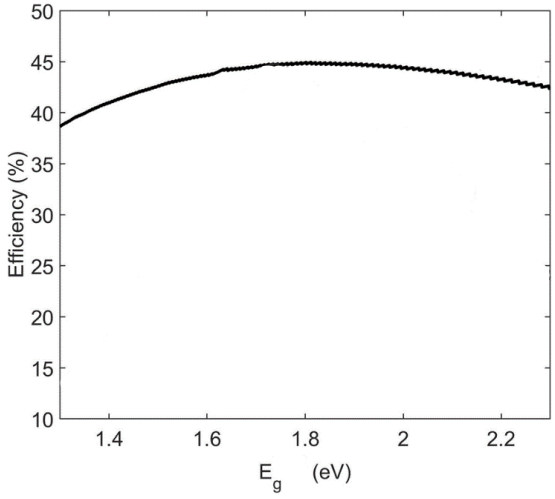

Figure 1-9: *Detailed balance efficiency limit of Si (1.12 eV) based architectures as a function of the top cell bandgap under AM1.5G illumination.*[69]

Silicon-based tandem solar cells are currently at the forefront of PV research, leveraging the industrial maturity and high efficiency of c-Si as a bottom cell combined with a WBG top cell. Notably, PSC/Si tandems have recently achieved PCE above 35 %, while other

approaches such as III–V/Si tandems have also demonstrated efficiencies exceeding 36.1 %, highlighting the strong potential of tandem strategies for next-generation photovoltaics.[3] For c-Si, the most widely used PV material today, the bandgap is 1.12 eV, leading to a more constrained SQ limit of about 29.4 **%**, taking into account Auger recombination. Current commercial Si solar cells have achieved PCE above 27.81 **%**, approaching this theoretical limit. In parallel, alternative materials such as organic semiconductors are being explored as wide-bandgap top cells in tandem configurations. Although OSC exhibit lower efficiencies in single-junction architectures, they offer unique advantages including metal-free photoactive materials, tunable bandgaps, solution processability, and compatibility with low-temperature fabrication. These properties make them promising candidates for integration in hybrid tandem devices with silicon.[70–73]

In the case of the OPV/Si tandem cells investigated in this work, combining an organic top cell with a silicon bottom cell enables several key advantages. Organic materials can be engineered with WBG, typically in the 1.6 to 2.0 eV range, making them ideal candidates for the top cell (**Figure 1-9**), which absorbs the high-energy part of the solar spectrum. The underlying c-Si bottom cell, with its LBG, is then well-suited to absorb the lower-energy photons that pass through the top layer. This spectral complementarity between organic and Si materials is a key motivation for this tandem association. Furthermore, organic semiconductors can generally be processed at low temperatures (< 200 °C), which is compatible with the underlying Si layers and enables monolithic integration without damaging the Si bottom cell.[74] Deposition techniques such as spin-coating, printing, or slot-die coating allow for low-cost, scalable fabrication processes.[75] This hybrid architecture thus combines the maturity, long-term stability, and high performance of Si with the tunability, flexibility, and cost-effectiveness of OPV**.** Consequently, OPV/Si tandem solar cells represent a highly promising route to exceed the performance limitations of conventional technologies while maintaining manufacturing scalability and material compatibility for next-generation PV systems.

1.4.2 Tandem architectures: 2T, 3T, and 4T configurations

Tandem solar cells can be implemented through various architectures, depending on how the sub-cells are connected and integrated. There are three main architectural approaches, commonly classified based on their electrical interconnection scheme: two-terminal (2T), three-terminal (3T), and four-terminal (4T) configurations.

The **2T** configuration, also known as monolithic tandem, is the most compact and industry-compatible architecture. In this setup, the top and bottom sub-cells are connected in series, and the entire tandem structure is treated as a single PV device with one pair of external electrodes (**Figure 1-10a**).[76] The advantage of such a configuration is that it is compact and compatible with standard module interconnection and requires fewer processing steps compared to multi-terminal configurations. However, there are several challenges to overcome with such a configuration. First, current matching is required. Since the sub-cells are in series, the total current is limited by the sub-cell producing the lowest current.

Therefore, the optical and electrical design must ensure spectral balancing, where the current generated by the top cell closely matches that of the bottom cell under standard illumination. Second, the interconnecting layer between the two sub-cells must be electrically conductive and optically transparent (commonly a recombination layer or tunnel junction) to allow efficient charge transfer and photon transmission.

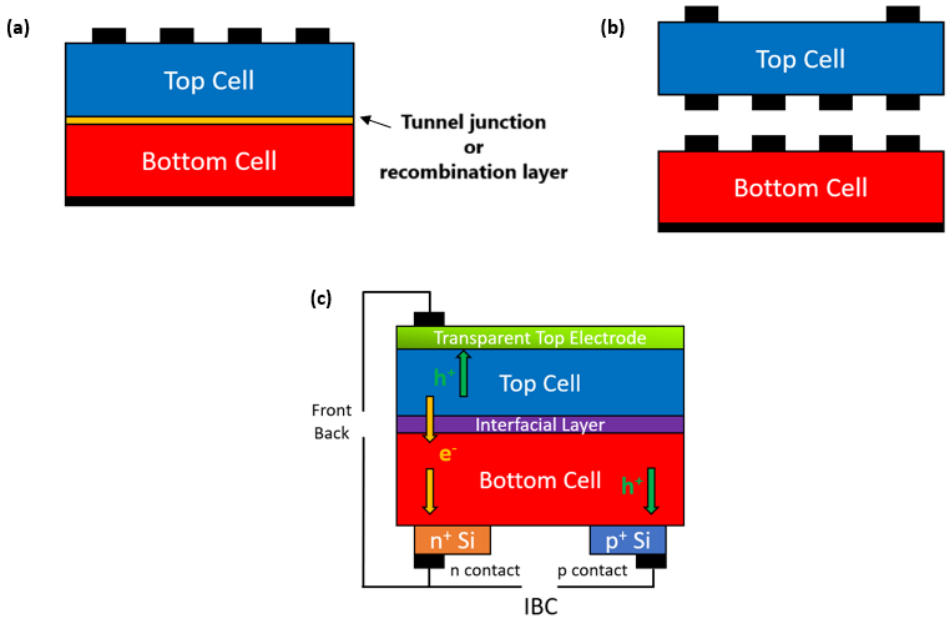

Figure 1-10: *Tandem cell in (a) 2T, (b) 4T and (c) 3T configuration.*

The **4T** architecture involves two independent solar cells, optically stacked but electrically separated, each with its own pair of terminals and power output. The top cell absorbs high-energy photons, while the remaining light is transmitted to the bottom cell (**Figure 1-10b**).[77] Since both sub-cells operate independently, there is no current-matching requirement, and each can operate at its maximum power point. However, optical coupling between the layers is crucial. Transparent substrates or intermediate optical layers are often used to maximize photon transmission to the bottom cell. The advantages are the high design flexibility for materials and thicknesses. Each cell can be optimized independently, simplifying development. For laboratory research, such a configuration can be ideal for early-stage prototyping of tandem systems combining different technologies.

In recent years, **3T** tandem configurations have attracted increasing attention as an intermediate solution between 2T and 4T designs. Several studies, particularly on perovskite/Si tandems, have demonstrated that 3T architectures can mitigate current-matching constraints while maintaining a relatively simple device structure. This approach is especially relevant for hybrid tandems combining sub-cells with different electrical characteristics, reinforcing the interest of 3T configurations for OPV/Si systems. In this work, the 3T architecture is used. The 3T configuration is a hybrid configuration that lies between 2T and 4T. It includes one shared electrode between the sub-cells, while keeping independent contacts for the other terminals.[78] There are two typical types of 3T architectures. The first is referred to as "series-interconnected 3T". In this case, the sub-cells share a common middle

contact, while the top and bottom cells have their own outer terminals. The second is referred to as "parallel-interconnected 3T". In this configuration, sub-cells are optically stacked, and the electrical output is combined at the shared contact. The latter is based on IBC-Si cell as bottom cell and is used in this work (**Figure 1-10c**). This configuration allows partial decoupling of the current generation in the sub-cells, reducing the strict current-matching requirement present in 2T designs. The main advantage lies in the reduced sensitivity to current mismatch. This feature makes 3T particularly attractive for hybrid tandems combining technologies with different current-voltage characteristics, such as OSC and Si. In the case of a 3T OPV/Si tandem solar cell, the front contact is used to collect the holes photogenerated in the OSC and the back contacts (p and n) are used to collect the holes photogenerated in the Si cell and the electrons photogenerated in both the organic and the Si cells, respectively. The main challenges of such a configuration are to design a transparent electrode on top of the device to optimize the illumination of the tandem cell and to design an interfacial layer between both cells that allows the electrons generated in the OSC to pass into the Si while blocking holes.

1.4.3 State-of-the-art of organic and hybrid tandem solar cells

Silicon-based tandem solar cells currently represent the most advanced multijunction photovoltaic technologies. PSC/Si tandems have achieved certified efficiencies above 33 %, making them leading candidates for industrial deployment. In parallel, III–V/Si tandems have demonstrated efficiencies exceeding 35 %, although their high fabrication cost remains a limitation for large-scale applications. CIGS/Si tandems have also been investigated as an alternative approach, benefiting from good spectral complementarity and compatibility with thin-film processing. Numerous tandem solar cell architectures incorporating either organic or Si sub-cells have been investigated and have demonstrated promising potential.

Firstly, **OPV/OPV tandem solar cells** have achieved a certified PCE of 20.6 %.[67] Both sub-cells are organic BHJ devices incorporating WBG donor-acceptor systems to enable high V_{OC} values. The state-of-the-art OPV/OPV tandem is integrated in a 2T architecture, featuring a ternary blend (PBDB-TCl:AITC:BTP-eC9) top cell, a binary blend (PFBCPZ:AITC) bottom cell, and an optimized interconnecting layer to minimize voltage losses. Key innovations include the use of ternary acceptors to suppress non-radiative recombination, improve morphology, and enhance V_{OC}, culminating in a record-setting PCE for this type of multijunction.

In the case of **PSC/OPV tandem solar cells**, a record efficiency of 26.7 % has been reported.[79] This 2T monolithic tandem device features a WBG PSC (1.8 eV) as the top cell, designed to minimize voltage losses, and a LBG OSC (1.3 eV) as the bottom cell. The structure incorporates a carefully engineered transparent intermediate recombination layer. Notable achievements include high V_{OC} values and reduced non-radiative voltage losses through molecular acceptor engineering and precise morphology control.

In recent years, **OPV/Si tandem solar cells** have been comparatively scarcely investigated. One notable association combined a narrow bandgap blend of PTB7-Th:IEICO-4F with an a-Si:H subcell leading to efficiencies of 15.1 %.[80] State-of-the-art devices in 2 and 4T configurations, combining a PBDB-T:ITIC-based organic top cell with a c-Si bottom cell, have

achieved efficiencies of 8.32 % and 15.25 %, respectively.[81] However, the 3T configuration for this type of multijunction device has not yet been systematically investigated in the literature. These observations highlight both the strong potential and the current limitations of OPV/Si tandem solar cells. In particular, the absence of studies on 3T OPV/Si architectures underscores the need for alternative device concepts enabling independent current extraction while preserving efficient optical coupling. This thesis is therefore dedicated to the investigation of 3T OPV/Si tandem solar cells, with a specific focus on interface engineering, charge-selective contacts, and device integration strategies aimed at unlocking the full potential of this hybrid tandem approach.

Chapter 2
Experimental Methods and Characterization Techniques

This chapter presents the experimental methods and characterization techniques employed throughout this work for the fabrication and analysis of OSC and tandem devices. It is organized into two main parts.

First, the different thin-film deposition techniques are introduced, including solution-based, vacuum-based, and printing methods, which are used to fabricate the various functional layers of the devices. Particular attention is given to the processing parameters that govern film formation, morphology, and reproducibility.

Then, a comprehensive set of characterization techniques is presented. These include electrical measurements to evaluate device performance and charge transport, morphological analyses to probe thin-film quality and nanoscale organization, optical and optoelectronic methods to assess light absorption and conversion efficiency, and structural techniques to investigate molecular ordering within the active layers.

2.1. Thin-film deposition techniques

2.1.1 Solution-processed deposition: spin-coating

Spin coating is a widely used solution-based deposition technique for producing uniform thin films with controlled thickness. The method relies on the spreading of a liquid precursor onto a substrate that is subsequently accelerated to high rotational speeds. Under rotation, centrifugal forces drive the excess solution outward, while a combination of viscous flow, hydrodynamic thinning, solvent evaporation, and solute redistribution governs the thinning and solidification of the film (**Figure 2-1**). Two main deposition approaches can be distinguished: static deposition and dynamic deposition. In static deposition, the solution is dispensed onto the substrate prior to rotation, allowing initial spreading before acceleration. In contrast, in dynamic deposition, the solution is dispensed while the substrate is already rotating, which can improve film uniformity and reduce edge effects, particularly for low-viscosity inks.

The process typically begins with dispensing a defined volume of solution onto the center of a cleaned substrate. The substrate is then subjected to a preset spinning sequence, usually consisting of an acceleration phase followed by one or more constant-speed steps. Typical spin-coating speeds range from 1000 to 5000 rpm, with acceleration ramps on the order of 500 to 3000 $rpm \cdot s^{-1}$, and spinning durations between 30 and 60 s. Other key processing parameters include solution viscosity, and solvent volatility. Collectively, these parameters determine the final film thickness, surface morphology, and uniformity. In most cases, higher spin speeds and longer spinning times yield thinner films, whereas more viscous inks or slower evaporation rates produce thicker coatings. Achieving reproducible films therefore requires tight control over the solution formulation (concentration, aging, additives) and environmental factors such as temperature and relative humidity. For materials sensitive to ambient conditions, such as organic semiconductors, spin coating is often performed inside a nitrogen-filled glovebox to avoid degradation or uncontrolled crystallization. In this work, films were deposited using a POLOS SPIN150i spin coater, ensuring precise control of

rotational parameters and process reproducibility. After deposition, the as-spun films frequently undergo a thermal annealing step to improve structural order, promote phase separation or crystallization when relevant, remove residual solvents, and enhance optical or electronic properties.[82]

In OSC fabrication, spin coating is commonly used to deposit the ETL, HTL**,** BHJ and interfacial modifiers or passivation layers. This technique is particularly suitable for laboratory-scale fabrication, although it is less compatible with large-area industrial processing.

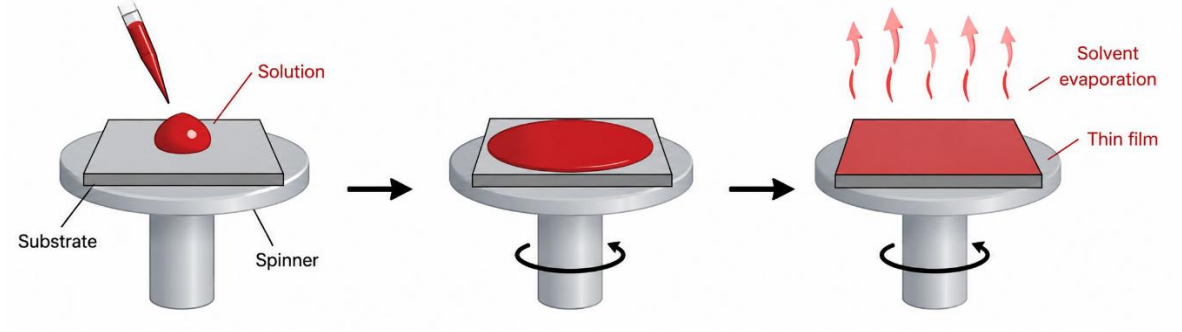

Figure 2-1: *Spin-coating thin-film deposition process.*

2.1.2 Printing-based deposition: screen-printing

Screen printing is a versatile, solution-based deposition technique commonly used for fabricating thick and patterned films, particularly in applications such as printed electronics, OPV, sensors, and ceramic or polymer-based devices. This approach enables the controlled deposition of relatively thick films, ranging from typically a few micrometers to several tens of micrometers, directly onto a wide variety of substrates.

The method relies on transferring a paste or ink through a patterned mesh screen onto the substrate. The screen defines the geometry of the printed features using a photolithographically produced stencil. During the printing process, a squeegee moves across the screen, applying pressure that forces the ink through the open areas of the mesh. The rheological properties of the ink, such as viscosity, play a central role in determining film thickness, edge definition, and printing fidelity (**Figure 2-2**). Ink formulation is critical for achieving reproducible results. Typical screen-printing inks contain functional particles, solvents, binders, and various additives that control flow behavior and drying characteristics. Proper matching between ink viscosity and mesh characteristics ensures a uniform transfer of material without defects such as pinholes, streaks, or incomplete patterns. The choice of mesh size, mesh count, emulsion thickness, and squeegee hardness further influences the printed film quality. After deposition, the printed layer undergoes a drying or curing step to remove solvents and solidify the printed structure. Depending on the material system, this may involve thermal annealing, UV curing, or chemical crosslinking.[83] The ability to locally deposit thick layers in a single pass makes screen printing particularly attractive, for example, for fabricating thick electrodes, current collectors, or patterned conductive layers in OSC. Screen printing is inherently scalable and compatible with roll-to-roll manufacturing, making it suitable for both laboratory and industrial production. Its robustness, low cost, and compatibility with flexible

and rigid substrates contribute to its widespread adoption in printed electronics and energy-related technologies. Compared to blade coating or slot-die coating, screen printing allows direct patterning without additional lithography steps. However, this method generally provides lower spatial resolution and may require more extensive optimization of ink rheology and process parameters. In this work, the screen-printing process is carried out using an Ekra X5 screen printer.

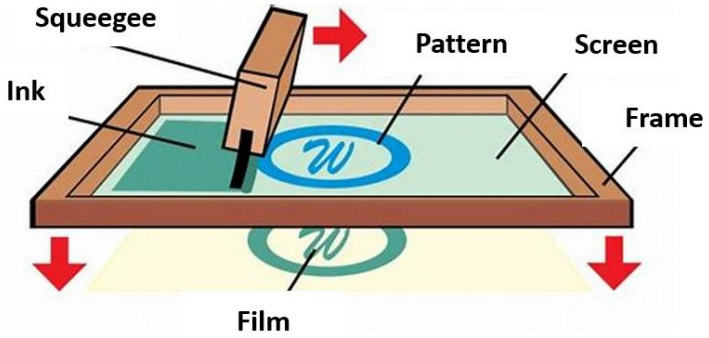

Figure 2-2: *Schematic of screen-printing deposition technique.*

2.1.3 Vacuum deposition: thermal evaporation

Thermal evaporation is a physical vapor deposition (PVD) technique widely employed for depositing high-purity thin films of metals, small organic molecules, and certain inorganic compounds. The method relies on heating a solid source material under high vacuum until its vapor pressure is high enough to allow evaporation. The vaporized atoms or molecules then travel ballistically through the vacuum chamber and condense onto a cooler substrate, forming a thin film whose density and microstructure depend strongly on the deposition rate and substrate temperature (**Figure 2-3**).

The process typically operates at pressures in the range of 10^{-6} mbar to minimize collisions between evaporated species and residual gas molecules. Such low pressures ensure a long mean free path, allowing the evaporated flux to reach the substrate without significant scattering, thereby improving film purity and directionality. Heating is commonly achieved using resistive evaporation sources, such as tungsten boats, crucibles, or filaments. Film growth is governed by several key parameters, including the evaporation rate, source–substrate distance, chamber pressure, and substrate temperature. The deposition rate, typically measured using a quartz crystal microbalance, plays a critical role in determining the film's microstructure, density, and surface roughness. Lower deposition rates generally yield smoother and more uniform coatings, whereas higher deposition rates can promote columnar growth or increased defect density. Because thermal evaporation is a line-of-sight technique, film thickness uniformity may depend on substrate positioning and the geometry of the evaporation source. To improve homogeneity, substrates are often rotated during deposition. Additionally, multilayer structures can be fabricated by sequentially evaporating different materials without breaking vacuum, an advantage for applications requiring controlled interfaces, such as in OPV.

In OSC fabrication, thermal evaporation is mainly used for the deposition of silver (Ag) top electrodes or HTL such as molybdenum trioxide (MoO_3). This technique results in dense and high-purity films but offers limited control over film stoichiometry for complex compounds.

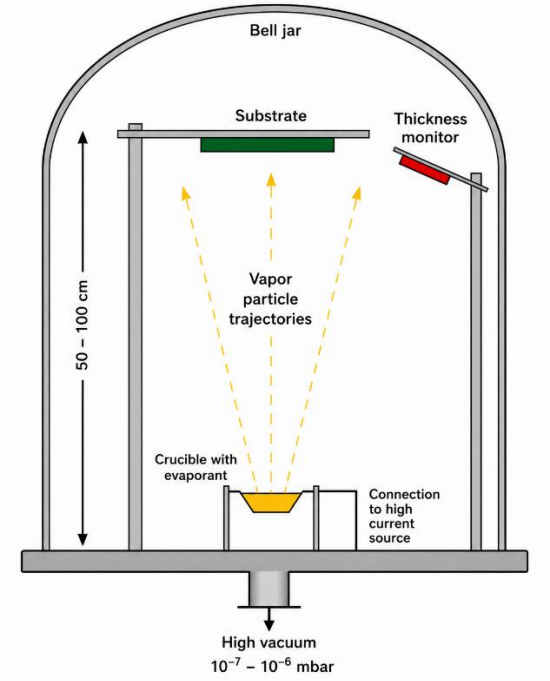

Figure 2-3: *Schematic of thermal evaporation technique under high vacuum.*

2.1.4 Physical vapor deposition: RF magnetron sputtering

Magnetron sputtering is a dry PVD technique widely used for depositing thin films of metals, metal oxides, and nitrides, particularly in applications requiring transparent conductive electrodes**,** barrier layers, or dielectric coatings. Due to its good uniformity, excellent adhesion, and scalability, it is frequently used in the fabrication of semiconductor devices.

Sputtering involves the ejection of atoms from a solid target material by bombardment with energetic ions, typically argon ions (Ar^+), in a low-pressure plasma environment. A negative voltage is applied to the target (cathode), creating an electric field between the target and the chamber walls (anode). Argon gas is introduced into the vacuum chamber and ionized through electron-impact processes in a plasma discharge, forming a plasma. The positively charged Ar^+ are accelerated toward the negatively biased target, colliding with it and dislodging atoms from its surface. In magnetron sputtering, a magnetic field is applied perpendicular to the electric field at the target surface using permanent magnets placed behind the target. This configuration traps the secondary electrons near the target, enhancing ionization efficiency and maintaining a dense plasma at lower operating pressures. The sputtered atoms travel through the vacuum and deposit onto the substrate, forming a thin film (**Figure 2-4**). Key parameters governing the sputtering process include the applied power (direct current or radiofrequency, depending on the target conductivity), working pressure,

target–substrate distance, gas flow rate, and substrate temperature. Higher radiofrequency (RF) power generally increases the sputtering rate but may also enhance film stress or induce target heating. The working pressure determines the energy and scattering of sputtered atoms, influencing film density and morphology: low pressures yield smoother and more compact films, while higher pressures promote a more porous or columnar structure. Substrate heating or biasing can be used to tune adatom mobility, crystal growth, and grain orientation.[84]

Reactive sputtering, where oxygen, nitrogen, or other reactive gases are added to the chamber, enables the synthesis of compound thin films directly during deposition.
In most cases, OSC are fabricated on glass substrates coated with a TCO, typically Indium Tin Oxide (ITO), which is commonly deposited by magnetron sputtering.

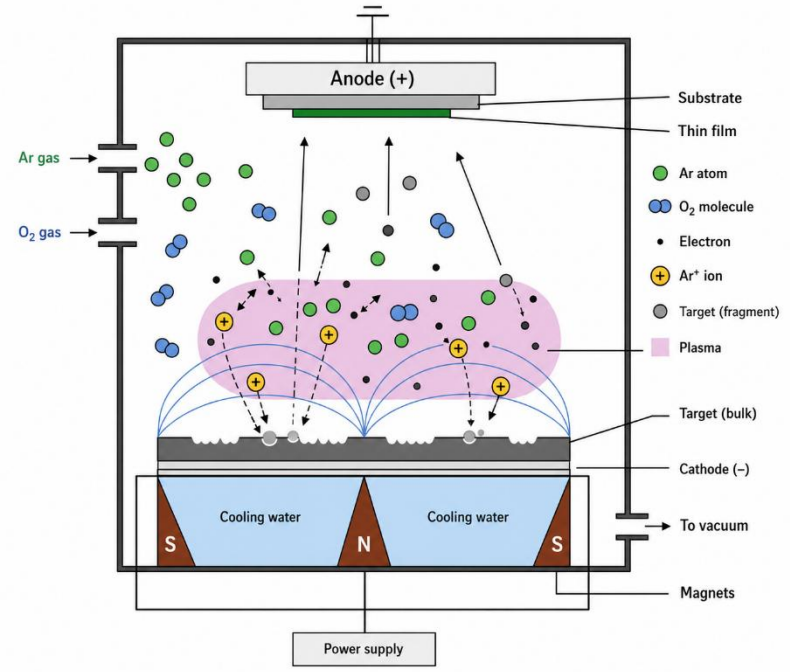

Figure 2-4: *RF magnetron sputtering deposition process.*

2.2. Laser scribing for thin-film electrode patterning

Laser scribing is a direct patterning technique used to locally remove or modify thin films in order to define specific device geometries. In contrast to deposition methods that directly produce patterned layers, laser scribing enables a continuous thin film to be deposited over the entire substrate before removing material along predefined paths. This approach is particularly attractive for the fabrication of transparent conductive electrodes, as it allows wet-processed materials to be deposited over a full-area substrate and subsequently patterned into electrically isolated electrodes without the use of physical masks during deposition, or even photolithography after deposition.

The process relies on the interaction between a focused laser beam and the thin film. When the laser radiation is absorbed by the material, the deposited energy is converted into heat, which can induce localized melting, vaporization, decomposition, or ablation depending

on the laser wavelength, power density, and thermal properties of the material. By scanning the laser beam along a predefined trajectory, a narrow region of the thin film can therefore be selectively removed, producing a scribe line that separates adjacent conductive regions. The quality of the resulting pattern depends on the optical absorption of the material at the selected wavelength, laser power, scanning speed, spot size, and number of laser passes. These parameters must be carefully adjusted to achieve complete electrical isolation while minimizing thermal damage to the surrounding film and substrate.

The choice of laser wavelength is particularly important for thin-film patterning because the interaction between the laser radiation and the material is strongly dependent on its optical absorption. The SCULPFUN G9 system used in this work is equipped with two laser sources: a 2 W infrared laser operating at 1064 nm and a 10 W blue diode laser operating at 455 nm. The infrared source is primarily intended for the processing of materials such as metals, whereas the 455 nm diode laser is suitable for materials exhibiting significant absorption in the visible spectral range. The system uses a galvanometric scanning mechanism to control the position of the laser beam and provides a nominal working area of 105 x 105 mm. According to the manufacturer, the nominal laser spot size is approximately 0.01 mm, with maximum marking speeds of 5000 $mm.s^{-1}$ and 4000 mm s^{-1} for the infrared and blue diode lasers, respectively. In this work, the 455 nm blue diode laser was used to pattern transparent conductive thin films. The conductive layer was first deposited over the entire substrate using the corresponding deposition technique. The laser was then scanned along predefined patterns to locally remove the conductive film and define electrically isolated electrode regions. This approach enables the fabrication of patterned electrodes from full-area coatings and is particularly advantageous for solution-processed device architectures, where the functional layers can be deposited over the entire substrate by wet-processing techniques prior to electrode definition. The laser processing parameters, including laser power, scanning speed, and number of passes, were adjusted according to the properties and thickness of the conductive thin films. The optimized conditions were selected to obtain a continuous and electrically insulating scribe line while preserving the transparency and electrical conductivity of the remaining electrode areas. The resulting patterned electrodes were subsequently used for device fabrication and electrical characterization.

2.3. Characterization techniques

2.3.1 Electrical characterization of devices

a) Current-voltage (*J-V*) characteristics under AM1.5 G illumination

J-V measurements under standard illumination are the primary method used to evaluate the PV performance of OSC. This characterization provides key parameters including J_{SC}, V_{OC}, FF and PCE. As shown in **Figure 2-5**, measurements were performed using a solar simulator with a Xenon source and AM 1.5G filters (Newport LCS-100) following international PV standards (IEC 60904). The light intensity of the lamp was set at 100 mW cm^{-2} using a

calibrated silicon reference cell from Newport Co. The *J-V* curves were recorded in the dark and under 1-sun using a Keithley 2400 SMU, and parameters were directly extracted *via* a homemade LabVIEW program. *J–V* characterization was performed in a nitrogen-filled glovebox.

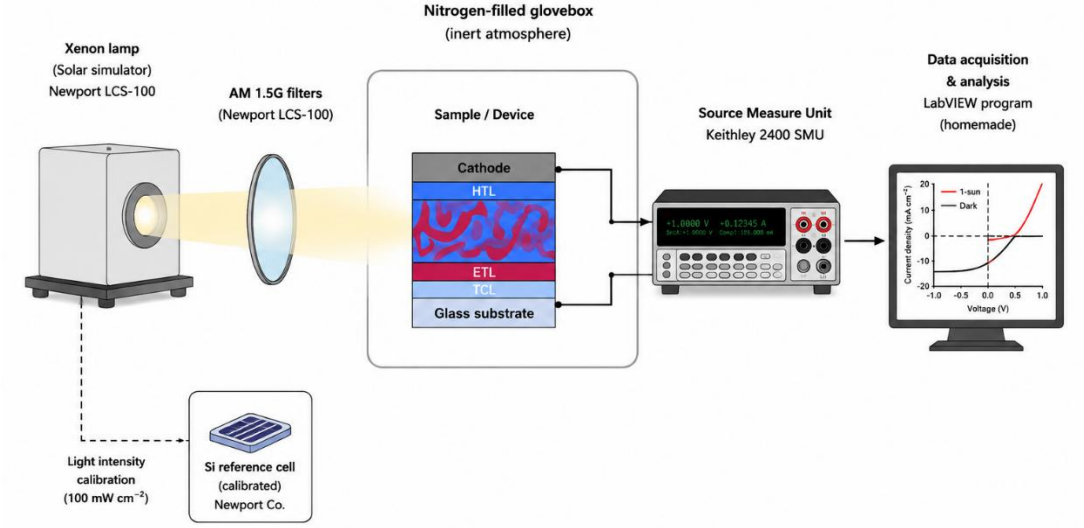

Figure 2-5: *J-V characteristics measurement configuration (under AM1.5 G).*

As shown in **Figure 2-6**, the AM1.5G spectrum represents the solar irradiance received at the Earth's surface when sunlight travels through 1.5 times the thickness of the Earth's atmosphere relative to the zenith. The air mass is defined as **Equation 2-1**.

$$\mathrm{AM} = \frac{1}{\cos(\theta)} \qquad \textbf{(2-1)}$$

where θ is the solar zenith angle, defined as the angle between the direction of incoming sunlight and the normal to the Earth's surface at the point of observation. In this work, θ = 48.2° for AM1.5.

The AM1.5G, where "G" indicates "Global" (direct + diffuse components), is used as the reference spectrum for PV characterization because it represents typical mid-latitude conditions. Since OSC operate outdoors in the presence of scattered light, AM1.5G is the most relevant illumination source.[85]

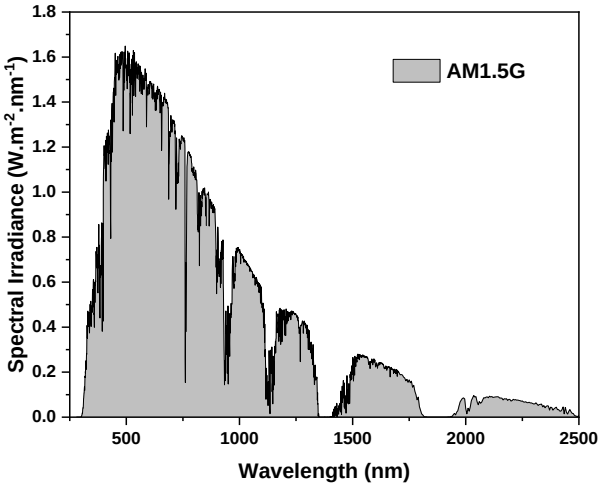

Figure 2-6: *Standard AM1.5G solar spectrum.*

As shown in **Figure 2-7a**, a dark solar cell behaves like a diode, characterized by a parallel resistance called the shunt resistance (R_{SH}) and a series one called the series resistance (R_S), both in $\Omega.cm^2$. These parameters provide important information about the device. A low R_{SH} can indicate poor film quality, notably the presence of defects such as pinholes, inhomogeneities, or unintentional doping of the active layer, leading to leakage currents when reverse biased in the dark.[86] R_S, on the other hand, reflects the resistance of the various layers under forward bias, providing information on the quality of the electrical contacts within the device.[86] In an ideal solar cell, R_{SH} is extremely high and R_S very low, resulting in a *J-V* characteristic that conforms to the Shockley diode equation. This equation involves several parameters such as J_0 the saturation current density, n the diode ideality factor, q the elementary charge, k the Boltzmann constant and T the temperature. The current density is expressed by **Equation 2-2**, where overall cell performance is mainly influenced by R_S and R_{SH}, which account for non-ideal transport and leakage pathways in devices.

$$J = J_0\left(e^{\frac{q(V-JR_S)}{nkT}} - 1\right) + \frac{V-JR_S}{R_{SH}} - J_{ph} \qquad \textbf{(2-2)}$$

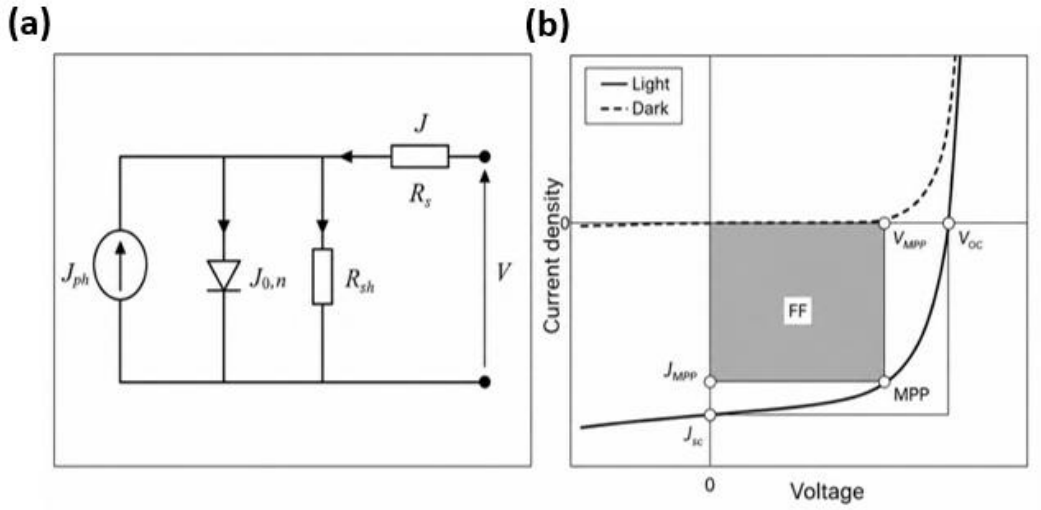

Figure 2-7: *(a) Equivalent circuit and (b) J-V characteristics of a solar cell.*

Concerning the key PV parameters, four values can be extracted from *J-V* measurements. V_{OC} is the voltage across the solar cell in the open-circuit state ($J = 0$) and J_{SC} is the current density measured in the short-circuit state ($V = 0$). In OSC, J_{SC} generally reflects the efficiency of light absorption, exciton diffusion and dissociation, charge transport, and charge collection at the electrodes (**Equation 2-3**). The V_{OC} is linked to the energy level of the active materials, and in particular to the way in which the quasi-Fermi levels of electrons and holes are split under illumination, but it is also influenced by non-radiative recombination losses and energetic disorder (**Equation 2-4**).

$$J_{SC} = -J_{ph} \quad \textbf{(2-3)}$$

$$V_{OC} = \frac{nkT}{q} \ln\left(\frac{J_{SC}}{J_0} + 1\right) \quad \textbf{(2-4)}$$

The last two points (J_{MPP} and V_{MPP}) are the solar cell's operating conditions, where the power density supplied by the cell is at its maximum power point (P_{MPP}). With these four values, we obtain the FF (**Equation 2-5**). This factor has a value between 0 and 1, with 1 being the ideal solar cell (**Figure 2-7b**).

$$FF = \frac{V_{MPP} \cdot J_{MPP}}{V_{OC} \cdot J_{SC}} = \frac{P_{MPP}}{V_{OC} \cdot J_{SC}} \quad \textbf{(2-5)}$$

Finally, the important figure of merit of a solar cell is expressed by the PCE, which is the ratio of the maximum electrical output power to the incident illumination (P_{IN}), thereby accounting for both voltage and current losses as well as resistive recombination effects (**Equation 2-6**).

$$PCE = \frac{P_{MPP}}{P_{IN}} = \frac{J_{SC} \cdot V_{OC} \cdot FF}{P_{IN}} \times 100 \quad \textbf{(2-6)}$$

b) Current-voltage (*J-V*) characteristics under indoor illumination

J-V measurements under indoor illumination were performed to evaluate the PV performance of the OSC. These measurements were carried out at the IM2NP laboratory (Marseille, France) by Carmen Ruiz Herrero.[87] The *J-V* characteristics were recorded using a Keithley 2450 source measure unit controlled by a dedicated LabVIEW program (**Figure 2-8**). The devices were illuminated with a Philips Hue Aurelle White Ambiance Light Emitted Diode (LED) panel (60 × 60 cm), providing adjustable correlated color temperatures (CCT) between 2200 and 6500 K (**Figure 2-8**). The incident light intensity, typically ranging from 100 to 1000 lux, was adjusted by varying the distance between the LED panel and the sample. Illuminance, spectral irradiance, and CCT were measured using a calibrated Black-Comet-CXR-SR spectrometer (StellarNet Inc., 220-1100 nm) coupled to SpectraWiz software (**Figure 2-8**). PV parameters were extracted directly from the recorded curves.

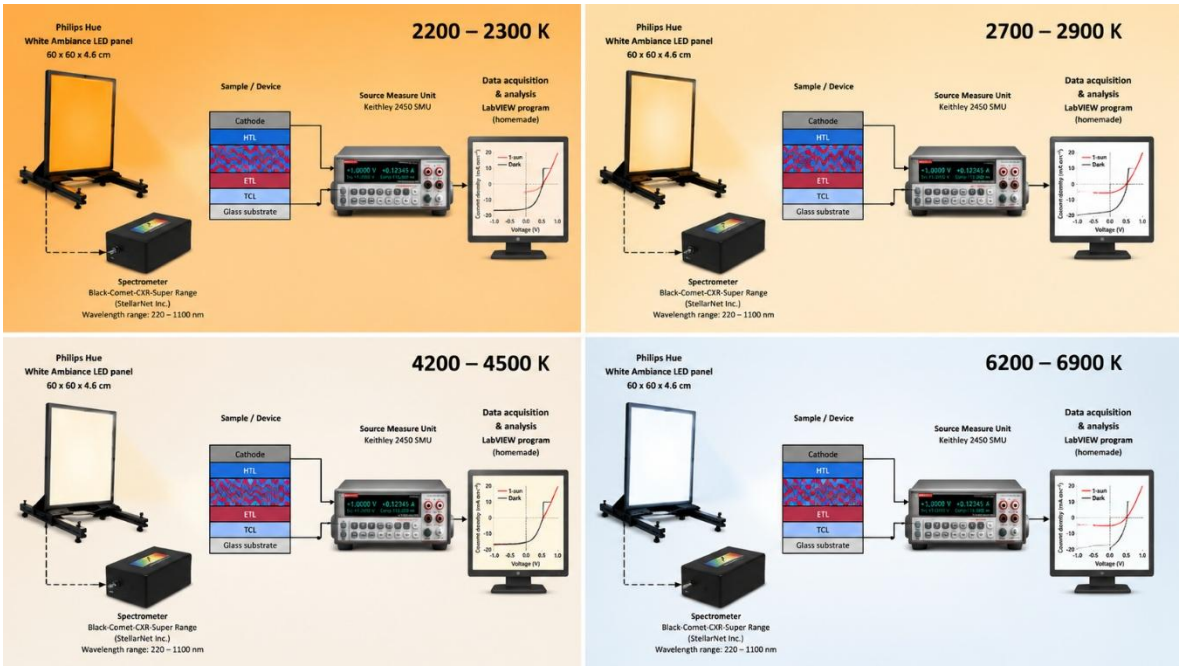

Figure 2-8: *J-V characteristics measurement configuration (under LED illumination for different CCT).*[87]

c) Four-point probe conductivity measurements

The four-point probe measurement is used to obtain the sheet resistance (R_{sheet}) of various thin layers. This method is particularly relevant for assessing the uniformity, quality and electrical performance of thin films. As shown in **Figure 2-9**, the setup consists of four aligned metallic tips that make contact with the film surface. A constant current I is injected through the outer probes, while the resulting voltage drop *V* is measured across the two inner probes, thereby minimizing the influence of contact resistance.

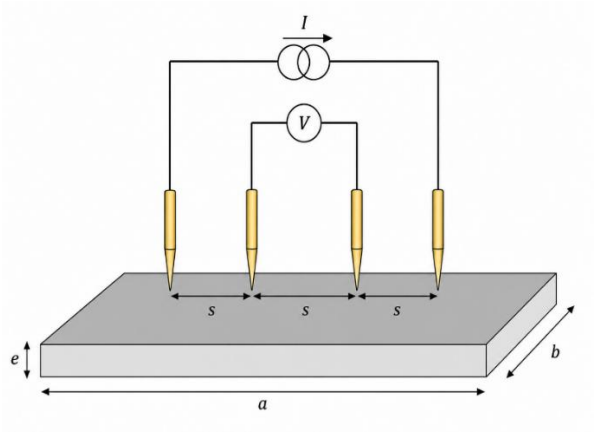

Figure 2-9: *Four-point probe measurement configuration.*

For a semi-infinite thin film of thickness much smaller than the lateral dimensions, and assuming equally spaced probes, R_{sheet} is obtained from **Equation 2-7**.

$$R_{sheet} = \frac{\pi}{\ln(2)} \times \frac{U}{I} = 4.53 \times \frac{U}{I} \quad \textbf{(2-7)}$$

d) Charge transport and mobility: SCLC method

Charge transport in organic semiconductors is governed by hopping processes, energetic disorder, and trap states, making the evaluation of carrier mobility essential for understanding device operation. The Space-Charge-Limited Current (SCLC) method is one of the most widely used techniques to quantify the mobility of electrons and holes in thin films. This technique relies on the analysis of *J–V* characteristics of single-carrier devices in which charge injection from the electrodes is efficient and not rate-limiting.

To perform SCLC measurements, dedicated device structures are fabricated to selectively inject one carrier type. For hole-only devices, high work-function electrodes are used, giving an ITO/PEDOT:PSS/PAL/MoO_3/Ag structure (**Figure 2-10a**) whereas electron-only devices typically employ low work-function contacts giving ITO/ZnO/PAL/Ca/Al structure (**Figure 2-10b**). Under these conditions, the current flowing through the device is dominated by space-charge effects rather than injection barriers or recombination processes, although residual injection limitations or contact effects cannot be completely excluded in practical devices.

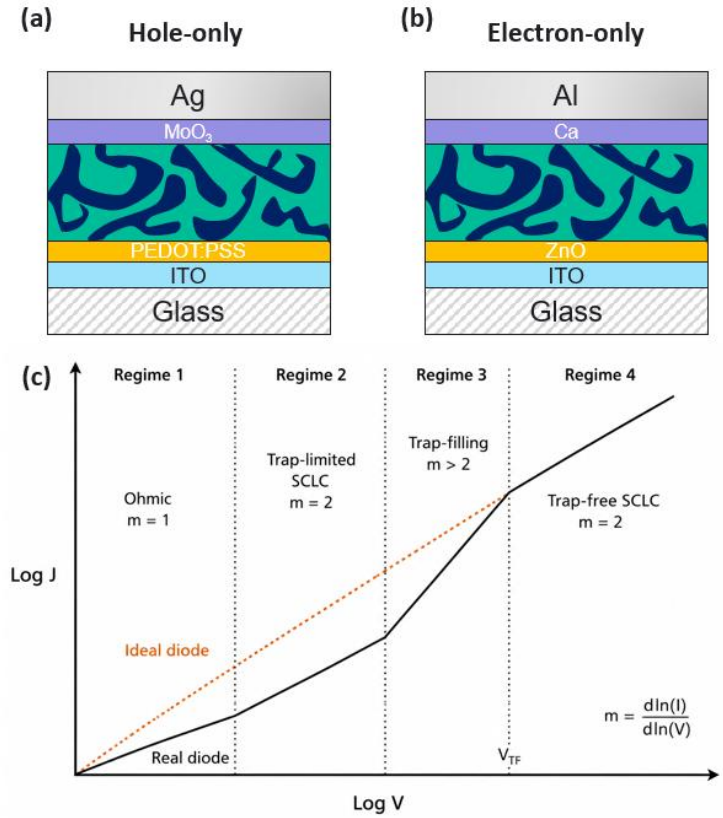

Figure 2-10: *(a) Hole-only and (b) electron-only devices. (c) Current-voltage regimes in space-charge-limited current (SCLC) measurements.*

As shown in **Figure 2-10c**, the *J-V* curve obtained from an SCLC device generally exhibits four distinct regimes.[88]

At low applied voltages (Regime 1), the device operates in the **ohmic regime**, where the current is governed by the equilibrium free carriers already present in the material. In this region, the current density scales linearly with voltage ($J \propto V$) and is given by **Equation 2-8**. [88]

$$J = qn_0\mu\frac{V}{L} \qquad \textbf{(2-8)}$$

where n_0 is the equilibrium free carrier concentration, μ the hole or electron mobility depending on the device, q the elementary charge, and L the active layer thickness. This regime reflects the intrinsic conductivity of the material.

As the voltage increases, injected carriers progressively dominate over the equilibrium carrier population, and the device transitions into the **trap-limited SCLC regime** (Regime 2). In this regime, the current follows a quadratic dependence ($J \propto V^2$), but transport is still strongly affected by the presence of trap states within the bandgap. Only a fraction of the injected carriers contributes to conduction, while the rest are captured by traps, leading to an effective mobility lower than the intrinsic one. Consequently, extracting mobility in this region is not reliable.

Upon further increase in voltage, the device reaches the **trap-filling regime** (Regime 3). In this intermediate region, the injected carriers begin to progressively fill the available trap states. This results in a steep increase in current, characterized by a power-law dependence $J \propto V^m$ with $m > 2$. The onset of this regime corresponds to the trap-filled limit voltage (V_{TF}), which provides direct insight into the trap density in the material. However, as highlighted in the literature, this transition is often gradual rather than abrupt due to a distribution of trap energies

Finally, once all traps are filled, the device reaches the **trap-free SCLC regime** (Regime 4). In this regime, all injected carriers contribute to conduction, and the current density follows the ideal Mott–Gurney law in **Equation 2-9**. [88]

$$J = \frac{9}{3}\varepsilon_0\varepsilon_r\mu\frac{V^2}{L^3} \quad \textbf{(2-9)}$$

where ε_o is the vacuum permittivity and ε_r the relative dielectric constant of the semiconductor. This regime corresponds to a purely space-charge-limited transport without trapping effects ($J \propto V^2$). Under the assumptions of ohmic contacts, negligible injection barriers, and field-independent mobility, this region allows for a reliable extraction of the effective carrier mobility μ.

e) Transient Photovoltage (TPV) measurements

Transient Photovoltage (TPV) is a characterization technique used to probe the recombination dynamics of photogenerated charge carriers in a solar cell under open-circuit conditions. It provides direct access to the small-perturbation carrier lifetime and reveals how recombination evolves with carrier density, offering valuable insight into mechanisms that limit device performance.

In this work, TPV measurements were carried out using a measurement system composed of a function generator (Keithley 3390) producing a pulse at 1.1 Hz with an amplitude of 5 V and a duration of 500 ms, a pre-amplifier, a digital oscilloscope (Keysight Technologies DSOX1202A), and a 532 nm LED used as the light perturbation source (**Figure 2-11**).

During TPV measurements, the device is maintained at open circuit in the dark. A small optical perturbation, typically a LED pulse, induces a slight increase in photovoltage. Because the perturbation is kept sufficiently small, the response remains in the linear regime, and the decay of the photovoltage transient originates from recombination of the excess carriers. The photovoltage decay is recorded as a function of time and can often be described by a mono-exponential, bi-exponential, or stretched-exponential behavior, depending on the material system and recombination mechanisms. When a bi-exponential decay is observed, the constants correspond to a fast decay component τ_{fast} associated with rapid recombination of free carriers or shallow trap states, and a slow decay component τ_{slow} attributed to deeper traps, delayed release processes, or long-lived spatially separated carriers. The relative amplitudes and timescales of these two components provide insight into the distribution and

occupation of trap states, interfacial recombination dynamics, and carrier delocalization effects. A longer τ_{slow} generally indicates reduced trap-assisted recombination and improved charge retention, while faster τ_{fast} values correspond to more rapid carrier loss.

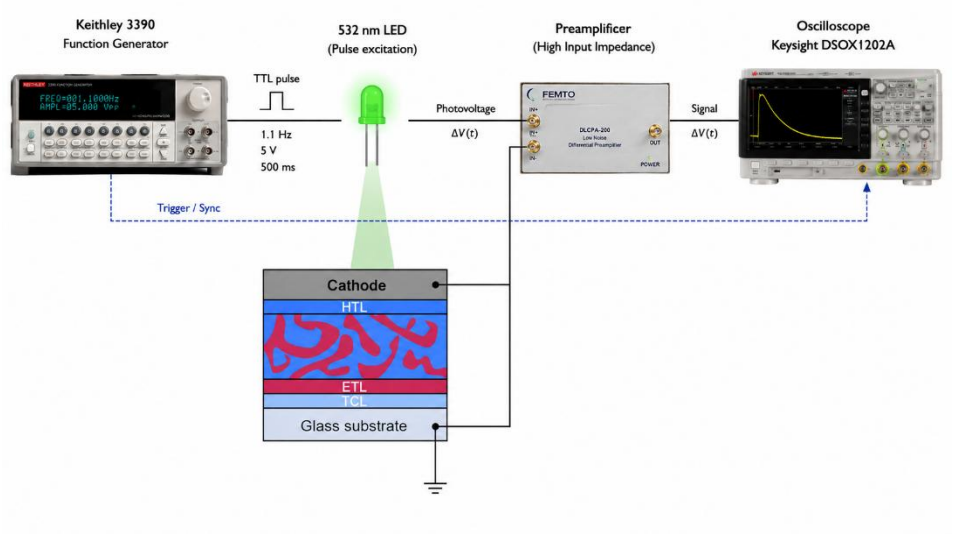

Figure 2-11: *TPV measurement configuration.*

f) Light-intensity dependence of J_{SC} and V_{OC}

The dependence of J_{SC} and V_{OC} on light intensity is a powerful characterization method for identifying recombination mechanisms in OSC. By varying the illumination intensity over several orders of magnitude, it is possible to gain insight into whether the device is affected by bimolecular recombination, trap-assisted recombination, or space-charge effects. In this work, the light intensity was controlled by adjusting the driving current of a 528 nm LED using a Keithley 2400 source measure unit. A prior calibration of the LED enabled a direct correlation between the applied current and the resulting optical power density incident on the device. Under short-circuit conditions, the photogenerated charges are efficiently extracted, and the recombination pathways have a reduced influence on the measured current (**Figure 2-12**). The variation of J_{SC} with incident light intensity P_{in} typically follows a power-law dependence given in **Equation 2-10**.

$$J_{SC} \propto {P_{in}}^{\alpha} \qquad \textbf{(2-10)}$$

where α is an indicator of charge extraction and recombination losses. In ideal devices dominated by free carrier transport, $\alpha \approx 1$, meaning that the current increases linearly with light intensity. Deviations from unity (i.e., $\alpha < 1$) indicate the presence of space-charge effects, trap-limited extraction or significant recombination losses.[89]

Under open-circuit conditions, no net current flows through the device, and all photogenerated carriers recombine. The dependence of V_{OC} on light intensity is therefore particularly sensitive to recombination dynamics. According to the diode equation, the V_{OC} scales as in **Equation 2-11**.

$$V_{OC} = \frac{nkT}{q}\ln(\frac{Jsc}{J_0}) \quad \textbf{(2-11)}$$

where n is the ideality factor, k the Boltzmann constant, T the temperature, q the elementary charge, and J_0 the dark saturation current density.

Experimentally, the variation of V_{OC} with the natural logarithm of P_{in} is linear, as shown in **Equation 2-12**.

$$V_{OC} = \frac{nkT}{q}\ln(P_{in}) + C \quad \textbf{(2-12)}$$

where C is a constant.

The slope of this relation allows extraction of the ideality factor n, which provides insight into the dominant recombination pathways. Values around n = 1 are generally associated with bimolecular recombination, whereas higher ideality factors (n > 1) can indicate an increased contribution from trap-assisted recombination. These deviations can be associated with energetic disorder, interfacial defects, or other non-ideal recombination processes.[90] This analysis is complementary to TPV and provides insight under steady-state conditions.

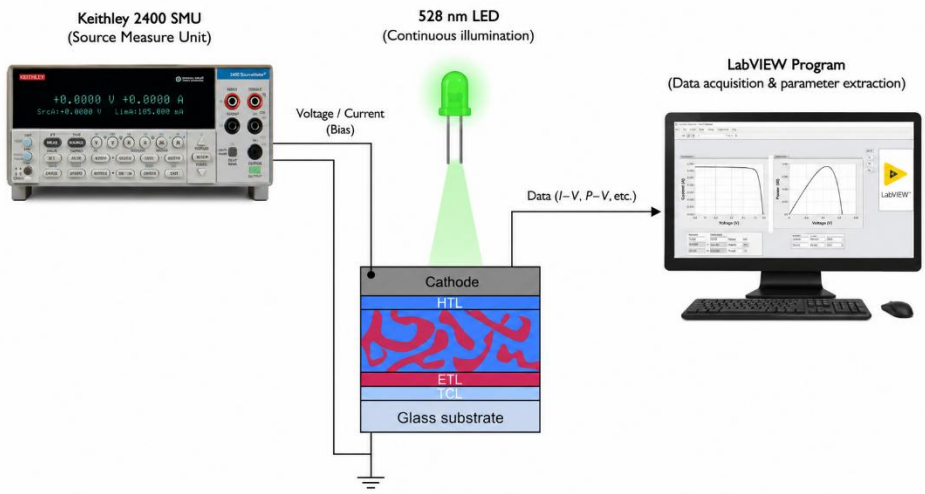

Figure 2-12: *Light Intensity Dependence measurement configuration.*

g) Aging and operational stability measurements

Aging and stability studies are essential to evaluate the long-term performance and degradation pathways of OSC. Due to their sensitivity to oxygen, moisture, heat, and prolonged illumination, OSC can undergo physical, chemical, and morphological changes that progressively impact their PV performance. Stability assessments provide key insights into these mechanisms and guide the development of more durable materials and device architectures. Stability testing follows standardized ISOS (International Summit on Organic

Solar Cells) procedures, which set conditions for aging under dark storage (ISOS-D), continuous illumination (ISOS-L), thermal stress (ISOS-T), or outdoor exposure (ISOS-O). In this work, stability tests were performed in ambient air (40-50% relative humidity) over 200 h under continuous illumination, following the ISOS-L-2 protocol. Illumination was provided by a LUMARTIX SUNIRAD solar simulator calibrated to an AM1.5G spectrum. The maximum MPP was tracked every 5 minutes during the first 5 hours and then every hour thereafter, allowing detailed monitoring of both early-stage and long-term degradation behavior (**Figure 2-13**).

During these tests, the evolution of J_{SC}, V_{OC}, FF, and PCE is monitored over time to quantify performance losses. Degradation is commonly evaluated using performance retention markers such as T_{80} and T_{50}, defined as the times required for the device to reach 80 % and 50 % of its initial PCE, respectively. The first metric reflects significant, but not yet severe, degradation, while the second is commonly regarded as an end-of-life indicator.

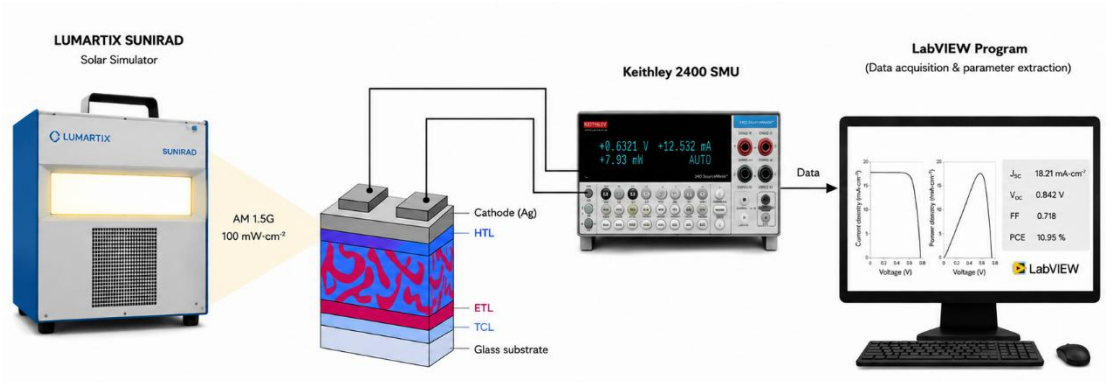

Figure 2-13: *Aging and stability measurement configuration.*

2.3.2 Morphological characterization of thin films

a) Optical microscopy

Optical microscopy is an imaging technique used to examine the surface morphology and uniformity of thin films at the micrometer scale. Based on the interaction of visible light with the sample, it provides rapid and straightforward visualization of large-area features, making it an essential first-step characterization method for identifying macroscopic defects such as pinholes, dewetting areas, or thickness inhomogeneities.

For OSC, optical microscopy is particularly valuable for assessing the overall quality of spin-coated or blade-coated films, verifying deposition uniformity, and detecting morphological defects that may lead to electrical shunting or decreased device performance. In this work, optical microscopy observations were performed using a Zeiss Axio Imager 2.

b) Stylus profilometry

Profilometry is a surface characterization technique used to measure the thickness and topography of thin films with high vertical resolution. A stylus profilometer operates by

mechanically scanning a sharp tip across the surface of the sample. As the tip moves along the surface, it follows the height variations of the film. These vertical displacements are detected with nanometer-scale precision and converted into a topographical profile. This method provides quantitative height measurements, making it an essential tool for validating layer thickness during device preparation and for detecting step edges and surface non-uniformities. In this work, profilometry measurements were performed with a Dektak XTL on organic semiconducting layers as well as on transparent ITO electrodes (**Figure 2-14**).



Figure 2-14: *Thin film profile measured by Dektak XTL profilometer.*

c) Scanning Electron Microscopy (SEM)

Scanning Electron Microscopy (SEM) is a technique capable of producing high-resolution images of the surface and cross-section of a sample through electron–matter interactions. As shown in **Figure 2-15**, a tungsten (W) filament generates an electron beam accelerated typically by a few kilovolts, which is then focused onto the sample. The beam is raster-scanned across the surface, allowing nanometer-scale structures to be visualized. The interaction of the primary electrons with the material leads to the emission of secondary electrons (SE), which are highly sensitive to surface topography, and backscattered electrons (BSE), whose intensity depends on the atomic number and therefore provides compositional contrast.[91] Detection of these electrons, synchronized with the scanning of the primary beam, enables the reconstruction of detailed SEM images. Depending on the sample preparation, SEM can be used in two complementary configurations. Surface (plan-view) imaging provides information on film uniformity, roughness, the presence of pinholes, or phase separation patterns. This mode is particularly useful for characterizing the morphology of thin functional layers deposited in OSC. In addition, cross-sectional SEM is obtained by cleaving or cutting the device stack. This configuration enables direct visualization of layer thicknesses, interface quality, and overall device architecture. It is widely used to verify deposition uniformity, detect delamination or interdiffusion, and evaluate morphological changes occurring during aging or after encapsulation failure. In this work, SEM measurements were performed in PLACAMAT by Philippe Legros, using a MEB HITACHI SU7000.

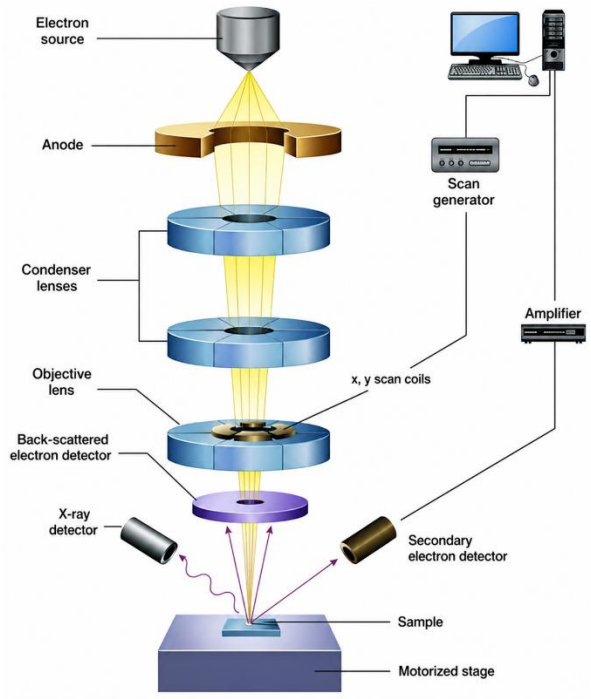

Figure 2-15: *Principle of scanning electron microscopy.*

d) Atomic Force Microscopy (AFM)

Atomic Force Microscopy (AFM) is a high-resolution scanning probe technique used to analyze the nanoscale topography of thin films. This method provides three-dimensional quantitative information on surface morphology, typically down to the sub-nanometer range in the vertical direction, while the lateral resolution is limited by the tip radius. This makes it particularly relevant for characterizing the active layers and interfacial structures in OSC, where nanoscale morphology strongly influences charge generation and transport.

AFM operates by raster-scanning a sharp probe mounted on a flexible cantilever across the sample surface. As the tip interacts with the surface through short-range forces (van der Waals forces, electrostatic interactions, or repulsive contact forces), the cantilever oscillates and its amplitude is affected by the tip-sample interaction. In tapping mode, the most widely used mode for OSC characterization, the cantilever is oscillated near its resonance frequency while the tip intermittently interacts with the sample surface. A feedback loop maintains a constant oscillation amplitude by adjusting the vertical position of the piezoelectric scanner, thereby keeping the tip-sample interaction at a controlled level and allowing reconstruction of the surface topography (**Figure 2-16**). This mode minimizes damage to soft organic films while providing high-resolution images. AFM can be used in contact mode, with a continuous contact between the tip and the sample or in non-contact mode, which probes attractive forces at a distance and is useful for extremely delicate surfaces. AFM provides quantitative parameters such as root-mean-square roughness (RMS), feature height distribution, domain size, and correlation length. These descriptors are essential for understanding film formation, phase separation in bulk heterojunctions, and the quality of interfacial layers.

In this work, AFM measurements were performed in tapping mode using an Innova AFM system from Bruker, equipped with an AC160TS probe from Oxford Instruments (nominal resonance frequency of 300 kHz and tip radius of approximately 8 nm).

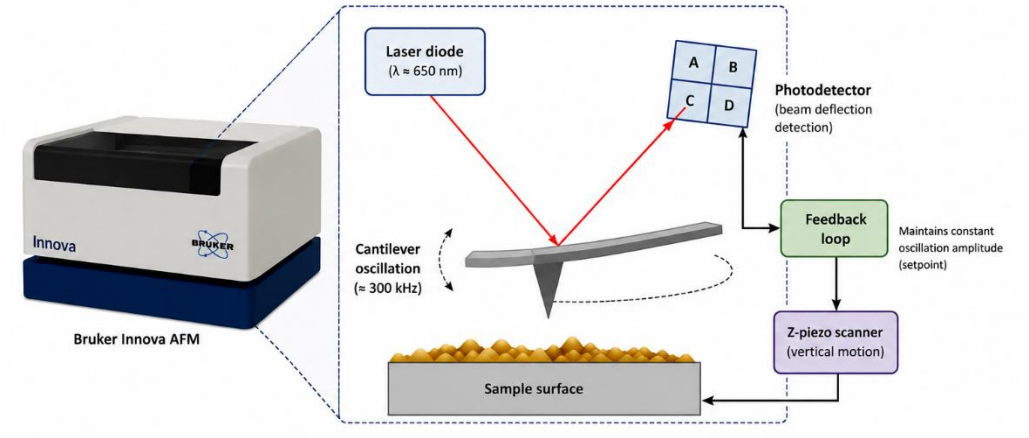

Figure 2-16: *Principle of atomic force microscopy in Tapping mode.*

The surface topographical data were analyzed using Gwyddion software. Grain size was determined using a threshold-based segmentation method, while the root-mean-square roughness was extracted using the rugosity analysis function (**Figure 2-17**).

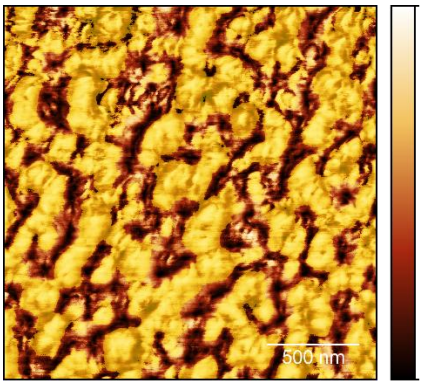

Figure 2-17: *AFM image analyzed with a threshold-based segmentation method.*

e) Contact angle measurements

Contact angle measurement is a surface characterization technique used to evaluate the wettability and surface energy of thin films and substrates. It provides insight into the interfacial compatibility between successive thin films, particularly in solution-processed devices where proper spreading and adhesion of liquid inks are essential for obtaining uniform and defect-free films.

As shown in **Figure 2-18**, the technique involves depositing a small droplet of liquid, typically deionized water or the solution under investigation, onto the surface of the material and imaging the droplet profile. The contact angle θ is defined as the angle formed at the three-phase boundary between the solid surface, the liquid droplet, and the surrounding

atmosphere. It reflects the balance of interfacial tensions according to Young's equation (**Equation 2-13**).

$$\gamma_{SV} = \gamma_{SL} + \gamma_{LV} \cos\theta \quad \textbf{(2-13)}$$

where γ_{SV} is the solid–vapor surface energy, γ_{SL} the solid–liquid interfacial energy, and γ_{LV} the liquid–vapor surface tension.

Lower contact angles indicate good wettability and strong spreading of coatings, while higher angles correspond to hydrophobic surfaces and reduced film adhesion. In OSC fabrication, contact angle measurements are particularly useful for assessing surface treatments, interlayer modifications, and the compatibility of underlying layers prior to deposition of the active layer or charge transport layers.

In this work, the surface energies of the different materials were determined using a Krüss DSA 100 goniometer, based on contact angle measurements of two different liquids deposited on the substrate surface at 20 °C in static mode.

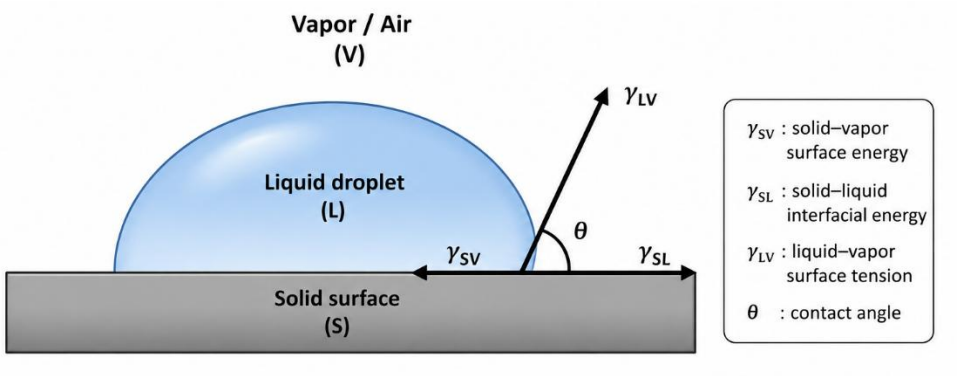

Figure 2-18: *Principle of contact angle measurement.*

2.3.3 Optical and optoelectronic characterization

a) UV-Visible absorption spectroscopy

UV-Visible spectroscopy provides essential information on the optical bandgap, molecular transitions, and light-harvesting capability of the materials used in OSC. In this method, a beam of light covering the ultraviolet and visible wavelength range is directed through or reflected from the sample. The transmitted or reflected intensity is recorded as a function of wavelength, enabling determination of the absorbance or optical density. In this work, UV-visible absorption spectra were acquired using a SAFAS UVmc2 spectrophotometer over the wavelength range of 300 to 1100 nm, with a step size of 2 nm (**Figure 2-19**). The absorbance A(λ) is defined by the Beer–Lambert law in **Equation 2-14**.

$$A(\lambda) = -log_{10}\left(\frac{I(\lambda)}{I_0(\lambda)}\right) \quad \textbf{(2-14)}$$

where $I_0(\lambda)$ is the incident light intensity and $I(\lambda)$ the transmitted intensity.

Absorbance is directly related to the absorption coefficient α(λ) through **Equation 2-15**.

$$A(\lambda) = \alpha(\lambda)L \quad \textbf{(2-15)}$$

with *L* the film thickness.

These relations provide insight into how efficiently the material absorbs photons at each wavelength. Thin-film UV-Vis measurements allow extraction of key optical parameters. The absorption onset or even Tauc plot are commonly used to estimate the optical bandgap $E_{g,opt}$, often via linear extrapolation of the low-energy absorption edge. Changes in the spectral shape or peak positions can reveal differences in molecular packing, aggregation, or crystallinity, which directly affect exciton diffusion and charge separation efficiency in OSC.

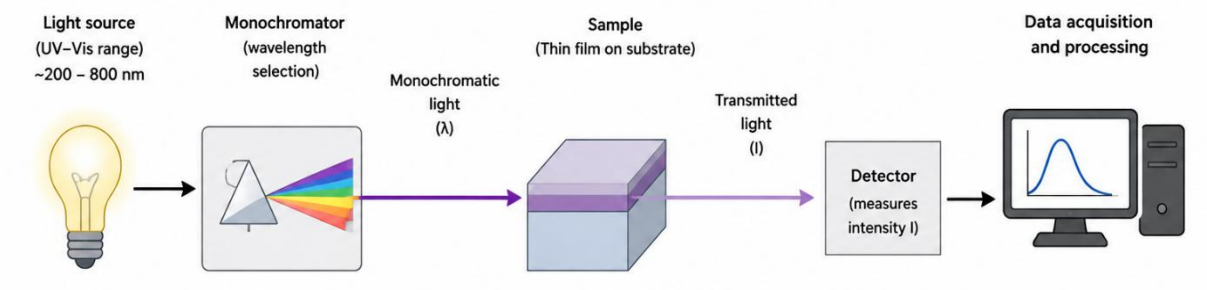

Figure 2-19: *Principle of UV-Visible absorption spectroscopy.*

b) External Quantum Efficiency (EQE)

External Quantum Efficiency (EQE) is measured by illuminating the OSC with a monochromatic light beam of known intensity and recording the resulting photocurrent at several wavelengths (**Figure 2-20**). The resulting value is the ratio of the number of collected charge carriers (N_E) to the number of incident photons (N_{Ph}) at each wavelength as shown in **Equation 2-16**.

$$EQE(\lambda) = \frac{N_E}{N_{Ph}} = \frac{I_{Ph}}{q.\phi_{Ph,\lambda}} \quad \textbf{(2-16)}$$

with ϕ_{Ph} the photon flux of the reference spectrum and I_{Ph} the photocurrent.

In this work, EQE measurements were carried out using a PVE300 Photovoltaic EQE system from Bentham Co. The EQE spectrum provides rich information about the optical and electronic processes within OSC. The spectral shape reflects the absorption profiles of the donor and acceptor materials, allowing identification of the contributions of each component to photocurrent generation. Lower EQE values may indicate incomplete exciton diffusion, inefficient charge separation, or recombination losses at specific wavelengths. Integration of the EQE spectrum over the AM1.5G solar spectrum allows the calculation of the expected short-circuit current density (**Equation 2-17**).

$$J_{SC} = -q \int_{\lambda_2}^{\lambda_1} EQE(\lambda).\phi_{ph}^{AM1.5G} d\lambda \quad \textbf{(2-17)}$$

Comparison between J_{SC}^{EQE} and the experimentally measured J_{SC} under 1 sun illumination provides a valuable consistency check and can reveal issues such as spectral mismatch, parasitic absorption, or inaccuracies in illumination calibration.

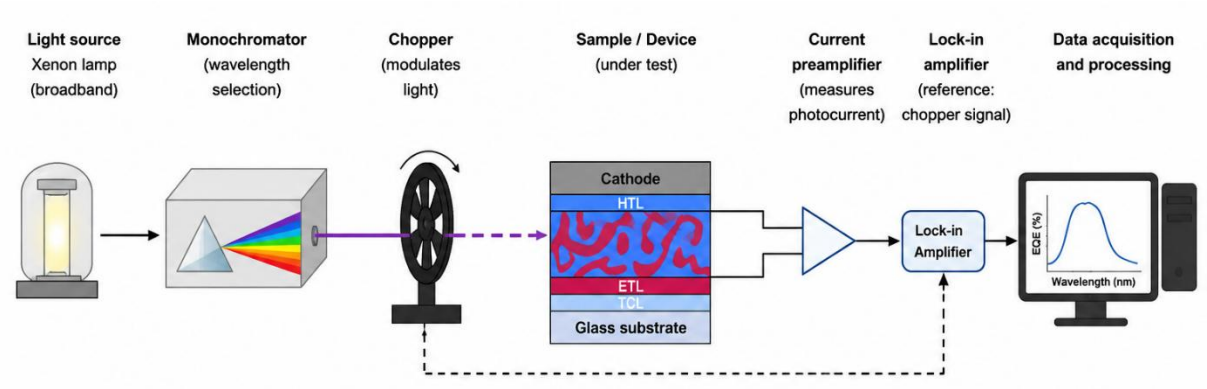

Figure 2-20: *Principle of external quantum efficiency.*

2.3.4 Structural characterization by Grazing-Incidence Wide-Angle X-ray Scattering (GIWAXS)

Grazing Incidence Wide-Angle X-ray Scattering (GIWAXS) is a powerful structural characterization technique used to probe the crystallinity, molecular orientation, and ordering in thin films. By using a shallow incident angle, typically below the critical angle of total external reflection, GIWAXS enhances surface sensitivity and minimizes substrate contributions, making it ideal for analyzing thin films and surface layers.

In this study, GIWAXS measurements were carried out by Arnaud Hemmerle, using the SIRIUS beamline at the French National Synchrotron Radiation facility SOLEIL, operating at an X-ray energy of 10 keV. The incident angle was set to 0.12° to ensure grazing incidence geometry, which allows for the selective probing of the near-surface region of the films. The scattered X-rays were collected using a two-dimensional area detector placed at an appropriate distance from the sample, enabling the capture of both in-plane and out-of-plane diffraction signals simultaneously.

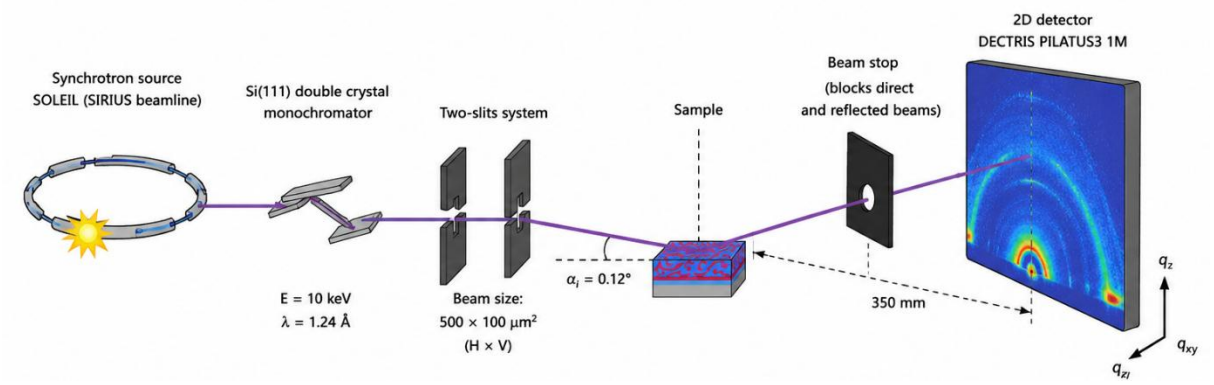

Figure 2-21: *Principle of GIWAXS measurement.*

The resulting 2D scattering patterns were analyzed to extract information about the crystalline structure, π–π stacking distances, lamellar spacing, and preferred orientation distribution of molecular domains (**Figure 2-21**). Radial and azimuthal integrations were performed to obtain 1D line profiles for quantitative analysis. Peak positions were used to calculate d-spacings via Bragg's law, while peak widths provided insights into the crystalline coherence length and degree of ordering using the Scherrer equation.[92]

Chapter 3
Optimization of the Top Organic Solar Cell to be Integrated in an Organic/Silicon Tandem Cell

3.1. Material selection and device architecture of the wide bandgap top cell

3.1.1 Choice of the PM6:GS-ISO system

The selection of the active layer materials for the OPV top cell is a critical step in the design of an efficient OPV/Si tandem solar cell. In such architectures, the top cell must satisfy specific optical and electrical requirements dictated by the tandem configuration rather than being optimized as a standalone device. In particular, the absorber must exhibit a sufficiently WBG to ensure efficient absorption of high-energy photons while allowing the transmission of lower-energy photons to the Si bottom cell.[93] Within the framework of the ORGANIST project, numerical simulations have demonstrated that, for a 3T tandem configuration based on a Si bottom cell, the optimal bandgap of the top cell lies in the range of 1.6 to 1.9 eV. With such an adapted bandgap, efficiencies of around 42 % can theoretically be achieved (**Figure 3-1**).[94]

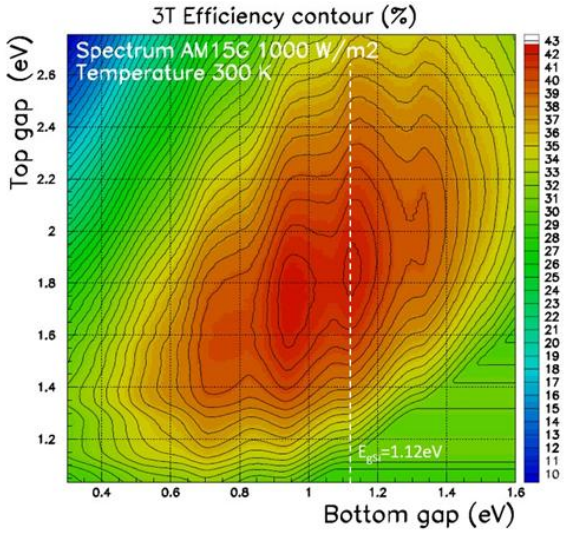

Figure 3-1: *Efficiency contour of a 3T tandem solar cell as a function of the gap of the bottom and the top subcells (under AM1.5G 1000W/m², T=300K).*[94]

This bandgap range enables an optimal trade-off between photocurrent generation and voltage output, while minimizing thermalization losses. In this context, organic semiconductors represent a highly attractive class of materials due to their tunable optoelectronic properties and the wide variety of available donor-acceptor combinations. Based on these considerations, the BHJ system composed of the polymer donor PBDB-T-2F (PM6) and the NFA GS-ISO was selected as the active layer for the WBG top cell (**Figure 3-2**). Both materials exhibit optical bandgaps of approximately 1.84 eV for PM6 and 1.82 eV for GS-ISO, placing this system within the optimal bandgap range for tandem applications (**Figure 3-3**).[95,96] In addition to this favorable spectral positioning, this donor-acceptor combination has been reported to exhibit high PV performance in single-junction devices, with PCE exceeding

11 % and EQE around 70 %, highlighting its ability to efficiently generate and collect charge carriers.[95]

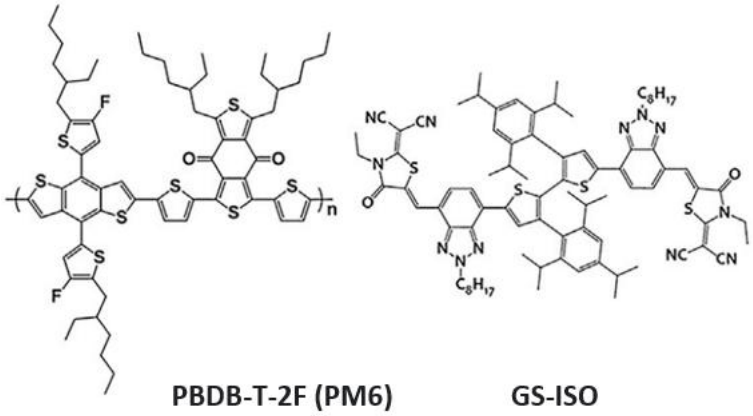

Figure 3-2: *Chemical structures of PM6 and GS-ISO.*

A key advantage of the PM6:GS-ISO system lies in its ability to achieve high V_{OC}, typically around 1.2 V.[95] This high V_{OC} is associated with relatively low energy losses, resulting from a favorable donor–acceptor energetics, a high-energy CT state, and reduced non-radiative recombination losses (**Figure 3-3**). In the context of tandem solar cells, maximizing V_{OC} is of primary importance, as the subcells (in a 3-terminal configuration) do not operate in series electrically, and therefore the total voltage is not simply the sum of the subcell voltages.[78] Therefore, materials exhibiting low non-radiative recombination losses and reduced energetic disorder are particularly desirable.

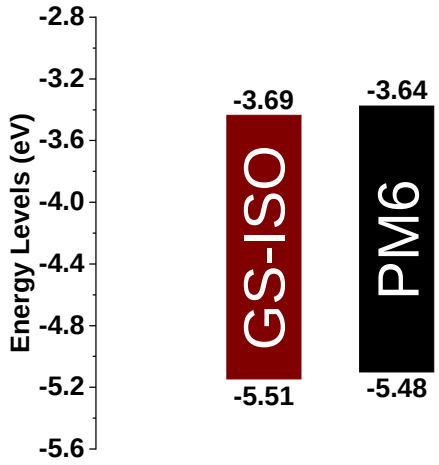

Figure 3-3: *Energy level diagram of PM6 and GS-ISO.*

In addition to its favorable energetic properties, the PM6:GS-ISO system benefits from the intrinsic advantages of NFA-based blends. NFAs offer strong and tunable absorption, reduced voltage losses, and often improved morphological stability compared to fullerene-based systems.[72] These features contribute to enhanced charge separation efficiency and

reduced recombination losses, making them particularly suitable for high-performance WBG OSC.

Furthermore, the selected materials are commercially available from established suppliers such as 1-Material and Brilliant Matters, eliminating the need for complex and time-consuming synthesis procedures. This aspect not only reduces experimental complexity and cost but also enhances the reproducibility and scalability of the fabrication process.

Finally, the selection of this material system is supported by numerical simulations carried out on Silvaco within the ORGANIST project. These simulations are performed with an inorganic semiconductor's model. Modeling indicates that a tandem device incorporating an organic top cell with a bandgap around 1.7 eV and a non-optimized IBC Silicon cell with a PCE of 22 % can achieve efficiencies around 26 % when considering realistic optical and recombination losses (**Figure 3-4a** and **Figure 3-4b**).[97] This result confirms the relevance of the PM6:GS-ISO system as a suitable candidate for integration into a high-efficiency OPV/Si tandem architecture.

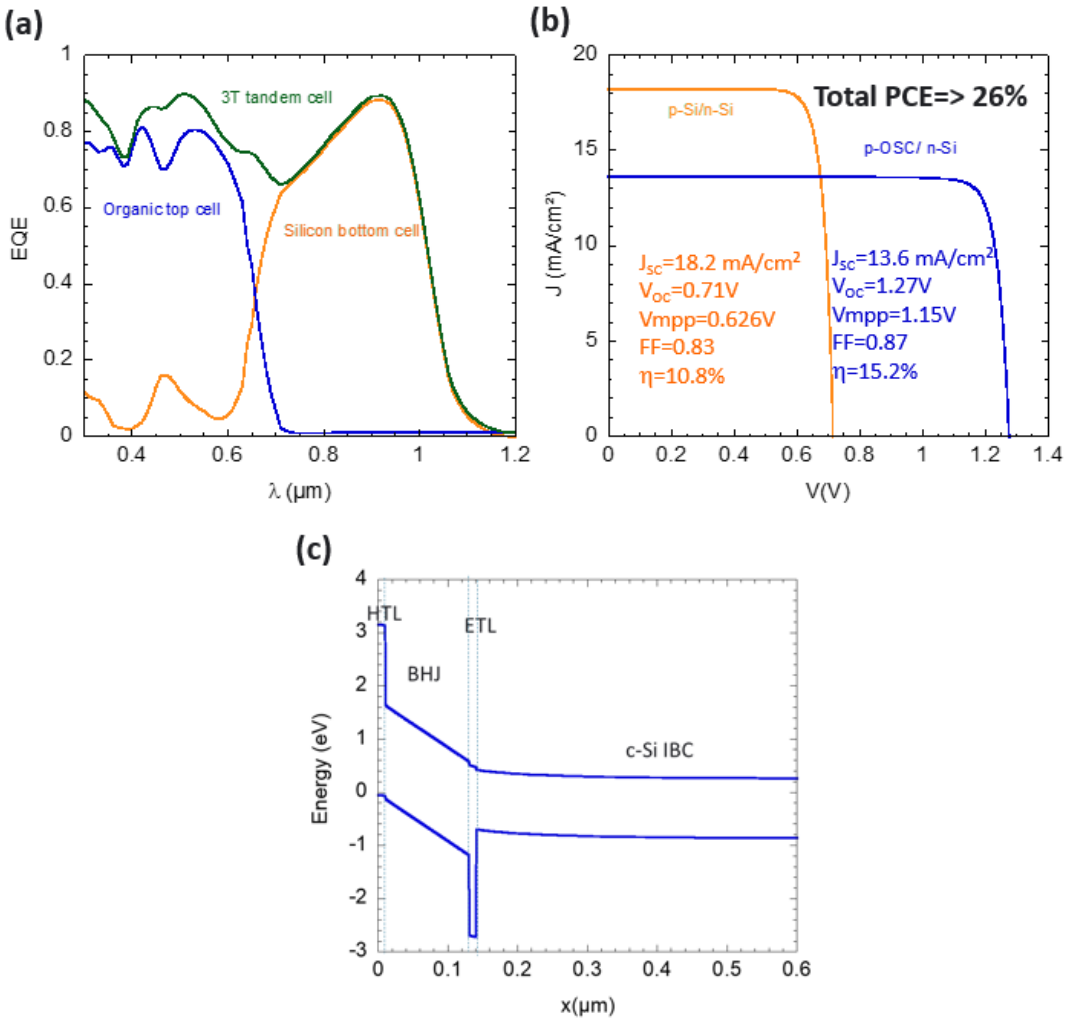

Figure 3-4: *Simulated (a) EQE, (b) J-V curves and (c) Energy band diagram for an OSC (Eg = 1.7 eV) and an IBC Silicon cell.*[97]

3.1.2 Device architecture: inverted structure

The design of the device architecture plays a key role in determining both the performance and the stability of OSC, particularly for WBG systems intended for tandem integration. In this work, an inverted architecture based on the structure ITO/ZnO/PAL/MoO_3/Ag was selected (**Figure 3-5**). This configuration corresponds to an n-i-p structure, in which electrons are extracted through the bottom contact (ZnO/ITO) while holes are collected through the top contact (MoO_3/Ag).

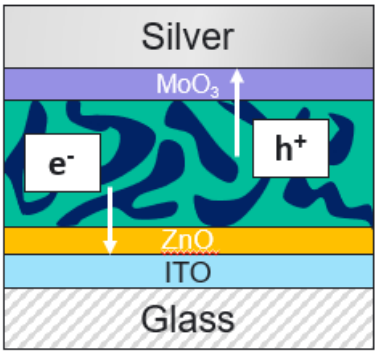

Figure 3-5: *Schematic representation of the inverted device architecture.*

The choice of an inverted architecture is primarily driven by the need to ensure efficient and selective charge extraction.[46,47] In a BHJ OSC, photogenerated excitons dissociate at the donor-acceptor interface, leading to the generation of free charge carriers following charge transfer and dissociation. This process requires proper energy level alignment between the PAL and the charge transport layers.

In the present configuration, Zinc Oxide (ZnO) is used as an ETL due to its suitable conduction band position, which aligns well with the LUMO of the acceptor material. This alignment enables efficient electron extraction while simultaneously blocking holes, thus reducing interfacial recombination losses. Conversely, MoO_3 acts as a HTL, providing a high work function interface that matches the HOMO of the donor, thereby facilitating hole extraction at the top electrode. Selective charge carrier extraction is essential to maintain a high V_{OC} and to minimize recombination processes within the device. Beyond energy level considerations, the inverted architecture is also well adapted to the intrinsic morphology of many donor-acceptor blends. In PM6:GS-ISO systems, as in many NFA-based BHJ, a vertical phase segregation is often reported during film formation. This typically leads to a preferential distribution of the acceptor material toward the bottom interface and the donor material toward the top surface.[98,99] Such a vertical composition gradient is particularly favorable in an inverted structure. Indeed, electrons generated in acceptor-rich regions near the ZnO interface can be efficiently extracted, while holes generated in donor-rich regions near the MoO_3 interface can be readily collected. This intrinsic alignment between morphology and device architecture contributes to improved charge transport and reduced recombination losses. Another key advantage of the inverted architecture lies in its enhanced environmental stability. Conventional (p-i-n) architecture typically relies on low-work-function metals (Ca or

Al) and organic hole transport layers such as PEDOT:PSS, which are highly sensitive to oxygen and moisture. Their degradation leads to increased R_S, interfacial defects, and a rapid decline in device performance. In contrast, inverted architectures replace these unstable materials with more chemically robust charge transport layers, such as ZnO and MoO_3, and high-work-function electrodes such as Ag. This improved material stability enhances resistance to environmental degradation, resulting in better operational stability and making inverted devices more suitable for long-term practical applications.[48]

The selection of the inverted architecture is also directly linked to the requirements of the OPV/Si tandem configuration developed in the ORGANIST project. In the 3T architecture considered in this work, the bottom cell is based on an n-type c-Si IBC cell. The polarity of the top organic cell must therefore be selected to ensure the appropriate alignment of the charge-selective contacts at the interface between the two subcells. In this configuration, an n-i-p architecture is adopted for the organic top cell, enabling the required electrical connection with the n-type IBC-Si bottom cell (**Figure 3-4c**).[69]

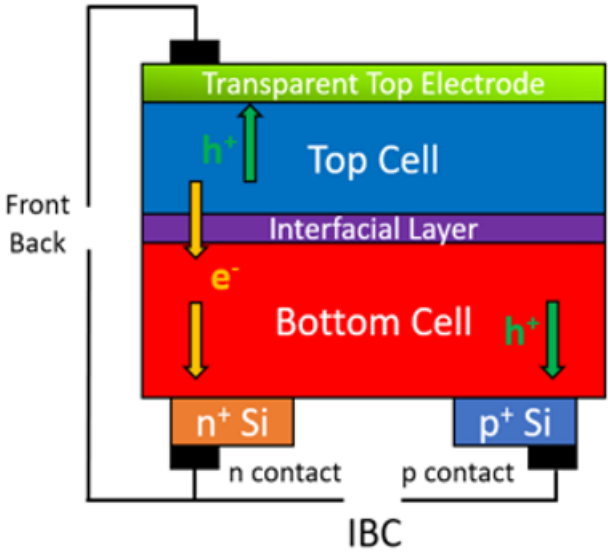

Figure 3-6: *Schematic of the 3-terminal OPV/Si tandem architecture.*

The integration of the organic top cell within the 3-terminal OPV/Si tandem architecture is illustrated in **Figure 3-6**. In this configuration, electrons photogenerated in the organic subcell are transported through the n-type interconnection toward the IBC-Si cells, while holes are selectively extracted through the top contact. Their transport must not be hindered by a potential barrier at the interface. This imposes strict constraints on the energy level alignment at the interface. To address this issue, an interfacial layer, often referred to as a selective band-offset barrier (SBOB), can be introduced between the OPV and Si subcells. This layer is designed to provide a low conduction band offset for electron transport and a large valence band offset to block holes. [94] Finally, the inverted architecture is highly compatible with solution-based fabrication techniques. All layers, including the PAL and interfacial materials, can be deposited using low-temperature processes, which is essential for scalable manufacturing methods such as roll-to-roll processing making this architecture particularly attractive for large-area and flexible PV applications.[58]

3.2. Device fabrication and sample preparation

Before integrating the organic top cell into the OPV/Si tandem architecture, the fabrication process was first optimized using single-junction OSC devices. This preliminary optimization was performed on glass/ITO substrates using a conventional bottom-illumination configuration, allowing the influence of the different fabrication parameters on the device performance to be systematically investigated under well-controlled conditions. Once the optimal fabrication conditions were established, the process was adapted to the top-illumination configuration required for integration with the c-Si bottom cell in the tandem architecture. The aim of this optimization step was therefore to establish a reliable fabrication protocol on glass substrates before transferring the optimized process to the c-Si based substrates used within the ORGANIST project.

OSC single-junction devices were fabricated using an inverted architecture consisting of glass/ITO/ZnO/BHJ/MoO_3/Ag, where ZnO serves as the ETL and MoO_3 as the HTL. The substrates are glass slides coated with ITO (1.5 × 1.5 cm, 10 Ω/sq, VisionTek). Prior to deposition, the substrates were cleaned by sequential ultrasonic treatment in diluted Hellmanex III solution, deionized water, acetone, deionized water, and isopropanol. After cleaning, the ITO substrates were treated with UV-ozone for 15 min before ETL deposition.
The ZnO precursor solution was prepared by dissolving zinc acetate dihydrate (166 mg) and ethanolamine (45 µL) in ultrapure ethanol (4.95 mL). The solution was stirred at 55 °C in air for 30 min, filtered through a 0.2 µm polytetrafluoroethylene (PTFE) filter, and kept under continuous stirring at room temperature prior to deposition. The ZnO layer was then deposited by spin coating at 2000 rpm for 30 s, resulting in a film thickness of approximately 40 nm. The substrates were subsequently annealed in air at 180 °C for 30 min, leading to the thermal decomposition of the precursor and the formation of a compact ZnO ETL. For the BHJ solution used in this work, PBDB-T-2F (PM6) and GS-ISO (1:1.3 wt%) were dissolved in o-xylene at a total concentration of 23 $mg.mL^{-1}$, with 1,8-diiodooctane (5 µL) added as a liquid additive. The solution was stirred for at least 3 h at 55 °C inside a nitrogen-filled glovebox to ensure complete dissolution and homogenization of the components. It was then deposited by spin coating at 2000 rpm for 60 s, forming an approximately 130 nm active layer, a thickness chosen as a trade-off between optical absorption and charge transport limitations. MoO_3 and Ag layers were deposited by thermal evaporation under high vacuum at a base pressure of 10^{-6} mbar. The MoO_3 HTL was deposited to a thickness of 7 nm at a rate of 0.5 $Å \cdot s^{-1}$, followed by deposition of the Ag top electrode to a thickness of 80 nm at 1 $Å \cdot s^{-1}$. Both layers were patterned using a shadow mask, defining four devices per substrate, each with an active area of 10.5 mm^2. These thicknesses were selected to ensure efficient hole extraction and low series resistance while maintaining good optical reflectivity of the top electrode.

3.3. Optimization of the PM6:GS-ISO active layer

The initial processing parameters were selected based on previously reported optimized conditions for the PM6:GS-ISO system made by *Zheng et al*.[68] In this work, they

investigated PM6:GS-ISO blend as the active material in a single cell, to be integrated in an OSC/OSC tandem cell at the end of the study. The optimized conditions compiled in this article are: a solution concentration of 23 mg·mL^{-1}, a spin-coating speed of 2000 rpm leading to an active layer thickness of approximately 120 nm, and a donor-to-acceptor ratio of 1:1.3 were used as a starting point. These conditions, identified as close to optimal in the literature, provide a solid baseline for device fabrication. However, in order to adapt the process to our specific experimental setup and further enhance device performance, a systematic optimization of these parameters was carried out.

3.3.1 Influence of solution concentration and film thickness

a) Solution concentration

The concentration of the active material in the solution is a key processing parameter that directly influences the thickness, the morphology, and ultimately the PV performance of the PAL. In solution-processed OSC, the deposited film thickness scales with the solution concentration, which in turn impacts light absorption, charge transport, and recombination processes.[100]

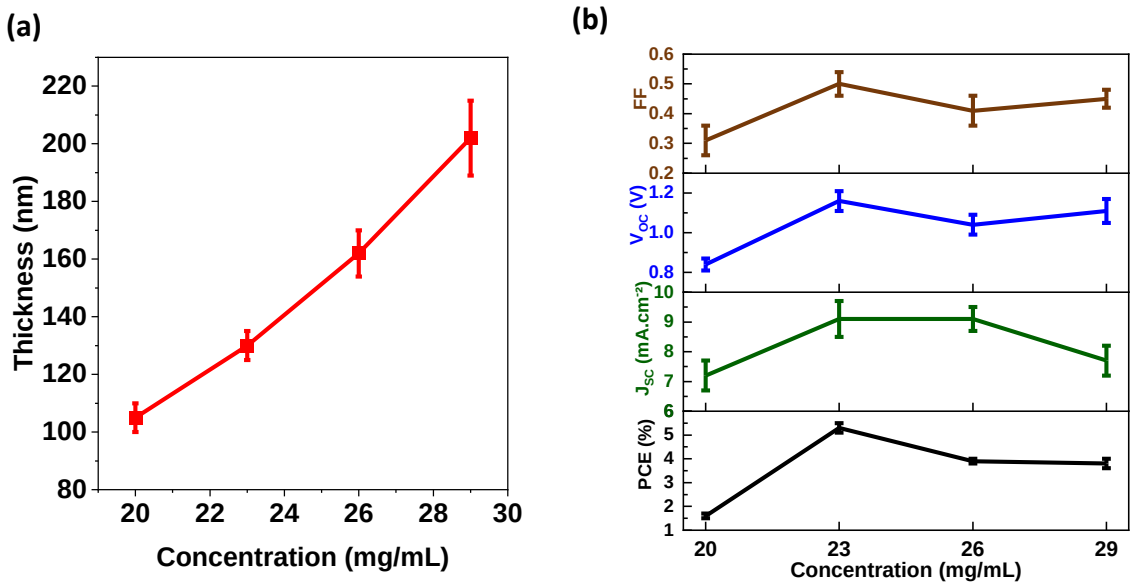

Figure 3-7: *(a) Active layer thickness and (b) PV parameters (PCE, J_{SC}, V_{OC} and FF) as a function of solution concentration.*

As shown in **Figure 3-7a**, the film thickness increases almost linearly with concentration, ranging from approximately 105 nm at 20 mg·mL^{-1} to about 202 nm at 29 mg·mL^{-1}. This trend is consistent with the expected behavior for spin-coated films, where a higher solute content leads to thicker deposited layers.

Concentration (mg/mL)	Thickness (nm)	PCE (%)	J_{SC} (mA.cm^{-2})	V_{OC} (V)	FF
20	105 ± 5	1.9 ± 0.1	7.2 ± 0.5	0.84 ± 0.03	0.31 ± 0.05
23	**130 ± 5**	**5.3 ± 0.2**	**9.1 ± 0.6**	**1.16 ± 0.05**	**0.50 ± 0.04**
26	162 ± 8	3.9 ± 0.1	9.1 ± 0.4	1.04 ± 0.05	0.41 ± 0.05
29	202 ± 13	3.8 ± 0.2	7.7 ± 0.5	1.11 ± 0.06	0.45 ± 0.03

Table 3-1: *Summary of PV parameters as a function of solution concentration.*

The impact of concentration on device performance is summarized in **Figure 3-7b** and **Table 3-1**. A strong dependence of the PV parameters on the solution concentration is observed. At low concentration (20 mg·mL^{-1}), the devices exhibit poor performance, with a PCE of 1.9 %, mainly limited by a low J_{SC} of 7.2 mA·cm^{-2} and a reduced FF of 0.31. This behavior is attributed to insufficient light absorption in the thin active layer, as well as incomplete charge transport pathways. Increasing the concentration to 23 mg·mL^{-1} leads to a significant improvement in device performance, with a maximum PCE of 5.3 %. This enhancement is primarily driven by an increase in J_{SC} (9.1 mA·cm^{-2}) and FF (0.50), as well as a consistent V_{OC} value around 1.16 V. The improvement in J_{SC} is consistent with enhanced photon absorption, due to increased thickness, while the higher FF suggests improved charge transport and reduced recombination losses. However, further increasing the concentration to 26 and 29 mg·mL^{-1} results in a decrease in PCE, despite relatively stable J_{SC} values around 9.1 mA·cm^{-2}. This performance drop is mainly associated with a reduction in FF and a slight decrease in V_{OC}. For instance, at 26 mg·mL^{-1}, the FF decreases to 0.41, indicating increased recombination losses within the thicker films.[101]

These results demonstrate the existence of an optimal concentration around 23 mg·mL^{-1}, corresponding to an optimal thickness of approximately 130 nm. At higher thicknesses, charge extraction becomes less efficient due to increased carrier recombination and longer transport pathways. This trade-off between optical absorption and charge transport must be carefully optimized to maximize device performance.

b) Film thickness

While solution concentration indirectly controls the film thickness, a more precise tuning can be achieved by adjusting the spin-coating speed. This allows decoupling thickness effects from other parameters and provides deeper insight into the role of PAL thickness on device performance.

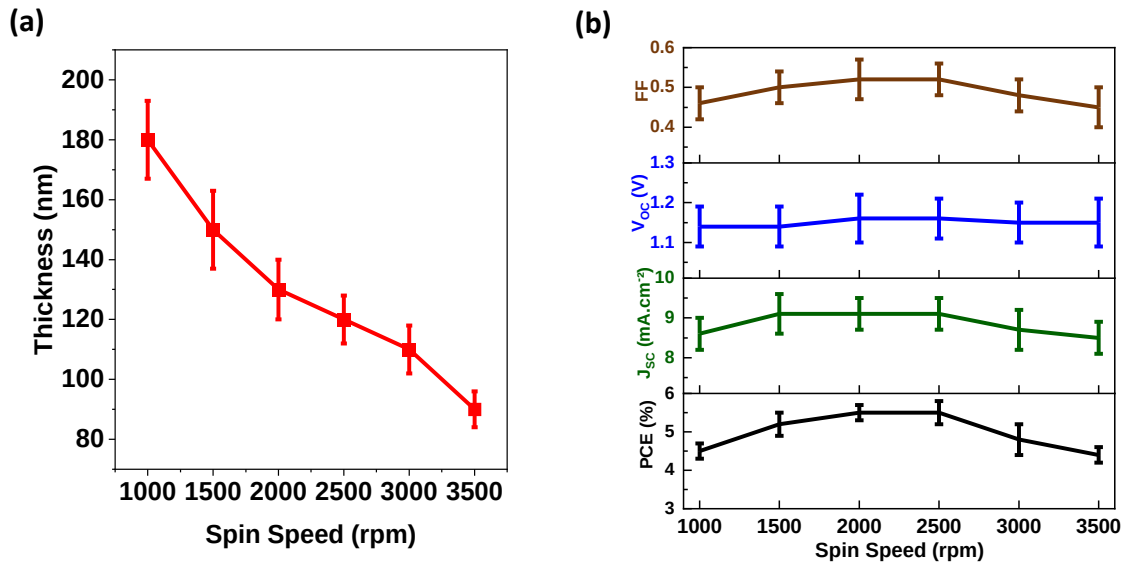

Figure 3-8: *(a) Film thickness and (b) PV parameters (PCE, J_{SC}, V_{OC} and FF) as a function of spin speed.*

As shown in **Figure 3-8a**, for an optimal solution concentration of 23 mg.mL^{-1}, increasing the spin speed from 1000 to 3500 rpm leads to a gradual decrease in film thickness from approximately 180 nm to 90 nm. This inverse relationship is typical of spin-coating processes, where higher rotational speeds promote solvent evaporation and reduce film thickness.

Spin Speed (rpm)	Thickness (nm)	PCE (%)	J_{SC} (mA.cm^{-2})	V_{OC} (V)	FF
1000	180 ± 13	4.5 ± 0.2	8.6 ± 0.4	1.14 ± 0.05	0.46 ± 0.04
1500	150 ± 13	5.2 ± 0.3	9.1 ± 0.5	1.14 ± 0.05	0.50 ± 0.04
2000	**130 ± 10**	**5.5 ± 0.2**	**9.1 ± 0.4**	**1.16 ± 0.06**	**0.52 ± 0.05**
2500	120 ± 8	5.5 ± 0.3	9.1 ± 0.4	1.16 ± 0.05	0.52 ± 0.04
3000	110 ± 8	4.8 ± 0.4	8.7 ± 0.5	1.15 ± 0.05	0.48 ± 0.04
3500	90 ± 6	4.4 ± 0.2	8.5 ± 0.4	1.15 ± 0.06	0.45 ± 0.05

Table 3-2: *Summary of PV parameters vs thickness.*

The PV performance as a function of thickness is presented in **Figure 3-8b** and **Table 3-2**. An optimal performance is observed for thicknesses in the range of 120-130 nm, corresponding to spin speeds of 2000-2500 rpm, where PCE reaches values up to 5.5 %. At large thicknesses (180 nm), the devices exhibit reduced performance (PCE = 4.5%), mainly due to lower FF (0.46) and slightly reduced J_{SC}. This behavior is attributed to increased recombination losses due to longer carrier transport distances. Conversely, at very low thicknesses (90 nm), the PCE also decreases to around 4.4 %, primarily due to reduced light absorption, as reflected by a lower J_{SC} (8.5 mA·cm^{-2}). Interestingly, V_{OC} remains relatively

constant across the entire thickness range (1.14-1.16 V), indicating that the energetic properties of the system are not significantly affected by thickness variations. In contrast, both J_{SC} and FF are strongly dependent on thickness, reflecting the interplay between optical absorption and charge transport.[101]

Overall, these results confirm that an optimal thickness exists around 120-130 nm, which provides the best compromise between efficient light harvesting and charge extraction. This thickness range is therefore selected for the subsequent optimization steps.

3.3.2 Optimization of donor/acceptor ratio

The donor-to-acceptor (D:A) ratio is a critical parameter governing the nanoscale morphology of the BHJ, and thus strongly impacts exciton dissociation, charge transport, and recombination processes. Adjusting this ratio allows fine-tuning of the phase separation, domain purity, and percolation pathways within the PAL.[102]

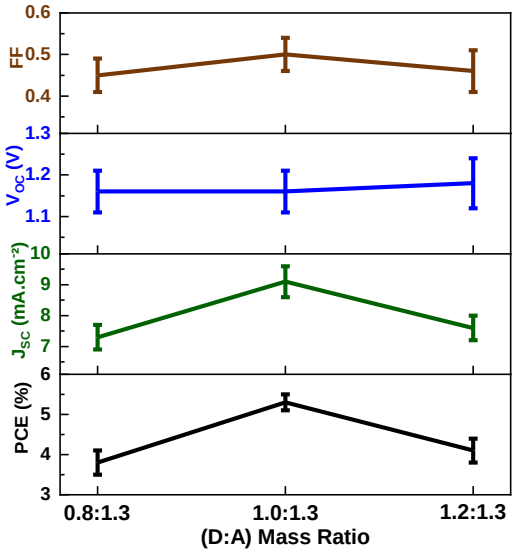

Figure 3-9: *PV parameters vs D:A ratio.*

(D:A) Mass Ratio	PCE (%)	J_{SC} (mA.cm^{-2})	V_{OC} (V)	FF
0.8:1.3	3.8 ± 0.3	7.3 ± 0.4	1.16 ± 0.05	0.45 ± 0.04
1:1.3	**5.3 ± 0.2**	**9.1 ± 0.5**	**1.16 ± 0.05**	**0.50 ± 0.04**
1.2:1.3	4.1 ± 0.3	7.6 ± 0.4	1.18 ± 0.06	0.46 ± 0.05

Table 3-3: *Summary of PV parameters vs D:A ratio.*

The effect of the donor-to-acceptor (D:A) ratio on device performance was investigated for three compositions: 0.8:1.3, 1:1.3, and 1.2:1.3. The D:A ratio of 1:1.3 was selected as the reference composition based on the literature, while the two additional ratios were chosen to evaluate the impact of both lower and higher donor contents by bracketing

the reference value. The corresponding PV parameters are summarized in **Figure 3-9** and **Table 3-3**. The best performance is obtained for a D:A ratio of 1:1.3, yielding a PCE of 5.3 %, with a J_{SC} of 9.1 mA·cm^{-2}, a V_{OC} of 1.16 V, and a FF of 0.50 . This result indicates that this composition provides an optimal balance between donor and acceptor phases, enabling efficient exciton dissociation and charge transport. At lower donor content (0.8:1.3), the PCE decreases to 3.8 %, mainly due to a significant drop in J_{SC} (7.3 mA·cm^{-2}) and FF (0.45). This behavior is attributed to an insufficient donor network limiting carrier transport. Conversely, increasing the donor content to a D:A ratio of 1.2:1.3 also results in lower device performance (PCE = 4.1%), despite a slight increase in V_{OC} (1.18 V). This performance degradation is attributed to a disruption of the optimized BHJ morphology. Excess donor content can promote the formation of larger donor-rich domains and reduce the donor-acceptor interfacial area, thereby hindering exciton dissociation, charge transport, and charge extraction while increasing recombination losses.[103]

3.3.3 Thermal annealing optimization

The effect of thermal annealing on the PM6:GS-ISO active layer was investigated by treating the films at different temperatures (as-cast, 80, 120, 160, and 200 °C) for 15 minutes prior to the deposition of the HTL. The corresponding *J-V* characteristics are presented in **Figure 3-10a**, while PV parameters (J_{SC}, V_{OC}, FF, and PCE) as a function of annealing temperature are shown in **Figure 3-10b** and **Table 3-4**. Devices fabricated without thermal treatment exhibit limited performance, with a J_{SC} of 9.1 mA·cm^{-2} and a FF of 0.50, which are insufficient to achieve high-efficiency devices. Upon thermal annealing, both J_{SC} and FF increase, resulting in an improvement of the PCE from 5.2 % for the as-cast device to 6.4 % for the device annealed at 160 °C. At this optimal temperature, the device exhibits a V_{OC} of 1.09 V, a J_{SC} of 10.5 mA·cm^{-2}, and a FF of 0.56. This improvement is likely associated with enhanced molecular organization and a more favorable BHJ morphology, as will be confirmed by the morphological analyses presented later. At higher annealing temperature (200 °C), the PCE decreases to 4.3 %, which is attributed to an unfavorable morphology, such as large phase segregation suggested by the drop of J_{SC} from 10.5 to 8.1 mA.cm^{-2}.[104]

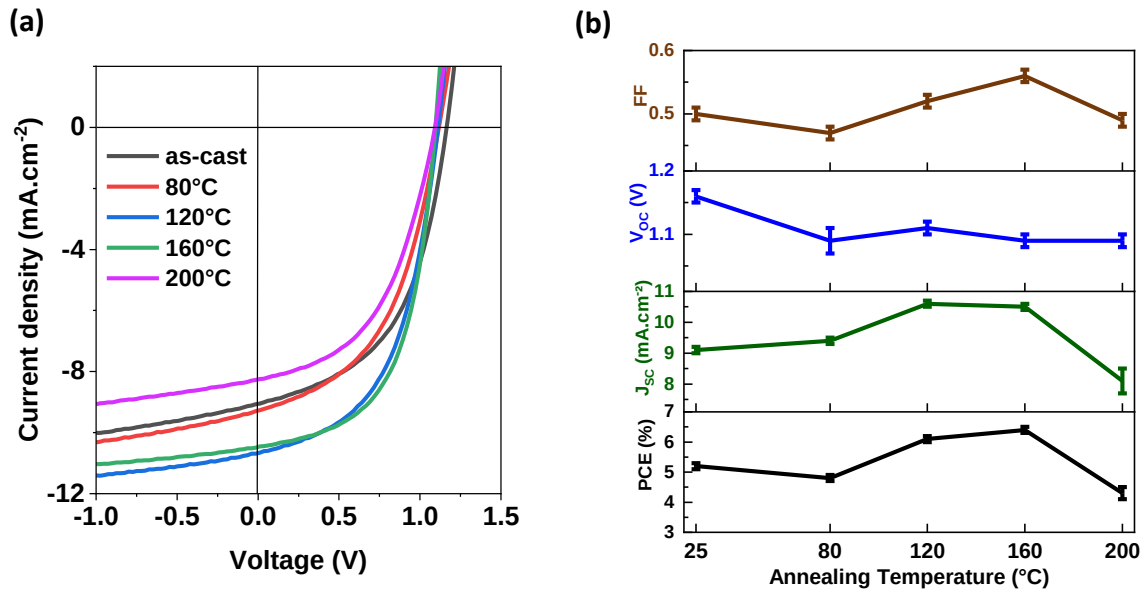

Figure 3-10: *(a) J-V characteristics and (b) PV parameters (PCE, J_{SC}, V_{OC} and FF) of PM6:GS-ISO devices as a function of annealing temperature.*

Annealing Temperature (°C)	PCE (%)	J_{SC} (mA.cm^{-2})	V_{OC} (V)	FF
As-cast	5.2 ± 0.1	9.1 ± 0.1	1.16 ± 0.01	0.50 ± 0.01
80	4.8 ± 0.1	9.4 ± 0.1	1.09 ± 0.02	0.47 ± 0.01
120	6.1 ± 0.1	10.6 ± 0.1	1.11 ± 0.01	0.52 ± 0.01
160	**6.4 ± 0.1**	**10.5 ± 0.1**	**1.09 ± 0.01**	**0.56 ± 0.01**
200	4.3 ± 0.2	8.1 ± 0.4	1.09 ± 0.01	0.49 ± 0.01

Table 3-4: *Summary of PV parameters as a function of annealing temperature.*

The impact of thermal annealing on the optical properties of both the pristine materials and the PM6:GS-ISO blend was investigated by UV–visible absorption spectroscopy, as shown in **Figure 3-11a**. The absorption spectrum of PM6 remains essentially unchanged after thermal treatment. In contrast, the pure GS-ISO film exhibits a pronounced red-shift ($\Delta\lambda$ = 24 nm), which is attributed to strong crystallization in the single-component film.[105] For the PM6:GS-ISO blend, thermal annealing induces a slight broadening of the absorption spectrum, with an increase in the full width at half maximum ($\Delta FWHM$ = 6 nm) and a slight red-shift. This behavior may indicate subtle changes in intermolecular interactions or film morphology.[106,107] The optical bandgap (E^{opt}_g) of the blend was estimated from Tauc plot analysis (**Figure 3-11b**). The extracted value remains nearly constant, around 1.85 eV, both before and after annealing, corresponding to the bandgap of GS-ISO.

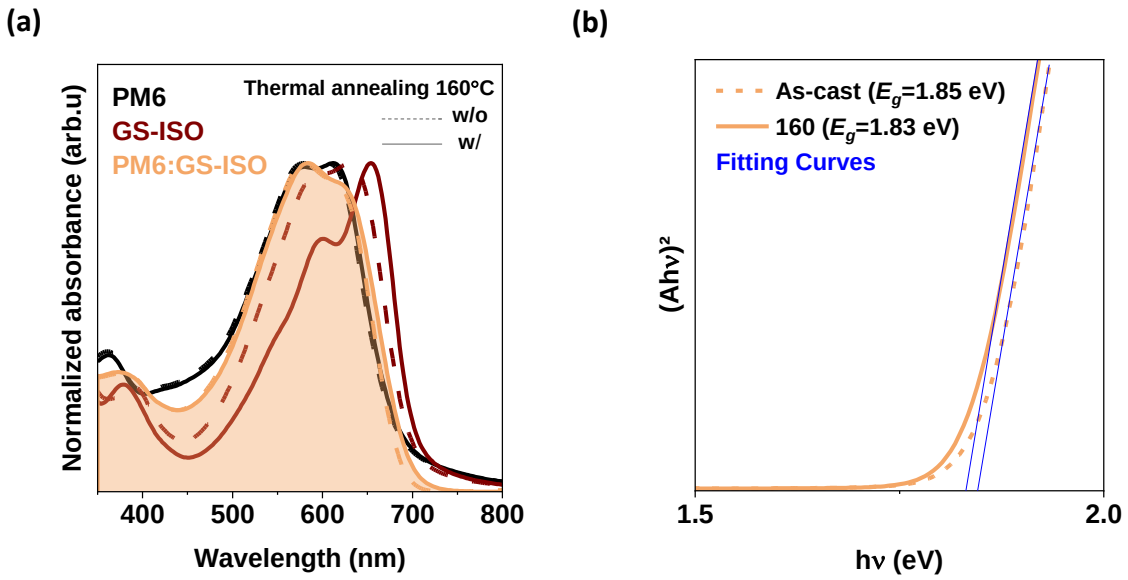

Figure 3-11: *(a) UV-Vis absorption spectra of PM6, GS-ISO and PM6:GS-ISO films and (b) Tauc plot of PM6:GS-ISO films with and without annealing.*

As shown in **Figure 3-12a** and **Figure 3-12b**, AFM images reveal a clear modification of the film morphology upon thermal annealing. The as-cast film exhibits a relatively smooth surface, with an average grain size (D_{avg}) of approximately 80 ± 20 nm and a root-mean-square roughness (σ_{rms}) of 1.4 nm. After annealing at 160 °C, the grain size increases significantly to approximately 90 ± 25 nm, while the surface roughness remains nearly unchanged (**Table 3-5**). This evolution is consistent with thermally induced molecular reorganization and crystallization within the blend film.[108]

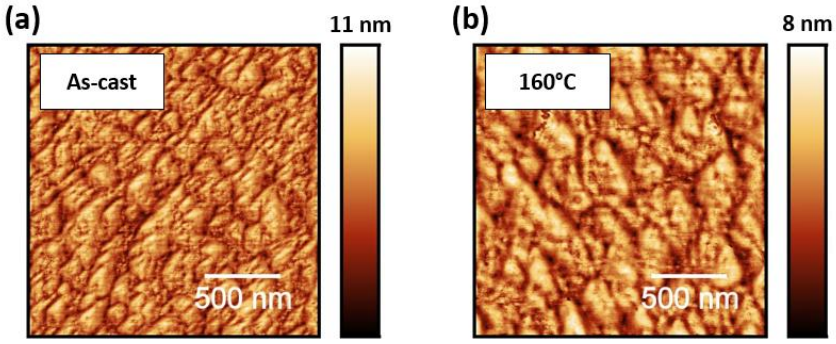

Figure 3-12: *AFM topographical images of PM6:GS-ISO films (a) as-cast and (b) annealed at 160 °C.*

Annealing Temperature (°C)	D_{avg} (nm)	σ_{rms} (nm)
As-cast	80 ± 20	1.4
160	90 ± 25	1.2

Table 3-5: *Influence of thermal annealing on BHJ morphology (average grain size and surface roughness).*

3.3.4 Solvent Additive Optimization

A small amount of the solvent additive 1,8-diiodooctane (DIO) was introduced in order to further enhance the PV performance of the devices (**Figure 3-13**). Blended solutions containing different DIO concentrations were used to fabricate OSC based on the same inverted architecture as previously described.

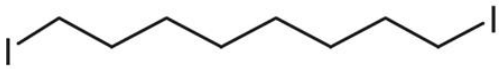

Figure 3-13: *Chemical structures of 1,8-diiodooctane (DIO).*

The use of DIO alone (0.5 v%), without applying thermal annealing, does not lead to high device efficiency, with a PCE limited to approximately 6 %. Therefore, the effect of DIO in combination with the optimal thermal treatment at 160 °C was investigated. The evolution of the *J-V* characteristics as a function of DIO content is presented in **Figure 3-14a**, while the corresponding PV parameters are summarized in **Figure 3-14b** and **Table 3-6**. The incorporation of an optimized DIO content (0.5 v%) into the blend solution results in a significant improvement in device performance, yielding a PCE of 7.4 %, a V_{OC} of 1.13 V, a J_{SC} of 11.5 mA·cm^{-2}, and a FF of 0.56. This optimal concentration is consistent with previously reported studies on PM6:GS-ISO systems.[68,95] It has been shown that the presence of DIO improves the morphology of the active layer, resulting in enhanced crystallinity, reduced energetic disorder, and improved charge transport pathways.[109,110] In contrast, increasing the DIO content to 1 v% leads to a marked degradation in device performance, characterized by a decrease in both J_{SC} and V_{OC}. This behavior is attributed to excessive crystallinity, poor phase organization, or large molecular aggregation within the film.[111,112]

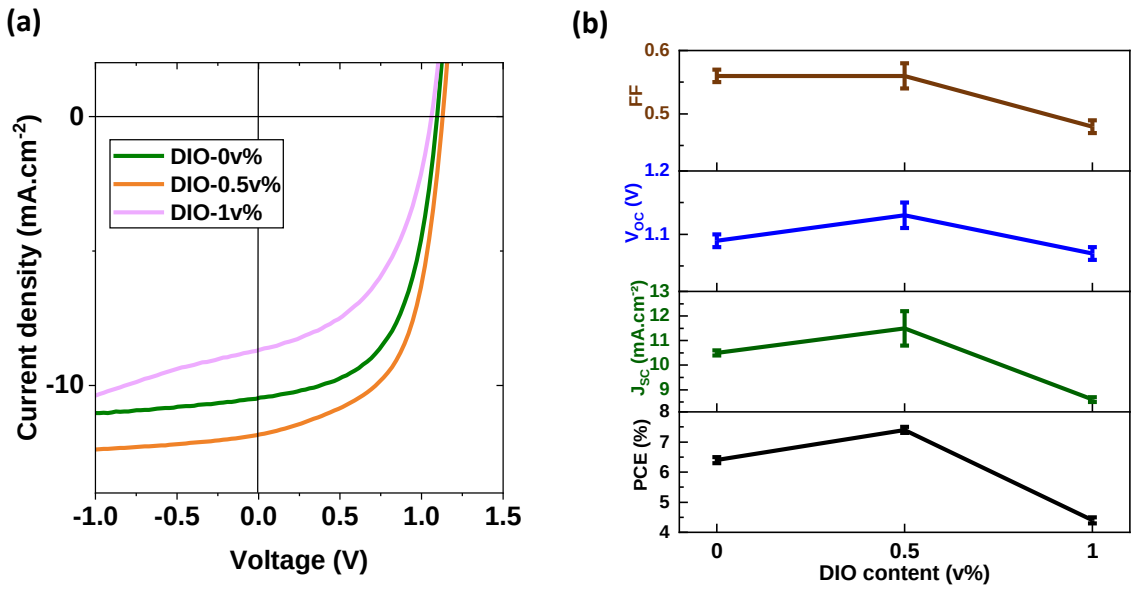

Figure 3-14: *(a) J-V characteristics and (b) PV parameters (PCE, J_{SC}, V_{OC} and FF) of PM6:GS-ISO devices as a function of DIO content.*

DIO content (v%)	PCE (%)	J_{SC} (mA.cm^{-2})	V_{OC} (V)	FF
0	6.4 ± 0.1	10.5 ± 0.1	1.09 ± 0.01	0.56 ± 0.01
0.5	**7.4 ± 0.1**	**11.5 ± 0.7**	**1.13 ± 0.02**	**0.56 ± 0.02**
1	4.4 ± 0.1	8.6 ± 0.1	1.07 ± 0.01	0.48 ± 0.01

Table 3-6: *Summary of PV parameters as a function of DIO content.*

The evolution of the film morphology with DIO content was further examined by AFM, as shown in **Figure 3-15**. The addition of a small amount of DIO (0.5 v%), combined with thermal annealing, results in the disappearance of larger grains and the formation of more homogeneous fibrillar domains (**Figure 3-15b**). This morphology reflects an improved phase separation between donor and acceptor materials, leading to enhanced charge transport pathways and more efficient exciton dissociation, reflected by both the increase of the FF and the J_{SC}.[113,114] At higher DIO content (1 v%), the fibrillar morphology is disrupted, with the appearance of larger domains (**Figure 3-15c**). This behavior is associated with over-aggregation of the donor phase, which disturbs the percolation pathways of the acceptor phase and reduces the interfacial area available for exciton dissociation.[114]

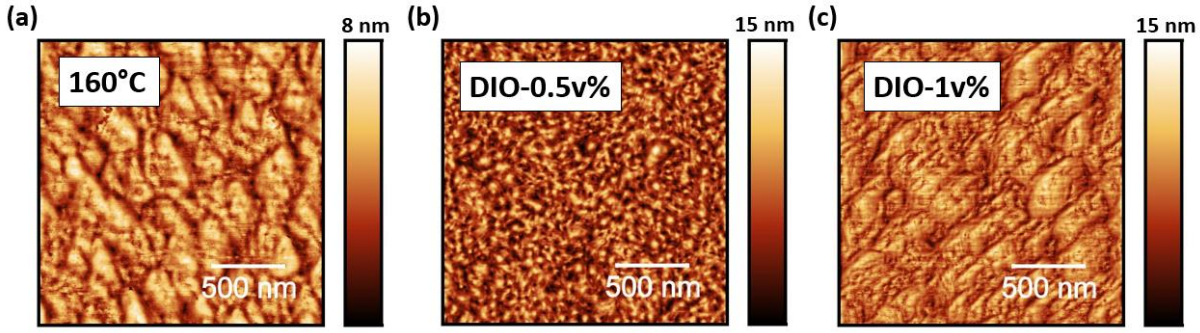

Figure 3-15: *AFM topographical images of PM6:GS-ISO films (a) w/o DIO, (b) w/ 0.5 v% DIO and (c) w/ 1 v% DIO.*

DIO content (v%)	D_{avg} (nm)	σ_{rms} (nm)
0	90 ± 25	1.2
0.5	55 ± 15	1.4
1	100 ± 20	2.1

Table 3-7: *Influence of DIO on BHJ morphology (average grain size and surface roughness).*

Key Point 3.3: Optimization of the PM6:GS-ISO active layer.

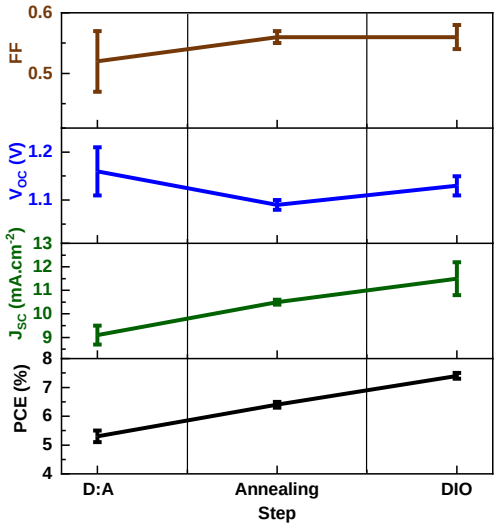

The PM6:GS-ISO active layer was successfully optimized by employing a solution concentration of 23 mg/mL, a spin-coating speed of 2000 rpm, a donor-to-acceptor ratio of 1:1.3, thermal annealing at 160 °C for 15 min, and the incorporation of 0.5 v% DIO as a processing additive.

3.4. Solid Additive Engineering: F8T2

3.4.1 Motivation

Following the optimization of the PM6:GS-ISO active layer through thermal annealing and solvent additive engineering, the device performance remains limited by intrinsic constraints associated with binary donor-acceptor systems. In particular, further improvements in PCE are increasingly difficult to achieve due to the complex interplay between morphology, charge transport, and recombination processes, which cannot always be simultaneously optimized within a two-component blend. In this context, multicomponent strategies have emerged as an effective approach to overcome the limitations of binary BHJ.[55,115] The introduction of a third component provides additional degrees of freedom to tune both the optoelectronic properties and the nanoscale morphology of the PAL, potentially leading to enhanced device performance.[115] Among the different approaches, the use of conjugated polymers as additives has attracted increasing attention.[116] These materials can act either as dopants or as morphological regulators, depending on their concentration and interaction with the host matrix. Previous studies have shown that the incorporation of a small amount of a conjugated polymer can modify the mesoscale organization of the BHJ, influence phase separation, and impact charge transport properties, ultimately improving device performance.[116]

In this work, poly(9,9-dioctylfluorene-co-bithiophene) (F8T2) was selected as a solid additive (**Figure 3-16**).

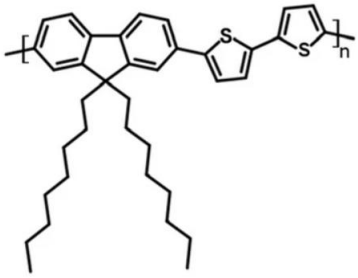

Figure 3-16: *Chemical structures of poly(9,9-dioctylfluorene-co-bithiophene) (F8T2).*

F8T2 is a well-known p-type semiconducting polymer with efficient hole transport properties and a high degree of crystallinity.[117] Despite these attractive characteristics, F8T2 has so far been only scarcely employed in ternary OSC strategies and has not been extensively investigated in combination with the PM6:GS-ISO system.[118] The introduction of F8T2 in small quantities (typically below 1 wt%) is expected to influence the organization of the PAL without significantly altering its optical absorption or thickness. In this regime, F8T2 acts as a non-volatile solid additive rather than as a primary photoactive component.[116] Based on previous studies, several effects can be anticipated from the incorporation of such an additive. First, the presence of a highly crystalline conjugated polymer may promote improved molecular ordering within the blend. Second, it may contribute to tuning the size and distribution of domains within the BHJ. Third, it may enable a more controlled phase separation between

donor and acceptor materials.[116] Additionally, the introduction of a third component has been reported to influence charge transport and recombination processes, either through modifications of the percolation pathways or through changes in the local energetic landscape of the blend.[115] In particular, previous studies have demonstrated that the addition of small amounts of functional additives can alter mesoscale morphology and impact charge carrier dynamics, affecting the photovoltaic response of the device.[116] Therefore, the integration of F8T2 as a solid additive in the optimized PM6:GS-ISO system represents a promising strategy to further tailor the structural and electronic properties of the PAL. The following section aims to investigate the impact of this additive on the PV performance and to elucidate the underlying physical mechanisms.

3.4.2 Optimization of F8T2 Content and Impact on PV Performance

The influence of F8T2 incorporation on the PV performance of PM6:GS-ISO solar cells was investigated by introducing varying amounts of the additive into the optimized binary blend. The devices were fabricated using the same processing conditions previously established, ensuring that any variation in performance could be directly attributed to the presence and concentration of F8T2. In this section, the samples are designated as ''F8T2-x wt%'', where x corresponds to the F8T2 mass fraction expressed in wt%.

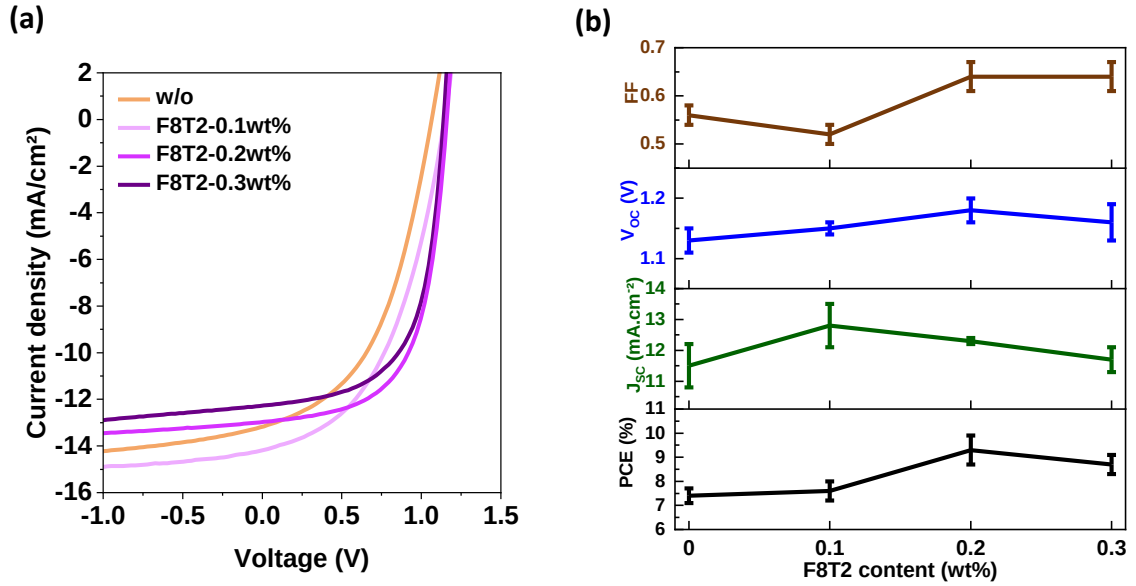

Figure 3-17: *(a) J-V characteristics and (b) PV parameters (PCE, J_{SC}, V_{OC} and FF) of PM6:GS-ISO devices as a function of F8T2 content.*

F8T2 content (wt%)	PCE (%)	J_{SC} (mA.cm^{-2})	V_{OC} (V)	FF
w/o	7.4 ± 0.3	11.5 ± 0.7	1.13 ± 0.02	0.56 ± 0.02
0.1	7.6 ± 0.4	12.8 ± 0.7	1.15 ± 0.01	0.52 ± 0.02
0.2	**9.3 ± 0.6** **[10.0]**	**12.3 ± 0.1** **[12.2]**	**1.18 ± 0.02** **[1.20]**	**0.64 ± 0.03** **[0.68]**
0.3	8.7 ± 0.4	11.7 ± 0.4	1.16 ± 0.03	0.64 ± 0.03

Table 3-8: *Summary of PV parameters as a function of F8T2 content. Values in square brackets correspond to the champion device.*

The *J-V* characteristics corresponding to different F8T2 contents are presented in **Figure 3-17a**, while the associated PV parameters (J_{SC}, V_{OC}, FF, and PCE) are summarized in **Figure 3-17b**, and **Table 3-8**. The introduction of a small amount of F8T2 into the PM6:GS-ISO blend leads to an improvement in device performance compared to the reference binary system. This improvement is reflected by an increase in the PCE from 7.4 % for the reference device (w/o) to values exceeding 9.3 % for optimized F8T2 content (F8T2-0.2wt%), and is mainly driven by variations in J_{SC} and FF. A slight increase in V_{OC} is observed upon the addition of F8T2, reaching values up to 1.20 V for the optimal condition (0.2 wt%), indicating that the energetic properties of the system are slightly modified. An optimal F8T2 content is identified at 0.2 wt%, for which the highest device performance is achieved with a PCE of 9.3 % (up to 10 % for the best device), a V_{OC} of 1.18 V (up to 1.20 V), J_{SC} of 12.3 mA.cm^{-2} and a FF of 0.64 (up to 0.68). At this concentration, the balance between the different PV parameters is optimized, resulting in the maximum efficiency. When the F8T2 content is further increased to 0.3 wt%, a degradation of the device performance is observed with the PCE decreasing to 8.7 %, mainly due to a reduction in J_{SC} and FF, while V_{OC} remains relatively stable. These results indicate that excessive F8T2 content negatively affects the PV performance, highlighting the existence of an optimal additive concentration.

3.4.3 Optical Properties

The EQE of the different devices was first investigated. The corresponding spectra are presented in **Figure 3-18a** for the reference device (without F8T2) and the optimized device containing 0.2 wt% F8T2, which exhibits the best PV performance. It is important to note that all devices, regardless of the processing conditions, possess active layers with comparable thicknesses of approximately 130 nm (± 5 nm). The integrated J_{SC} ($J_{SC\ int}$) calculated from the EQE spectra are reported in **Table 3-9** and are in good agreement with the trends observed in the *J-V* measurements. As shown in **Figure 3-18a**, the incorporation of 0.2 wt% F8T2 results in an enhanced photoresponse in the 400–500 nm and 600–700 nm spectral regions compared to the reference device. In addition, a slight broadening of the BHJ absorption spectrum is observed, with an increase in the full width at half maximum ($\Delta FWHM$ = 6 nm) in the 600–700 nm region. This spectral evolution may be attributed to improved intermolecular interactions

and a more favorable crystalline organization of the acceptor within the blend, as well as enhanced π–π stacking. Moreover, no significant change is observed in the absorption spectra of the individual donor and acceptor materials compared to their respective pristine films without F8T2, as shown in **Figure 3-18b**, indicating that F8T2 does not induce crystallization in the pure materials.

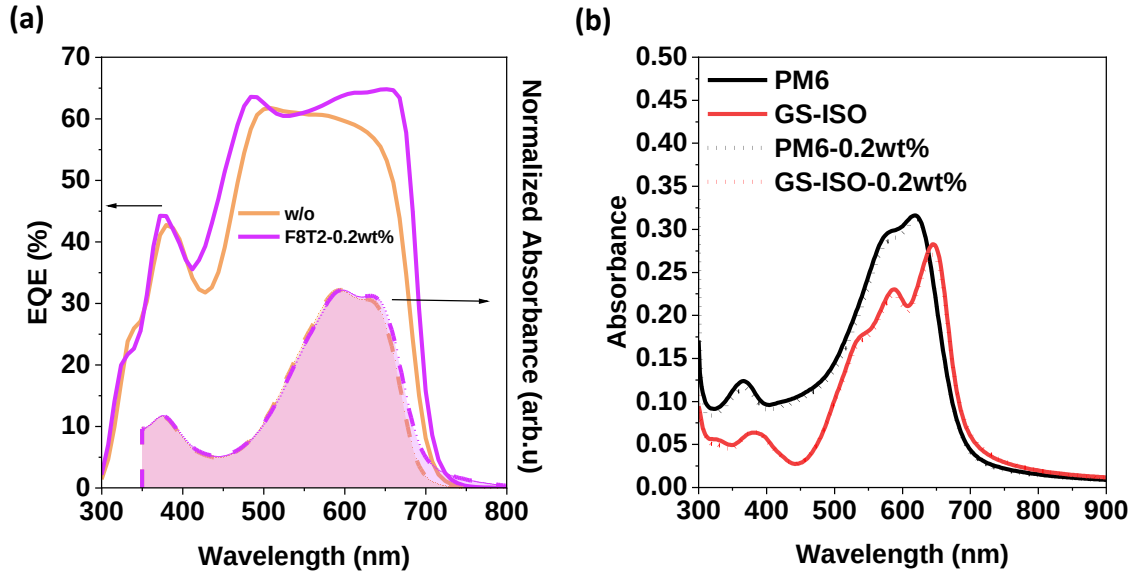

Figure 3-18: *(a) EQE and UV-Vis spectra of the BHJ with and without F8T2 and (b) UV-vis spectra of individual donor and acceptor with and without F8T2.*

F8T2 content (wt%)	J_{SC} (mA.cm^{-2})	$J_{SC\ int}$ (mA.cm^{-2})
w/o	11.5 ± 0.7	10.3
0.1	12.8 ± 0.7	11.4
0.2	**12.3 ± 0.1 [12.2]**	**11.6**
0.3	11.7 ± 0.4	10.5

Table 3-9: *Comparison of J_{SC} (from J-V) and integrated J_{SC} (from EQE) for varying F8T2 content*

3.4.4 Morphology and Structure

To further validate this hypothesis and to compare the molecular organization of PM6:GS-ISO films with and without 0.20 wt% F8T2, GIWAXS measurements were performed, as presented in **Figure 3-19**. As shown in **Figure 3-19c**, both samples exhibit pronounced in-plane (IP) diffraction peaks located at q_{xy} = 0.29 and 0.37 Å^{-1}, corresponding to the lamellar stacking of PM6 ((100) reflection, d-spacing = 21.7 Å) and GS-ISO (d-spacing = 17.0 Å), respectively.[95,119,120] In the out-of-plane (OOP) direction, these peaks are also detected, although slightly shifted, at q_z = 0.31 and 0.39 Å^{-1} (d-spacing = 20.3 and 16.1 Å). An additional

diffraction feature appears at q_z = 0.50 Å^{-1} (d-spacing = 12.6 Å), which may correspond to a different crystalline plane. The lamellar peak associated with PM6 is more intense in the OOP direction, whereas the GS-ISO lamellar peak is more prominent in the IP direction. Moreover, the diffraction peak corresponding to the π–π stacking distance (010) is clearly observed in the OOP direction at q_z = 1.77 Å^{-1} (d-spacing = 3.55 Å), while it is absent in the IP direction.[92] This indicates that, in both cases, the conjugated polymers and small molecules preferentially adopt a face-on orientation, which is favorable for vertical charge transport. The improvement in device performance upon F8T2 incorporation can be explained by two main mechanisms. First, the π–π stacking peak in the OOP direction is more intense for the F8T2-0.2wt% film. Since both films have comparable thicknesses (130 ± 5 nm), this increase reflects enhanced stacking of the aromatic units, which can promote vertical charge transport, improve percolation pathways for both electrons and holes, and reduce trap-assisted recombination, thereby contributing to the observed enhancement in FF.[121,122] Additionally, the GIWAXS pattern of the reference film exhibits a pronounced halo ring in the 1.4-1.6 Å^{-1} range, indicative of a significant amorphous fraction (**Figure 3-19a**). This feature is absent in the film containing 0.20 wt% F8T2, suggesting a reduction of the amorphous phase (**Figure 3-19b**).

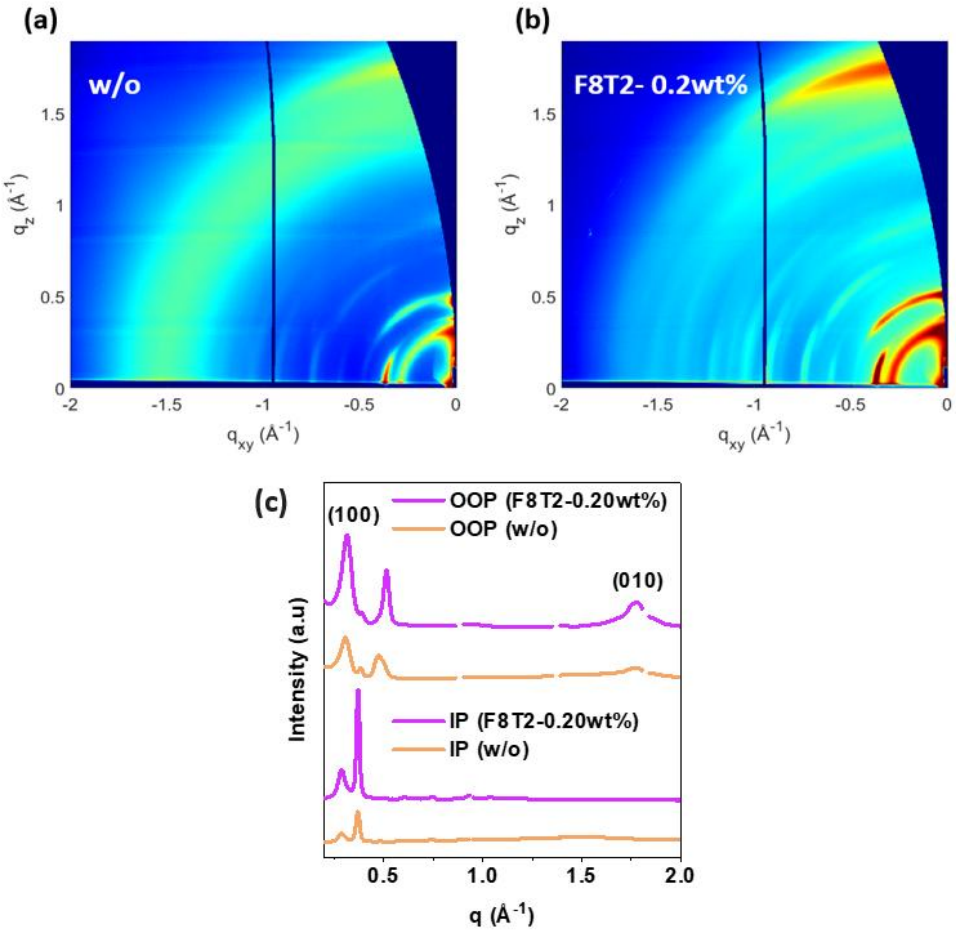

Figure 3-19: *2D-GIWAXS patterns of the active layers based on PM6:GS-ISO: (a) without F8T2 (w/o) and (b) with 0.20 wt% of F8T2 (F8T2-0.20%wt). (c) Corresponding in-plane (IP) and out-of-plane (OOP) line cuts (1D profiles which are vertically offset for clarity).*

The influence of F8T2 on the BHJ morphology was further investigated by AFM. The corresponding topographical images are shown in **Figure 3-20**, and the extracted roughness and average grain size values are reported in **Table 3-10**. The previously optimized film (with 0.5 v% DIO) is used as the reference (w/o) and exhibits an average grain size of 55 ± 15 nm, with a morphology composed predominantly of fibrillar domains. Upon incorporation of 0.2 wt% F8T2, the morphology is significantly altered, with the emergence of large, rounded GS-ISO-rich domains embedded within the fibrillar network, resulting in a structure distinct from the reference film. Consequently, the average grain size increases to 85 ± 20 nm, accompanied by a broader size distribution.

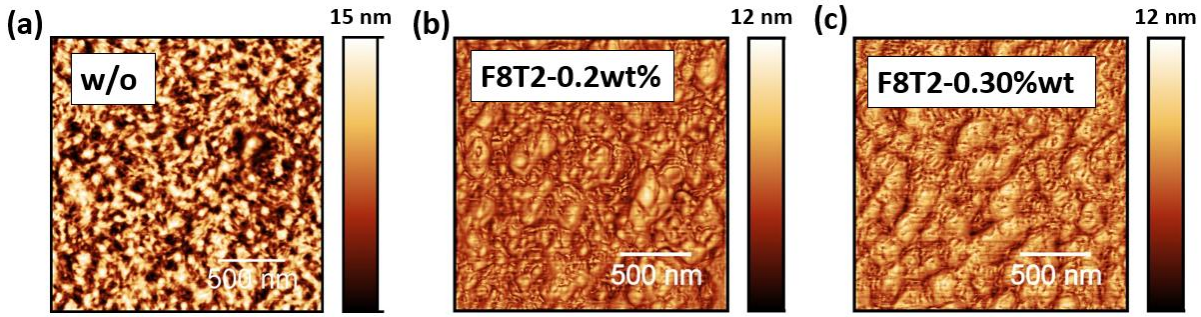

Figure 3-20: *AFM images for PM6:GS-ISO films: (a) without F8T2 (w/o). (b) With 0.20 wt% of F8T2 and (c) with 0.30 wt% of F8T2.*

Condition (wt%)	D_{avg} (nm)	σ_{rms} (nm)
w/o	55 ± 15	1.4
0.2	85 ± 20	3.9
0.3	70 ± 20	1.5

Table 3-10: *Influence of F8T2 on BHJ morphology (average grain size and surface roughness).*

This morphological evolution, together with the formation of larger domains, is consistent with an increase in acceptor crystallinity, in agreement with the red-shift observed in absorption spectra and the enhanced EQE response in the GS-ISO spectral region, as well as the GIWAXS results. Such morphological and structural modifications are consistent with the improved PV performance and enhanced EQE, particularly in the 400–500 nm and 600–700 nm wavelength ranges.

3.4.5 Charge Transport and Recombination

The influence of F8T2 on charge carrier transport was investigated by measuring μ_h and μ_e using hole-only and electron-only devices. Devices incorporating BHJ with varying F8T2 contents were fabricated and characterized. The transition from ohmic to space-charge-limited current behavior is identified by a transition from linear to quadratic dependence in the *J-V* characteristics, allowing the extraction of mobility values using the SCLC model.[123] The

corresponding results are presented in **Figure 3-21** and **Table 3-11**. For both charge carriers, the carrier mobilities remain largely unaffected by the incorporation of F8T2. In the pristine PM6:GS-ISO system, the hole mobility is approximately 3.7×10^{-4} cm² V⁻¹ s⁻¹, while it increases slightly to 4.6×10^{-4} cm² V⁻¹ s⁻¹ upon addition of 0.2 and 0.3 wt% F8T2. Similarly, the electron mobility remains nearly constant, with values of 1.4×10^{-4} and 1.8×10^{-4} cm² V⁻¹ s⁻¹, respectively. The μ_e/μ_h ratio is commonly used to assess the balance between electron and hole transport in the active layer. Upon the incorporation of 0.2 wt% F8T2, this ratio remains nearly unchanged, decreasing only slightly from 0.45 to 0.40. Although values below unity indicate moderately higher hole mobility than electron mobility, such ratios are commonly observed in high-performance OSC. The incorporation of F8T2 leads to improved device performance without significantly altering the charge carrier mobilities, indicating that the performance enhancement does not originate from changes in charge transport.[115]

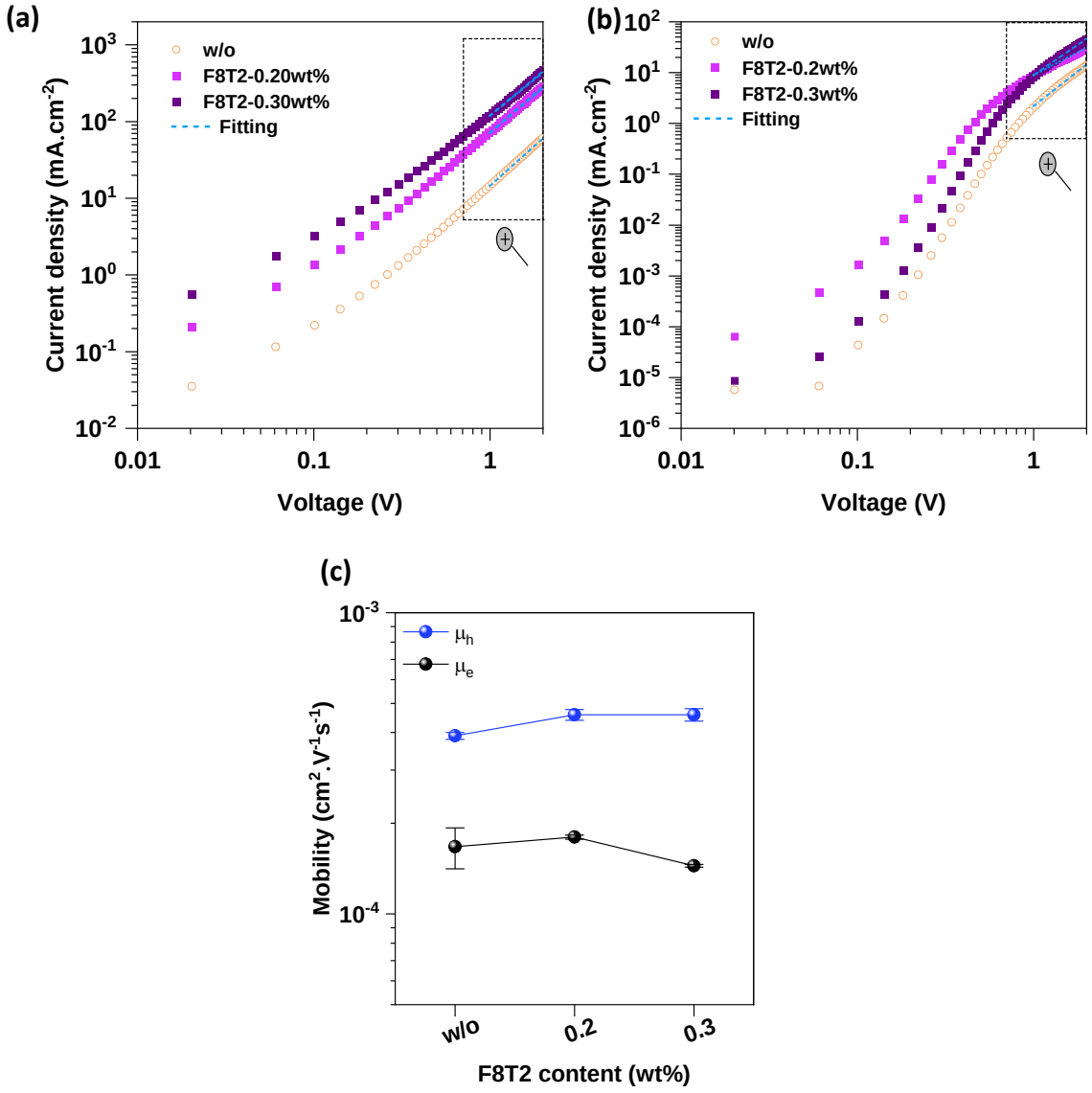

Figure 3-21: *J-V characteristics of (a) hole only devices, (b) electron only devices, and (c) extracted hole and electron mobilities (μ_h and μ_e respectively) as a function of F8T2 content (wt%) in the PM6:GS-ISO blend.*

Condition (wt%)	μ_h (×10^{-4} cm^2/(Vs))	μ_e (×10^{-4} cm^2/(Vs))	μ_e /μ_h ratio
w/o	3.74 ± 0.08	1.70 ± 0.10	0.453
0.2	4.59 ± 0.19	1.80 ± 0.03	0.392
0.3	4.58 ± 0.22	1.44 ± 0.02	0.315

Table 3-11: *Hole and electron mobilities (μ_h and μ_e respectively) and μ_e/μ_h ratio as a function of F8T2 content (wt%) in the PM6:GS-ISO blend.*

To further elucidate the role of F8T2, the recombination mechanisms were investigated through light intensity-dependent measurements of J_{SC} and V_{OC}.[124] Due to the relatively high R_{SH} of the devices (~1 MΩ·cm²), measurements were performed over a light intensity range from 0.01 to 20 mW·cm⁻². The corresponding *J-V* curves are shown in **Figure 3-22**.

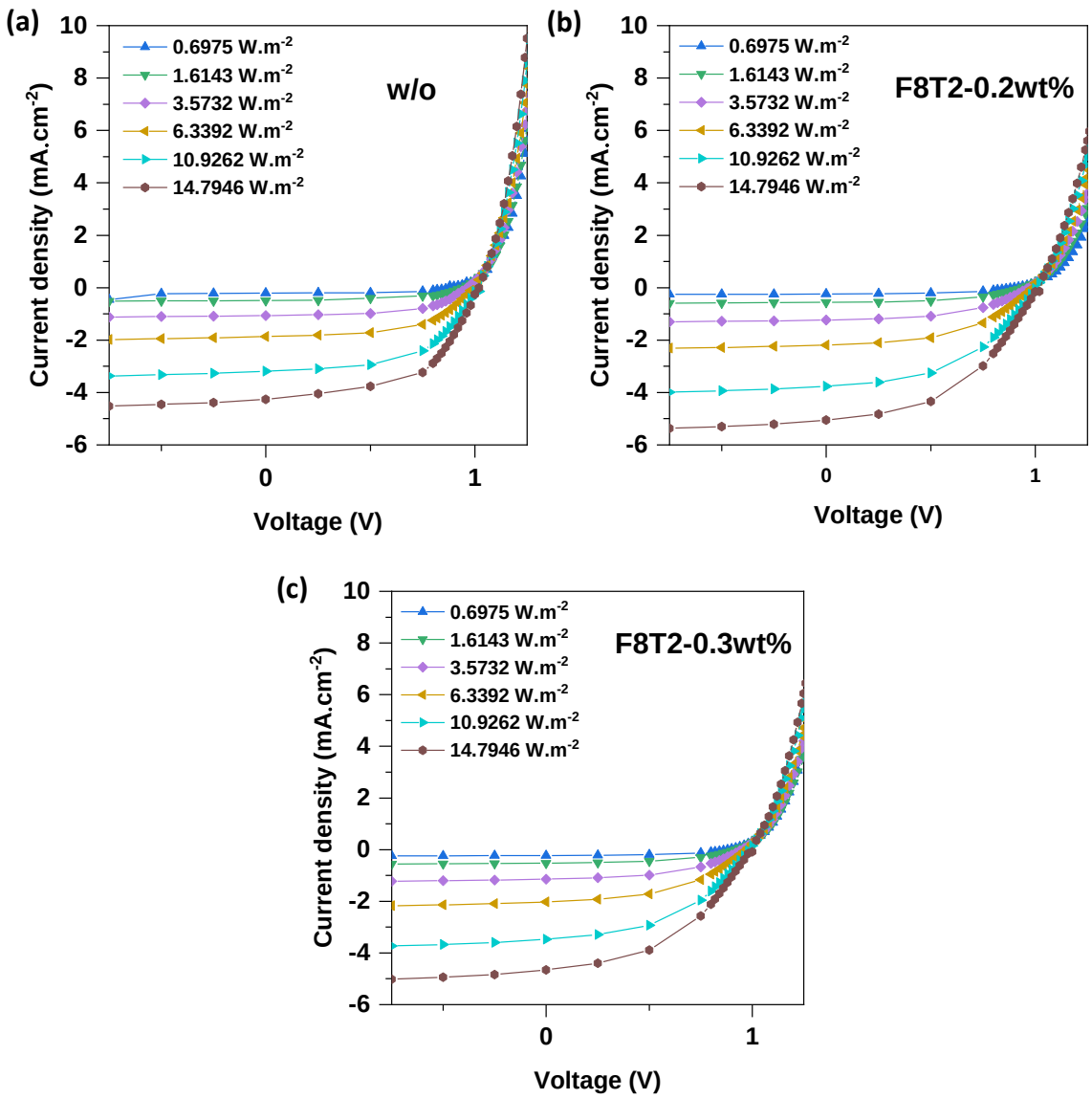

Figure 3-22: *J-V curves of the devices under various light intensities for different F8T2 contents.*

As shown in **Equation 3-1**, dependence of J_{SC} on light intensity (I_{light}) follows a power-law relationship allowing the extraction of the exponent α.[125]

$$J_{SC}\ \alpha\ I_{light}^{\alpha} \qquad \textbf{(3-1)}$$

A value of α close to unity indicates negligible bimolecular recombination losses.[89,126] As shown in **Figure 3-23a**, a linear relationship between log(J_{SC}) and log(I_{light}) is observed for all devices.[126] The extracted α values are 0.98 (w/o), 1.00 (F8T2-0.2wt%), and 0.99 (F8T2-0.3wt%), indicating that bimolecular recombination losses are negligible under all conditions.

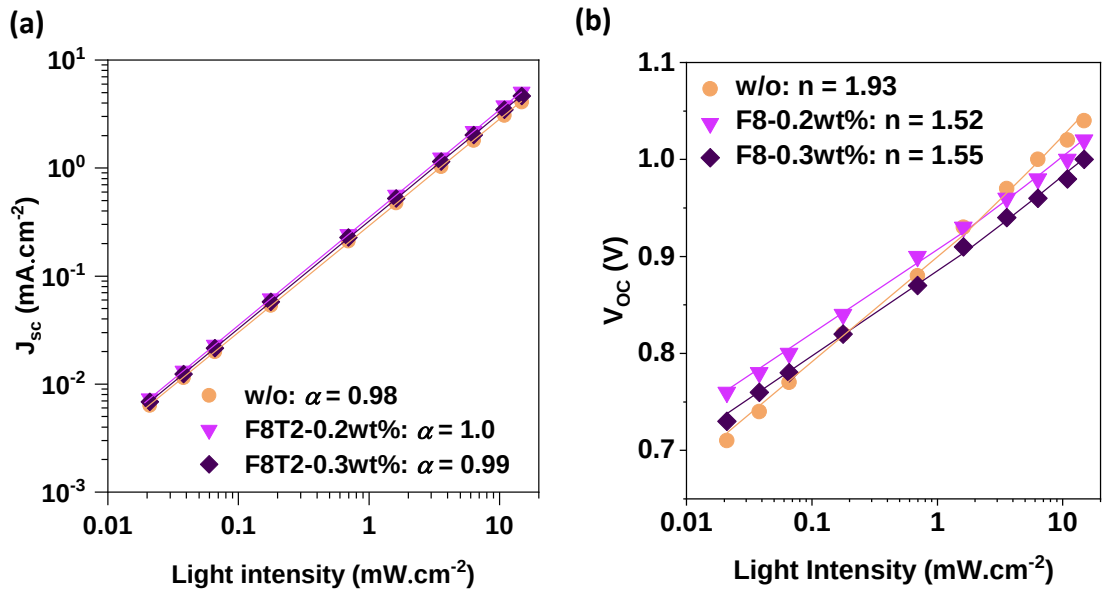

Figure 3-23: *Influence of F8T2 on (a) J_{SC} and (b) V_{OC} light intensity dependence.*

The contribution of trap-assisted recombination was further analyzed by studying the dependence of V_{OC} on light intensity, based on the Shockley equation (**Equation 3-2**).

$$V_{OC}\ \alpha\ \frac{nkT}{q}\ln(\frac{I}{I_0}) \qquad \textbf{(3-2)}$$

In this framework, the ideality factor (n) provides insight into the dominant recombination mechanism, with $n \approx 1$ indicating negligible trap-assisted recombination and $n \approx 2$ corresponding to a trap-dominated process. As shown in **Figure 3-23b**, the ideality factor for the reference device is found to be 1.93, indicating that trap-assisted recombination is dominant, which is consistent with the relatively low FF observed. In contrast, devices incorporating F8T2 exhibit significantly lower ideality factors of 1.52 and 1.55 for 0.2 wt% and 0.3 wt%, respectively. This reduction indicates a decrease in trap-assisted recombination upon incorporation of F8T2.

To account for leakage currents associated with finite R_{SH}, an extended model was used (**Equation 3-3**).[90]

$$V_{OC} = \frac{E_{gap}}{q} - \frac{nkT}{q}\ln(\frac{(1-P)\gamma N_C{}^2}{PG - V_{OC}/qLR_{SH}}) \qquad \textbf{(3-3)}$$

where P is the dissociation probability, of a bound electron-hole pair, γ is the bimolecular recombination rate coefficient, L represents the active layer thickness, R_{SH} denotes the shunt resistance and N_C the effective density of states (fixed at 2.5 x 10^{19} cm^3 by *Blom et al.*).[127] The photogeneration rate G is the only parameter assumed to be directly proportional to light intensity (**Equation 3-4**).

$$G = \frac{I_{abs}}{h\upsilon L} \qquad \textbf{(3-4)}$$

Consequently, V_{OC} follows a logarithmic dependence on irradiance

By plotting V_{OC} as a function of the corrected photogeneration term ($PG - V_{OC}/qLR_{SH}$), a more accurate determination of recombination mechanisms is obtained (**Figure 3-24a**). The extracted ideality factor for the reference device is 1.87, while lower values of 1.38 and 1.40 are obtained for 0.2 wt% and 0.3 wt% F8T2, respectively. These results confirm the same trend with improved accuracy, highlighting a significant reduction in trap-assisted recombination upon F8T2 incorporation.[128]

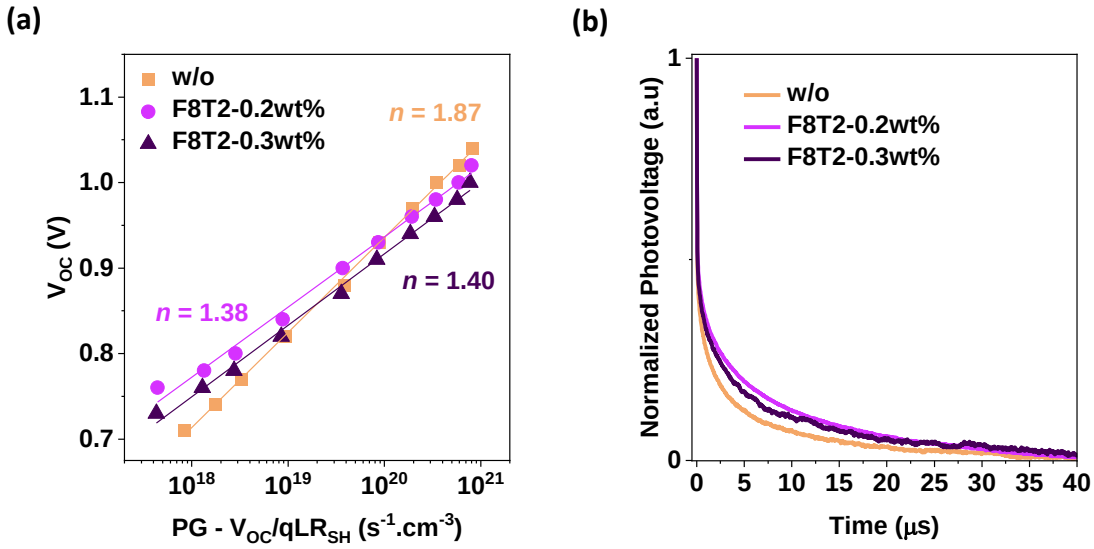

Figure 3-24: *(a) V_{OC} as a function of PG - V_{OC}/qLR_{SH} and (b) Transient photovoltage spectra.*

To further investigate recombination dynamics, TPV measurements were performed (**Figure 3-24b**).[129] The decay curves were fitted using a bi-exponential model to extract fast (τ_1) and slow (τ_2) recombination time constants. The fast component ($\tau_1 \approx 0.1$ µs) remains similar for all devices, indicating a comparable initial recombination process. In contrast, the slow component (τ_2) shows a significant increase from 5.9 µs (w/o) to 9.4 µs and 7.2 µs for the 0.2 wt% and 0.3 wt% F8T2 devices, respectively (**Table 3-12**). The increase in τ_2 indicates a slower recombination process, which is associated with a lower trap density in the active layer.

Condition (wt%)	τ_1 (µs)	τ_2 (µs)
w/o	0.11	5.9
0.2	0.16	9.4
0.3	0.10	7.2

Table 3-12: *Influence of F8T2 on decay times (τ_1 and τ_2).*

These results, combined with GIWAXS and AFM analyses, demonstrate that F8T2 incorporation reduces trap-assisted recombination by modifying the BHJ morphology.[130] This reduction contributes to the improvement of PV parameters, particularly V_{OC} and FF.

Key Point 3.4: Solid additive engineering: F8T2.

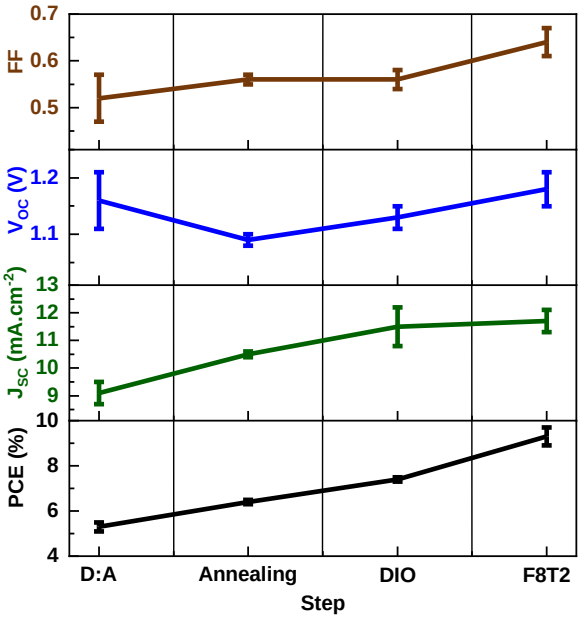

Adding 0.2 wt% F8T2 in the organic solution enabled the improvement of the crystallinity and the tuning of optical properties. This introduction permits the reduction of trap density in the film and consequently trap-assisted recombination.

3.5. Indoor OPV: Development and application of the optimized top organic solar cell

3.5.1 Context, applications, and state-of-the-art

As previously discussed in this manuscript, OSC have achieved remarkable progress in efficiency, with PCE now exceeding 20 % under AM1.5G conditions.[57] Nevertheless, OSC continue to encounter significant challenges in outdoor applications due to their sensitivity to moisture, oxygen and elevated temperatures. Moreover, the large-scale manufacturing of large-area solar modules has not yet reached full technological maturity.[131] Consequently, it is imperative to identify competitive applications that fully exploit the intrinsic advantages of OSC. The rapid advancement of the Internet of Things (IoT) has led to a significant increase in the number of connected devices, wireless sensor networks, and low-power electronic systems.[132] These off-grid devices require reliable energy sources to ensure the long-term operation of IoT systems. This development has consequently heightened interest in alternative energy harvesting technologies capable of operating efficiently under indoor lighting conditions.[133] In this context, OPV have emerged as a promising solution for powering autonomous systems. OSC with PCE up to 30 % under indoor illumination have been reported.[134] Recent reviews have demonstrated that this technology is capable of efficiently harvesting energy from indoor environments and delivering power levels ranging from the microwatt to the milliwatt scale, which is well suited for low-power electronic devices. (**Figure 3-25**).[133]

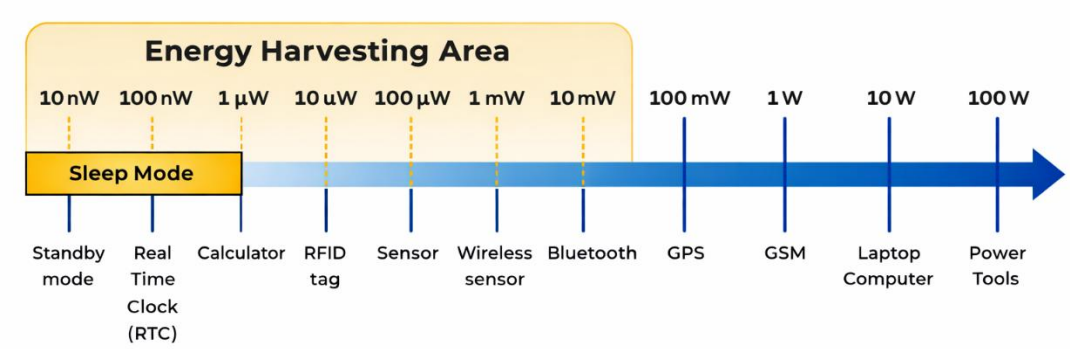

Figure 3-25: *Power levels for portable electronic devices and energy harvesting capabilities of PV cells for indoor applications.*[135]

3.5.2 Spectral characteristics of indoor light sources

Understanding the fundamental characteristics of indoor and low-irradiance light sources is essential for the rational design of high-performance indoor OPV (IOPV) devices. Indoor lighting conditions differ from standard solar illumination both in the available power density and the spectral distribution of the incident light.[136] Common artificial light sources used indoors, such as light-emitting diodes (LED) or fluorescent lamps (FL), have emission spectra that are considerably narrower than the solar spectrum and are primarily confined between 400 and 700 nm (**Figure 3-26**).[137] Among all the artificial light sources used for indoor

applications, LED are anticipated to become the predominant technology for indoor lighting in the near future.

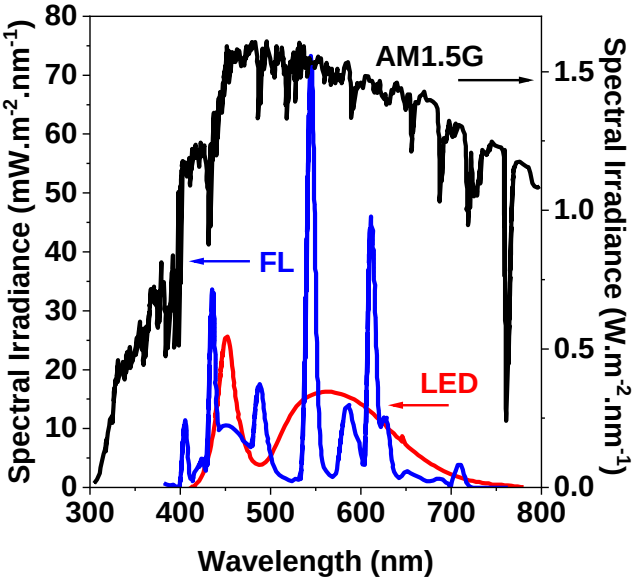

***Figure 3-26**: Spectral irradiance difference between AM1.5G solar spectrum (black), fluorescent lamp (blue), and LED (red).*[138]

In addition to spectral differences, indoor illumination is characterized by a significantly lower irradiance level. While standard solar testing is conducted at 100 mW·cm^{-2} under AM1.5G conditions, the incident power density in indoor environments is generally below 1 mW·cm^{-2}.[137] Depending on their applications, white LEDs with different correlated color temperatures (CCT) can be used. Generally, for IOPV, CCT values between 2700 and 5000 K are used. The difference in CCT results in variations in spectral distribution and relative intensity of blue and red components.[139] A 2700 K LED, referred to as “warm white", exhibits a yellowish tone. Its emission spectrum is rich in red components and relatively poor in blue (**Figure 3-27**). A 3500 K LED, referred to as “neutral white,” is closer to the color white. Its spectrum is more balanced between white and red (**Figure 3-27**). This is the most commonly used LED color in everyday life because it is the perfect compromise between comfort and efficiency. Finally, the 5000 K LED, referred to as “cool white,” leans more toward a bluish tone. It is close to natural daylight. Its spectrum has a strong blue component (**Figure 3-27**).

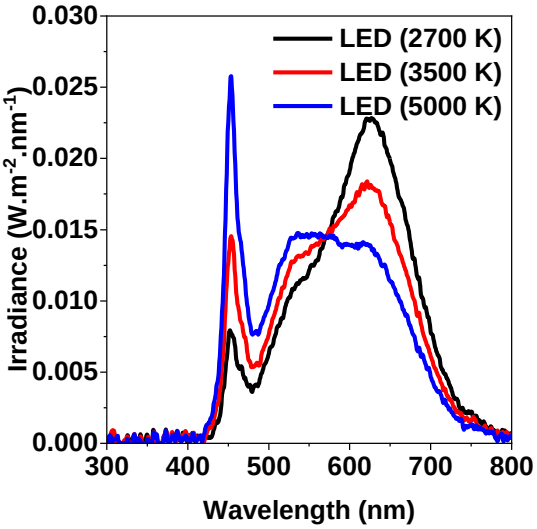

Figure 3-27: *LED irradiance spectra for different CCT.*

Another important parameter is the illuminance level, expressed in lux (lx). Typical indoor conditions range from 200 to 1000 lx, which is approximately three orders of magnitude lower than sunlight (**Figure 3-28**).[137] The range between 0 and 200 lx is called "basic illumination". This range is used for corridors or night lighting. The range between 200 and 450 lux is called “basic visual tasks.” This is an area where lighting is basic, typical of shops or simple work areas. The next range, between 450 and 750 lux, is related to reading activities. It is typical of libraries or areas where people work for long periods of time. Finally, the “high contrast purposes” range between 750 and 1000 lux is typical of workshops or laboratories.

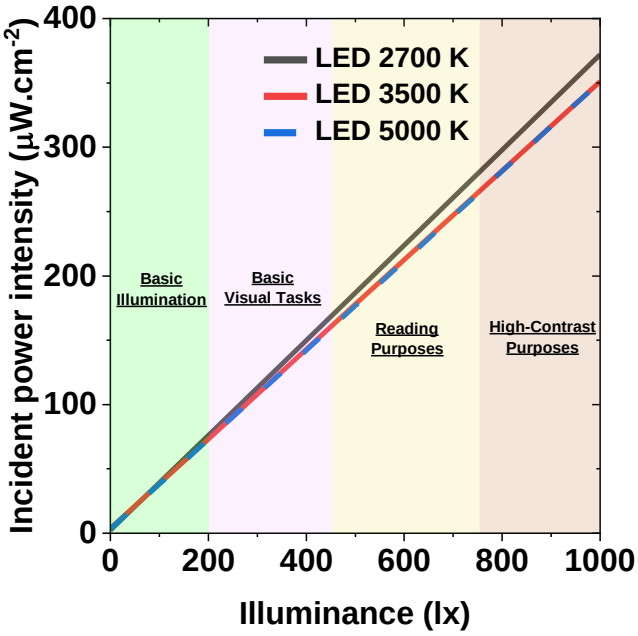

Figure 3-28: *Incident power intensity vs illuminance for three LED and indoor applications depending on the illuminance region.*[137]

These differences in both spectral content and intensity require specific optimization strategies for indoor PV devices, and a given solar cell can exhibit significantly different performances under indoor and outdoor illumination.[140]

3.5.3 Relevance of wide-bandgap organic semiconductors for IOPV

Unlike conventional outdoor illumination, the reduced photon flux of indoor light sources results in much lower carrier densities in the active layer. Consequently, the J_{SC} is significantly reduced. According to the diode model, V_{OC} is approximately proportional to the logarithm of the photocurrent, as described by **Equation 3-5**.[141]

$$V_{OC} = \frac{Eg}{q} + \frac{nkT}{q}\ln(\frac{I}{I_0}) \quad \textbf{(3-5)}$$

where *n* is the ideality factor, *k* the Boltzmann constant, *T* the temperature, *q* the elementary charge, I_0 the dark current, and *I* the photocurrent.

This equation indicates that a reduction in light intensity also leads to a decrease in V_{OC}. As a result, solar cells with higher V_{OC} values exhibit a smaller relative drop in efficiency under reduced illumination conditions.[141] High V_{OC} values can be achieved by minimizing the dark current, which generally benefits WBG semiconductors and device architectures with high R_{SH}. Consequently, reducing leakage pathways and non-radiative recombination is crucial for optimizing the efficiency of IOPV devices.[135] Simultaneously, the lower charge carrier density tends to reduce bimolecular recombination losses, which can lead to an improved FF and, in some cases, an enhanced PCE under low-light conditions.[135] Beyond intensity-related effects, the limited spectral range of indoor light sources significantly impacts material selection. Unlike sunlight, which spans from UV to IR, artificial indoor lighting is confined to a narrower visible range. Detailed balance calculations based on the Shockley-Queisser framework suggest that the optimal bandgap for indoor energy harvesting is shifted toward higher values. [142] In this context, *Ming Ju Wu et al*. demonstrated that bandgaps in the range of 1.8 to 1.9 eV are most suitable for indoor applications, whereas the optimal value for standard solar illumination is around 1.4 eV (**Figure 3-29**).[142] These studies reveal a non-intuitive regime in which the dependence of PCE on the bandgap under indoor illumination differs significantly from that observed under standard solar irradiation.

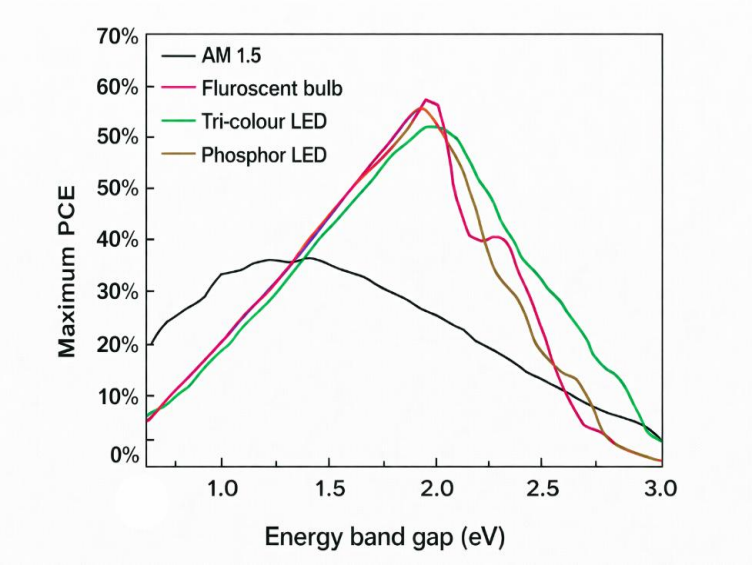

Figure 3-29: *Theoretical SQ limit depending on the semiconductor E_g for different illumination sources.*[142]

This behavior suggests that, under ideal conditions, an optimized OSC operating under indoor illumination could theoretically reach a maximum PCE of up to 58 %, compared to approximately 33 % under AM1.5G, highlighting the strong potential of OSC for indoor applications.[142] The bandgap of 1.85 eV of the active material used in this work falls close to the theoretically predicted optimal range for indoor illumination, providing a strong physical basis for high efficiencies.[141]

3.5.4 IOPV performance of the optimized top cell under controlled illumination

Because of their high bandgap, V_{OC} and optimized PV performance, PM6:GS-ISO cells with and without F8T2 are good candidates for indoor light harvesting. Indeed, the EQE of both blends (w/o and F8T2-0.2wt%) is presented together with the irradiance spectra of three LED (2700, 3500, and 5000 K) in **Figure 3-30**.

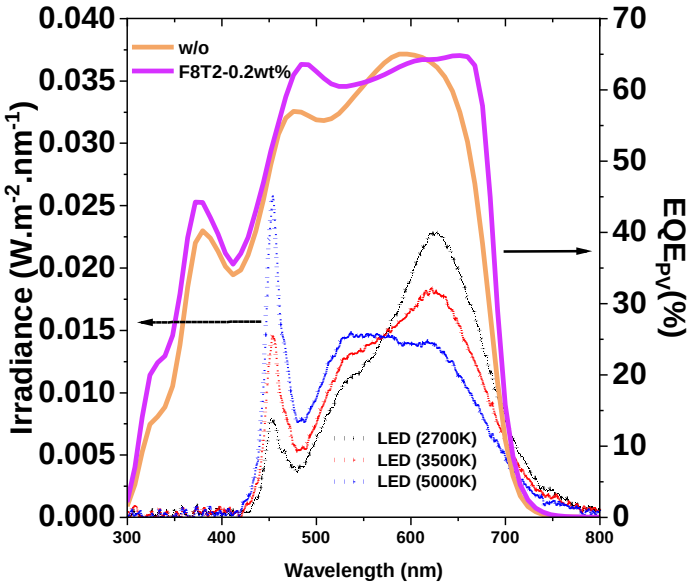

Figure 3-30: *LED spectra used for the indoor light characterization and EQE_{PV} for w/o and F8T2-0.2wt% devices.*

All the samples in this study were measured with three different CCT of LED (2700, 3500 and 5000 K) and at different illuminance levels (200, 500 and 1000 lx). The associated *J-V* characteristics are shown in **Figure 3-31**, and the extracted parameters are listed in **Table 3-13.**

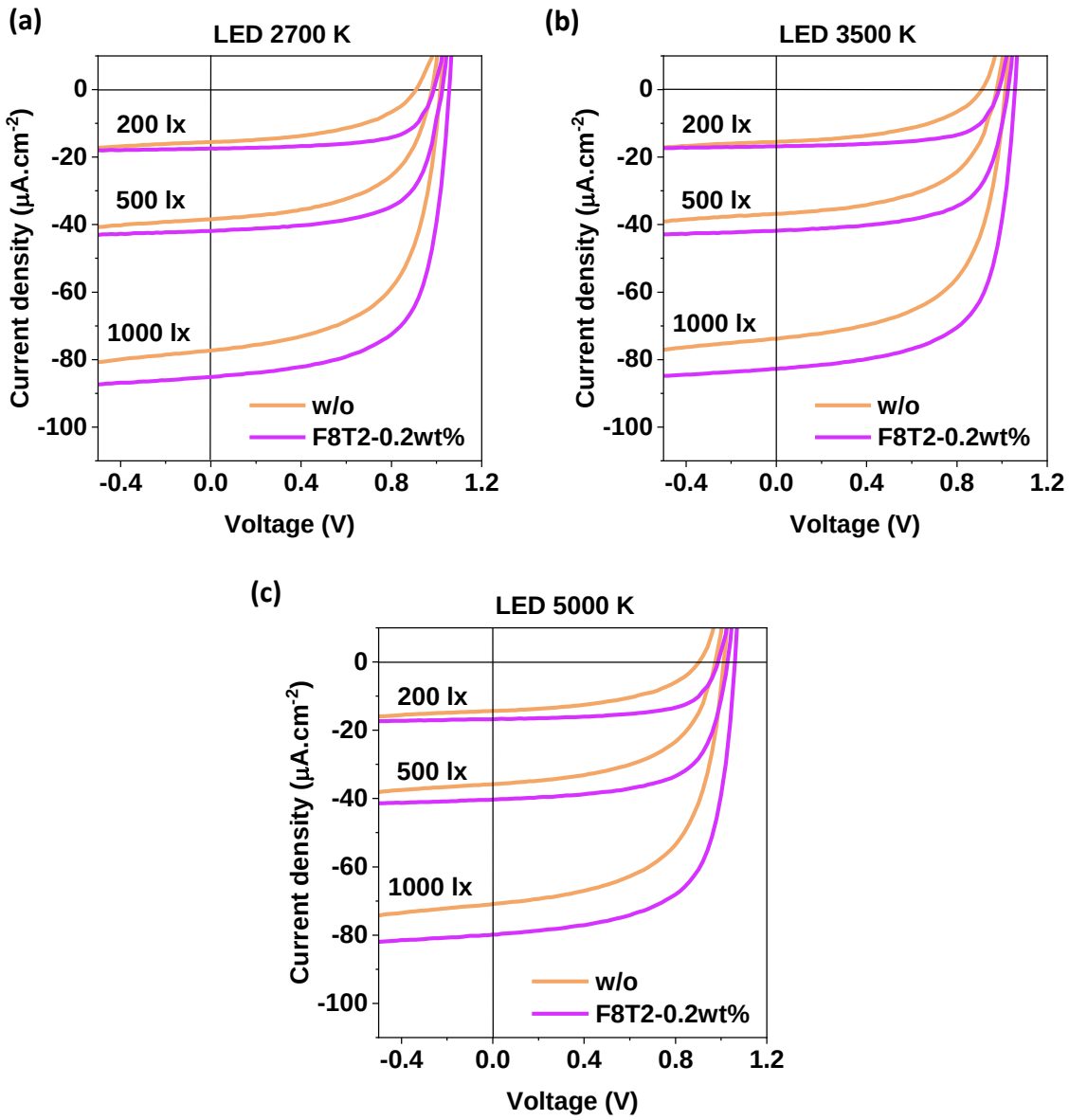

Figure 3-31: *J-V curves for w/o and F8T2-0.2wt% at 200, 500 and 1000 lx for LED (a) 2700 K, (b) 3500 K and (c) 5000 K.*

Condition (wt%)	T_{LED} (K)	Illuminance (lx)	J_{SC} (μA.cm^{-2})	V_{OC} (V)	FF	PCE (%)	P_{Max} (μW.cm^{-2})
w/o	2700	200	16	0.91	0.49	8.7	7
0.2			**17**	**0.99**	**0.66**	**14.3**	**11**
w/o		500	38	0.97	0.56	11.2	21
0.2			**42**	**1.03**	**0.65**	**14.8**	**28**
w/o		1000	77	1.01	0.60	12.7	47
0.2			**85**	**1.05**	**0.66**	**15.9**	**59**
w/o	3500	200	15	0.91	0.49	8.8	7
0.2			**17**	**0.99**	**0.64**	**13.8**	**11**
w/o		500	37	0.97	0.56	11.3	11
0.2			**42**	**1.03**	**0.64**	**15.6**	**20**
w/o		1000	74	1.01	0.60	12.6	44
0.2			**83**	**1.05**	**0.66**	**16.2**	**57**
w/o	5000	200	14	0.91	0.48	8.3	6
0.2			**17**	**0.99**	**0.65**	**14.1**	**6**
w/o		500	36	0.97	0.56	10.3	18
0.2			**40**	**1.03**	**0.65**	**15.0**	**27**
w/o		1000	71	1.01	0.60	12.2	43
0.2			**80**	**1.07**	**0.65**	**15.8**	**55**

Table 3-13: *IOPV characteristics (J_{SC}, V_{OC}, FF, PCE and P_{Max}) with different LED (2700, 3500 and 5000 K) and different illuminances (200, 500 and 1000 lx) for w/o and F8T2-0.2wt%.*

It is worth noting that the observed trends under indoor illumination are consistent with those typically reported for conventional photovoltaic operation, indicating that the

introduction of F8T2 improves device performance in a robust and illumination-independent manner. In particular, the FF shows a consistent improvement upon the incorporation of F8T2, indicating reduced trap-assisted recombination. The V_{OC} is also systematically high in the presence of F8T2, frequently exceeding 1.0 V under indoor illumination. This high V_{OC} is particularly beneficial for IOPV applications, where the available light intensity is significantly lower than under standard AM1.5G illumination and a high output voltage is therefore essential to maintain efficient power generation.

The best performance was obtained under indoor lighting conditions using a 3500 K LED at an illuminance of 1000 lx (340 $\mu W.cm^{-2}$). Under these conditions, F8T2-0.2wt% device exhibited a PCE of 16.2 %, with a J_{SC} of 83 $\mu A.cm^{-2}$, a V_{OC} of 1.05 V and a FF of 0.66. Moreover, the device demonstrated remarkable performance stability, with efficiencies in the range of 14-16% independently of the light source (2700, 3500 and 5000 K) and illuminance (200, 500 and 1000 lx). For comparison, the same device under AM1.5G illumination exhibits a PCE of 9.3 %, with a J_{SC} of 12.3 $mA.cm^{-2}$, a V_{OC} of 1.18 V and a FF of 0.64.

The improvement in FF upon F8T2 incorporation and the consistently high V_{OC} observed for the PM6:GS-ISO devices are particularly relevant for indoor operation, where these parameters contribute significantly to the high PCE achieved at low light intensities. Moreover, the limited dependence of the device performance on both the illumination spectrum and intensity highlights the robustness of the PM6:GS-ISO blend under indoor conditions.

Overall, these results, obtained without any device optimization for indoor operation, demonstrate the strong potential of this material system for IOPV application.

3.6. Conclusion of Chapter 3

In this chapter, the optimization of a WBG OSC intended for integration as the top subcell in an OPV/Si tandem architecture has been systematically investigated.

First, the selection of the PM6:GS-ISO system was shown to be particularly relevant for tandem applications, owing to its suitable bandgap (~ 1.8 eV) and its ability to deliver a high V_{OC}. Combined with an inverted device architecture (ITO/ZnO/PAL/MoO_3/Ag), this system ensures efficient and selective charge extraction while maintaining compatibility with the 3T tandem configuration. This architectural choice also could benefit from enhanced stability and favorable vertical phase segregation, contributing to improved charge transport. The optimization of the active layer processing parameters highlighted the critical role of morphology in determining device performance. The study of solution concentration and film thickness revealed the existence of an optimal thickness range around 120-130 nm, corresponding to the best compromise between light absorption and charge transport. Similarly, the adjustment of the donor-to-acceptor ratio confirmed that device performance is strongly governed by the nanoscale organization of the BHJ, which controls exciton dissociation and charge percolation pathways. Thermal annealing was identified as a key parameter for improving device efficiency, leading to a maximum PCE of 6.4 % at 160 °C. This improvement is attributed to enhanced molecular organization within the blend, as supported

by optical and morphological analyses. However, excessive annealing results in performance degradation, highlighting the sensitivity of the system to morphological changes and phase separation.

Further optimization was achieved through solvent additive engineering. The incorporation of an optimal amount of DIO (0.5 v%) enabled a significant enhancement in device performance, with a PCE reaching 7.4 %. This improvement is associated with a more favorable nanoscale morphology, promoting efficient charge transport and reduced recombination losses.

Finally, the introduction of a non-volatile solid additive, through the addition of the conjugated polymer F8T2, proved to be an effective strategy to overcome the intrinsic limitations of binary systems. An optimal F8T2 content of 0.2 wt% led to a substantial increase in performance, with PCE values up to 9.3 % (and up to 10 % for the best devices). Structural and morphological analyses revealed that this improvement originates from enhanced molecular ordering, stronger π–π stacking, and a reduction of the amorphous fraction, resulting in reduced trap-assisted recombination.

Overall, this chapter demonstrates that the performance of WBG OSC can be significantly enhanced through a combined optimization of material selection, processing conditions, and multicomponent strategies. It highlights the strong interdependence between processing, morphology, and optoelectronic properties, emphasizing the necessity of a holistic approach to device optimization. These results provide a solid foundation for the development of optimized OSC into semi-transparent devices, through the optimization of transparent electrodes, which will be addressed in the following chapter.

Chapter 4
Development, Optimization and Integration of Transparent Top Electrodes for Semi-Transparent Organic Solar Cells

4.1. Introduction

Following the optimization of the WBG OSC presented in **Chapter III**, the next step toward its integration into an OPV/Si tandem architecture consists in developing semi-transparent organic solar cells (ST-OSC). Indeed, in a tandem configuration, the top cell must not only exhibit high PV performance but also transmit a sufficient fraction of the solar spectrum to the underlying Si subcell. This dual requirement introduces additional design constraints compared with conventional OSC with reflective electrode, making the realization of highly efficient ST-OSC particularly challenging.

ST-OSC have attracted considerable attention in recent years, for both tandem PV applications and building-integrated photovoltaics (BIPV).[143] Their development relies on the replacement of the reflective metallic top electrode by a transparent conductive electrode, enabling light transmission through the device. However, replacing the metallic electrode generally introduces a trade-off between optical transparency and electrical performance, resulting in reduced efficiencies compared to their opaque counterparts.[144]

One of the main technological bottlenecks lies in the fabrication of a transparent top electrode that simultaneously combines high *AVT* and $AT_{300–1000nm}$, low R_{sheet}, and compatibility with the underlying organic layers. Accordingly, the objective of this chapter is to develop transparent top electrodes for ST-OSC, optimize their optoelectronic performances, and evaluate their integration into complete PV devices.

To compare the different transparent electrode technologies investigated in this work, three key optoelectronic parameters were selected. The electrical performance of the transparent electrodes can be evaluated through their sheet resistance (R_{sheet}) which characterizes the lateral electrical conductivity of thin conductive films. The optical performance of transparent electrodes can be evaluated using two complementary transmittance metrics: the average visible transmittance (*AVT*) and the average transmittance over the 300-1000 nm spectral range ($AT_{300–1000nm}$).[145] Although both quantities quantify the optical transparency of the electrode, they provide complementary information depending on the targeted application. The corresponding measurement procedures are described in **Chapter 2**.

AVT represents the transparency perceived by the human eye and is therefore widely adopted to evaluate transparent electrodes. It is calculated by weighting the measured transmittance spectrum with both the AM1.5G solar spectrum and the photopic response of the human eye according to **Equation 4-1.**[145]

$$AVT = \frac{\int_{380}^{780} T(\lambda)\times V(\lambda)\times AM1.5G(\lambda)d(\lambda)}{\int_{380}^{780} V(\lambda)\times AM1.5G(\lambda)d(\lambda)} \quad \textbf{(4-1)}$$

where $T(\lambda)$ and $V(\lambda)$ denote, respectively, the film transmittance and the photopic luminous efficiency function as a function of the wavelength λ. AM1.5G(λ) corresponds to the light flux associated with the AM1.5G solar spectrum irradiance.

Conversely, the $AT_{300–1000nm}$ provides a broadband evaluation of the optical transparency over the spectral range relevant for PV applications (**Equation 4-2**). Unlike AVT, this quantity is not spectrally weighted and corresponds to the wavelength-averaged transmittance over the 300-1000 nm range. The transmittance spectrum is therefore integrated over this wavelength range and normalized by the corresponding spectral interval. In practice, the integral is numerically evaluated from the experimental transmittance spectra recorded at regular 2 nm intervals.

$$AT_{300-1000nm} = \frac{1}{1000-300}\int_{300}^{1000} T(\lambda)d\lambda \quad \textbf{(4-2)}$$

Several transparent electrode technologies are investigated, including thermally evaporated oxide/metal/oxide (OMO) stacks[146], screen-printed[83] and spin-coated silver nanowires (Ag-NWs)[147], as well as sputtered ITO electrodes.[148] Particular attention is paid to understanding the relationship between electrode fabrication processes, optical and electrical properties, and their impact on device performance.

Finally, the optimized transparent electrodes are integrated into ST-OSC employing different active layers including the previously developed PM6:GS-ISO blend as well as more recent blends (PTQ10:FCC-Cl and PTB7-Th:IEICO-4F). The performance, optical properties, and stability of the resulting devices are systematically analyzed. This work aims to establish a robust framework for the development of efficient ST-OSC, as a key step toward their integration in OPV/Si tandem architectures.

4.2. Comparative development of transparent top electrodes

4.2.1 Thermally evaporated oxide-metal-oxide electrodes

a) State-of-the-art and motivation

Among the transparent electrode technologies investigated for ST-OSC, OMO multilayers have attracted considerable interest because they offer an attractive compromise between fabrication simplicity, R_{sheet}, *AVT*, and $AT_{300–1000nm}$.[146] Rather than relying on a single transparent conductive material, OMO electrodes combine an ultrathin metallic layer, responsible for electrical transport, with two surrounding dielectric oxide layers that fulfil optical, electrical and protective functions. This architecture partially decouples the electrical and optical functions of the electrode. The ultrathin metallic layer provides lateral charge transport, whereas the surrounding dielectric layers reduce optical losses through interference effects while protecting the metal against environmental degradation.[149] A major advantage of the OMO concept lies in its versatility. Numerous OMO architectures have been investigated, including ITO-, ZnO-, TiO_2-, NiO- and dielectric-based architectures.[150] Among these architectures, MoO_3-based electrodes are particularly attractive for OPV applications.[151] Despite the diversity of materials, all these multilayers rely on the same design philosophy: an

ultrathin metallic interlayer, typically between 7 and 15 nm thick, provides lateral electrical conduction, whereas oxide layers with thicknesses generally ranging from 20 to 40 nm are optimized to maximize optical transmission through interference effects while preserving smooth surfaces and adequate mechanical stability.[150]

Among these different OMO architectures, MoO_3/Ag/MoO_3 has become one of the most extensively investigated for OPV applications (**Figure 4-1**). Unlike many dielectric materials whose deposition requires sputtering or electron-beam evaporation, MoO_3 can be readily deposited by thermal evaporation because of its relatively low sublimation temperature.[152] This enables the complete electrode to be fabricated by thermal evaporation, making it fully compatible with standard OPV processing. Furthermore, MoO_3 is already widely employed as a high-work-function HTL in inverted OSC.[153]



Figure 4-1: *Schematic representation of an MoO_3/Ag/MoO_3 transparent electrode.*

Therefore, the bottom MoO_3 layer of the OMO electrode can simultaneously serve as the HTL and as the lower dielectric layer of the multilayer electrode. This dual functionality considerably simplifies the device architecture. The applicability of MoO_3/Ag/MoO_3 electrodes to ST-OSC was demonstrated by *Lim et al.*, who employed thermally evaporated OMO electrodes as transparent top contacts in PTB7:PCBM solar cells.[154] Devices exhibiting approximately 50 % maximum visible transparency (T_{max}) reached a PCE of 4.5 %, whereas increasing the Ag thickness improved the PV performance up to 9.1 %, at the expense of reducing the T_{max} to approximately 5 %.[154] Their study also reported that optimized OMO electrodes can exhibit R_{sheet} below 10 $\Omega.sq^{-1}$ while maintaining T_{max} approaching 85 %, highlighting the remarkable optoelectronic potential of these multilayer structures.[155] Based on this literature review, the MoO_3/Ag/MoO_3 architecture was selected as the first transparent electrode investigated in this work. Since the lower MoO_3 layer already served as the HTL of the reference inverted architecture, only the Ag interlayer and the upper optical capping layer required optimization.

The objective was therefore to identify the minimum Ag thickness ensuring electrical continuity before optimizing the MoO_3 capping layer to maximize optical transmission.

b) Physical principles

Unlike conventional TCO, whose electrical conductivity originates from highly doped semiconductor layers, the conductivity of OMO electrodes is almost exclusively governed by the ultrathin metallic interlayer.[154] Since charge transport is almost entirely governed by the metallic layer, the electrical behavior of OMO electrodes primarily depends on the morphology and continuity of the ultrathin Ag film. Ag is particularly attractive as the metallic interlayer because it possesses a very low electrical resistivity, allowing efficient lateral charge

transport to be achieved with only a few nanometres of material.[156] However, obtaining a highly conductive ultrathin Ag film is not straightforward. During thermal evaporation, Ag atoms interact only weakly with the oxide surface and therefore follow a Volmer-Weber growth mode, also referred to as island growth (**Figure 4-2**).[157] In this growth regime, the cohesion between Ag atoms is stronger than their adhesion to the substrate surface. Consequently, the system minimizes its total surface energy by forming isolated three-dimensional metallic islands rather than a continuous wetting layer.

This behavior is generally observed when the surface energy of the metallic film (γ_F) is high compared with the surface energy of the substrate (γ_S) and the film/substrate interfacial interactions are insufficient to promote complete wetting of the substrate. Under these conditions, island formation becomes energetically more favourable than the formation of a continuous two-dimensional layer. As deposition proceeds, isolated Ag islands nucleate, grow, and progressively coalesce. A continuous conductive pathway is established only once the percolation threshold is reached, when neighbouring metallic islands become sufficiently interconnected to allow efficient lateral electron transport. Below this threshold, electron transport mainly occurs through tunnelling between isolated islands, resulting in extremely high R_{sheet} values. The progressive transition from isolated islands to a continuous metallic network is therefore a key parameter governing the electrical properties of ultrathin Ag films deposited by thermal evaporation.

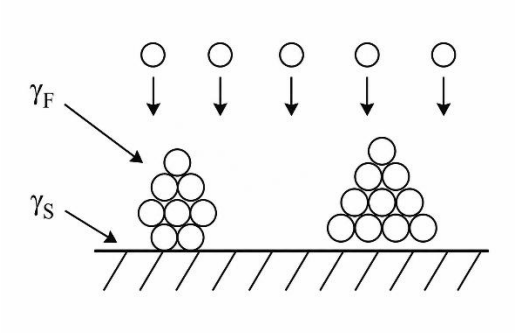

Figure 4-2: *Schematic illustration of the Volmer-Weber (island) growth mode of Ag on an oxide surface. γ_F and γ_S denote the surface energies of the metallic film and the substrate, respectively.*

Electrical conduction is only established once the percolation threshold is reached, when neighbouring islands become interconnected. Below this threshold, electron transport relies mainly on tunnelling between isolated islands, resulting in extremely high R_{sheet}.[158] Although increasing the Ag thickness improves electrical conductivity, it simultaneously degrades the optical properties of the multilayer. The free electrons responsible for the excellent conductivity of Ag also interact strongly with incident electromagnetic radiation, leading to increased reflection and parasitic absorption within the visible spectrum.[159] Consequently, thicker metallic layers inevitably reduce the amount of light transmitted through the electrode. This electrical-optical trade-off constitutes the fundamental design constraint of OMO electrodes and explains why the metallic interlayer is the primary parameter optimized in all reported studies.[154]

The dielectric MoO_3 layers surrounding the Ag film play a crucial role in partially compensating for these optical losses. Because the refractive index changes abruptly at each interface (air/MoO_3, MoO_3/Ag and Ag/MoO_3), incident light undergoes multiple reflections while propagating through the multilayer.[160] By selecting appropriate dielectric thicknesses, destructive interference of the reflected waves can be promoted over a large part of the visible spectrum, thereby reducing reflectance and enhancing optical transmission.[160] The upper MoO_3 layer therefore acts as an optical matching layer analogous to an antireflection coating, while the lower MoO_3 layer simultaneously contributes to optical transparency and serves as a HTL at the interface with the organic semiconductor.[154] Beyond their optical function, the MoO_3 layers also improve the structural stability of the metallic film. Encapsulation of the Ag layer between two oxide films also improves its environmental and mechanical stability by limiting oxidation and morphological degradation.[150] These physical mechanisms establish the framework for the experimental optimization presented in the following sections.

c) Optimization of the Ag interlayer

The first stage of the optimization therefore consisted in identifying the minimum Ag thickness capable of providing sufficiently low R_{sheet} while maintaining acceptable transparency. Since the objective at this stage was to isolate the effect of the Ag thickness, only the 7 nm bottom MoO_3 layer was included, while the upper MoO_3 layer was intentionally omitted. OMO films were deposited on soda-lime glass substrates for both electrical and optical characterizations. The optical transmittance spectra were recorded relative to an uncoated glass substrate used as the baseline reference, thereby isolating the optical response of the OMO electrode itself. The resulting R_{sheet}, *AVT* and $AT_{300\text{-}1000nm}$ are presented in **Figure 4-3** and summarized in **Table 4-1**.

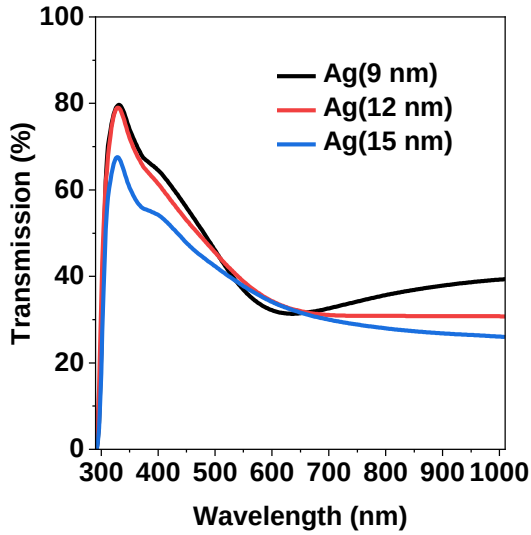

Figure 4-3: *Optical transmittance spectra of MoO_3(7 nm)/Ag(x nm) electrodes as a function of Ag thickness.*

Ag thickness (nm)	R_{sheet} **(Ω.sq^{-1})**	***AVT*** **(%)**	$AT_{300\text{-}1000nm}$ **(%)**	**Physical Interpretation**
9	> 10^6	37	43	Discontinuous Ag film
12	190	38	41	Partial percolation
15	22	37	38	Continuous conductive film

Table 4-1: *Effect of Ag interlayer thickness on the optoelectronic properties of thermally evaporated MoO_3(7 nm)/Ag(x nm) electrodes.*

For the 9 nm Ag film, the R_{sheet} could not be reliably measured because the discontinuous morphology resulted in an extremely high resistance exceeding the measurement range of the four-point probe setup. This behavior is consistent with the Volmer-Weber growth mechanism discussed previously, where isolated metallic islands are not yet sufficiently interconnected to provide efficient lateral charge transport. Increasing the Ag thickness to 12 nm resulted in a substantial reduction of the R_{sheet}, which reached approximately 190 Ω.sq^{-1}. The R_{sheet} remained too high for efficient charge collection, indicating that electrical percolation had not yet been fully achieved. A further increase of the Ag thickness to 15 nm dramatically reduced the R_{sheet} to approximately 22 Ω.sq^{-1}, indicating that electrical continuity had been achieved.The abrupt decrease in R_{sheet} between 12 and 15 nm strongly suggests that the percolation threshold is reached within this range.[158] Consequently, 15 nm was selected for the subsequent optimization.

d) Optimization of the MoO_3 upper layer

With the Ag thickness fixed at 15 nm, the upper MoO_3 capping layer was varied between 0 and 30 nm in order to optimize the optical response of the multilayer. The lower MoO_3 layer remained fixed at 7 nm. The resulting optoelectronic properties are presented in **Figure 4-4** and summarized in **Table 4-2**.

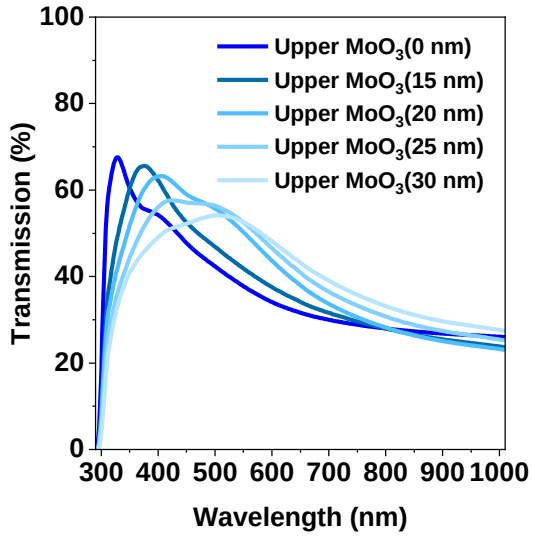

Figure 4-4: *Optical transmittance spectra of MoO_3(7 nm)/Ag(15 nm)/MoO_3(x nm) electrodes as a function of the upper MoO_3 thickness.*

Upper MoO_3 thickness (nm)	R_{sheet} ($\Omega.sq^{-1}$)	*AVT* (%)	$AT_{300\text{-}1000nm}$ (%)
0	22	37	38
15	21	41	38
20	18	49	40
25	19	51	40
30	19	51	40

Table 4-2: *Effect of upper MoO_3 capping layer thickness on the optoelectronic properties of thermally evaporated MoO_3(7 nm)/Ag(15 nm)/MoO_3(x nm) electrodes.*

The R_{sheet} remained nearly constant (18-21 $\Omega.sq^{-1}$), confirming that electrical transport is governed almost exclusively by the continuous Ag interlayer. In contrast, the optical response exhibited a clear dependence on the MoO_3 capping-layer thickness. Increasing the thickness from 15 to 25 nm progressively enhanced the *AVT* from approximately 41 % to 51 %, while the $AT_{300\text{-}1000nm}$ increased from 38 % to 40 %. Both parameters therefore indicate an improvement in optical transmission upon increasing the MoO_3 thickness until 25 nm. Beyond 25 nm, neither *AVT* or $AT_{300\text{-}1000nm}$ exhibited any further improvement, indicating that the optimum optical interference condition was reached at a MoO_3 thickness of approximately 25 nm.[154] The resulting combination of high optical transmission and nearly unchanged R_{sheet} makes the 25 nm MoO_3 capping layer the most suitable configuration among those investigated for semi-transparent PV applications. Nevertheless, the maximum *AVT* of

approximately 51 % and $AT_{300\text{-}1000nm}$ of 40 % indicate that a significant fraction of the incident light remains lost through reflection and absorption in the MoO_3/Ag/MoO_3 electrode.

Key Point 4.2.1: Thermally evaporated oxide-metal-oxide electrodes

OMO electrode	R_{sheet} ($\Omega.sq^{-1}$)	*AVT* (%)	$AT_{300\text{-}1000nm}$ (%)
MoO_3(7nm)/Ag(15nm)/MoO_3(25nm)	19	51	40

This level of optical transparency remained intrinsically insufficient for high-performance ST-OSC. Further improvements required replacing continuous Ag films by an alternative conductive network, motivating the investigation of Ag-NWs electrodes in the following section.

4.2.2 Screen-printed silver-nanowires electrodes

a) State-of-the-art and motivation

Silver nanowires (Ag-NWs) networks have emerged as one of the most promising transparent electrode technologies for flexible and semi-transparent PV devices.[161] Unlike continuous conductive films such as sputtered TCO or evaporated metals, Ag-NWs consist of a random percolating network of metallic NWs. Electrical conduction occurs through percolating interconnected NWs, while optical transparency is maintained through the voids separating neighbouring wires.[162] As a result, Ag-NWs electrodes combine high optical transparency, low R_{sheet} and excellent mechanical flexibility, making them attractive candidates for ST-OSC. Compared with conventional TCO, they can furthermore be processed from solution at low temperature and are readily compatible with roll-to-roll manufacturing, which further broadens their potential for flexible PV applications.[161,163] The optoelectronic performance of Ag-NWs electrodes is governed by the percolation of the NWs network. Increasing the NWs density decreases the R_{sheet} but simultaneously reduces the optical transparency because of the larger metallic surface coverage.[164] Consequently, optimizing Ag-NWs electrodes therefore consists in identifying the optimum balance between conductivity and transparency.

Several deposition techniques have been developed for Ag-NWs electrodes, including spray coating, doctor blading, spin coating and screen printing.[163,165–167] For example, *Krantz et al.* demonstrated that spray-coated Ag-NWs electrodes can achieve *AVT* values above 85 % while maintaining PV performances close to those obtained with evaporated metallic electrodes, highlighting their strong potential for ST-OSC.[165] Based on our literature review, a commercial Ag-NWs ink commercialized by Dycotec Materials was selected. According to the

manufacturer's specifications, the cured films exhibit a R_{sheet} of approximately 100 Ω.sq^{-1} together with a T_{max} exceeding 97 % at 550 nm. The objective of this study was therefore to determine whether the recommended screen-printing process could provide both the expected optoelectronic properties and a patterning resolution compatible with laboratory-scale ST-OSC fabrication.

b) Electrode fabrication and characterization

The commercial Ag-NWs ink supplied by Dycotec Materials was deposited by screen printing according to the manufacturer's recommended processing conditions. Screen printing was performed using a 120 mesh.cm^{-1} screen with a wire diameter of 31 µm. A squeegee pressure of 3 N.cm^{-1} and a printing speed of 300 mm.s^{-1} were employed to ensure uniform ink transfer through the screen. After deposition, the printed electrodes were thermally cured in an oven at 110 °C for 2 min to remove the solvent and promote the formation of a conductive Ag-NWs network. Ag-NWs films were deposited on soda-lime glass substrates for both electrical and optical characterizations. The optical transmittance spectra were recorded relative to an uncoated glass substrate used as the baseline reference, thereby isolating the optical response of the Ag-NWs network itself. The resulting optoelectronic properties and corresponding transmittance spectrum are summarized in **Figure 4-5** and **Table 4-3**, respectively.

Ag-NWs (nm)	R_{sheet} (Ω.sq^{-1})	*AVT* (%)	$AT_{300\text{-}1000nm}$ (%)
200	65	91	90

Table 4-3: *Optoelectronic properties of the screen-printed Ag-NWs electrode.*

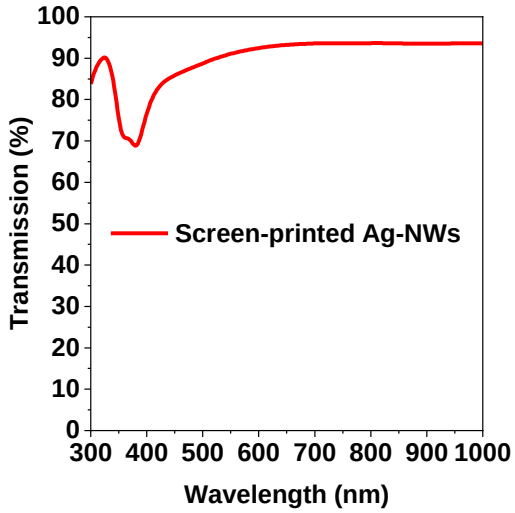

Figure 4-5: *Optical transmittance spectrum of the screen-printed Ag-NWs electrode.*

The screen-printed Ag-NWs electrodes exhibited a R_{sheet} of approximately 65 $\Omega.sq^{-1}$ together with an *AVT* and $AT_{300\text{-}1000nm}$ of 91 % and 90 %, respectively, confirming the excellent intrinsic optoelectronic performances of the commercial ink. In order to evaluate the compatibility of this deposition technique with the subsequent fabrication of ST-OSC devices, the Ag-NWs ink was not only deposited as a continuous film but also patterned using the electrode geometry intended for the OSC top contacts, including the millimetre-scale structures required to define electrically isolated cells. Under these conditions, photographs and optical microscopy observations revealed pronounced edge spreading, irregular line definition, and insufficient lateral patterning resolution for the fabrication of well-defined laboratory-scale ST-OSC (**Figure 4-6**). The printed features were significantly wider than the nominal screen openings, and neighbouring patterned regions occasionally exhibited partial merging.

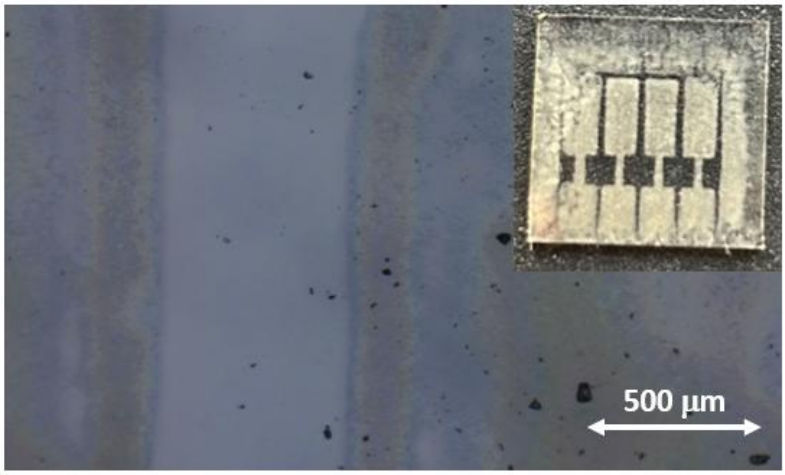

Figure 4-6: *Photograph and optical microscopy image of the patterned screen-printed Ag-NWs electrode.*

These observations can be attributed to the combined influence of the rheological behavior of the Ag-NWs ink during printing, the wetting and capillary spreading of the ink on the glass substrate, and the 120 $mesh.cm^{-1}$ screen geometry. As a consequence, although the screen-printed electrodes exhibit excellent optical transparency and satisfactory electrical conductivity, the achievable patterning resolution remained insufficient for the millimetre-scale electrode geometries required for laboratory ST-OSC fabrication.

4.2.3 Spin-coated silver nanowires electrodes

a) State-of-the-art and motivation

As shown in the previous section, the commercial Ag-NWs ink exhibited optoelectronic performances fully compatible with ST-OSC. However, the limited resolution of the screen-printing process prevented the fabrication of well-defined laboratory-scale devices, indicating

that the main limitation originated from the deposition process rather than from the Ag-NWs material itself.

Among the solution-based deposition techniques reported for Ag-NWs transparent conductive films, spin coating has become one of the most widely adopted laboratory-scale deposition methods owing to its simplicity, excellent reproducibility and precise control over the deposited NWs density.[163] While spin-coated Ag-NWs have been extensively investigated as transparent conductive films, their integration as patterned top electrodes for ST-OSC has received comparatively limited attention in the literature. Most published studies focus on improving the intrinsic properties of the deposited Ag-NWs layer, whereas the subsequent patterning step is generally achieved using shadow masks, photolithography or dedicated printing strategies rather than being investigated as a key fabrication challenge.[167,168] However, for ST-OSC, the transparent top electrode must not only provide excellent optoelectronic performances but also be patterned with sufficient resolution to define electrically isolated cells while preserving the integrity of the underlying functional layers. This additional constraint becomes particularly critical for laboratory-scale devices with millimetre-scale dimensions, where the patterning process can ultimately determine the successful integration of the transparent electrode.

The objective of this work was therefore to evaluate whether replacing screen printing by spin coating could overcome the patterning limitations while preserving the excellent optoelectronic properties of the commercial Ag-NWs ink. The influence of the spin-coating conditions and the subsequent laser-patterning process was therefore investigated to assess the feasibility of integrating spin-coated Ag-NWs electrodes into ST-OSC.

b) Optimization of the Ag-NWs network

During spin coating, the rotation speed directly controls the amount of Ag-NWs remaining on the substrate after solvent evaporation and thereby governs the morphology, optical transparency and electrical conductivity of the resulting electrode.[169] To determine the optimal deposition conditions, Ag-NWs layers were deposited on glass at rotation speeds ranging from 1000 to 7000 rpm and followed by annealing at 140 °C for 20 min. **Figure 4-7a** shows the transmission spectra together with the corresponding thicknesses, and **Figure 4-7b** presents R_{sheet} and *AVT* obtained for the different spin-coating conditions. The corresponding optoelectronic properties are summarized in **Table 4-4**.

Spin Speed (rpm)	Thickness (nm)	R_{sheet} ($\Omega.sq^{-1}$)	*AVT* (%)	$AT_{300\text{-}1000nm}$ (%)
1000	380	155	78	74
2000	270	110	86	84
3000	175	100	89	88
4000	150	88	91	90
5000	135	105	93	92
6000	120	138	94	93
7000	110	177	95	93

Table 4-4: *Effect of spin-coating speed on the thickness and optoelectronic properties of Ag-NWs electrodes.*

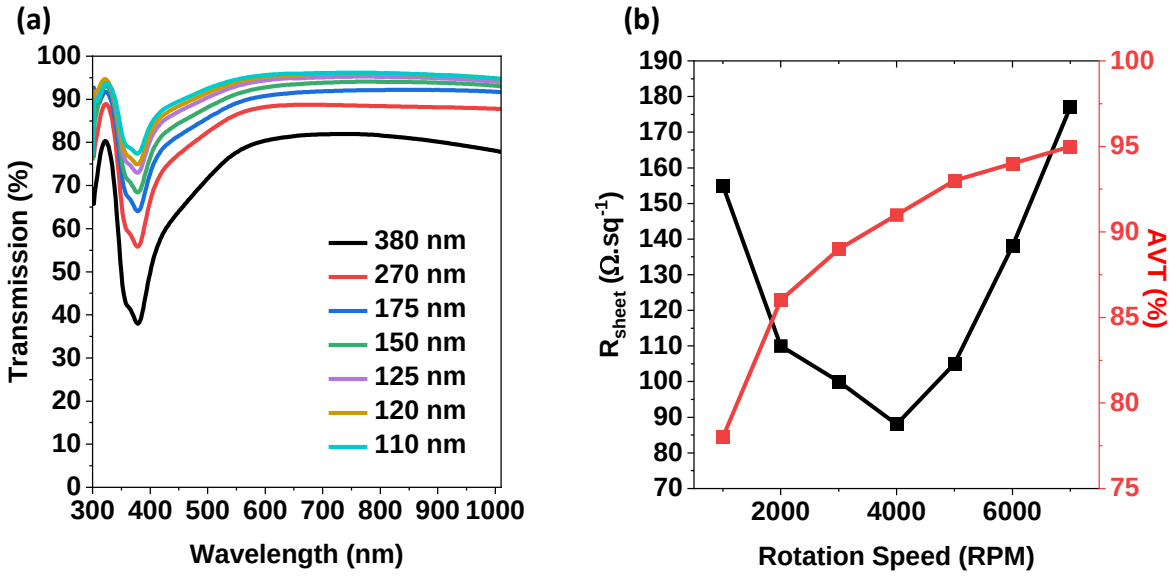

Figure 4-7: *Effect of spin-coating speed on the (a) optical transmittance spectra and (b) optoelectronic properties of Ag-NWs electrodes.*

Although the optical behavior follows a monotonic evolution, the electrical properties exhibit a significantly different trend. The R_{sheet} initially decreases from 155 $\Omega.sq^{-1}$ at 1000 rpm to a minimum value of 88 $\Omega.sq^{-1}$ obtained at 4000 rpm, before increasing again to 177 $\Omega.sq^{-1}$ at 7000 rpm. This non-monotonic trend indicates that the electrical conductivity does not simply depend on the deposited thickness but rather on the organization of the percolating NWs network. To quantitatively correlate the electrical properties with the morphology of the deposited Ag-NWs network, the surface coverage (C_{NWS}) was determined from optical microscopy images (**Figure 4-8**).

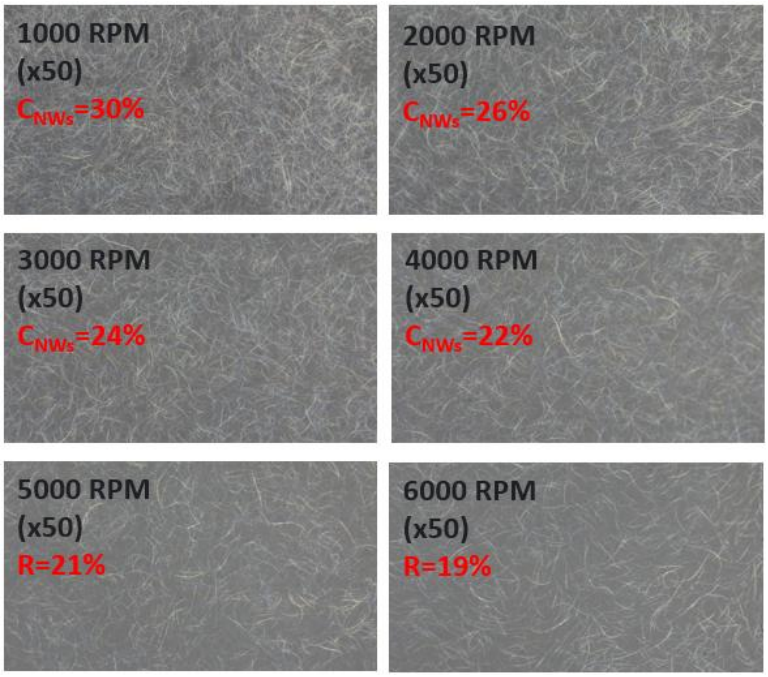

Figure 4-8: *Optical microscopy images and corresponding surface coverage of Ag-NWs as a function of spin-coating speed.*

C_{NWs} quantification was done using Otsu's automatic thresholding method, which converts grayscale micrographs into binary images by separating the foreground (Ag-NWs) from the background (uncovered substrate).[170] The binary images were subsequently analysed using ImageJ to calculate the fraction of the substrate area occupied by Ag-NWs. The resulting parameter, hereafter referred to as the Ag-NWs surface coverage, corresponds to the percentage of the surface covered by nanowires and provides a quantitative descriptor of the network density. Thickness and Ag-NWs surface coverage as a function of rotation speed are presented in **Figure 4-9**.

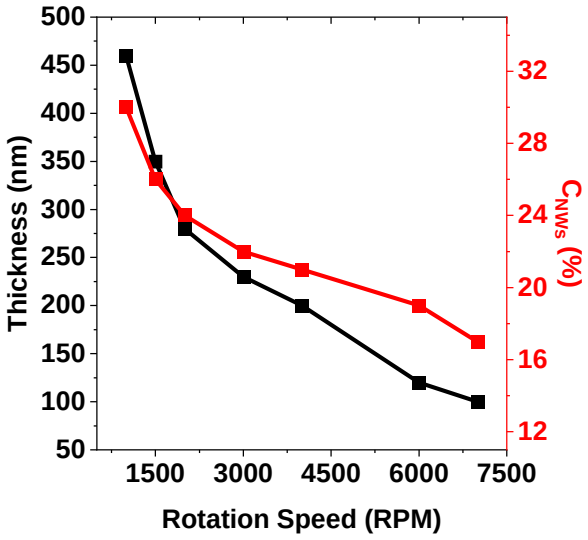

Figure 4-9: *Evolution of Ag-NWs thickness and surface coverage as a function of spin-coating speed.*

At low rotation speeds (1000-2000 rpm), corresponding to a C_{NWs} of 30-26 %, the substrate is densely covered by overlapping NWs forming a highly interconnected network. Although this high coverage provides numerous conductive pathways, it may also result in a large number of NWs junctions and local stacking. Since each junction contributes an additional contact resistance (R_C), overly dense networks do not necessarily provide the lowest R_{sheet} despite containing a larger amount of conductive material.[171,172] As the rotation speed increases (3000-4000 rpm), C_{NWs} progressively decreases to approximately 24-22 %, producing a more homogeneous network with fewer overlapping junctions while maintaining sufficient interconnections for efficient electrical percolation. This intermediate coverage regime, corresponding approximately to rotation speeds between 3000 and 4000 rpm, provides the most favourable trade-off between optical transmission and electrical conductivity. Within this intermediate regime, the 4000 rpm condition was therefore selected. This condition corresponds to a film thickness of approximately 150 nm, a C_{NWs} of 22 %, a R_{sheet} of 88 $\Omega.sq^{-1}$, an $AT_{300–1000nm}$ of 90 %, and an *AVT* of 91 %. Under these conditions, the NWs density remains sufficiently high to preserve a continuous percolating network while limiting optical losses associated with excessive metallic coverage. For rotation speeds above 4000 rpm, the C_{NWs} decreases to 21 % at 5000 rpm and 19 % at 6000 rpm. Despite the continued improvement in optical transparency, the R_{sheet} increases rapidly, indicating that the conductive network may progressively approach its percolation threshold.[173] In this regime, the reduction in conductive pathways becomes the dominant factor governing charge transport, leading to degraded electrical conductivity even though optical transmission continues to increase. Similar behavior has previously been reported for Ag-NWs transparent films.[173]

Based on the combined optical, electrical and morphological characterizations, the Ag-NWs electrode deposited at 4000 rpm was selected for the remainder of this work.

c) Laser patterning of Ag-NWs electrodes

Following the optimization of the spin-coated Ag-NWs transparent electrode on glass substrate, a "SCULPFUN G9" laser-patterning process was developed to define electrically isolated top electrodes while preserving the surrounding transparent electrode (**Chapter 2**). Laser power was first optimized while maintaining the scanning speed (1 $mm.s^{-1}$), pulse frequency (20 kHz) and number of passes constant. Below a laser power of 20 %, the engraved tracks remained electrically conductive, whereas complete electrical interruption of the Ag-NWs network was achieved above this threshold.

The influence of the scanning speed was subsequently investigated. Reducing the scan speed increases the interaction time between the laser beam and the Ag-NWs film, thereby increasing the deposited energy.[174] As shown in **Figure 4-10**, the lowest scanning speed (1 $mm.s^{-1}$) resulted in a broader and less well-defined processed area, which may be attributed to a larger heat-affected region caused by the higher energy deposition. Conversely, increasing the scanning speed to 10 mm.s-1 produced cleaner and sharper edges while maintaining efficient removal of the Ag- NWs network. Above this scanning speed (20 $mm.s^{-}$

^{1}), the processed edges appeared less well defined. The lower energy delivered to the film may limit the efficiency of Ag-NWs removal. An optimum scanning speed of 10 mm.s^{-1} was identified.

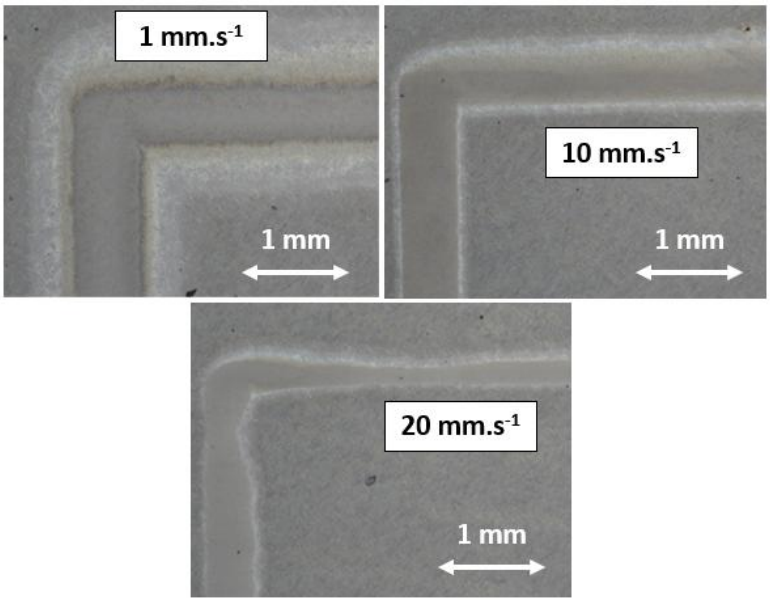

Figure 4-10: *Effect of laser scanning speed on the patterning of Ag-NWs electrode deposited on glass substrate.*

The number of laser passes also played a significant role. A single pass was insufficient to ensure complete interruption of the conductive network over the entire engraved line, whereas increasing the number of repetitions progressively improved the continuity of the ablated region. Beyond three passes, however, no further improvement in electrical isolation was observed while the thermal impact on the surrounding material became increasingly pronounced (**Figure 4-11**).

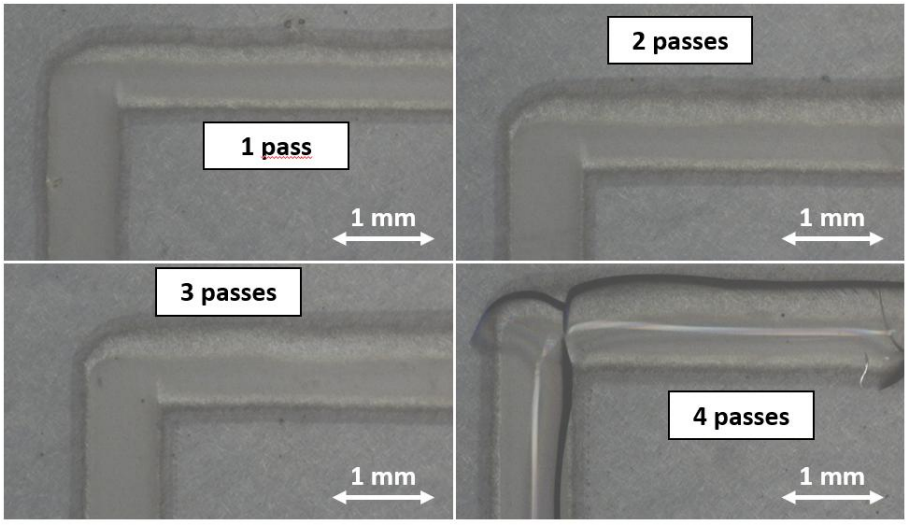

Figure 4-11: *Effect of the number of laser passes on the patterning of Ag-NWs electrode deposited on glass substrate.*

Finally, the pulse repetition frequency was optimized. Within the investigated range, no significant improvement was observed at higher or lower frequencies. A frequency of 20 kHz provided the most reproducible results, allowing homogeneous patterning while limiting excessive heat accumulation. Based on these investigations, the optimum laser parameters for Ag-NWs films deposited directly on glass were determined as 20 % laser power, 10 $mm.s^{-1}$ scanning speed, 20 kHz pulse frequency and three laser passes**.** To verify that these parameters effectively interrupted the conductive NWs network, optical microscopy observations were performed on the laser-patterned regions (**Figure 4-12**).

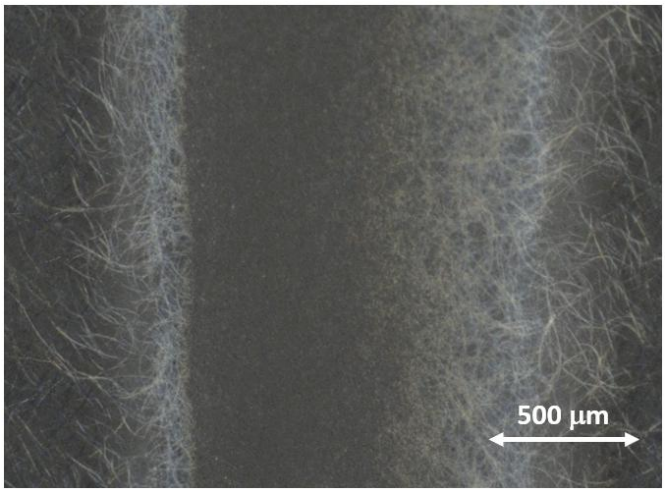

Figure 4-12: *Optical microscopy images of patterned Ag-NWs electrode deposited on glass substrate.*

The micrographs reveal that the engraved lines could be characterized by three distinct morphological regions. A dark central zone corresponded to the complete disappearance of Ag-NWs, indicating successful interruption of the conductive network. This central region was surrounded by a granular intermediate zone, where only isolated metallic residues remained visible. Finally, both edges of the laser track exhibited a significant accumulation of Ag-NWs, producing brighter regions with a noticeably higher NWs density.

These observations suggest that laser irradiation does not simply remove the Ag-NWs by direct ablation but may rather induce a sequence of thermally driven morphological transformations. Under laser irradiation, the metallic NWs are likely to experience rapid local heating, leading to partial melting of the network.[175] Once molten, the NWs become unstable owing to surface-tension-driven mechanisms and progressively fragment into shorter segments. Such behavior has previously been described through the Rayleigh instability.[175]

In addition to this fragmentation process, the accumulation of material observed along both sides of the engraved track suggests that molten silver undergoes lateral redistribution during laser irradiation. A plausible explanation is the occurrence of Marangoni-driven flow, where gradients of surface tension generated by the strong thermal gradient induce the migration of molten metal from the hottest region toward cooler surrounding areas.[176] Similar

thermocapillary transport mechanisms have previously been reported during pulsed laser melting of metallic filaments.[176]

Following the optimization performed on Ag-NWs films deposited on glass, the laser process was subsequently applied to a quasi-complete PV device stack (glass/P3HT/MoO_3/Ag-NWs) in order to evaluate its compatibility with complete ST-OSC fabrication. The laser parameters previously identified as optimal for isolated Ag-NWs films (20 % laser power, 10 $mm.s^{-1}$ scanning speed, 20 kHz pulse frequency and three laser passes) were initially applied without modification.

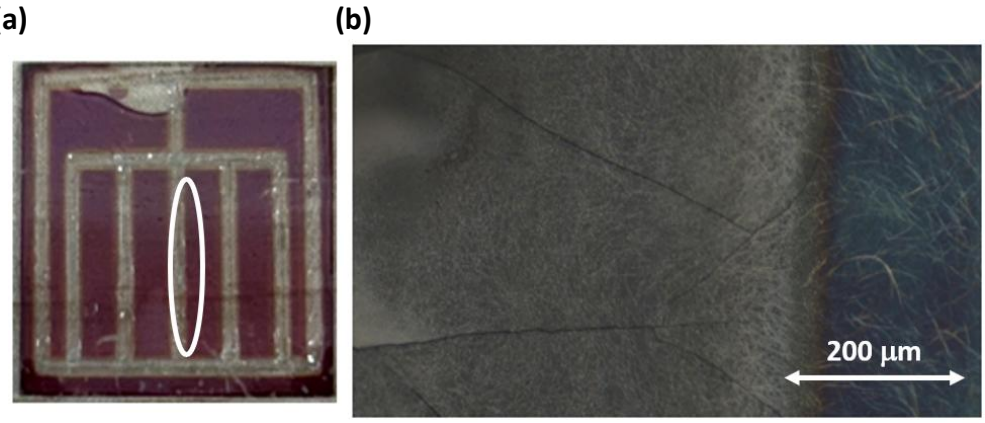

Figure 4-13: *(a) Photograph and (b) optical microscopy image of laser-patterned glass/P3HT/MoO_3/Ag-NWs using the initial laser conditions (20 % laser power, 10 $mm.s^{-1}$ scanning speed, 20 kHz pulse frequency and three laser passes).*

Unlike the results obtained with glass/Ag-NWs, these conditions systematically produced visible damage to the PV stack. Images and optical microscopy revealed pronounced degradation of the patterned regions, extending beyond the Ag-NWs layer and affecting the underlying functional layers (**Figure 4-13a** and **Figure 4-13b**). Such damage indicates that the laser energy delivered under these conditions exceeded the thermal tolerance of the complete multilayer architecture.[174] This behavior can be explained by the different optical and thermal properties of the complete device compared with a bare glass substrate. In the latter case, the laser energy is primarily absorbed by the Ag-NWs network, while the glass substrate remains largely transparent at the laser wavelength (455 nm). In contrast, the presence of the P3HT active layer significantly modifies the energy distribution within the multilayer stack. The organic semiconductor exhibits a substantially higher optical absorption than glass, promoting local heat generation beneath the Ag-NWs electrode. Consequently, a larger fraction of the incident laser energy is converted into heat within the PV stack, leading to excessive local temperatures and ultimately to the degradation of the underlying organic layers.[177]

To reduce the thermal load while maintaining efficient interruption of the Ag-NWs network, the laser power was decreased to 20 %, the scanning speed increased to 100 $mm.s^{-1}$ and the number of passes reduced to one while maintaining a pulse repetition frequency of 20 kHz. These modifications significantly reduced the deposited energy density without altering the fundamental patterning mechanism.

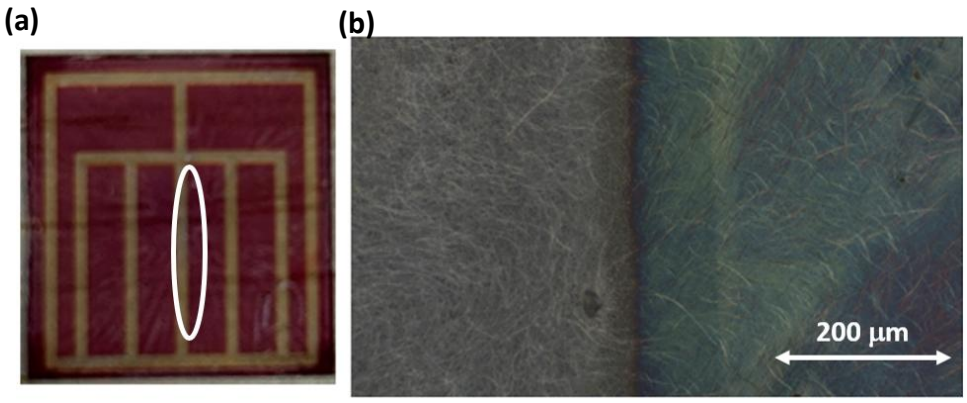

Figure 4-14: *(a) Photograph and (b) optical microscopy image of laser-patterned glass/P3HT/MoO_3/Ag-NWs using the optimized laser conditions (20 % laser power, 100 mm.s^{-1} scanning speed, 20 kHz pulse frequency and one laser pass).*

Under these optimized conditions, narrow and well-defined laser tracks were successfully produced throughout the complete PV architecture. Images and optical microscopy confirmed that the Ag-NWs electrode was cleanly patterned while no visible degradation of the surrounding layers or substrate could be observed (**Figure 4-14a** and **Figure 4-14b**). The resulting electrode geometry exhibited sharp edges and sufficient resolution for the fabrication of laboratory-scale ST-OSC. However, the laser patterning was not fully selective to the Ag-NWs electrode, and the removal of the metallic network was accompanied by removal of the underlying organic active layer. This aspect represents an important limitation of the current laser-patterning process, since damage to the active layer can possibly affect the electrical performance of the resulting ST-OSC.

To verify that the optimized laser process effectively interrupted the conductive Ag-NWs electrode after patterning of the complete devices, electrical continuity measurements were subsequently performed between adjacent electrodes separated by the engraved line.

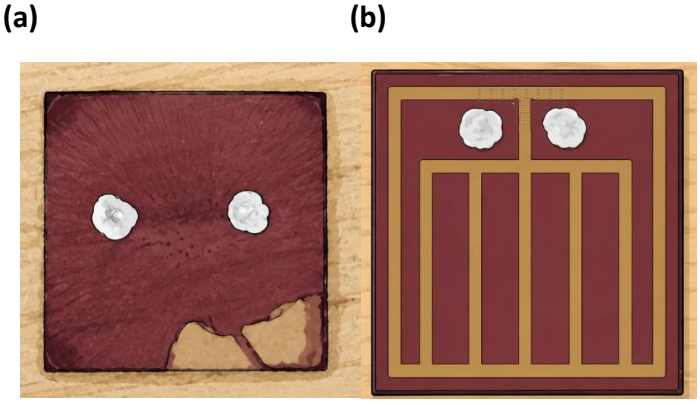

Figure 4-15: *Electrical characterization of the (a) unpatterned glass/P3HT/MoO_3/Ag-NWs and (b) patterned glass/P3HT/MoO_3/Ag-NWs stack.*

As a first validation, the electrical resistance of the unpatterned Ag-NWs electrode was measured across the active area (**Figure 4-15a**). As expected, the continuous Ag-NWs network exhibited a low electrical resistance (80 Ω), confirming the existence of uninterrupted

conductive pathways throughout the transparent electrode. Following laser patterning, the same measurement was repeated across two adjacent electrode regions separated by the engraved track (**Figure 4-15b**). In contrast to the unpatterned electrode, no measurable electrical conduction could be detected after laser processing, indicating that the conductive NWs network had been completely interrupted. These electrical measurements are fully consistent with the microscopy observations and confirm that the optimized laser process produces complete lateral electrical isolation of the Ag-NWs electrodes, making the process suitable for laboratory-scale electrode definition.[178]

Following this successful validation, the optimized laser process was applied to fabricate complete ST-OSC. Surprisingly, despite the demonstrated lateral electrical isolation of the Ag-NWs electrode, all fabricated PV devices systematically exhibited electrical short circuits during current density-voltage (*J*-*V*) measurements. None of the patterned devices displayed a rectifying PV behavior, indicating that an alternative conduction pathway remained within the multilayer structure.[179] Although no direct structural evidence could be obtained to identify the origin of these conductive bridges, the microscopy observations performed on the laser-patterned Ag-NWs films provide a plausible explanation. First, as discussed before, it was not possible to selectively remove the Ag-NWs without removal of the active layer, leaving the bottom ITO electrode accessible. Then, laser irradiation induces local melting of the NWs, followed by fragmentation through Rayleigh instability and lateral redistribution of molten silver driven by Marangoni flow.[175,176] One possible explanation is therefore that, during laser irradiation of the complete multilayer stack, part of the redistributed molten silver can redistribute laterally and create bridges between the exposed underlying ITO layer and the top electrode. Alternatively, they can locally penetrate defects or thermally degraded regions within the underlying MoO_3 and organic layers before resolidification.[180] Such localized metallic penetration could generate isolated conductive bridges between the Ag-NWs top electrode and the bottom electrode. Both phenomena would create vertical short circuits while preserving complete lateral electrical isolation between neighbouring cells.[180,181]

Overall, this study demonstrates that spin-coated Ag-NWs electrodes combine excellent optoelectronic properties with efficient low-temperature processing. Although infrared laser patterning successfully produced electrically isolated electrodes, its integration into complete ST-OSC remains limited by the thermal sensitivity of the multilayer architecture and the non-selective ablation of the Ag-NWs layer rather than by the intrinsic properties of the electrode itself.

Key Point 4.2.2 & 4.2.3: Screen-printed and spin-coated silver nanowire electrodes.

Ag-NWs electrodes	R_{sheet} ($\Omega.sq^{-1}$)	*AVT* (%)	$AT_{300\text{-}1000nm}$ (%)
Screen-printed	65	91	90
Spin-coated	88	91	90

Ag-NWs electrodes demonstrated outstanding optoelectronic performances but could not be successfully integrated into complete ST-OSC owing to screen-printing resolution or laser-induced vertical short circuits.

4.2.4 Room-temperature sputtered ITO electrodes

a) State-of-the-art and motivation

Transparent conductive oxides constitute the benchmark technology for transparent electrodes owing to their unique ability to simultaneously combine high electrical conductivity with excellent optical transparency in the visible spectral range.[182] Among the different TCO investigated over the past decades, ITO (In_2O_3:Sn) remains by far the most widely employed material in optoelectronic devices.[183] Its unique combination of optoelectronic properties, including *AVT* typically exceeding 85 %, low electrical resistivity approaching 10^{-4} Ω·cm, wide optical bandgap (3.5-4.2 eV), excellent chemical stability and compatibility with conventional microfabrication processes have established ITO as the reference transparent electrode for applications including flat-panel displays and touch screens to light-emitting diodes, PV devices and electrochromic windows.[184]

ITO thin films can be deposited using numerous techniques, including chemical vapor deposition,[185] spray pyrolysis,[186] pulsed laser deposition,[187] sol-gel synthesis,[188] electron-beam evaporation[189] and sputtering.[190] Among these methods, magnetron sputtering has become the industrial standard because it provides excellent control over film composition, thickness uniformity and reproducibility while remaining fully compatible with large-area substrates.[191] Compared with solution processing, sputtering produces dense, compact films exhibiting superior adhesion and improved electrical performance.[192] Furthermore, unlike evaporation processes, sputtering allows the direct transfer of the target composition to the deposited film while offering precise control over deposition parameters such as plasma power, gas pressure, oxygen partial pressure and substrate temperature.[192] The excellent optoelectronic properties of sputtered ITO originate from the particular electronic structure of heavily Sn-doped In_2O_3.[193] Tin atoms substitute for indium atoms within the bixbyite crystal lattice and act as donor impurities, providing free electrons to the conduction band.[193,194] In addition, oxygen vacancies generated during deposition may contribute to the free carrier

concentration.[195] The combination of a high carrier density with relatively high electron mobility results in metal-like conductivity while maintaining high optical transparency because the WBG prevents significant absorption throughout the visible spectrum.[196] The final optoelectronic performance therefore depends on the delicate balance between carrier concentration, carrier mobility, crystallinity and defect density, all of which are strongly governed by the sputtering conditions employed during film growth. Despite these advantages, producing high-quality ITO remains far from trivial.

Numerous studies have demonstrated that its electrical and optical performances are extremely sensitive to deposition parameters.[194] The surface power density (φ) influences both the deposition rate and the kinetic energy of the sputtered species, whereas the working pressure (p) determines the collision frequency within the plasma and therefore the energy reaching the substrate.[197] Among all process parameters, however, the oxygen partial pressure, particularly the argon-to-oxygen flow ratio (Ar/O_2), is generally regarded as one of the most critical.[195] An insufficient oxygen supply promotes the formation of oxygen vacancies thereby generally increasing the carrier concentration and reducing electrical resistivity. Excessive oxygen deficiency, however, can simultaneously deteriorate crystallinity and increase optical absorption.[198] By contrast, excessive oxygen flow suppresses vacancy formation, leading to higher transparency but significantly reduced conductivity.[198] Achieving high-performance ITO therefore requires identifying an optimum oxygen concentration that provides the best compromise between carrier concentration and carrier mobility. Substrate temperature constitutes another key parameter governing ITO growth.[194] Conventionally, the highest quality films are obtained either by depositing the oxide at temperatures above 200 °C or by applying a post-deposition annealing treatment.[198] Thermal energy promotes crystal growth, increases grain size, relieves internal stresses, and improves carrier mobility through the reduction of grain-boundary scattering.[198] As a result, high-temperature processing generally yields lower electrical resistivity together with higher optical transparency. However, these conventional processing conditions are incompatible with OSC because the organic layers cannot withstand temperatures above approximately 100 °C.[199] Consequently, room-temperature sputtering becomes essential despite the more limited crystallization and higher defect density generally obtained under these conditions.

Beyond the intrinsic challenge of low-temperature deposition, sputtering introduces an additional difficulty that is specific to OPV. During magnetron sputtering, energetic ions, electrons, neutral particles, and UV radiation generated within the plasma can penetrate the growing film and interact with the underlying organic layers.[200] This bombardment may induce chemical degradation, defect formation, morphological changes and interfacial damage, which may ultimately lead to reduced PV performance.[201] Early demonstrations of sputtered ITO top electrodes in ST-OSC successfully proved the feasibility of the approach but also revealed significant efficiency losses associated with plasma-induced degradation.[148] Since then, numerous studies have explored strategies to mitigate sputtering damage, including reducing plasma power, increasing the working pressure to decrease particle energy, optimizing film thickness[202] or introducing protective buffer layers between the active device

and the sputtered oxide.[203] These studies highlight that successful implementation of sputtered ITO in OSC requires not only optimizing the intrinsic properties of the electrode itself but also carefully controlling the interaction between the plasma and the sensitive organic layers. Recent investigations have nevertheless demonstrated that high-quality ITO can indeed be deposited at room temperature provided that sputtering parameters are carefully optimized.[204] Under optimized conditions, room-temperature deposited ITO films can achieve visible transmittance above 80 % while maintaining resistivities approaching those obtained using conventional high-temperature processes.[204]

These advances demonstrate that room-temperature sputtering has now become sufficiently mature to address the stringent requirements of flexible and organic electronics, although the available process window remains considerably narrower than that of conventional high-temperature deposition. Before studying its integration into ST-OSC, it was therefore necessary to establish deposition conditions capable of producing highly transparent and sufficiently conductive ITO films at room temperature while remaining fully compatible with the thermal constraints imposed by OSC.

b) Optimization of sputtering conditions

Optimization of the sputtered ITO transparent electrode was carried out by systematically investigating the influence of the main deposition parameters on the electrical and optical properties of the deposited films. The starting deposition conditions were based on a RF sputtering process previously developed by our partner laboratory, the Laboratoire de Physique des Interfaces et Couches Minces (LPICM). Although this process had originally been developed for applications other than ST-OSC, its demonstrated ability to produce high-quality room-temperature ITO films made it an appropriate starting point for the present optimization.

The reference process employed an Ar/O_2 flow ratio of 45.9/0.1 sccm, a power density of approximately 7 $W \cdot in^{-2}$, a working pressure of 0.15 Pa and an ITO thickness (t) of about 120 nm. Starting from these reference conditions, each deposition parameter was varied individually while maintaining the others constant (thickness included) in order to identify its individual influence on the electrode properties. ITO films were deposited on soda-lime glass substrates for both electrical and optical characterizations. The optical transmittance spectra were recorded relative to an uncoated glass substrate used as the baseline reference, thereby isolating the optical response of the ITO electrode itself.

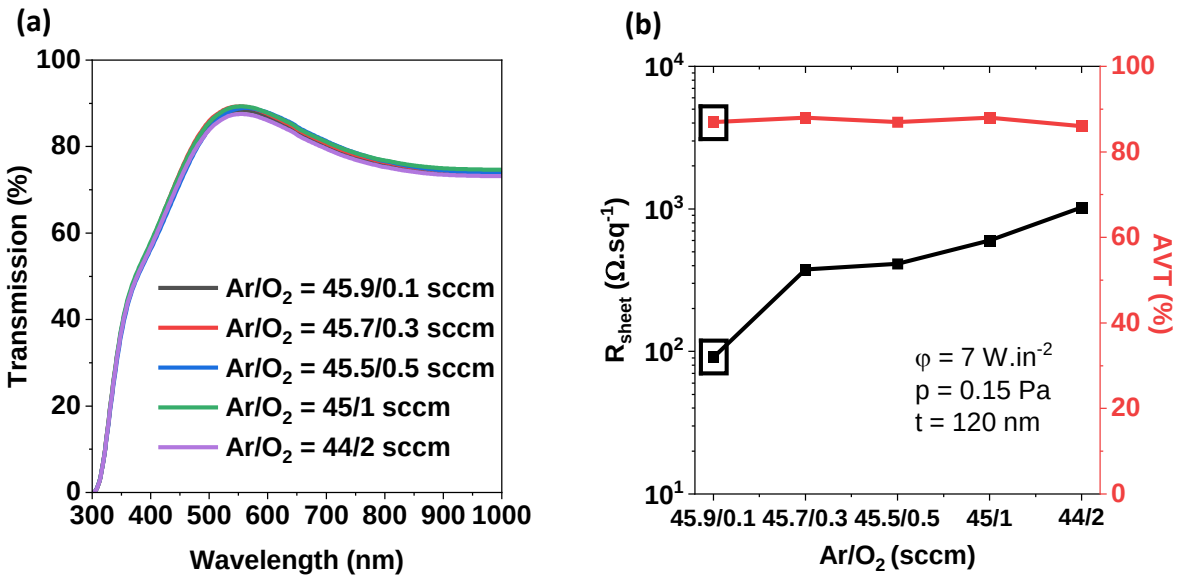

Figure 4-16: *Effect of the Ar/O_2 flow ratio on the (a) optical transmittance spectra and (b) optoelectronic properties of sputtered ITO films deposited on glass.*

As illustrated in **Figure 4-16a and Figure 4-16b**, decreasing the Ar/O_2 ratio from 44/2 to 45.9/0.1 sccm resulted in a drastic decrease in R_{sheet}, from approximately 1023 $\Omega.sq^{-1}$ to only 91 $\Omega.sq^{-1}$, while maintaining an *AVT* close to 87 %. This behavior suggests that reducing the oxygen flow promotes the formation of oxygen-deficient films, thereby increasing the free carrier concentration and reducing the electrical resistivity.[195] Consequently, the lowest investigated oxygen flow was selected for the remainder of the optimization procedure. Once the oxygen flow ratio had been optimized, the influence of φ was investigated under these conditions.

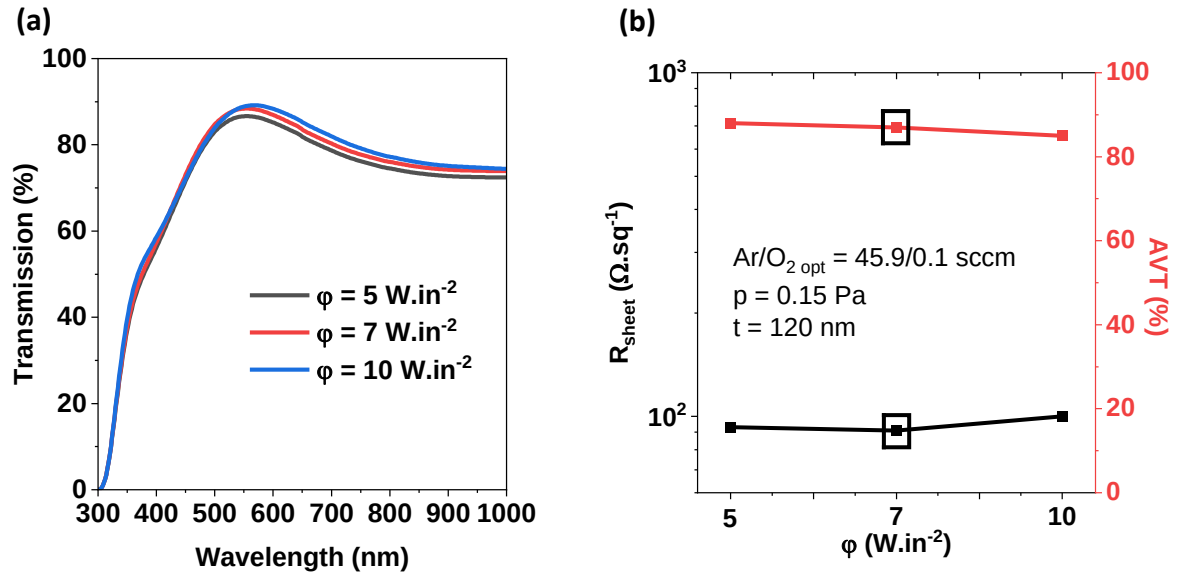

Figure 4-17: *Effect of the RF power density on the (a) optical transmittance spectra and (b) optoelectronic properties of sputtered ITO films deposited on glass.*

Within the investigated range (φ between 5-10 W.in^{-2}), neither the R_{sheet} nor the *AVT* exhibited significant changes, indicating that the deposition process remained only weakly affected by this parameter (**Figure 4-17a and Figure 4-17b**). Since increasing φ accelerates the deposition rate at the expense of increased target erosion, an intermediate value of approximately 7 W·in^{-2} was selected as the most appropriate operating condition, providing an appropriate compromise between deposition efficiency and target durability. After selecting the RF power density, the optimization was extended to the working pressure.

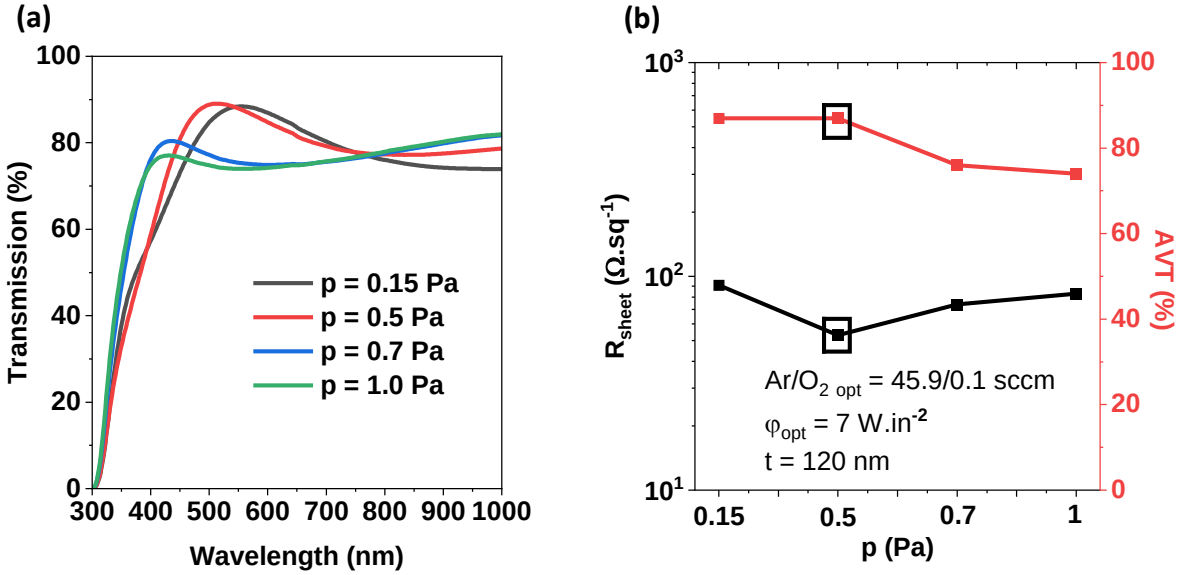

Figure 4-18: *Effect of the working pressure on the (a) optical transmittance spectra and (b) optoelectronic properties of sputtered ITO films deposited on glass.*

As shown in **Figure 4-18a** and **Figure 4-18b**, the electrical properties reached an optimum at a working pressure of 0.5 Pa. At this pressure, the deposited films exhibited the lowest R_{sheet} while maintaining excellent optical transparency. This behavior can be related to the balance between the kinetic energy of the sputtered species and the evolution of the film microstructure during growth.[197] At intermediate pressure *p*, such as 0.5 Pa, the sputtered species retain sufficient kinetic energy to reach the substrate and promote surface diffusion, while the collision frequency remains high enough to avoid excessively energetic bombardment. This favourable balance can promote the formation of dense and homogeneous ITO films, thereby improving their electrical conductivity. At the lowest pressure investigated (0.15 Pa), the higher kinetic energy of the sputtered species does not necessarily lead to improved film properties. The reduced number of collisions in the plasma results in more energetic species reaching the substrate, which can modify the growth regime and potentially induce re-sputtering, defect formation, or either non-optimal growth effects.[205] Consequently, despite the higher particle energy, the resulting film exhibit poorer electrical properties than those deposited at 0.5 Pa. At higher pressures, frequent collisions within the plasma reduce the kinetic energy of the sputtered species before they reach the substrate, thereby limiting adatom mobility and film densification, which results in higher

R_{sheet}.[205] The optimum at 0.5 Pa therefore results from a balance between insufficient adatom mobility at higher pressure and excessively energetic growth conditions at very low pressure.

The transmittance spectra also exhibit a noticeable dependence on the working pressure, particularly between the films deposited at 0.15 and 0.5 Pa and those deposited at 0.7 and 1 Pa (**Figure 4-18a**). The differences in the spectral shape and in the position of the T_{max} suggest that the optical properties of the ITO films vary with the deposition pressure. Since the film thickness was kept constant (around 120-130 nm), these variations may be related to changes in the refractive index associated with pressure-dependent growth conditions and film microstructure. In particular, variations in refractive index can modify the optical interference conditions within the ITO layer and consequently affect the position and shape of the transmission features.[206] Since the optical constants were not independently determined for each pressure condition, this interpretation remains a plausible hypothesis rather than a direct attribution. Overall, a working pressure of 0.5 Pa provides the best compromise between electrical conductivity and optical transparency, promoting the formation of dense and electrically conductive ITO films while maintaining high transmission.

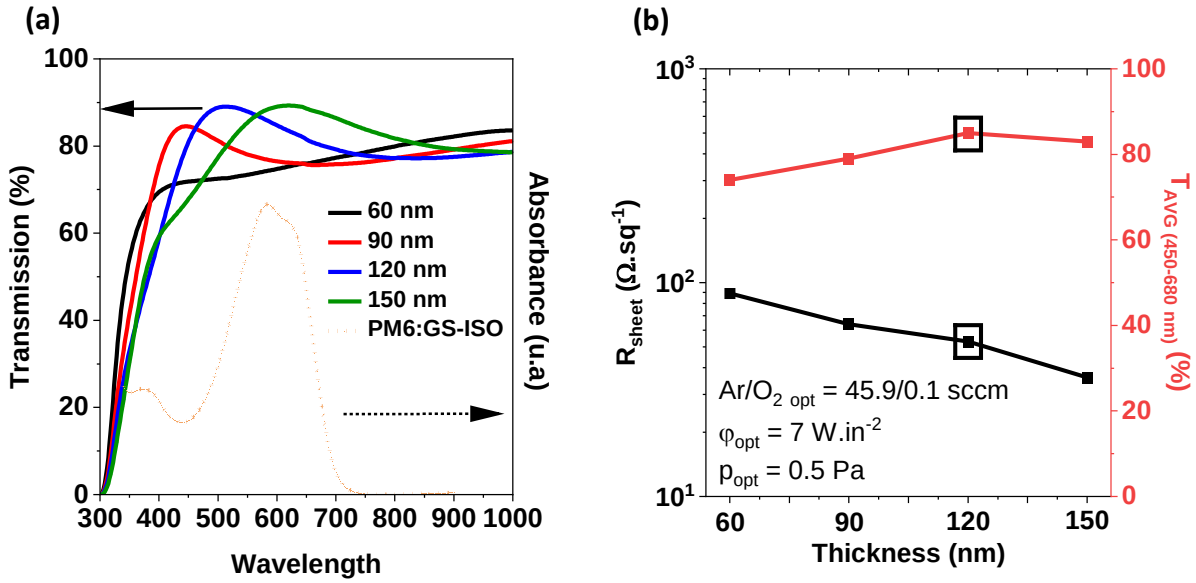

Figure 4-19: *Effect of ITO thickness on the (a) optical transmittance spectra and (b) optoelectronic properties of sputtered ITO films.*

Once the plasma conditions had been optimized, attention was focused on the film thickness. Film thickness plays a decisive role since it simultaneously governs both the electrical conductivity and the optical transparency of the electrode. While increasing *t* generally improves charge transport by reducing the R_{sheet}, it also modifies the optical behavior of the electrode through increased absorption, reflection and interference effects.[207] Consequently, determining an optimum thickness is essential for ST-OSC, where both efficient current collection and high optical transmission are required. **Figure 4-19a** presents the optical transmission spectra measured for ITO layers deposited on glass with thicknesses ranging from 60 to 150 nm. Regardless of the film thickness, all films exhibited the characteristic

optical response of ITO, with high transparency throughout the visible spectral range and a sharp decrease in transmission below approximately 350 nm corresponding to the fundamental absorption edge of the oxide. No significant shift of the absorption edge was observed with increasing thickness. Although the overall transparency remained high for all investigated thicknesses, noticeable differences appeared within the visible range. The T_{max} progressively shifted and its amplitude evolved as *t* increased, illustrating the combined influence of optical interferences and thickness-dependent absorption within the conducting oxide layer.[182] The transmission spectra were also compared with the absorption spectrum of the PM6:GS-ISO active layer, also shown in **Figure 4-19a**. This comparison is especially relevant for ST-OSC design since only photons transmitted through the transparent electrode can subsequently be absorbed by the active layer. The photoactive blend exhibits its strongest absorption between approximately 450 and 680 nm, defining the spectral window where the optical properties of the transparent electrode become the most critical. This wavelength interval was therefore selected for the calculation of the transmittance over the absorption range of the active material T_{avg}. Increasing *t* progressively reduced R_{sheet} owing to the larger conducting cross-section and the improved structural quality of the deposited oxide. Thicker ITO layers often exhibit larger crystalline grains and fewer grain boundaries, thereby reducing electron scattering and facilitating charge transport throughout the electrode.[207] As a consequence, electrical conductivity progressively improved as the thickness increased from 60 to 150 nm. However, this improvement was accompanied by a progressive modification of the optical transmission, illustrating the intrinsic compromise that characterizes transparent conductive oxides.[182] As shown in **Figure 4-19b**, T_{avg} values of 74, 79, 85 and 83 % were obtained for ITO thicknesses of 60, 90, 120 and 150 nm, respectively. The highest optical performance was not achieved for the thinnest electrode but for the 120 nm film. These results indicate that the optical response of the electrode cannot be interpreted solely as a monotonic decrease of transmission with increasing thickness. Instead, interference phenomena occurring within the multilayer system contribute to the redistribution of the transmitted light, allowing intermediate thicknesses to exhibit enhanced transmission over the wavelength range that is most relevant for PV operation.[160]

Considering both the electrical and optical performances, an ITO thickness of 120 nm provided the best compromise, yielding a R_{sheet} of approximately 53 $\Omega.sq^{-1}$, an *AVT* close to 87 % and an $AT_{300\text{-}1000nm}$ of 74 %. These performances demonstrate that optimized room-temperature RF sputtering can produce transparent conductive electrodes suitable for OPV integration without post-deposition annealing.

Key Point 4.2.4: Room-temperature sputtered ITO electrodes.

Optimized deposition conditions:
Ar/O_2 = 45.9/0.1 sccm
φ = 7 W.in^{-2}
P = 0.5 Pa
t = 120 nm

	R_{sheet} (Ω.sq^{-1})	AVT (%)	$AT_{300\text{-}1000nm}$ (%)	T_{avg} (%)
ITO	53	87	74	85

Room-temperature RF sputtering enabled the fabrication of highly transparent and conductive ITO electrodes compatible with OSC processing.

4.2.5 Selection of the transparent electrode

a) Figures of merit for transparent electrodes

Although the optimization successfully identified the optimum sputtering conditions for ITO, an objective comparison with the other transparent electrodes developed in this work requires a common evaluation criterion. However, comparing different transparent electrode technologies remains challenging because neither the R_{sheet} nor the optical transmittance alone is sufficient to describe the overall quality of a transparent conductive electrode. A highly conductive electrode generally exhibits reduced transparency, whereas maximizing optical transmission often results in increased electrical resistance. Accordingly, a quantitative criterion combining both properties is required to objectively compare different electrode architectures. For this purpose, several figures of merit (FOM) have been proposed in the literature to simultaneously evaluate the optical and electrical performances of transparent conductive films. Among the proposed FOM, the two most widely adopted are the Fraser & Cook[208] (**Equation 4-3**) and the Haacke[209] figure of merit (**Equation 4-4**).

$$\Phi_{FC} = \frac{AT_{300-1000nm}}{R_{sheet}} \quad \textbf{(4-3)}$$

$$\Phi_{H} = \frac{(AT_{300-1000nm})^{10}}{R_{sheet}} \quad \textbf{(4-4)}$$

Although both expressions combine the same physical quantities, they do not attribute the same importance to $AT_{300\text{-}1000nm}$ and R_{sheet}. The Fraser & Cook criterion considers both quantities linearly, whereas the Haacke formulation introduces a tenth-power dependence on $AT_{300\text{-}1000nm}$ to strongly favour highly transparent electrodes. This modification was originally proposed to avoid selecting electrodes exhibiting excellent conductivity but insufficient transparency for optoelectronic applications. More recently, Cisneros-Contreras *et al.* proposed a modified version of the Haacke figure of merit, referred to as the Haacke High Resolution (H-HR) figure of merit in **Equation 4-5**.[210]

$$\Phi_{H-HR} = \frac{(AT_{300-1000nm})^{10}}{\sqrt[10]{R_{sheet}}} \quad \textbf{(4-5)}$$

This formulation preserves the original weighting between $AT_{300\text{-}1000nm}$ and R_{sheet} while significantly improving the discrimination between samples presenting very similar optoelectronic performances. Their study demonstrated that the classical Haacke FOM may exhibit insufficient resolution when comparing high-performance transparent electrodes, whereas the H-HR formulation provides a more sensitive comparison without altering the underlying physical interpretation. The three FOM were therefore calculated for the optimized transparent electrodes developed in this work in order to establish an objective comparison between OMO, Ag-NWs and ITO electrodes.

b) Comparative assessment and electrode selection

According to the Fraser & Cook criterion, the OMO electrode exhibits the highest FOM (0.021), despite its relatively low $AT_{300\text{-}1000nm}$ (40 %). This behavior results from the linear relationship between $AT_{300\text{-}1000nm}$ and R_{sheet} adopted in this formulation, which strongly favours electrodes exhibiting very low R_{sheet}.[208] As previously pointed out by Haacke, this criterion may overestimate the performance of highly conductive electrodes whose transparency is insufficient for transparent optoelectronic applications.

By contrast, the Haacke and Haacke H-R FOM lead to a markedly different ranking by assigning greater importance to $AT_{300\text{-}1000nm}$.[210] Using the H-HR formulation, screen-printed Ag-NWs exhibit the highest FOM (0.23), followed by spin-coated Ag-NWs (0.22), ITO (0.03) and finally the OMO electrode (7.8×10^{-5}). The small difference between the two best-performing electrodes indicates that both methods provide an excellent compromise between optical transparency and electrical conductivity, while the lower transparency of the OMO electrode significantly limits its overall performance despite its excellent electrical conductivity.

However, FOM alone are insufficient to identify the most suitable transparent electrode for ST-OSC. For this reason, an additional practical criterion evaluating the feasibility of patterning each electrode in the ST-OSC architecture is developed in this work. This criterion reflects the successful fabrication of patterned top electrodes and complete functional devices, thereby accounting for technological constraints that are not considered

by conventional FOM. Although the screen-printed and spin-coated Ag-NWs electrodes exhibited the highest H-HR FOM, neither technology could be successfully integrated into complete ST-OSC. In contrast, both OMO and sputtered ITO electrodes enabled successful device fabrication.

Table 4-5 summarizes the optoelectronic properties of the optimized transparent electrodes together with the corresponding FOM and their suitability as top electrodes for ST-OSC.

Electrode	$AT_{300\text{-}1000nm}$ (%)	R_{sheet} ($\Omega.sq^{-1}$)	Fraser & Cook FOM	Haacke FOM	Haacke H-HR FOM	Patterning feasibility in IMS
OMO	40	19	0.021	5.5×10^{-6}	7.8×10^{-5}	Yes
Screen-printed Ag-NWs	90	65	0.014	5.4×10^{-3}	0.23	No
Spin-coated Ag-NWs	90	88	0.010	4.0×10^{-3}	0.22	No
ITO	74	53	0.014	9.3×10^{-4}	0.03	Yes

Table 4-5: *Comparison of the optoelectronic properties, figures of merit and feasibility of the transparent electrodes investigated in this work.*

Considering both the optoelectronic FOM and the successful integration into complete devices, sputtered ITO emerged as the most suitable transparent electrode. The optimized sputtered ITO electrode was therefore selected for integration into ST-OSC, and its impact on device fabrication and photovoltaic performances is investigated in the following section.

4.3. Integration of the selected transparent electrode into semi-transparent organic solar cells

Following the optimization of the transparent electrodes, sputtered ITO was selected for integration into ST-OSC. The objective of this section is therefore to evaluate the integration of the optimized ITO electrode into complete ST-OSC and to assess its impact on both PV performance and operational stability. First, the optimized sputtered ITO electrode is integrated into PM6:GS-ISO WBG OSC, validating the proposed architecture for tandem PV applications. The operational stability of these devices is then investigated under continuous illumination in order to evaluate the robustness of the transparent electrode and its interfaces. Finally, the optimized transparent electrode is extended to emerging PV blends developed for semi-transparent PV applications, demonstrating the versatility of the proposed integration strategy beyond the PM6:GS-ISO system.

4.3.1 Integration into PM6:GS-ISO semi-transparent organic solar cells

a) Device architecture and transparent electrode integration

The deposition of TCO by RF magnetron sputtering directly onto OPV devices remains challenging because energetic ions, neutral particles and plasma radiation generated during the deposition process may damage the underlying organic materials.[200] Such damage may induce structural defects or enhance interfacial recombination, ultimately leading to a deterioration of the device performances.[201]

To mitigate these effects, a MoO_3 interlayer was introduced between the active layer and the sputtered ITO electrode. Besides its conventional role as a HTL, MoO_3 was also expected to act as a protective buffer layer capable of mitigating sputtering-induced damage while maintaining efficient hole extraction (**Chapter 3**).[148] Before investigating the complete semi-transparent architecture, the thickness of the MoO_3 interlayer was first optimized using conventional opaque reference devices incorporating a thermally evaporated Ag top electrode. This preliminary experiment aimed to identify a thickness providing sufficient protection against sputtering-induced damage while preserving efficient charge extraction. The corresponding PV parameters are summarized in **Table 4-6**.

MoO_3 thickness (nm)	**PCE (%)**	**J_{SC} (mA.cm^{-2})**	**V_{OC} (V)**	**FF**
3	7.3	10.1	1.14	0.63
7	7.4	10.2	1.14	0.64
15	7.3	9.9	1.14	0.65
22	7.0	9.8	1.13	0.63
30	6.3	9.2	1.12	0.61

Table 4-6: *PV parameters of $Ref_{PM6:GS-ISO}$ devices as a function of MoO_3 interlayer thickness.*

For thicknesses between 3 and 15 nm, the device performances remained nearly unchanged, with PCE between 7.3 and 7.4 %, a V_{OC} close to 1.14 V and FF ranging from 0.63 to 0.65. Increasing the MoO_3 thickness beyond 15 nm resulted in a progressive reduction in device performance, with the PCE decreasing to 7.0 % for a 22 nm layer and 6.3 % for a 30 nm

layer, accompanied by lower J_{SC} and FF. This decrease can be partly attributed to the increase in R_S associated with the thicker MoO_3 layer, which can hinder hole extraction and transport. Similar thickness-dependant effects have been reported for MoO_3 interlayers in OSC.[211] These results indicate that MoO_3 thicknesses up to 15 nm have little influence on the PV performance of the reference devices, whereas thicker layers may introduce additional R_S and charge extraction losses.

Based on these results, ST-OSC were fabricated using the inverted architecture Glass/ITO/ZnO/PM6:GS-ISO/MoO_3/ITO. A schematic representation of the device together with a cross-sectional SEM image is presented in **Figure 4-20a** and **Figure 4-20b**.

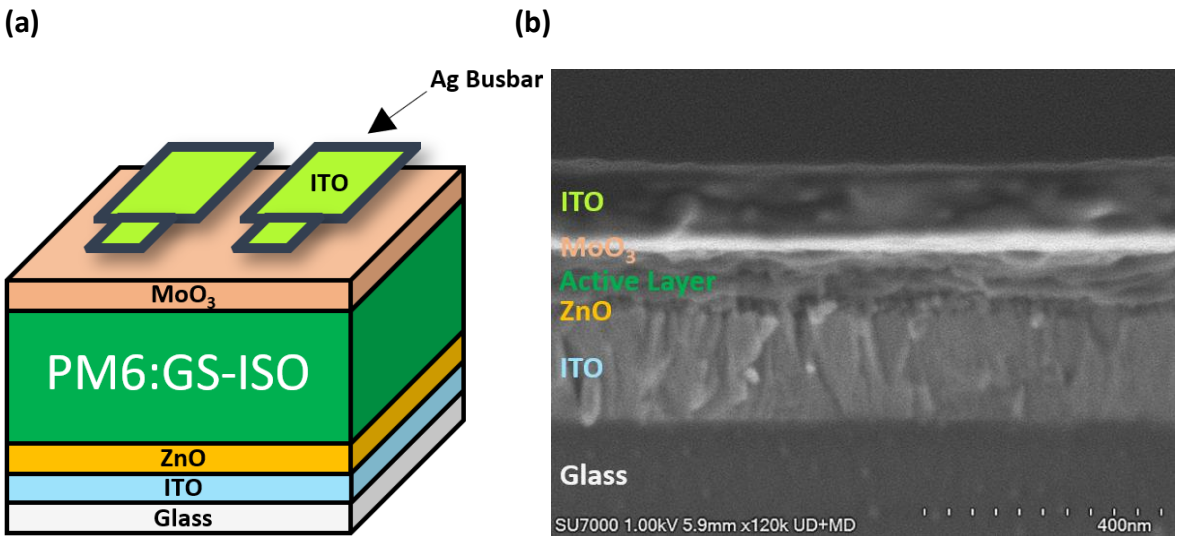

Figure 4-20: *(a) Schematic architecture and (b) cross-sectional SEM image of the* $ST_{PM6:GS-ISO}$ *device.*

The SEM micrograph reveals well-defined interfaces throughout the multilayer stack, while the sputtered ITO layer appears continuous and homogeneous over the MoO_3 surface. No obvious penetration of the sputtered ITO into the underlying organic layers was observed. Although SEM observations alone cannot provide direct information on the interfacial chemistry, the absence of visible interfacial mixing supports the hypothesis that the 15 nm MoO_3 layer effectively limits sputtering-induced damage during ITO deposition.[207] Having verified that the multilayer architecture remained structurally intact after ITO deposition, the optical properties of the complete device were subsequently investigated.

While the sputtered ITO films exhibited high transparency and conductivity when deposited on glass, these optical and electronic properties had to be assessed on the complete PV stack. **Figure 4-21** compares the transmission spectra of the device before and after deposition of the transparent top electrode.

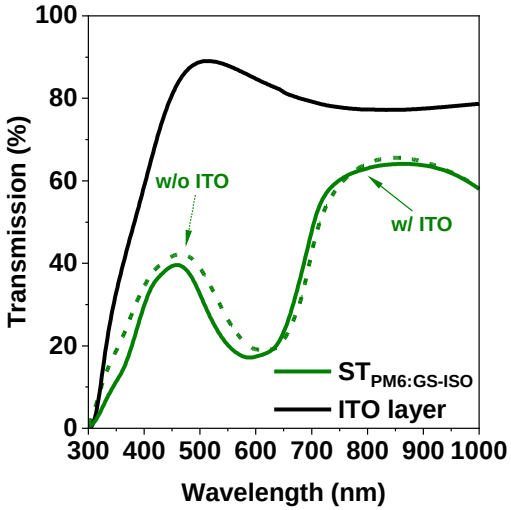

Figure 4-21: *Optical transmittance spectra of $ST_{PM6:GS-ISO}$ devices before and after deposition of the sputtered ITO top electrode.*

Condition	Top Electrode	R_{sheet} ($\Omega.sq^{-1}$)	AVT (%)
$ST_{PM6:GS-ISO}$	No	2×10^5	26
	Yes	38	22

Table 4-7: *Electrical and optical properties of $ST_{PM6:GS-ISO}$ devices before and after deposition of the sputtered ITO top electrode.*

The incomplete PV stack without top electrode (Glass/ITO/ZnO/PM6:GS-ISO/MoO_3) exhibited an *AVT* of 26 %. This low value is naturally expected since the PM6:GS-ISO active layer has a strong absorption in the visible range. The complete ST-OSC including ITO top electrode retained an *AVT* of 22 %. The limited decrease between the two spectra indicates that the introduction of the sputtered ITO layer does not significantly modify the optical transparency of the complete device. In addition, R_{sheet} of the ITO deposited on the PM6:GS-ISO/MoO_3 stack reached 38 $\Omega.sq^{-1}$, which is comparable to the value measured for ITO deposited on glass 53 $\Omega.sq^{-1}$. These results suggest that the MoO_3 interlayer does not hinder the formation of a conductive ITO film during sputtering.

b) Photovoltaic performance

Although the structural and optical characterizations suggest that the sputtered ITO electrode can be successfully integrated into the device architecture, these observations alone cannot demonstrate whether the PV properties of the cells are preserved. The PV performance of the resulting semi-transparent devices ($ST_{PM6:GS-ISO}$) was therefore evaluated under AM1.5G illumination and compared with that of opaque reference devices incorporating a thermally evaporated Ag top electrode ($Ref_{PM6:GS-ISO}$). Photographs and schematic representations of both cells are presented in **Figure 4-22**.

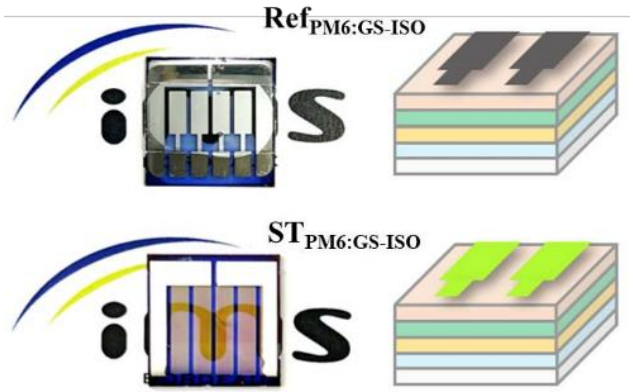

Figure 4-22: *Photograph and schematic architecture of the opaque reference ($Ref_{PM6:GS-ISO}$) and semi-transparent ($ST_{PM6:GS-ISO}$) devices.*

Figure 4-23 presents the *J-V* characteristics measured in the dark and under AM1.5G illumination, as well as EQE measurements, while the corresponding PV parameters are summarized in **Table 4-8**.

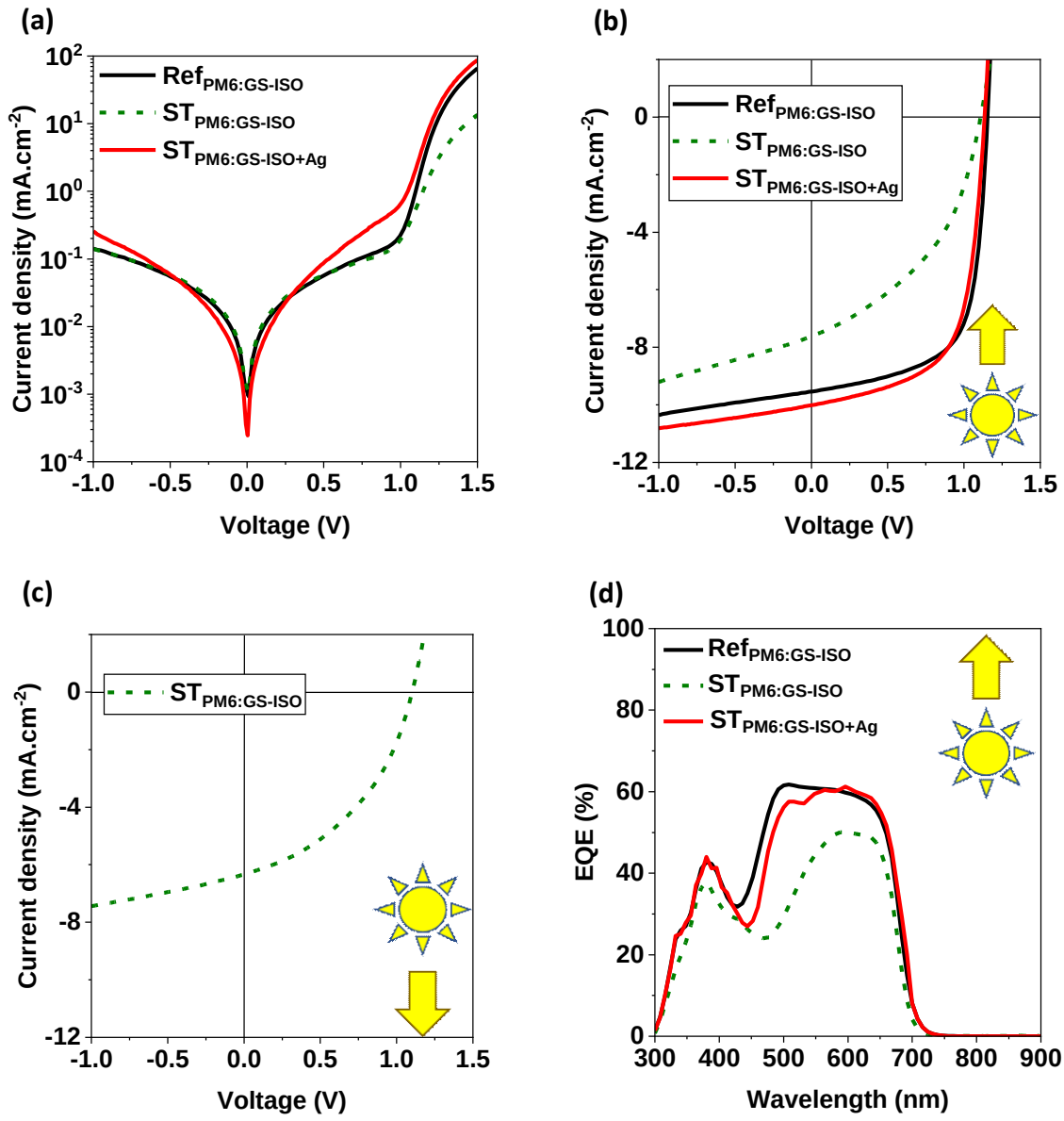

Figure 4-23: *J-V characteristics of $Ref_{PM6:GS-ISO}$, $ST_{PM6:GS-ISO}$ and $ST_{PM6:GS-ISO+Ag}$ (a) in the dark, (b) under AM1.5G for bottom illumination (glass/ITO side) and (c) under AM1.5G for top illumination (ITO/MoO_3 side). (d) Corresponding EQE spectra.*

Device	PCE (%)	$J_{SC}/J_{SC\ int}$ (mA.cm^{-2})	V_{OC} (V)	FF	R_S (Ω)
$Ref_{PM6:GS-ISO}$	7.3	9.9 / 10.0	1.14	0.65	52
$ST_{PM6:GS-ISO}$	3.6	7.6 / 7.4	1.11	0.43	294
$ST_{PM6:GS-ISO+Ag}$	7.2	10.0 / 9.1	1.13	0.63	61

Table 4-8: *PV parameters of $Ref_{PM6:GS-ISO}$, $ST_{PM6:GS-ISO}$, and $ST_{PM6:GS-ISO+Ag}$ devices. J_{SC} was extracted from the illuminated J-V curves, whereas $J_{SC\ int}$ was calculated by integrating the EQE spectrum under the AM1.5G solar spectrum.*

Throughout this section, bottom illumination refers to light entering through the glass/ITO substrate, whereas top illumination corresponds to illumination from the sputtered ITO/MoO_3 side. Under bottom illumination (**Figure 4-23a** and **Figure 4-23b**), the reference opaque device ($Ref_{PM6:GS-ISO}$) exhibited a PCE of 7.3 %, associated with a J_{SC} of 9.9 mA.cm^{-2}, a V_{OC} of 1.14 V and a FF of 0.65. These values are in good agreement with those previously reported for this active layer and device architecture. In comparison, the semi-transparent device ($ST_{PM6:GS-ISO}$) retained a comparable V_{OC} (1.11 V), while the PCE decreased to 3.6 %. This reduction mainly resulted from decreases in both J_{SC} (7.6 mA.cm^{-2}) and FF (0.43).

To better understand the origin of these performance losses, the EQE spectra of the reference and semi-transparent devices were compared. As shown in **Figure 4-23d**, the ST-OSC exhibited a lower photoresponse over the main absorption range of the PM6:GS-ISO blend, particularly between approximately 500 and 650 nm. $J_{SC\ int}$ calculated from the EQE spectra reached 10.0 and 7.4 mA.cm^{-2} for $Ref_{PM6:GS-ISO}$ and $ST_{PM6:GS-ISO}$, respectively, in good agreement with the *J-V* measurements. The lower photocurrent may primarily result from the replacement of the highly reflective Ag electrode by the transparent ITO electrode. In the reference device, the metallic electrode promotes optical confinement through back reflection, increasing the optical path length within the active layer and therefore enhancing photon absorption.[212] In contrast, the transparent ITO electrode allows a fraction of the incident light to leave the device through the rear side instead of being reflected back into the photoactive layer, thereby reducing the effective optical path length and photocurrent generation.

Besides the reduction in photocurrent, the FF also decreased significantly after replacing the Ag electrode by sputtered ITO. The Dark *J-V* characteristics presented in **Figure 4-23a** revealed an increase in R_S from 52 Ω for $Ref_{PM6:GS-ISO}$ to 294 Ω for $ST_{PM6:GS-ISO}$. This increase is likely associated to the higher electrical resistivity of the TCO compared with a

metallic Ag electrode, leading to larger ohmic losses during charge collection.[86] As a consequence, the reduction in FF may therefore originate predominantly from electrical limitations associated with the transparent electrode rather than from irreversible degradation of the photoactive layer.

At this stage, it remained unclear whether the reduced PV performance originated from sputtering-induced damage to the organic layers or simply from the intrinsic optical and electrical limitations of the transparent electrode. To distinguish between these two possibilities, a control experiment was performed by depositing a thermally evaporated Ag electrode directly onto the sputtered ITO layer whithout modifying the previously deposited multilayer stack. This additional metallization was expected to restore the high electrical conductivity and optical reflectivity of the top electrode while preserving the underlying organic layers. As illustrated in **Figure 4-23b** and summarized in **Table 4-8**, the PV performances of these control devices ($ST_{PM6:GS-ISO+Ag}$) recovered values very close to those measured for the opaque reference cells. The FF increased from 0.43 to 0.63, while J_{SC} increased from 7.6 to 10.0 mA.cm^{-2}. Similarly, R_S decreased from 294 to 61 Ω, approaching the value measured for the reference device (52 Ω). The EQE spectra also closely matched those of the opaque reference cell, with a $J_{SC\ int}$ of 9.1 mA.cm^{-2} compared with 10.0 mA.cm^{-2} for $Ref_{PM6:GS-ISO}$. These control experiments provide additional insight into the origin of the performance losses observed in ST-OSC. Since the deposition of a metallic electrode on top of the sputtered ITO largely restores the PV performances, the reduction in efficiency is more likely governed by the optical and electrical characteristics of the transparent electrode than by irreversible sputtering-induced degradation of the organic layers. Moreover, the recovery of both the FF and the photocurrent, together with the preservation of a high V_{OC} and the absence of S-shaped *J-V* characteristics, strongly suggest that the photoactive layer and the MoO_3/ITO interface remain largely preserved following sputtering. These observations therefore are consistent with the hypothesis that the optimized MoO_3 interlayer effectively limits sputtering-induced damage while maintaining efficient charge extraction.

Finally, the PV performances were also evaluated under top illumination through the transparent ITO electrode (**Figure 4-23c**). In this configuration, ST-OSC exhibited a PCE of 2.9 %, with a J_{SC} of 6.3 mA.cm^{-2}, while the V_{OC} and FF remained nearly unchanged compared with bottom illumination. The lower J_{SC} may result from differences in the optical field distribution within the multilayer stack as well as differences in reflective losses depending on whether light enters the device from the glass/ITO side or from the ITO/MoO_3 side.[148,213] In addition, the measured hole-to-electron mobility ratio ($\mu_h/\mu_e \approx 2.2$) may further contribute to the reduced photocurrent under top illumination.[141] Since hole transport is more efficient than electron transport, illumination through the ZnO side is expected to favor charge extraction, whereas illumination through the MoO_3 side requires electrons, the less mobile carriers, to travel longer average distances before collection at the ZnO contact, thereby increasing the probability of recombination. These results suggest that the transparent architecture remains operational under illumination from either side, although the optical asymmetry of the device,

combined with the slight imbalance in charge transport, may lead to different photocurrent generation efficiencies.

c) Electrical limitations and current collection optimization

While the ITO/Ag additional metalization experiment provided valuable insight into the origin of the performance losses, it completely suppressed the semi-transparency of the device and therefore could not be considered as a practical solution. To improve lateral current collection while preserving the semi-transparent architecture, Ag busbars were instead deposited exclusively on the non-photoactive regions of the device (**Figure 4-24**).[141]

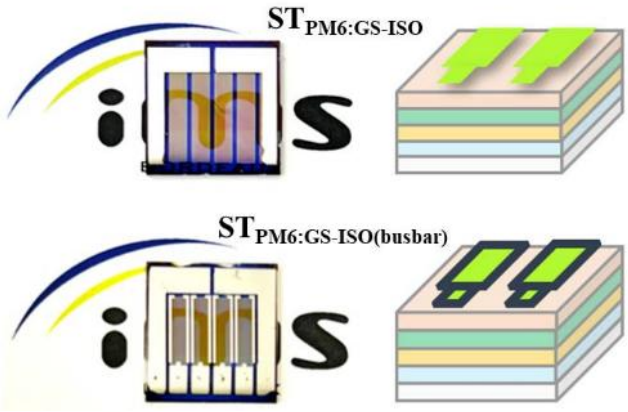

Figure 4-24: *Photograph and schematic architecture of $ST_{PM6:GS-ISO}$ and semi-transparent cell with Ag busbars ($ST_{PM6:GS-ISO(busbars)}$).*

Consequently, neither the dimensions of the photoactive area nor the composition of the PV stack were modified. The active region was kept strictly identical to that of the standard semi-transparent device, allowing the influence of the busbars on the electrical behavior of the transparent electrode to be evaluated independently from any change in light-harvesting area or active layer architecture. This strategy was designed to reduce the lateral resistance of the sputtered ITO electrode by shortening the current collection path while maintaining the optical aperture of the photoactive region.[214] As shown in **Table 4-9**, the introduction of Ag busbars resulted in a significant improvement in the PV performances.

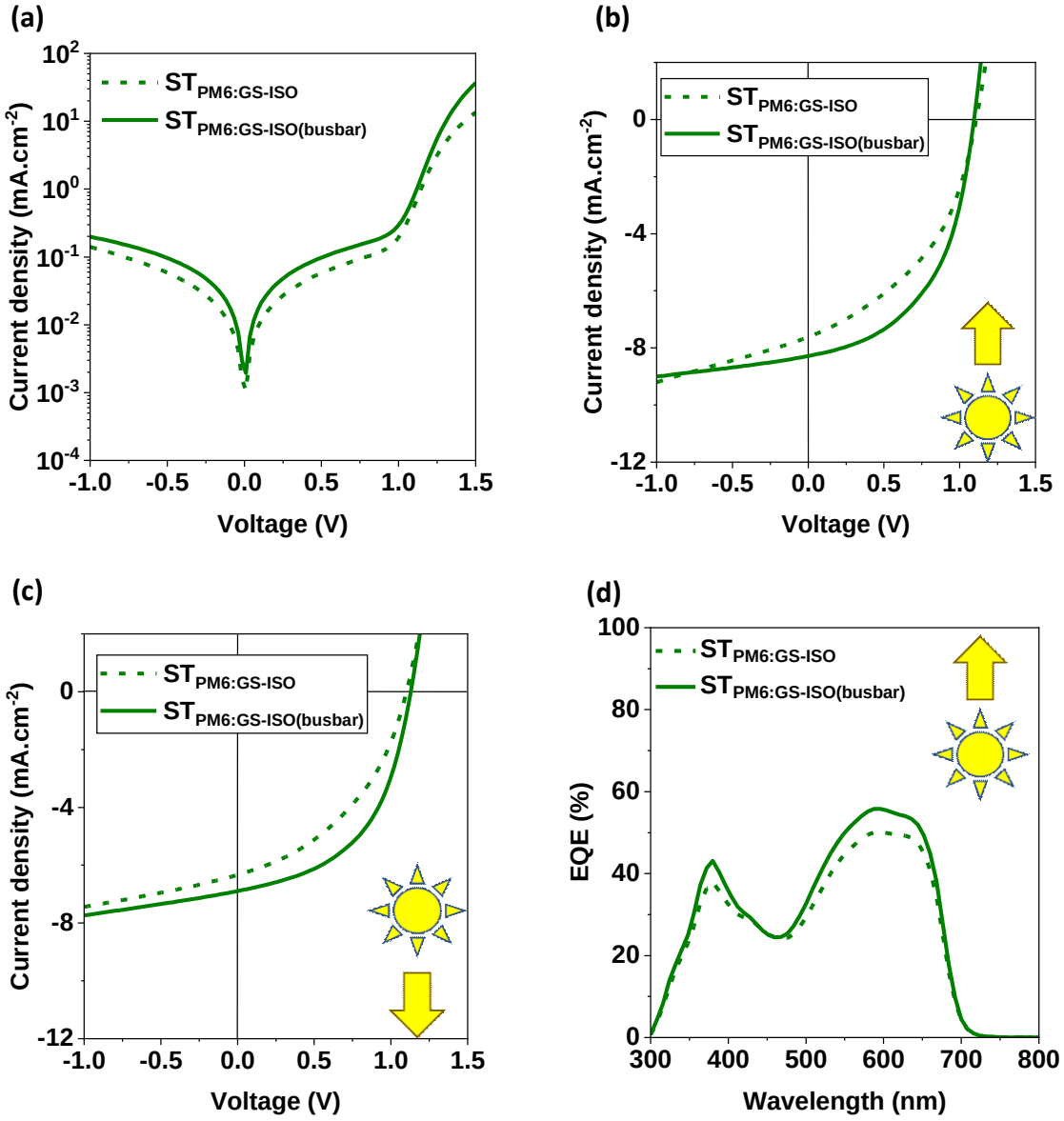

Figure 4-25: *J-V characteristics of $ST_{PM6:GS-ISO}$, and $ST_{PM6:GS-ISO(busbar)}$: (a) in the dark, (b) under AM1.5G for bottom illumination (glass/ITO side), and (c) under AM1.5G for top illumination (ITO/MoO_3 side). (d) Corresponding EQE spectra.*

Device	Illumination	PCE (%)	J_{SC} (mA.cm^{-2})	V_{OC} (V)	FF	R_S (Ω)
$Ref_{PM6:GS-ISO}$	Bottom	7.3 ± 0.2	9.9 ± 0.4	1.14 ± 0.01	0.65 ± 0.01	52
$ST_{PM6:GS-ISO}$	Bottom	3.6 ± 0.2	7.6 ± 0.4	1.11 ± 0.01	0.43 ± 0.01	294
	Top	2.9 ± 0.2	6.3 ± 0.3	1.10 ± 0.01	0.42 ± 0.01	350
$ST_{PM6:GS-ISO(busbar)}$	Bottom	4.6 ± 0.1	8.3 ± 0.4	1.09 ± 0.01	0.51 ± 0.01	200
	Top	4.0 ± 0.2	6.9 ± 0.3	1.13 ± 0.01	0.51 ± 0.01	260

Table 4-9: *PV parameters of $Ref_{PM6:GS-ISO}$, $ST_{PM6:GS-ISO}$, and $ST_{PM6:GS-ISO(busbars)}$ devices.*

Under bottom illumination, PCE increased from 3.6 to 4.6 %, while FF increases from 0.43 to 0.51 (**Figure 4-25b**). Similar improvements are obtained under top illumination, for which the PCE increases from 2.9 to 4.0 % (**Figure 4-25c**). In both illumination configurations, V_{OC} remains close to 1.1 V, indicating that the additional current-collecting lines deposited outside the photoactive area do not significantly modify the electronic properties of the PV junction. Instead, the improvement in device performance may mainly result from enhanced charge collection associated with the lower lateral resistance of the transparent electrode.[214]

The predominantly electrical origin of this improvement is further supported by the dark *J-V* characteristics (**Figure 4-25a**) and EQE measurements (**Figure 4-25d**). Following the introduction of the Ag busbars, R_S decreases from 294 to 200 Ω, while the $J_{SC\ int}$ derived from the EQE spectra increases from 7.4 to 8.1 mA.cm^{-2}. In contrast, the spectral shape and the absorption onset remain almost unchanged. These observations suggest that the performance enhancement may mainly originate from improved lateral charge collection resulting from the lower R_{sheet} of the transparent electrode rather than from modifications of the optical absorption of the active layer. Although the introduction of Ag busbars does not fully recover the performances of the opaque reference devices, it significantly improves the compromise between optical transparency and PV performance without modifying the photoactive area of the device.

Overall, these results demonstrate that optimizing the current collection geometry constitutes an effective strategy for partially compensating the electrical limitations associated with transparent ITO electrodes while preserving the semi-transparent architecture. Owing to this improved balance between transparency and PV performance,

these devices were selected for the operational stability study presented in the following section.

4.3.2 Operational stability

Although the optimized ST-OSC demonstrated promising PV performances, its long-term operational stability remained an equally important criterion for assessing the suitability of the sputtered ITO top electrode. The optimized architecture was therefore subjected to accelerated ageing under continuous AM1.5G illumination (1000 $W \cdot m^{-2}$) following the ISOS-L-2 protocol with maximum power point tracking over 200 h.[215] The evolution of the PV parameters was monitored to determine whether the integration of the sputtered ITO electrode affected the long-term behavior of ST-OSC.

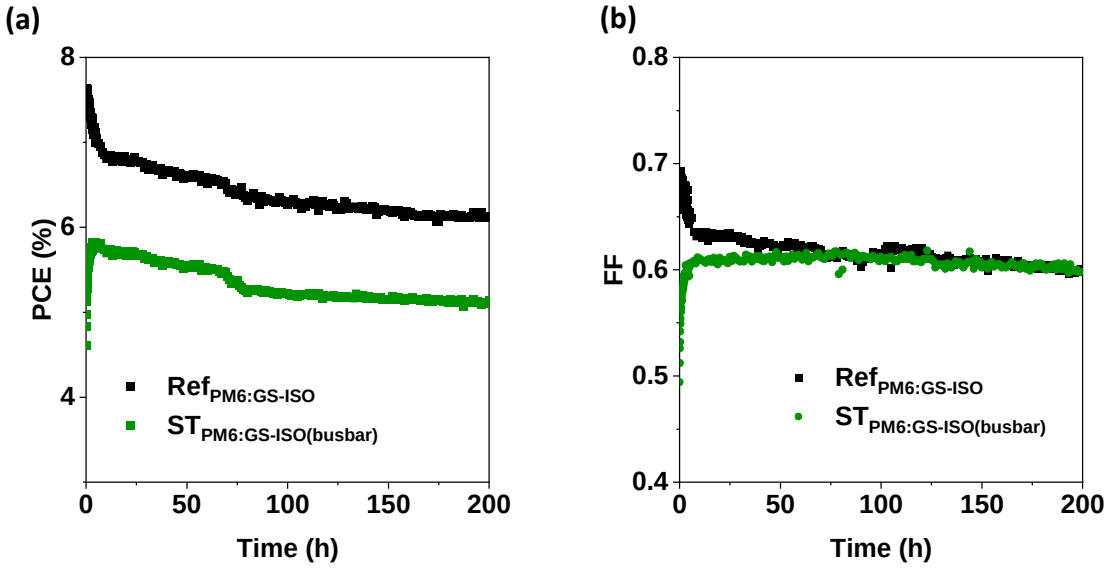

Figure 4-26: *Evolution of (a) PCE and (b) FF of $Ref_{PM6:GS-ISO}$ and $ST_{PM6:GS-ISO(busbar)}$ during operational stability testing.*

The evolution of PCE and FF during the ageing test is presented in **Figure 4-26a** and **Figure 4-26b**. Unexpectedly, the optimized semi-transparent devices did not exhibit the monotonic degradation typically expected for OSC under continuous operation. Instead, an initial improvement in PV performance was observed before the devices reached a stable operating regime. Between t_{0h} and t_{200h}, the PCE of the reference device decreases by approximately 25 %, whereas the ST device exhibits an increase of about 12 %. A similar trend is observed for the FF, which decreases by around 15 % for the reference OSC but increases by approximately 22 % for the ST-OSC.

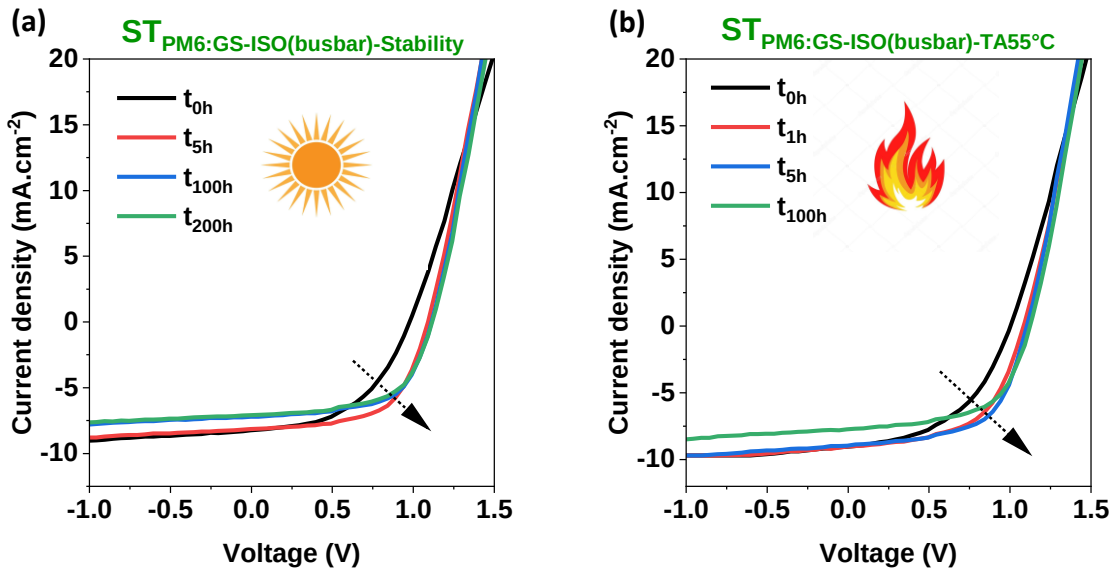

Figure 4-27: *Evolution of the J-V characteristics of $ST_{PM6:GS-ISO(busbar)}$ after (a) continuous AM1.5 G illumination and (b) thermal annealing at 55°C.*

A closer examination of the *J-V* characteristics recorded during the ageing test (**Figure 4-27a**) indicates that most of this apparent improvement occurs during the first five hours of operation. During this initial conditioning period, the R_S decreases markedly from 250 Ω to 156 Ω, while the FF increases from 0.48 to 0.58. Simultaneously, the V_{OC} rises from 1.03 V to 1.12 V before stabilizing. Consequently, the device reaches a maximum PCE of 5.8 % after only 5 h of continuous illumination, after which the PV parameters remain essentially unchanged throughout the remainder of the ageing test.

Device	Illumination	PCE	J_{SC} (mA.cm^{-2})	V_{OC} (V)	FF	R_S (Ω)
$ST_{PM6:GS-ISO(busbar)}$	Bottom	4.6 ± 0.1	8.3 ± 0.4	1.09 ± 0.01	0.51 ± 0.01	250
	Top	4.0 ± 0.2	6.9 ± 0.3	1.13 ± 0.01	0.51 ± 0.01	280
$ST_{PM6:GS-ISO(busbar)\ Stability}$ at t_{5h}	Bottom	5.8	9.0	1.12	0.58	156
$ST_{PM6:GS-ISO(busbar)\ TA55°C}$ at t_{5h}	Bottom	5.9	8.9	1.10	0.60	149

Table 4-10: *PV parameters of $ST_{PM6:GS-ISO(busbars)}$ devices at t_{0h}, t_{5h} and t_{5h} after a 55°C thermal annealing.*

The PV parameters measured after 5 h are summarized in **Table 4-10**, giving a PCE of 5.8 %, a J_{SC} of 9.0 mA·cm^{-2}, a V_{OC} of 1.12 V and a FF of 0.58. Since the stability measurements were performed while the device temperature was maintained around 55 °C in the setup, the initial performance enhancement could originate from an intrinsic thermal annealing of the complete device rather than from a genuine light-soaking effect.

To test this hypothesis, identical ST-OSC were annealed on a hot plate at 55 °C and characterized after 0, 1, 5 and 100 h. The corresponding *J-V* characteristics are shown in **Figure 4-27b**. The evolution closely matches that observed during the operational stability test. Indeed, the R_S decreases from 227 Ω to 149 Ω, while the FF increases from 0.48 to 0.60 and the V_{OC} from 1.03 V to 1.10 V. The excellent agreement between both experiments strongly suggests that the initial improvement observed under continuous illumination is primarily driven by thermal annealing of the device. The close agreement between both experiments further supports this hypothesis as illustred in the **Table 4-10**. After 5 h of thermal annealing, the ST-OSC reaches a PCE of 5.9 %, together with a J_{SC} of 8.9 mA·cm^{-2}, a V_{OC} of 1.10 V and a FF of 0.60, values that are remarkably close to those obtained after 5 h of continuous illumination.

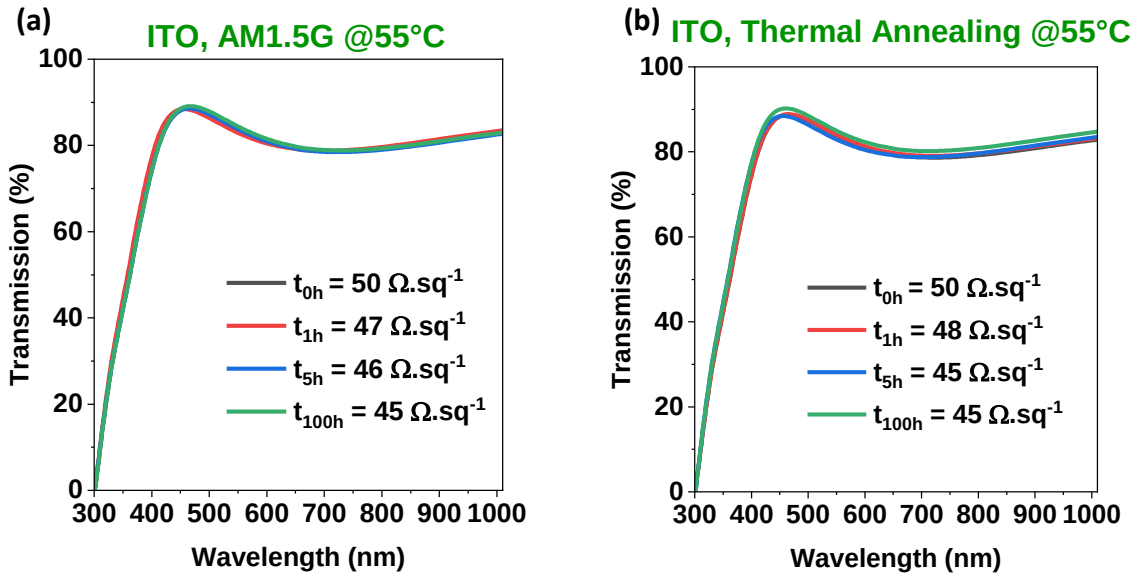

Figure 4-28: *Optical transmittance spectra and corresponding R_{Sheet} values of sputtered ITO films after (a) continuous AM1.5G illumination and (b) thermal annealing at 55°C after 0, 1, 5 and 100 h.*

To determine whether the performance enhancement could originate from modifications of the sputtered ITO electrode itself, additional control experiments were carried out on standalone sputtered ITO layers deposited on glass. The optical transmission spectra and R_{sheet} were measured for devices exposed to a continuous AM1.5G illumination at 55 °C (**Figure 4-28a**) and for devices exposed to a thermal annealing treatment at the same temperature (**Figure 4-28b**). For both treatments, the transmission spectra remain essentially unchanged throughout the visible spectral range, indicating that the optical properties of the transparent electrode are preserved during the treatments. Similarly, only a slight decrease in R_{sheet} is observed, from approximately 50 to 45 Ω·sq^{-1} after 100 h, indicating that the electrical properties of the sputtered ITO electrode remain largely unchanged during the treatments. Since the transparent electrode itself undergoes only negligible changes during both treatments, the observed performance enhancement most likely originates from the multilayer device stack rather than from the ITO electrode itself.

The reduction in series resistance (R_S) may be associated with an improvement of the electrical contact at the MoO_3/ITO interface, leading to lower contact resistance (R_C) and more efficient charge extraction.[216] The simultaneous increase in V_{OC} may result from an interfacial reorganization reducing non-radiative recombination losses.[217] Taken together, these observations suggest that the initial increase in device performance originates from a progressive electrical stabilization of the MoO_3/ITO top contact rather than from modifications of the sputtered ITO layer itself. Although the exact microscopic mechanisms remain to be elucidated, the very good agreement between the illumination and thermal annealing experiments strongly supports a thermally activated interfacial reorganization within the upper contact stack.

Overall, these results demonstrate that the optimized ST-OSC exhibit excellent operational stability while benefiting from a thermal self-conditioning process during the first hours of operation. Following this initial stabilization period, the PV performances remain essentially unchanged over the remainder of the 200 h ageing test, further supporting the suitability of the optimized MoO_3/ITO top contact for semi-transparent OSC.

Key Point 4.3.1 & 4.3.2: Integration of the optimized transparent electrode into PM6:GS-ISO.

The introduction of a 15 nm MoO_3 protective layer enabled the successful integration of room-temperature sputtered ITO electrodes into PM6:GS-ISO ST-OSC, while Ag busbars effectively mitigated current collection losses associated with the transparent electrode. In addition, the devices exhibited improved operational stability together with a thermally induced performance enhancement, highlighting the robustness of the proposed transparent electrode architecture.

4.3.3 Transferability toward emerging photoactive systems

The previous sections demonstrated the successful integration of the optimized sputtered ITO transparent top electrode using PM6:GS-ISO as a model photoactive system. Although these results establish the feasibility of the proposed integration strategy, they do not demonstrate whether it is specific to PM6:GS-ISO or can be extended to emerging OPV systems exhibiting different optical and electronic properties.

To assess the transferability of the optimized transparent electrode, two complementary photoactive blends were selected. The first, PTQ10:FCC-Cl, is a WBG system exhibiting an E_g^{opt} of 1.71 eV, corresponding to the FCC-Cl acceptor material.[218] Owing to its WBG, this blend is considered as a promising candidate for the top cell of tandem PV architectures. The second, PTB7-Th:IEICO-4F is a LBG system with an E_g^{opt} close to 1.31 eV, corresponding to the IEICO-4F acceptor material, extending its absorption well into the near-infrared region.[219] Such spectral characteristics make this blend particularly attractive for semi-transparent agrivoltaic applications, where harvesting a larger fraction of the near-

infrared solar spectrum while maintaining partial transmission of the visible wavelengths could be advantageous.[220]

Both photoactive blends were originally developed at the Institut de Ciència de Materials de Barcelona (ICMAB) by Prof. Campoy-Quiles' group for scalable blade-coated OSC. In the present work, these material systems were adapted to a laboratory-scale spin-coated architecture in order to establish opaque reference devices before integrating the optimized transparent top electrode developed throughout this thesis. This experimental strategy enables the influence of the transparent electrode to be evaluated independently of any modification to its fabrication process.

a) Opaque reference devices

Figure 4-29 compares the energy level of each material and the optical absorption spectra of the optimized spin-coated PTQ10:FCC-Cl and PTB7-Th:IEICO-4F active layers.

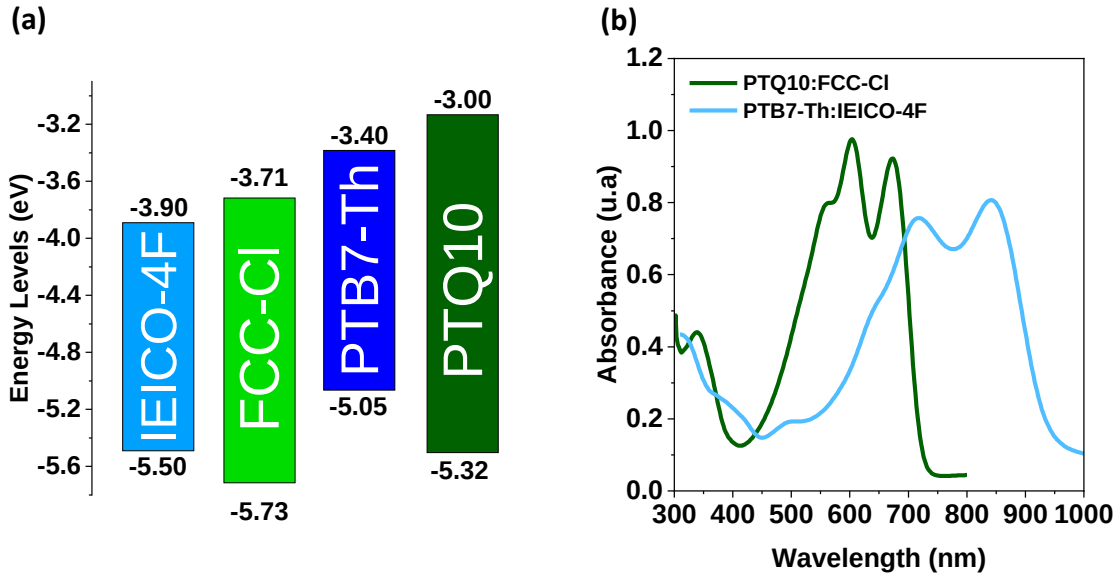

Figure 4-29: *(a) Energy level diagram of PTQ10, PTB7-Th, FCC-Cl and IEICO-4F. (b) Optical absorption spectra of PTQ10:FCC-Cl and PTB7-Th:IEICO-4F active layers.*

As expected for a WBG absorber, PTQ10:FCC-Cl absorbs predominantly throughout the visible spectral range, with a sharp absorption edge around 700 nm.[221] Such an absorption profile is particularly well suited for tandem PV architectures, where photons at longer wavelengths must be transmitted towards the bottom sub-cell. In contrast, PTB7-Th:IEICO-4F exhibits a significantly broader absorption window extending from the visible to nearly 1000 nm owing to its lower optical bandgap.[219] This broader spectral response accounts for its substantially larger photocurrent generation capability and highlights the complementary nature of these two photoactive systems.

Following optimization of the spin-coated active layers, opaque reference devices exhibiting PV performances in good agreement with those previously reported for the blade-

coated architecture were successfully obtained.[218] *J-V* characteristics are reported in **Figure 4-30a** and **Figure 4-30b**. Results are summarized in **Table 4-11**.

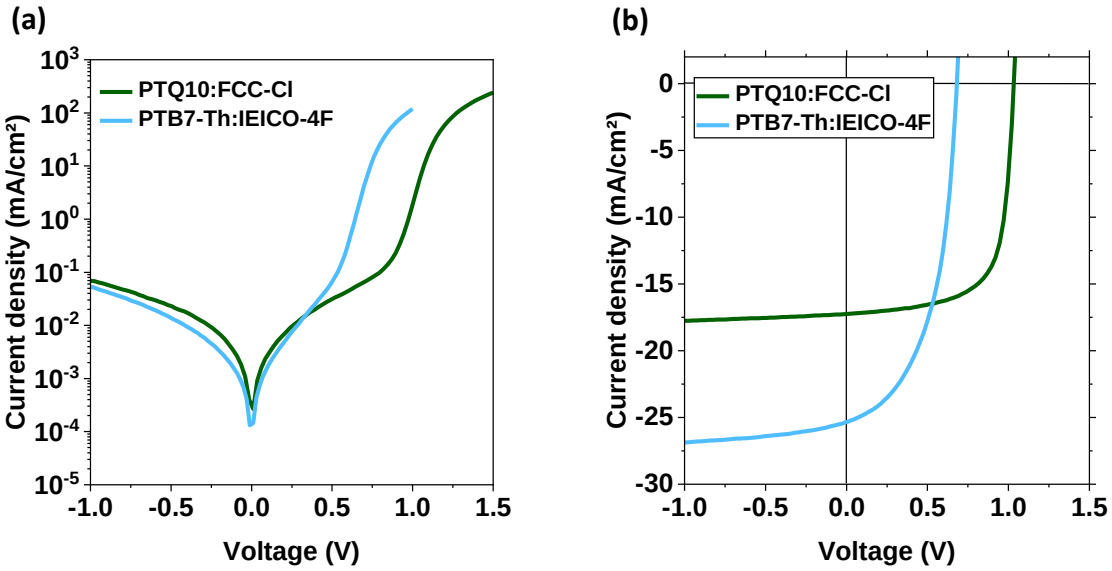

Figure 4-30: *J-V characteristics of PTQ10:FCC-Cl and PTB7-Th:IEICO-4F: (a) in the dark and (b) under AM1.5G.*

Device	Thickness (nm)	PCE (%)	J_{SC} / $J_{SC\ int}$ (mA.cm^{-2})	V_{OC} (V)	FF	R_S (Ω)
PTQ10:FCC-Cl	150	12.1 ± 0.3	17.0 ± 0.5 13.7	1.03 ± 0.01	0.69 ± 0.01	37
PTB7-Th:IEICO-4F	110	8.5 ± 0.2	24.4 ± 0.5 21.7	0.68 ± 0.01	0.51 ± 0.01	38

Table 4-11: *PV parameters of opaque PTQ10:FCC-Cl and PTB7-Th devices.*

The optimized active-layer thicknesses were found to be approximately 150 nm for PTQ10:FCC-Cl and 110 nm for PTB7-Th:IEICO-4F, reflecting the different optical and charge-transport requirements of the two material systems.

The PTQ10:FCC-Cl devices reached a PCE of 12.1 %, with a V_{OC} of 1.03 V, a J_{SC} of 17.0 mA.cm^{-2} and a FF of 0.69. These values are consistent with the expected behavior of high-

performance WBG OSC, where the larger optical bandgap promotes high photovoltage while limiting the achievable photocurrent.[141] Conversely, the PTB7-Th:IEICO-4F opaque devices exhibited a lower V_{OC} of 0.68 V but a substantially larger J_{SC} of 24.4 mA.cm^{-2} owing to their extended absorption into the near-infrared region. Despite a lower FF of 0.51, the devices still achieved a PCE of 8.5 %, thereby providing a suitable opaque reference for evaluating the integration of the transparent top electrode. The corresponding EQE spectra closely follow the absorption characteristics of both photoactive blends (**Figure 4-31**).

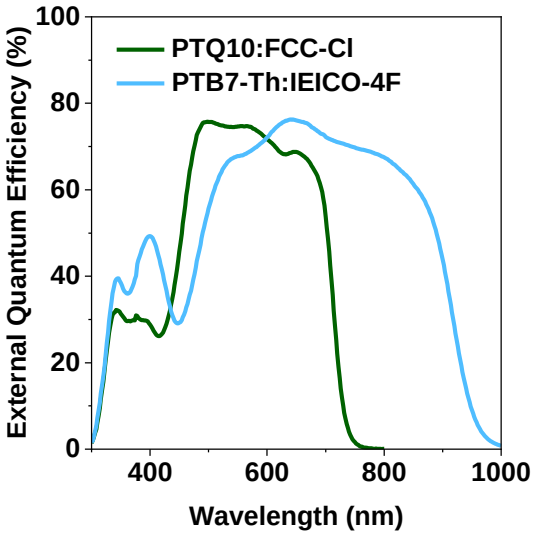

Figure 4-31: *EQE spectra of optimized PTQ10:FCC-Cl and PTB7-Th solar cells.*

The EQE spectra closely reproduce the optical absorption profiles of both active layers. PTQ10:FCC-Cl exhibits a broad photoresponse between approximately 400 and 700 nm, with maximum EQE values approaching 75 %, whereas PTB7-Th:IEICO-4F extends its photoresponse well into the near-infrared region while maintaining maximum EQE values of approximately 70-75 %. These complementary spectral responses are consistent with the intended applications of both systems. Moreover, the $J_{SC\ int}$ remain in good agreement with those extracted from the *J-V* characteristics, confirming that the optimized spin-coated devices exhibit the expected photoresponse of each active layer.

Having established opaque reference devices exhibiting the expected PV and optical characteristics, the optimized ITO transparent top electrode developed throughout this work was subsequently integrated following the identical integration procedure previously optimized for PM6:GS-ISO.[222] No modification of either the sputtering parameters, the MoO_3 thickness or the device architecture was introduced, allowing the transferability of the proposed transparent electrode integration strategy to be directly assessed.

b) Semi-transparent devices

The optical and electrical properties of the resulting ST-OSC (without busbar) are summarized in **Figure 4-32**.

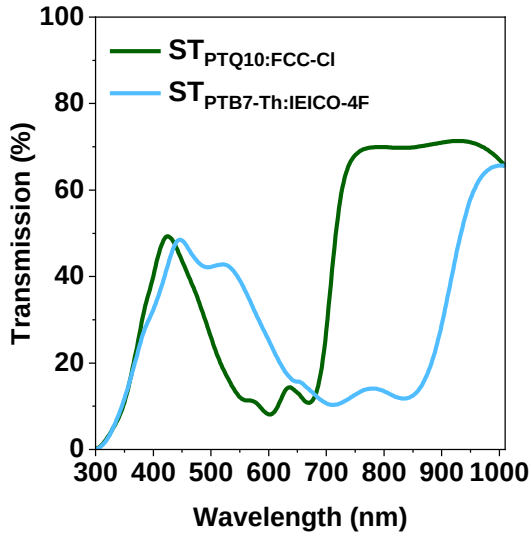

Figure 4-32: *Optical transmittance spectra of $ST_{PTQ10:FCC-Cl}$ and $ST_{PTB7-Th:IEICO-4F}$ incorporating the optimized sputtered ITO top electrode.*

Device	R_{sheet} ($\Omega.sq^{-1}$)	*AVT* (%)
$ST_{PTQ10:FCC-Cl}$	15	14
$ST_{PTB7-Th:IEICO-4F}$	17	34

Table 4-12: *Electrical and optical properties of $ST_{PTQ10:FCC-Cl}$ and $ST_{PTB7-Th:IEICO-4F}$ devices.*

The optical transmittance of the resulting ST-OSC is primarily governed by the absorption profile of the photoactive layers. As shown in **Table 4-12**, the $ST_{PTQ10:FCC-Cl}$ device exhibits an *AVT* of 14 %, consistent with its strong absorption across the visible spectrum of the active layer. Conversely, the $ST_{PTB7-Th:IEICO-4F}$ device reaches an *AVT* of 34 %, more than twice that of the PTQ10:FCC-Cl architecture, owing to its reduced absorption over a significant fraction of the visible region despite its strong near-infrared absorption. The more than twofold increase in *AVT* from PTQ10:FCC-Cl (14 %) to PTB7-Th:IEICO-4F (34 %) further illustrates how the transparency of the complete device is predominantly dictated by the absorption profile of the photoactive layer rather than by the transparent electrode itself.[223] Despite these pronounced differences in optical behavior, both devices exhibit similarly low R_{sheet} values of approximately 15-17 $\Omega \cdot sq^{-1}$. Interestingly, these values are lower than the approximately 38 $\Omega \cdot sq^{-1}$ previously measured for the PM6:GS-ISO-based ST-OSC. This lower

R_{sheet} is also accompanied by a reduction in the R_S of the complete devices, from approximately 52 Ω for PM6:GS-ISO to 37-38 Ω for the PTQ10:FCC-Cl and PTB7-Th:IEICO-4F devices. Although this correlation suggests an overall improvement in the electrical properties of the newly investigated devices, the R_S results from the combined contributions of the electrodes, transport layers, active layer, and interfaces, and therefore cannot be directly used to identify the origin of the lower R_{sheet}. Nevertheless, the similar R_{sheet} values obtained for the two newly investigated blends indicate that the optimized sputtered ITO electrode maintains good electrical conductivity when integrated with both photoactive systems. Consequently, the sputtering process appears to be compatible with photoactive layers exhibiting markedly different compositions and optoelectronic properties, while providing a low-resistance transparent top electrode suitable for efficient charge collection.

The PV performances of the resulting ST-OSC are presented in **Figure 4-33.**

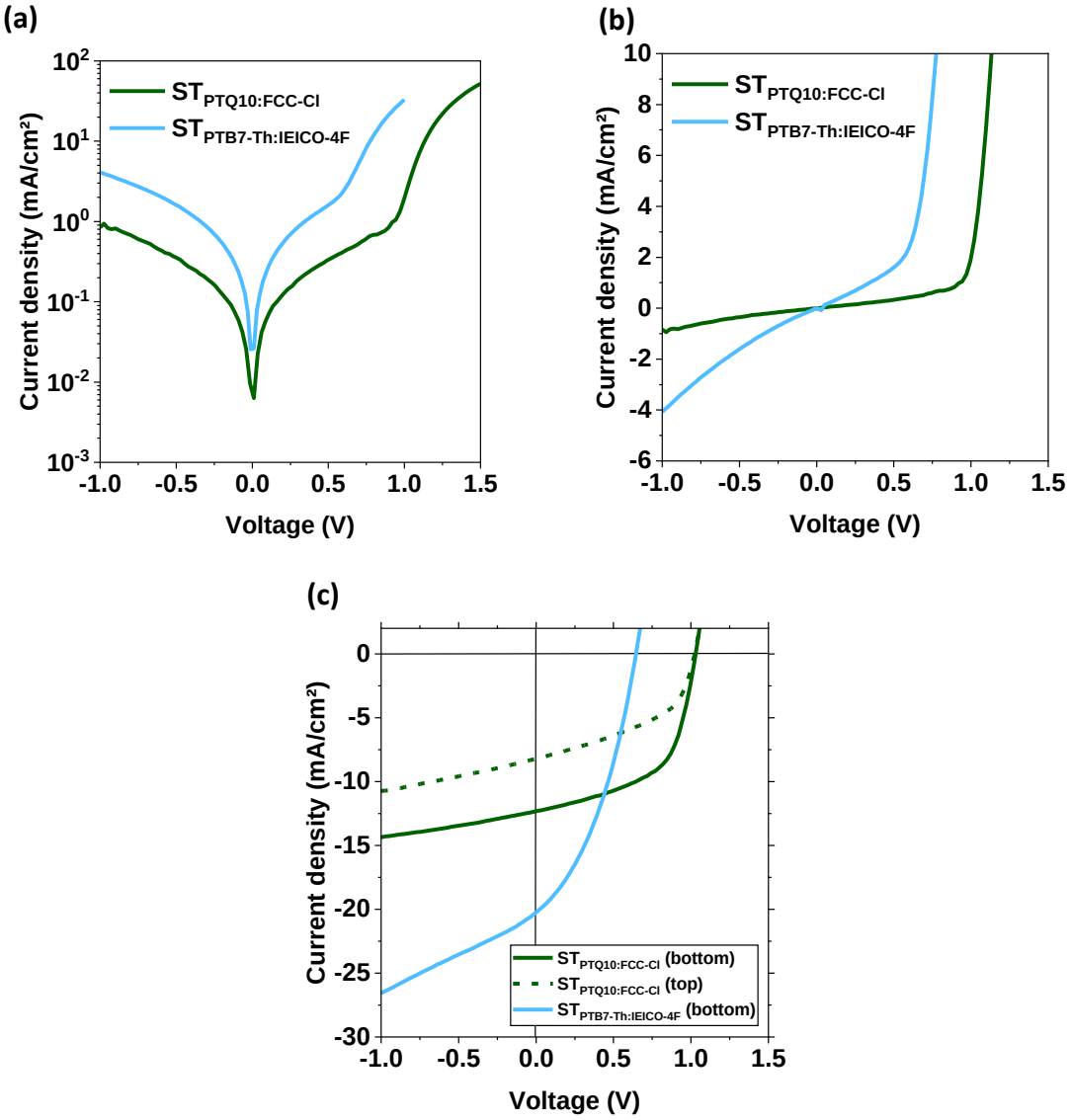

Figure 4-33: *J-V characteristics of $ST_{PTQ10:FCC-Cl}$, and $ST_{PTB7-Th:IEICO-4F}$: (a) in the dark (logarithmic), (b) in the dark (linear), and (c) under AM1.5G for bottom illumination (glass/ITO side) and top illumination (ITO/MoO_3 side).*

Device	Illumination	PCE (%)	J_{SC} / $J_{SC\ int}$ (mA.cm^{-2})	V_{OC} (V)	FF	R_S (Ω)
$ST_{PTQ10:FCC-Cl}$	Bottom	7.1 ± 0.3	12.3 ± 0.3 / 9.3	1.03 ± 0.01	0.56 ± 0.01	123
	Top	4.0 ± 0.4	8.4 ± 0.4	1.02 ± 0.01	0.46 ± 0.01	170
$ST_{PTB7-Th:IEICO-4F}$	Bottom	5.0 ± 0.2	20.2 ± 0.5 / 15.9	0.65 ± 0.01	0.38 ± 0.02	126

Table 4-13: *PV parameters of $ST_{PTQ10:FCC-Cl}$, $ST_{PTB7-Th:IEICO-4F}$ devices.*

Following integration of the transparent top electrode, both material systems remained fully operational, confirming the robustness of the proposed integration strategy. As shown in **Table 4-13**, the $ST_{PTQ10:FCC-Cl}$ device delivered a PCE of 7.1 % under bottom illumination, corresponding to a J_{SC} of 12.3 mA.cm^{-2}, while preserving a V_{OC} of 1.03 V. The FF decreased from 0.69 to 0.56, consistent with the increase in R_S associated with the transparent top electrode.[86] Under top illumination, the same device remained operational, yielding a PCE of 4.0 %, with a J_{SC} of 8.4 mA.cm^{-2} and a V_{OC} remaining essentially unchanged at 1.02 V. This ability to operate under both bottom and top illumination confirms the suitability of this architecture for tandem PV applications. The $ST_{PTB7-Th:IEICO-4F}$ device also remained fully functional after ITO deposition, reaching a PCE of 5.0 %, together with a J_{SC} of 20.2 mA.cm^{-2}, a V_{OC} of 0.65 V and a FF of 0.38 %. Although these performances remain below those of the opaque reference device, they demonstrate that the optimized transparent electrode remains compatible with LBG PV systems exhibiting markedly different electronic and optical properties. The linear-scale dark *J-V* characteristics provide further insight into the electrical limitations of the transparent devices (**Figure 4-33b**). A more pronounced reverse-bias leakage current is observed for the $ST_{PTB7-Th:IEICO-4F}$ device, reaching approximately -4 mA.cm^{-2} at -1 V, compared with approximately -1 mA.cm^{-2} for the $ST_{PTQ10:FCC-Cl}$ device. This behavior indicates a stronger parasitic leakage pathway in the PTB7-Th:IEICO-4F device. Such leakage may originate from imperfect electrical isolation or local shunt pathways within the transparent device architecture, although its specific origin could not be determined from the present

measurements. The more pronounced leakage current, combined with the relatively high R_S of 126 Ω, is consistent with the low FF of 0.38 observed for the $ST_{PTB7\text{-}Th:IEICO\text{-}4F}$ device. In comparison, the $ST_{PTQ10:FCC\text{-}Cl}$ device exhibits substantially lower leakage currents, although its R_S remains similarly equivalent (123 Ω), indicating that the difference in FF between the two devices cannot be attributed solely to R_S. Overall, the reduced PCE of the transparent devices can therefore be attributed to the combined effect of several electrical losses. In particular, the relatively high R_S and the pronounced leakage currents contribute to the degradation of the FF, while the reduced J_{SC} compared with the corresponding opaque devices further limits the achievable PCE. These results indicate that further optimization of the transparent device architecture should focus on minimizing parasitic leakage pathways and reducing R_S while maintaining sufficient optical transparency.

The EQE spectra remain fully consistent with the characteristic absorption windows of both photoactive systems (**Figure 4-34**).

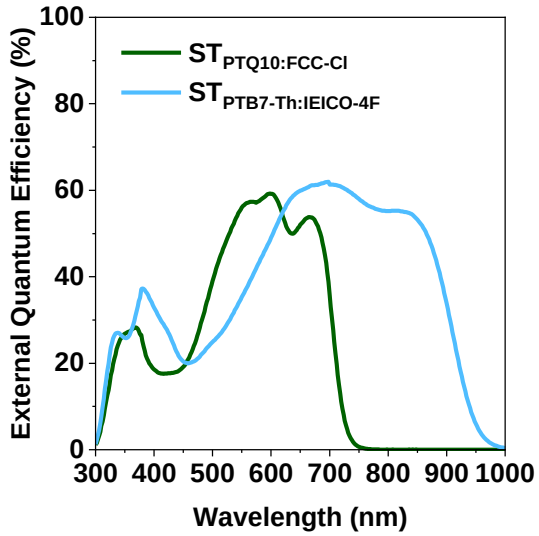

Figure 4-34: *EQE spectra of $ST_{PTQ10:FCC\text{-}Cl}$ and $ST_{PTB7\text{-}Th:IEICO\text{-}4F}$ devices.*

While the overall EQE decrease following the integration of the transparent electrode, the characteristic spectral shapes remain largely preserved. Moreover, the $J_{SC\ int}$ follow the same trends as those extracted from the *J-V* measurements, confirming that the integration of the optimized transparent electrode preserves the fundamental photoresponse of both photoactive blends.

Overall, these results demonstrate that the optimized transparent electrode developed throughout this work can be successfully transferred to photoactive systems spanning a broad range of optical bandgaps without requiring any modification of the integration process. Beyond the specific material systems investigated here, this result demonstrates the robustness and versatility of the proposed room-temperature ITO integration strategy, considerably extending its potential for future ST-OSC technologies targeting tandem PV and light-transmitting energy-harvesting applications.

4.4. Conclusion of Chapter 4

This chapter addressed one of the major technological challenges limiting the development of ST-OSC: the fabrication of a transparent top electrode combining high optical transparency, low electrical resistance and full compatibility with sensitive organic semiconductor stacks. To address this challenge, three transparent electrode technologies were systematically investigated, optimized and compared before their integration into complete PV devices.

Thermally evaporated MoO_3/Ag/MoO_3 electrodes demonstrated that continuous ultrathin metallic films can provide low R_{sheet} while remaining compatible with inverted OSC architectures. However, their optical transparency remained intrinsically limited by the unavoidable trade-off between electrical conductivity and optical transmission.

In contrast, both screen-printed and spin-coated Ag-NWs electrodes exhibited excellent optoelectronic properties, achieving *AVT* above 90 % together with low R_{sheet}. Nevertheless, despite successful optimization of the deposition and laser-patterning processes, their integration into complete ST-OSC was ultimately prevented by insufficient patterning resolution and the formation of vertical short circuits, respectively. These results demonstrate that excellent optoelectronic properties alone are insufficient and highlight the importance of considering process compatibility and device integration constraints during transparent electrode development.

Among the investigated technologies, room-temperature RF-sputtered ITO emerged as the most suitable transparent electrode by successfully combining high conductivity, good optical transparency and full compatibility with the OPV fabrication process. Optimization of the sputtering conditions yielded conductive and highly transparent ITO films deposited without exceeding the thermal limitations imposed by the organic layers, while the introduction of a 15 nm MoO_3 interlayer efficiently protected the underlying multilayer stack against sputtering-induced damage. The resulting ST-OSC achieved a balanced compromise between optical transparency and photovoltaic performance. Furthermore, the implementation of Ag busbars significantly reduced current-collection losses associated with the transparent electrode, while long-term stability experiments demonstrated that the optimized MoO_3/ITO top contact remained robust under prolonged operation.

Finally, the successful integration of the optimized transparent electrode into two emerging photoactive systems exhibiting markedly different optical bandgaps demonstrated that the proposed integration strategy is not restricted to a single donor-acceptor blend. The absence of any re-optimization of the sputtering process or device architecture highlights the robustness and transferability of the developed approach, considerably broadening its potential for future tandem photovoltaic and other light-transmitting PV applications.

Overall, this chapter demonstrates that the development of high-performance transparent electrodes for OPV cannot rely solely on maximizing their optoelectronic properties. Instead, successful implementation requires simultaneously addressing material performance, process compatibility and device integration. Beyond the optimization of a

single transparent electrode, this work establishes a general methodology for integrating transparent conductive contacts into OPV devices without compromising their electrical or PV functionality. The robust and transferable room-temperature ITO integration strategy established in this chapter provides the technological foundation for the tandem PV architectures investigated in the following chapter.

Chapter 5
Organic/Silicon Tandem Solar Cells

5.1. Introduction

The previous chapters of this manuscript were devoted to the development and optimization of the key technological building blocks required for the realization of an OPV/Si tandem solar cell. **Chapter 3** focused on the optimization of a WBG inverted OSC based on the PM6:GS-ISO active layer, leading to devices combining high V_{OC} with improved PCE. **Chapter 4** subsequently addressed the development of ST-OSC through the optimization of a room-temperature sputtered ITO top electrode, resulting in transparent devices suitable for tandem PV applications. Together, these developments established the technological foundations required for integrating an organic top cell with a c-Si bottom cell. Although the organic top cell and the semi-transparent electrode have been independently optimized in the previous chapters, their integration onto a high-efficiency silicon bottom cell introduces new technological challenges that cannot be addressed by considering each component separately.

The next stage of this work consists of integrating these independently optimized components into complete hybrid PV architectures. This integration represents considerably more than the simple superposition of two PV devices. It requires the development of a common technological platform that ensures electrical compatibility, optical transparency, and process compatibility between the Si and organic sub-cells, while preserving the high performance previously achieved for each individual device.[78] Within the framework of the ORGANIST project, IBC c-Si solar cells were selected as the bottom PV technology. As introduced in **Chapter 1**, the absence of front-side metallic contacts makes this architecture particularly attractive for tandem integration, since the illuminated surface remains entirely available for the deposition of the OPV stack. In addition, the high efficiencies routinely achieved by IBC solar cells make them ideal bottom-cell candidates for hybrid OPV/Si tandem solar cells.[37]

The first objective of this chapter is to establish a complete technological route for the monolithic integration of ST-OSC onto IBC Si bottom cells. The Si bottom cells employed throughout this work are first introduced, with particular emphasis on the evolution of their front-side architecture toward a configuration specifically designed for tandem integration. The development of the transparent conductive interfacial layer connecting the OPV and Si sub-cells is then presented, followed by the fabrication and characterization of a monolithic 3T OPV/Si tandem solar cell. Although the complete tandem device could not be fully characterized due to technological limitations, the different stages of the integration process are detailed and experimentally investigated, providing a comprehensive assessment of the developed integration strategy. Finally, this chapter broadens the scope of the study by investigating an alternative tandem strategy based on the RAINBOW concept. Instead of vertically stacking the PV junctions, this approach relies on spectral splitting and laterally distributed sub-cells, thereby eliminating current-matching constraints while maintaining spectral complementarity between the organic and Si absorbers. Numerical simulations together with experimental validation are presented to assess the potential of this original

architecture for future hybrid OPV/Si tandem solar cells. Overall, this chapter presents the final developments to fabricate an OPV/Si tandem device based on all the results presented in the previous chapters.

5.2. IBC silicon bottom cells for hybrid OPV/Si tandem integration

5.2.1 Motivation for using IBC silicon solar cells

The choice of the Si bottom cell is a critical step in the development of monolithic OPV/Si tandem solar cells. Among the various c-Si architectures currently available, IBC solar cells are particularly attractive because all electrical contacts are located on the rear side of the device. Consequently, the illuminated front surface is entirely free of metallic shading, thereby maximizing light absorption while providing an unobstructed surface for the subsequent deposition of the OPV stack. Within the framework of the ORGANIST project, the fabrication of the hybrid OPV/Si tandem devices was distributed between several research laboratories according to their respective expertise. The IBC Si bottom cells were fabricated at ISC Konstanz (International Solar Energy Research Center), subsequently received in GeePs (Laboratoire de Génie Electrique et Electronique de Paris), modified through front-side surface engineering at LPICM (Laboratoire de Physique des Interfaces et des Couches Minces), and finally transferred to IMS Bordeaux, where the OPV stack was deposited. This collaborative work required the development of fabrication processes fully compatible with the technological constraints of each partner while preserving the electrical performance of the Si bottom cell throughout the successive processing steps.

Although all IBC cells share the same rear-contact architecture, two successive generations were developed in ISC Konstanz and used during the project. Their main difference lies in the design of the illuminated front surface, which plays a crucial role in the subsequent tandem integration process. The evolution of this front-side architecture is therefore particularly relevant for the present work and is discussed in the following section.

5.2.2 Evolution of the IBC architecture: from Generation 1 to Generation 2

Two generations of IBC Si solar cells were investigated during this work, and their architectures are presented schematically in **Figure 5-1**.

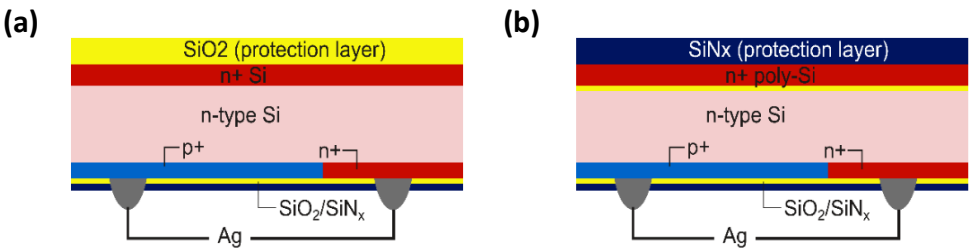

Figure 5-1: *Cross-sectional schematics of the two generations of IBC silicon solar cells investigated in this work: (a) Gen1 incorporating a phosphorus-diffused front surface field and (b) Gen2 incorporating a TOPCon-like n^+ poly-Si/SiO_2 passivating contact.*

While both devices share the same interdigitated rear-contact architecture, they differ significantly in the design of their illuminated front surface. The first-generation device (IBC-Gen1) incorporates a conventional phosphorus-diffused front surface field (FSF) covered by a SiO_2 protective layer. In this configuration, the diffused n^+ region generates an electric field that repels minority carriers away from the front surface, thereby reducing surface recombination. However, the quality of the front-side passivation strongly relies on the presence of the dielectric SiO_2 layer deposited on top of the diffused emitter. More importantly, this architecture presents a major limitation for monolithic tandem integration due to the presence of the thick insulating layer. Indeed, since the transparent conductive interfacial layer must be deposited directly onto the silicon surface, the front dielectric layer must be removed prior to the subsequent tandem processing steps, or be sufficiently thin to allow charges to be injected into the silicon sub-cell. Because the SiO_2 layer is electrically insulating, its presence would prevent efficient electrical contact and charge transfer between the silicon surface and the transparent conductive interfacial layer. The removal of this dielectric layer significantly deteriorates the front-surface passivation, leading to an increased density of interface recombination centers and consequently to enhanced carrier recombination. As a result, the electrical performance of the Si bottom cell is substantially degraded, particularly through a reduction of the V_{OC}. The effect of this front-side SiO_2 protective-layer removal is particularly pronounced for IBC-Gen1. Measurements performed by ISC Konstanz showed an initial V_{OC} of 700 mV for IBC-Gen1 with the SiO_2 capping layer, and a V_{OC} of 620 mV after etching of the capping layer, representing a loss of 80 mV.

A second generation of IBC cells (IBC-Gen2) was subsequently developed with a different front-side passivation architecture. In this architecture, the conventional diffused front surface field is replaced by a TOPCon-like passivating contact consisting of a heavily doped n^+ polycrystalline silicon layer deposited on an ultrathin SiO_2 tunnel oxide. Unlike the Gen1 architecture, the passivation mechanism is intrinsically provided by the poly-Si/SiO_2 stack itself. In Gen1, the front-side SiO_2 layer plays a key role in surface passivation, whereas in Gen2 the passivation is provided by the underlying SiO_2/poly-Si contact and the SiN_x layer primarily acts as a protective capping layer. The ultrathin SiO_2 layer provides chemical passivation of the silicon surface while remaining sufficiently thin to enable majority-carrier tunnelling. Combined with the heavily doped poly-Si layer, it forms a passivating contact that simultaneously minimizes recombination losses and ensures efficient carrier transport. The thickness of the n^+ poly-Si layer was optimized during the development of Gen2. Lifetime samples with 20 nm and 50 nm-thick poly-Si layers were investigated. The 20 nm layer yielded an implied V_{OC} of 725 mV, whereas the 50 nm layer provided superior passivation, with an implied V_{OC} as high as 740 mV. This value is near upper limit achievable with n^+ poly-Si tunnel junction obtained on thicker poly-Si layers and therefore the thickness was not further increased. Furthermore, a thicker poly-Si layer would have a negative absorption effect on the IBC cells. The final Gen2 structure therefore consists of an n-type c-Si wafer with a thickness of 140 ± 10 µm. On the front side, an approximately 1.5 nm-thick SiO_2 tunnel oxide is combined with a 50 nm-thick n^+ poly-Si layer to form the passivating contact. On the rear side, a dielectric

stack composed of approximately 20 ± 5 nm of SiO_2 and 70-100 nm of SiN_x provides surface passivation and contributes to rear-side optical reflection. The Gen2 fabrication process also involved an increase in cell size, from 14.3 × 14.3 mm² for Gen1 subcells to approximately 21.8 × 21.8 mm² in the Gen2 process developed by ISC Konstanz. The corresponding geometrical area is approximately 4.75 cm². This increase reduces the relative contribution of edge recombination and improves process stability. Measurements performed by ISC Konstanz showed that the IBC-Gen2 cells exhibited an initial V_{OC} of 710 mV with the protective SiN_x capping layer, which decreased to 680 mV after etching of the protective layer, corresponding to a loss of approximately 30 mV. This relatively small V_{OC} reduction further demonstrates the robustness of the Gen2 passivating-contact architecture to the surface preparation required for tandem integration.

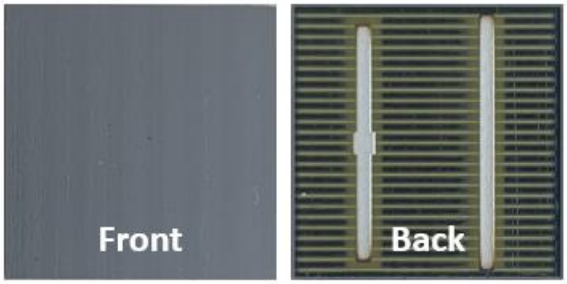

Figure 5-2: *Photographs of the front and rear surfaces of the IBC-Gen2 solar cell used in this work.*

The front and rear surfaces of the Gen2 cell are shown in **Figure 5-2**. The front side is dedicated to light absorption and subsequent tandem integration, while the rear side contains the interdigitated electrical contacts characteristic of the IBC architecture. The absence of front-side metal contacts allows the entire illuminated surface to remain available for optical transmission and deposition of the top-cell stack. The front surface morphology also needs to be considered when describing the cells used for tandem integration. The Gen2 IBC technology was developed for integration processes requiring a flat front surface. The cells considered for the tandem integration featured a flat, untextured illuminated surface, allowing the subsequent deposition of the OPV stack. The initial PCE values measured for the cells received for the present work (without protective layer) were approximately 7.4 % for Gen1 and 11 % for Gen2, respectively. These values provide the reference performance of the two IBC generations before the subsequent processing steps associated with their integration into the different tandem architectures.

It is therefore important to distinguish the fabrication of the IBC bottom cell from its preparation for monolithic tandem integration. Additional processing steps are required between the delivery of the IBC cells by ISC Konstanz and the deposition of the OPV top cell. For the Gen2 cells used in this work, ISC Konstanz performed the removal of the front-side SiN_x capping layer before shipment to the partner laboratories. This significantly simplified the subsequent integration process, as the cells could be directly subjected to the additional surface engineering step at LPICM.

In contrast to the monolithic tandem architecture, the lateral RAINBOW concept does not require direct deposition of the OPV stack onto the silicon surface. The two photovoltaic components are spatially separated, and the silicon front surface does not need to be prepared for direct deposition of the OPV stack. Consequently, removal of the front-side protective layer is not required for the RAINBOW configuration. Both Gen1 and Gen2 IBC cells were therefore considered for the RAINBOW concept, allowing the influence of the different silicon front-side architectures to be investigated. Overall, Gen2 was selected for the monolithic OPV/Si tandem integration because of its improved robustness to protective-layer removal and its compatibility with the preparation sequence implemented in this work. Both Gen1 and Gen2 were also considered for the RAINBOW architecture, which is discussed separately later in this chapter.

5.2.3 Front-side engineering and electrical validation of the IBC bottom cells

The selection of Gen2 as the silicon bottom-cell architecture was based not only on its improved robustness to the removal of the front-side protective layer, but also on the possibility of implementing an additional passivation and transparent conductive interface prior to OPV deposition. Before proceeding to the integration of the organic top cell, the impact of these front-side processing steps on the electrical performance of the IBC bottom cell was therefore investigated.

a) Development and validation of the front-side treatment

Before integrating the OPV stack onto the Si bottom cell, it is essential to verify that the additional processing steps required for tandem fabrication do not compromise the performance of the Si device. Ideally, the implementation of the interfacial architecture should preserve, or even improve, the PV characteristics of the bottom cell.

For this purpose, several IBC cells were ordered and electrically characterized at LPICM. A first reference device was measured after removal of the original front dielectric layer, corresponding to an unpassivated Si surface. A second one incorporated a nanocrystalline silicon oxide (nc-SiO_x) layer with a thickness of approximately 70 nm, acting as an additional front-side layer. Such layers are widely employed in high-efficiency Si solar cells because they simultaneously provide chemical passivation of Si dangling bonds and field-effect passivation, thereby significantly reducing carrier recombination at the Si surface. [36] Finally, an ITO layer was deposited by magnetron sputtering on top of this passivating contact in order to reproduce the final configuration intended for the monolithic tandem device. The PV performances of these different architectures were evaluated by *J-V* measurements (**Figure 5-3**) and are summarized in **Table 5-1**.

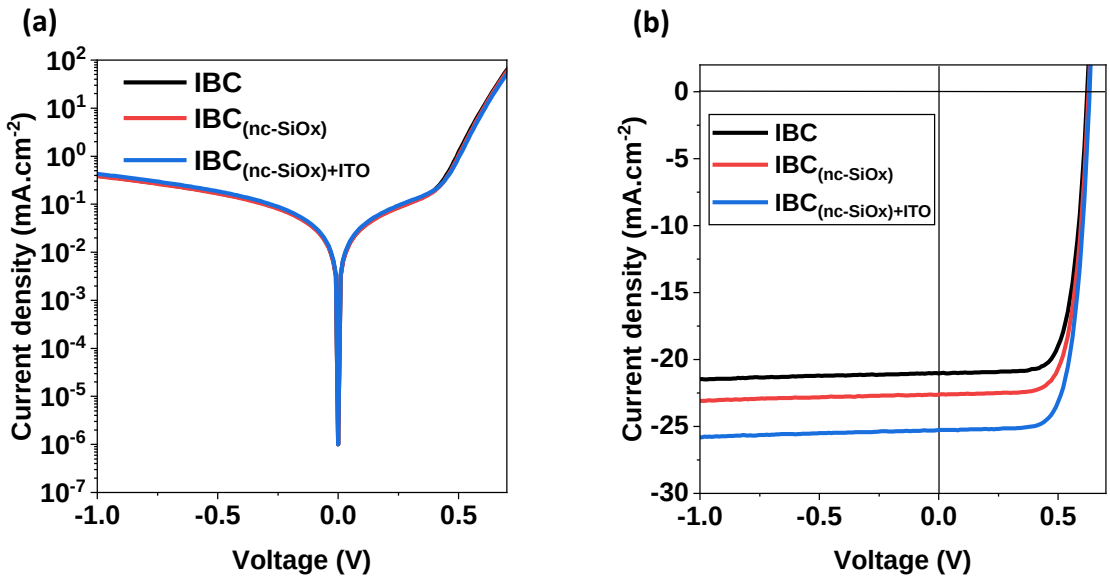

Figure 5-3: *J-V characteristics of IBC, $IBC_{(a\text{-}Si:H/nc\text{-}SiOx)}$, and $IBC_{(nc\text{-}SiOx)+ITO}$: (a) in the dark and (b) under AM1.5G.*

Device	PCE (%)	J_{SC} (mA.cm^{-2})	V_{OC} (V)	FF
IBC	9.5	21.0	0.62	0.73
$IBC_{(nc\text{-}SiOx)}$	10.4	22.6	0.63	0.73
$IBC_{(nc\text{-}SiOx)+ITO}$	11.8	25.3	0.64	0.73

Table 5-1: *PV parameters of the different IBC silicon bottom-cell architectures before and after deposition of the passivating contact and transparent conductive ITO layer.*

The results clearly demonstrate the beneficial effect of the successive front-side modifications. The deposition of the nc-SiO_x passivating contact leads to only a slight increase in the V_{OC}, indicating limited improvement in front-side passivation. More importantly, the subsequent deposition of the ITO conductive layer does not degrade the PV characteristics of the Si device. On the contrary, the PCE increases from 10.4 % to 11.8 %, mainly owing to an increase in J_{SC}. This enhancement could be attributed to the additional antireflective effect of the ITO layer, which improves light coupling into the Si absorber.[224] Overall, these results demonstrate that the proposed interfacial architecture is compatible with the Si bottom cell while simultaneously improving its PV performance.

b) Validation of the received IBC-Gen2 silicon bottom cells

Following the validation of the front-side engineering and ITO architecture, the Gen2 IBC cells prepared for the final integration were characterized at IMS Bordeaux. These measurements provided the reference electrical performance of the Si bottom cells immediately before OPV deposition and allowed the reproducibility of the PV characterization

between GeePs and IMS Bordeaux to be assessed. This initial characterization established a reference for evaluating the impact of the subsequent OPV integration steps on the Si bottom-cell performance.

The Gen2 IBC Si solar cells were received from LPICM with their front-side passivating contact and transparent ITO interfacial layer already deposited. As described in the previous section, the illuminated surface consisted of an nc-SiO_x passivating contact coated with a sputtered ITO layer, providing the transparent conductive interface required for the subsequent integration of the OPV stack.

Figure 5-4 presents the experimental setup used at IMS Bordeaux to characterize the received IBC Si bottom cells under AM1.5G illumination. The measurements were performed using a dedicated sample holder equipped with two magnetic probes for electrical contacting of the IBC device. The cell was mechanically fixed within the holder, while two electrical probes were used to contact the rear-side electrodes of the device. The front side remained exposed to the incident illumination during the measurement. The sample holder was specifically adapted to IBC cells, for which the electrical contacts are located exclusively on the rear side. The design minimizes obstruction of the illuminated surface while ensuring mechanical stability and reproducible electrical contact during the measurement.

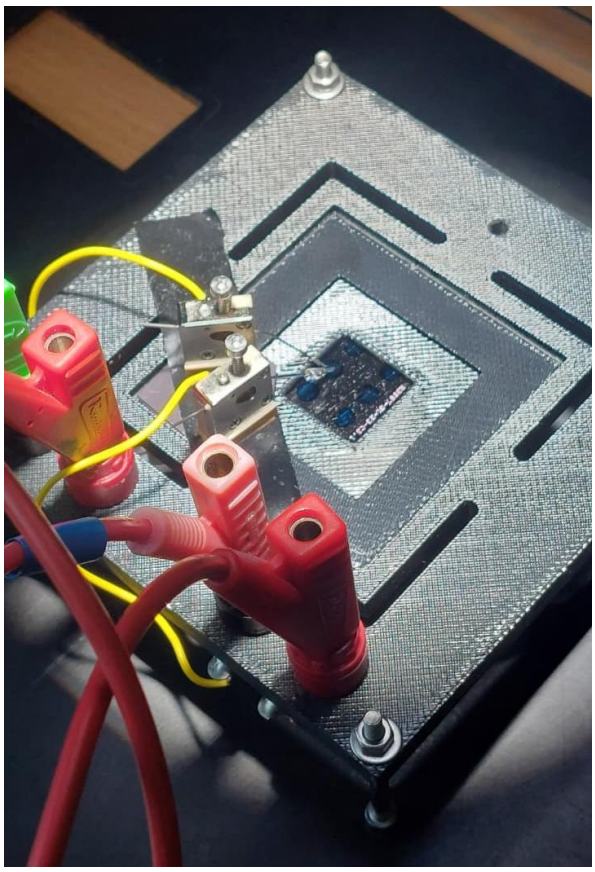

Figure 5-4: *Experimental setup developed at GeePs and used at IMS Bordeaux for the photovoltaic characterization of the received* $IBC_{(nc\text{-}SiOx)+ITO}$ *bottom cells under AM1.5G illumination. The setup includes a dedicated sample holder, two electrical probes contacting the rear side IBC electrodes and two additional probes contacting the front surface, which remains exposed to illumination.*

Each device was characterized at IMS Bordeaux under AM1.5G illumination using a calibrated solar simulator, and the measured *J-V* characteristics were compared with those previously obtained at GeePs. This comparison was performed to evaluate the reproducibility of the PV characterization and to verify that no significant degradation had occurred during transportation or handling.

The *J-V* characteristics measured at GeePs and IMS Bordeaux are compared in **Figure 5-5**, while the corresponding PV parameters are summarized in **Table 5-2**.

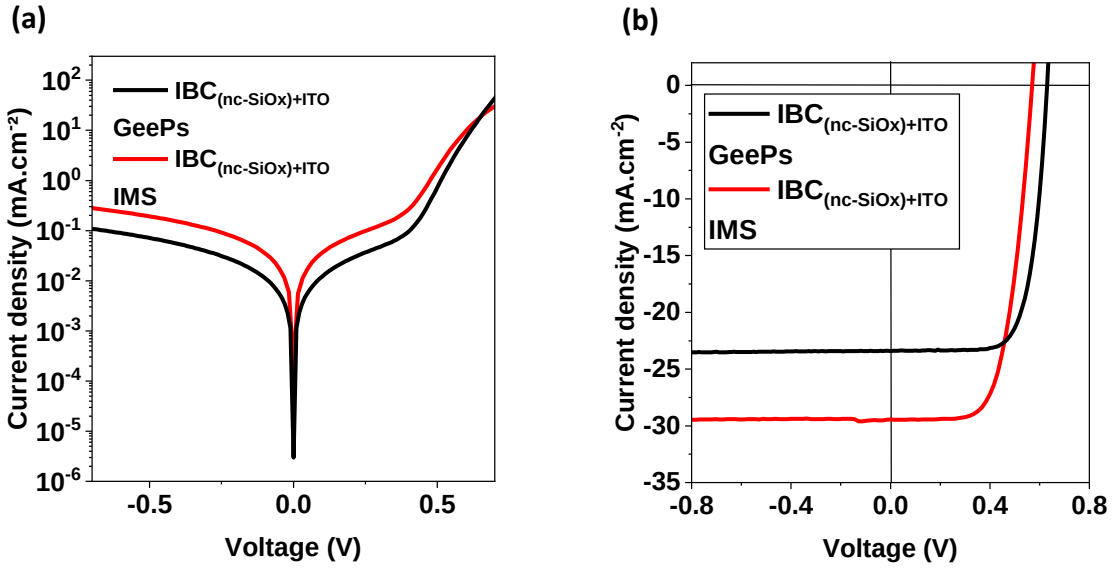

Figure 5-5: *J-V characteristics of $IBC_{(nc\text{-}SiOx)+ITO}$ tested in GeePs and $IBC_{(nc\text{-}SiOx)+ITO}$ tested in IMS: (a) in the dark and (b) under AM1.5G.*

Device	PCE (%)	J_{SC} (mA.cm^{-2})	V_{OC} (V)	FF
$IBC_{(nc\text{-}SiOx)+ITO}$ (GeePs)	11.8	25.3	0.64	0.73
$IBC_{(nc\text{-}SiOx)+ITO}$ (IMS)	11.0	29.5	0.57	0.65

Table 5-2: *PV parameters of the Gen2 IBC silicon bottom cells measured at GeePs and IMS Bordeaux after transportation between the two laboratories.*

Although the overall PCE remains relatively close between the two measurements, noticeable differences are observed in the individual photovoltaic parameters. The J_{SC} increases from 25.3 to 29.5 mA.cm^{-2}, while the V_{OC} decreases from 0.64 to 0.57 V and the FF decreases from 0.73 to 0.65. In particular, the variations observed in V_{OC} and FF are substantial and cannot be considered negligible. At this stage, the origin of these differences is not yet fully understood, and investigations are ongoing to determine whether they arise from differences in solar-simulator calibration, illumination intensity, contacting conditions, or

measurement protocols between the two laboratories. Consequently, these differences cannot currently be unambiguously attributed either to device degradation during transportation or to measurement-related effects.

Nevertheless, the devices retain a good overall photovoltaic performance, demonstrating the robustness of the Gen2 IBC Si bottom cells with respect to time, transportation, and handling. They can therefore be considered reliable substrates for the subsequent fabrication of monolithic OPV/Si tandem cells. Having established the initial performance of the Gen2 bottom cells and validated the front-side layer/ITO architecture, the next step was to assess whether this interface could support the deposition and operation of the organic top cell.

5.3. Development and integration of the interfacial architecture for monolithic OPV/Si tandem cells

5.3.1 Requirements and selection of the interfacial layer

The front-side engineering and ITO architecture introduced and electrically validated in the previous section must now be considered from the perspective of the complete monolithic tandem integration. In particular, the transparent conductive interfacial layer must fulfil several electrical, optical, and technological requirements. Beyond simply providing an electrical connection, this layer plays a central role in the operation of the tandem device and therefore represents one of the key elements of the overall architecture.[225]

Several requirements must be fulfilled by this interfacial layer. First, it must efficiently collect the electrons photogenerated in the organic top cell. The extracted electrons must then be transferred to the Si bottom cell with minimal resistive losses in order to preserve the overall electrical performance of the tandem device. As the interfacial layer lies directly in the optical path, it must also exhibit high optical transparency to maximize photon transmission toward the silicon absorber. Finally, from a technological point of view, the interfacial layer must remain compatible with both the fabrication processes developed at LPICM for the preparation of the Si bottom cells and the processing sequence employed at IMS Bordeaux for the fabrication of the organic top cell.

Among the different TCO commonly employed in PV devices, ITO was selected as the most suitable candidate. This choice was primarily motivated by the work presented in **Chapter 3** and **Chapter 4**, where ITO was successfully employed as the transparent bottom electrode of the optimized inverted OSC.[141,222] Its compatibility with the ZnO ETL, the organic active layer, and the overall device architecture has therefore already been demonstrated, ensuring appropriate energy-level alignment and efficient electron extraction. Furthermore, since the IBC bottom cells were fabricated at ISC Konstanz, transferred to LPICM for front-side engineering, and finally sent to IMS Bordeaux for organic deposition, the possibility of depositing the ITO layer directly at LPICM before shipment considerably simplified the fabrication workflow while ensuring technological compatibility between the two laboratories. In parallel, AZO was investigated as an alternative TCO for the Si/OPV interface.

The objective was to determine whether the integration of the OPV stack onto the silicon substrate could also be achieved using a TCO other than ITO, thereby assessing the compatibility of the OPV deposition process with different transparent conductive interfacial layers. AZO was selected in particular because its deposition process is well established at LPICM, where it can be implemented using the same technological infrastructure available for the preparation of the Si-based substrates. The comparison between ITO and AZO therefore provides an additional validation of the general compatibility of TCO-based interfacial architectures with the subsequent OPV processing.

The following sections therefore focus on the compatibility of this interfacial architecture with the organic photovoltaic stack, from the initial deposition studies to the subsequent scale-up toward the dimensions of the IBC bottom cells.

5.3.2 Compatibility with the organic photovoltaic stack

Although the previous results demonstrate the compatibility of the selected interfacial layer with the Si bottom cell, it remains necessary to verify that this modified surface also allows the successful fabrication of the OPV stack. This verification is particularly important because, unlike the commercial glass/ITO substrates used for the reference OSC devices presented in the previous chapters, the TCO layers used in the present architecture (ITO or AZO) are deposited by RF magnetron sputtering at LPICM directly onto the Si-based substrate. The surface properties of the resulting Si-based substrate/TCO interface may therefore differ from those of the standard glass/ITO substrates. Because complete IBC Si solar cells are expensive prototypes, all preliminary process-development studies were carried out on heavily doped n^+ Si substrates instead of complete IBC devices. These substrates provide an electrically conductive surface while considerably reducing the cost associated with process development.

As a first step, the compatibility of the OPV deposition process with different TCO-based interfacial architectures was investigated using two candidate TCO, namely ITO and AZO. The objective was to determine whether the integration of the organic stack onto the Si substrate could be achieved independently of the nature of the underlying transparent conductive layer. P3HT:PCBM was selected for these preliminary experiments as a benchmark system because of its well-established and highly reproducible processing, as well as the low cost and easy preparation of its constituent materials. With a relative wide bandgap of approximately 1.9 eV and typical PCE in the 3-4 % range, this system provides a convenient reference for evaluating the compatibility of the different Si/TCO interfaces before using the more technologically advanced PM6:GS-ISO system developed throughout this thesis.[226]

Following the deposition of the TCO layer (50 nm), the ZnO ETL (40 nm) was deposited by spin-coating directly onto the respective TCO surfaces, following the bottom-interface architecture of the inverted OSC optimized in **Chapter 3**. Since the morphology of the subsequently deposited organic active layer strongly depends on the wetting properties of the underlying surface, the wettability of the TCO/ZnO stack was first evaluated by contact-angle measurements using the P3HT:PCBM active-layer solutions (**Figure 5-6**).

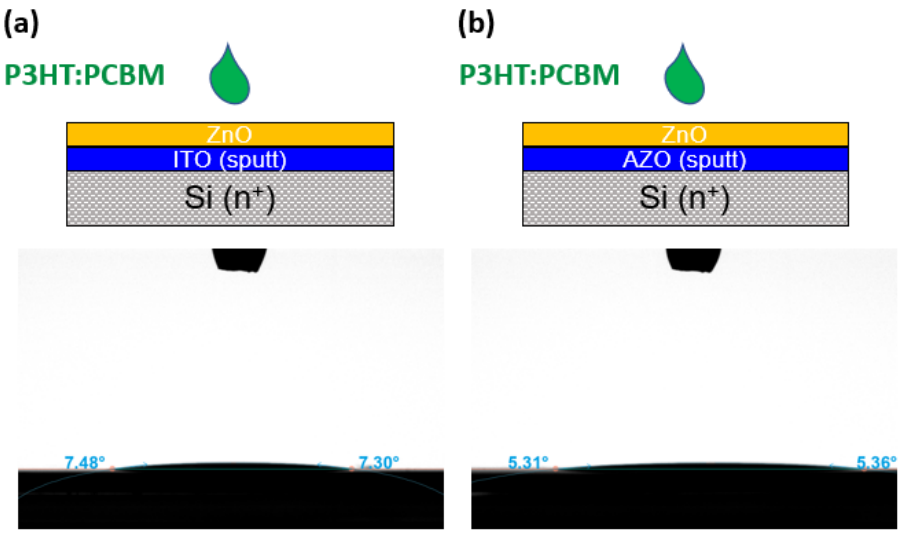

Figure 5-6: *Wettability characterization of the (a) Si(n⁺)/ITO/ZnO and (b) Si(n⁺)/AZO/ZnO stacks by contact-angle measurement using the P3HT:PCBM active-layer solution.*

The first contact angle measurement, between the Si(n⁺)/ITO/ZnO stack and the P3HT:PCBM active layer, is approximately equal to 7.4° (**Figure 5-6a**). The second one measured between the Si(n⁺)/AZO/ZnO stack and the same P3HT:PCBM active layer is approximately equal to 5.3° (**Figure 5-6b**). Such low contact angles indicate good spreading of the solution over both substrate surfaces, which is expected to promote the formation of continuous and homogeneous active-layer films after spin coating.[227] The quality of the deposited layers was then examined by optical microscopy (**Figure 5-7**).

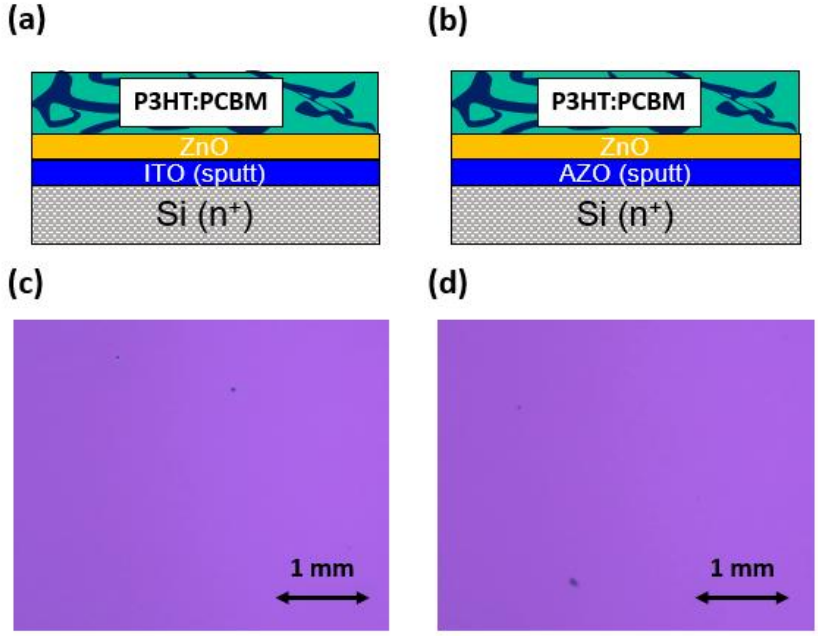

Figure 5-7: *Schematic representation of the (a) Si(n⁺)/ITO/ZnO and (b) Si(n⁺)/AZO/ZnO stacks used to assess the homogeneity of the P3HT:PCBM organic active layer deposition and top-view optical microscopy image of the deposited P3HT:PCBM active-layer on (c) Si(n⁺)/ITO/ZnO and (d) Si(n⁺)/AZO/ZnO.*

Optical microscopy observations were performed at several locations distributed across the substrates. No significant coating defects, dewetting regions, or thickness inhomogeneities were observed for either configuration, confirming the good quality of the deposited P3HT:PCBM organic film on both the Si(n^+)/ITO/ZnO and the Si(n^+)/AZO/ZnO stacks (**Figure 5-7c and Figure 5-7d**). The individual microscopy fields covered approximately 4.0 x 4.0 mm², corresponding to 9 measurement locations distributed across the substrate.

The photovoltaic performance of the two architectures was then evaluated by fabricating complete P3HT:PCBM devices without busbars, featuring the Si(n^+)/ITO/ZnO/PAL/MoO_3/ITO and Si(n^+)/AZO/ZnO/PAL/MoO_3/ITO stacks. Their PV performance was compared with that of the standard P3HT:PCBM-based ST-OSC fabricated on conventional glass/ITO substrates and optimized in **Chapter 4**. All results are summarized in **Table 5-3**.

Device	PCE (%)	J_{SC} (mA.cm^{-2})	V_{OC} (V)	FF
$ST_{P3HT:PCBM}$	1.6	5.9	0.54	0.50
P3HT:PCBM on Si(n^+)/ITO	1.5	5.6	0.54	0.48
P3HT:PCBM on Si(n^+)/AZO	1.3	5.4	0.52	0.46

***Table 5-3**: PV parameters of the reference P3HT:PCBM-based semi-transparent organic solar cells fabricated on glass/ITO and P3HT:PCBM-based organic solar cells fabricated on Si(n^+)/ITO and Si(n^+)/AZO substrates.*

The PV characteristics exhibit very similar behavior between the reference and both Si(n^+)/TCO substrates. A slight decrease in J_{SC} and FF is observed for both Si(n^+)/TCO-based architectures, resulting in lower overall PCE values of 1.5 % and 1.3 % for the ITO- and AZO-based devices, respectively, compared with 1.6 % for the reference device. The similar performance obtained with the two TCO confirms the compatibility of the OPV processing sequence with both interfacial architectures. Nevertheless, the slightly higher PCE obtained with the ITO-based devices supports the selection of ITO as the interfacial TCO for the subsequent integration steps.

Following this preliminary screening, the selected Si(n^+)/ITO substrate was further investigated using PM6:GS-ISO, the WBG active-layer system developed and optimized throughout this thesis. This second step was necessary to verify that the interfacial architecture selected from the preliminary P3HT:PCBM experiments could be successfully combined with the organic material ultimately targeted for the OPV/Si tandem device.

The wettability of the Si(n^+)/ITO/ZnO stack was therefore evaluated using the PM6:GS-ISO active-layer solution (**Figure 5-8**).

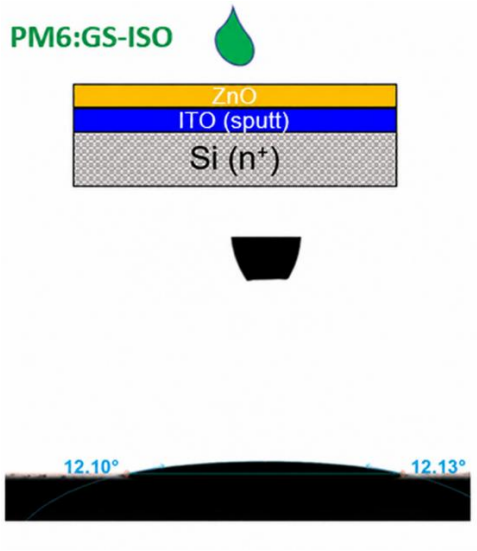

Figure 5-8: *Wettability characterization of the Si(n⁺)/ITO/ZnO stack by contact-angle measurement using the PM6:GS-ISO active-layer solution.*

The measured contact angle was approximately 12.1°, indicating a good spreading of the solution over the substrate surface and therefore favourable conditions for the formation of a homogeneous active layer during spin coating. The quality of the deposited PM6:GS-ISO film was subsequently assessed by optical microscopy (**Figure 5-9**).

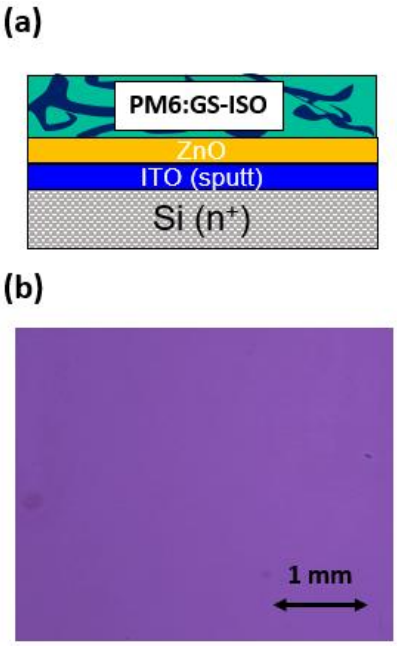

Figure 5-9: *(a) Schematic representation of the Si(n⁺)/ITO/ZnO stack used to assess the homogeneity of the PM6:GS-ISO organic active layer deposition and (b) top-view optical microscopy image of the deposited PM6:GS-ISO active-layer on Si(n⁺)/ITO/ZnO.*

Optical microscopy observations were performed at several locations distributed across the substrate. No significant coating defects, dewetting regions, or thickness

inhomogeneities were observed, confirming the good quality and homogeneity of the deposited PM6:GS-ISO film on the Si(n^+)/ITO/ZnO stack (**Figure 5-9**).

To further validate this integration strategy, complete PM6:GS-ISO devices without busbars and featuring the Si(n^+)/ITO/ZnO/PAL/MoO_3/ITO architecture were fabricated. As shown in **Figure 5-10**, their PV performance was compared with that of the standard PM6:GS-ISO-based ST-OSC fabricated on conventional glass/ITO substrates and optimized in **Chapter 4**. All results are summarized in **Table 5-4**.

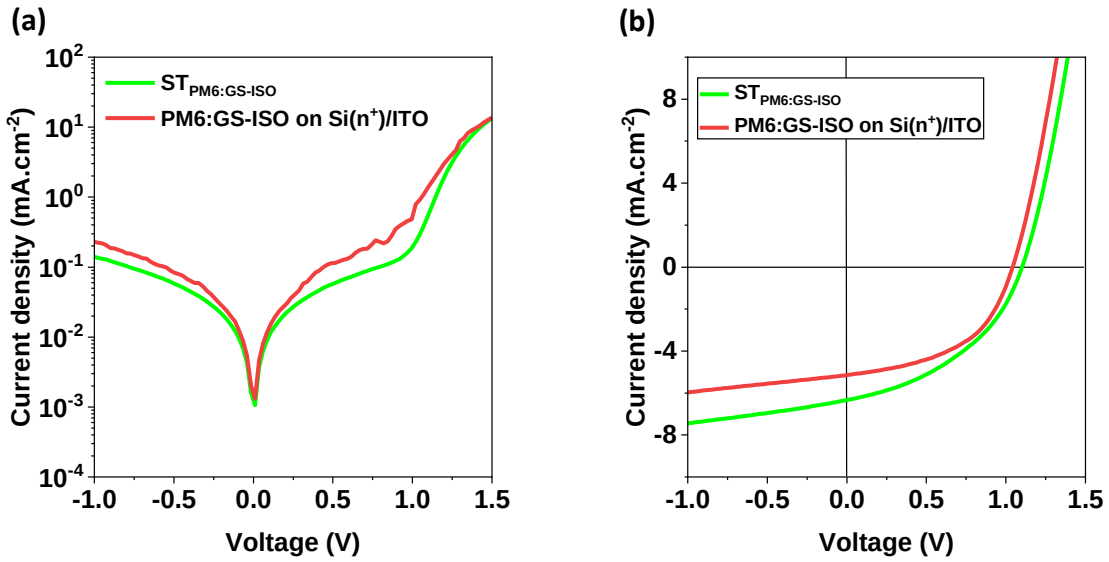

Figure 5-10: *J-V characteristics of $ST_{PM6:GS-ISO}$ on glass/ITO substrates and PM6:GS-ISO on Si(n^+)/ITO substrate: (a) in the dark and (b) under AM1.5G.*

Device	PCE (%)	J_{SC} (mA.cm^{-2})	V_{OC} (V)	FF
$ST_{PM6:GS-ISO}$	2.9	6.3	1.10	0.42
PM6:GS-ISO on Si(n^+)/ITO	2.6	5.1	1.04	0.49

Table 5-4: *PV parameters of the reference PM6:GS-ISO-based semi-transparent organic solar cells fabricated on glass/ITO and of the PM6:GS-ISO-based organic solar cells fabricated on the Si(n^+)/ITO substrate.*

The *J-V* characteristics exhibit similar diode behavior for both substrate configurations.[228] Although a decrease in J_{SC} and V_{OC} is observed for the device fabricated on Si(n^+)/ITO substrate. The FF of the Si-based device is superior to that of the reference ST-OSC. Consequently, the PCE decreases from 2.9 % for the reference device to 2.6 % for the Si-based device. Despite this slight reduction, the device retains a clear photovoltaic response, demonstrating that the PM6:GS-ISO active layer can be successfully processed on the Si(n^+)/ITO substrate. This result confirms the compatibility of the selected interfacial

architecture with the OPV system developed in this thesis and supports its subsequent integration onto IBC Si bottom cells.

5.3.3 Scale-up toward IBC dimensions

Following the validation of the interfacial architecture, the final technological step consisted in evaluating whether the deposition processes optimized on standard laboratory substrates could be directly transferred to the dimensions of the IBC silicon bottom cells. Indeed, all previous optimizations were carried out on laboratory substrates measuring 15 × 15 mm², whereas the IBC silicon bottom cells fabricated at ISC Konstanz have dimensions of 21.8 × 21.8 mm². For this purpose, the ZnO ETL and the studied PM6:GS-ISO organic active layer were deposited on 25 × 25 mm² glass substrates, deliberately larger than the final IBC cells (21.8 × 21.8 mm²). The deposited films were subsequently characterized by optical microscopy at several locations distributed over the entire substrate (**Figure 5-11**).

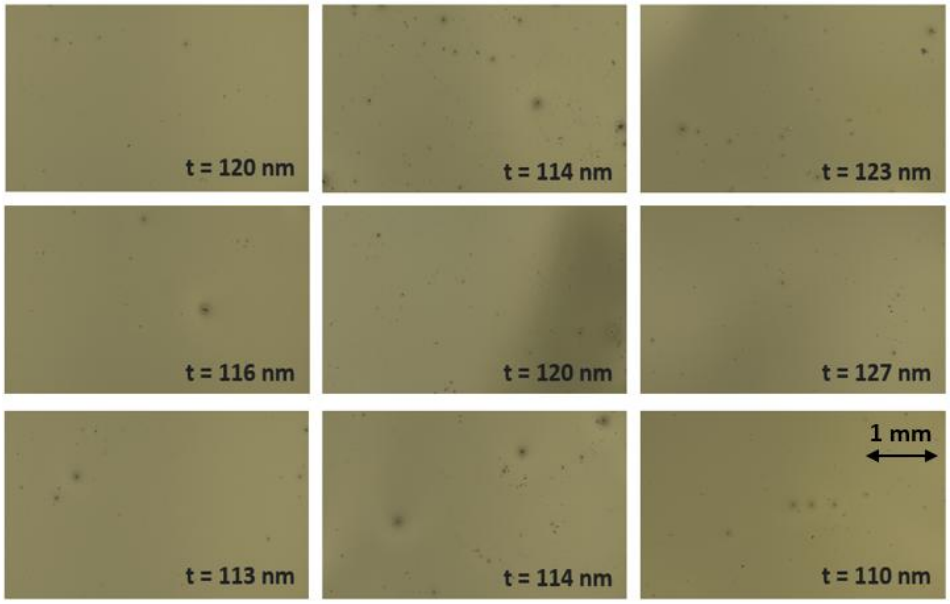

Figure 5-11: *Optical microscopy images acquired at different positions across the substrate and corresponding film-thickness measurements demonstrating the coating uniformity.*

Optical microscopy observations performed at different locations across the substrates revealed no additional coating defects compared with the standard 15 × 15 mm² samples. Thickness measurements further demonstrated an excellent coating uniformity, with a maximum thickness variation of only 17 nm over the entire substrate. These results confirm that the spin-coating processes developed throughout this work can be successfully scaled to the dimensions required for the IBC bottom cells, thereby validating the fabrication protocol prior to the realization of the complete monolithic OPV/Si tandem devices.

Key Point 5.3: Development and integration of the interfacial architecture for monolithic OPV/Si tandem cells.

- **ITO ensures efficient electron collection and transport, high optical transparency, and technological compatibility with the fabrication processes of both sub-cells.**
- **The deposition of the nc-SiO_x passivating contact and the ITO interfacial layer improve the Si bottom-cell performance by reducing surface recombination and enhancing light coupling.**
- **Experiments performed on Si/ITO substrates demonstrate the homogeneous deposition of the OSC while maintaining PV performances close to those obtained on the reference glass/ITO substrate.**
- **The optimized spin-coating processes were successfully scaled from standard substrates to the dimensions of the IBC Si bottom cells.**

5.4. Experimental implementation of the monolithic 3-terminal OPV/Si tandem cell

5.4.1 Fabrication of the monolithic tandem device

Following the validation of the Gen2 IBC bottom cells, the front-side treatment/ITO architecture, and the compatibility of the OPV deposition process with the Si-based substrate, the complete monolithic tandem device was fabricated following the fabrication procedures developed in **Chapter 3** and **Chapter 4**.

First, a ZnO ETL was deposited by spin coating directly onto the ITO-coated Si surface. The organic active layer was subsequently deposited by spin coating, followed by the thermal evaporation of the MoO_3 HTL. Finally, the semi-transparent ITO top electrode was deposited by room-temperature RF magnetron sputtering to complete the monolithic tandem architecture. Silver busbars were then deposited by thermal evaporation, following the procedure described in Chapter 4 (**Figure 5-12**). These busbars were implemented both to facilitate electrical contact between the top organic electrode and the measurement setup probes and to improve the lateral conductivity of the electrode, as previously demonstrated.

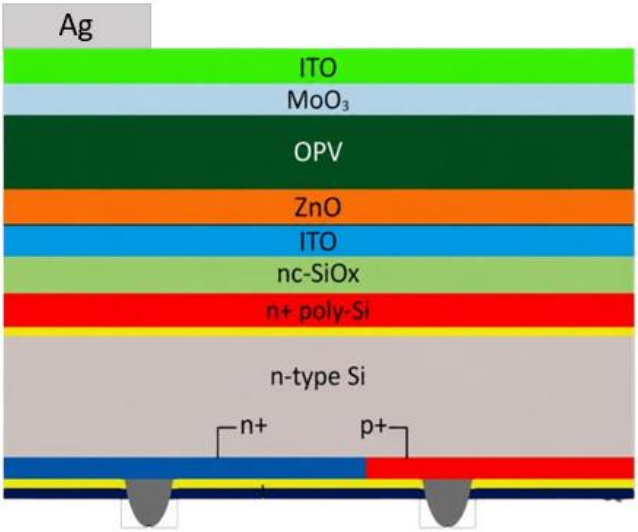

Figure 5-12: *Schematic cross-sectional architecture of the fabricated monolithic three-terminal OPV/Si tandem solar cell, showing the successive layers deposited onto the Gen2 IBC silicon bottom cell. For simplicity, only one p/n rear-contact motif is represented in the schematic, whereas the actual IBC cell consists of a succession of interdigitated p- and n-type contacts on the rear side.*

Both the ZnO ETL and the organic photoactive layer were deposited directly onto the 21.8 × 21.8 mm² IBC silicon substrates using the spin-coating procedures established in **Chapter 3**. As demonstrated previously in this chapter, the deposition of these layers could be successfully extended to substrate dimensions larger than those used for the standard OPV devices, with homogeneous coating obtained over the relevant substrate area. The same deposition conditions were therefore applied to the IBC cells used for the fabrication of the monolithic tandem devices. Two organic photoactive blends were investigated throughout this work. The PM6:GS-ISO blend, optimized in **Chapter 3**, was selected as the reference material owing to its high V_{OC} and its suitability for tandem integration.[141] In parallel, the PTQ10:FCC-Cl blend, developed in collaboration with ICMAB-CSIC and presented in **Chapter 4**, was also investigated because of its improved near-infrared transparency, which is expected to increase the photon flux reaching the Si bottom cell.[218]

While the ZnO ETL and organic photoactive layer could be deposited directly onto the IBC cells using the previously validated spin-coating processes, the subsequent electrode fabrication steps required dedicated sample holders. Indeed, the larger dimensions and specific geometry of the IBC cells required an adaptation of the sample positioning and masking strategies used for the standard OPV devices. Dedicated holders were therefore designed for the successive deposition of the MoO_3 HTL, the semi-transparent ITO top electrode, and the Ag busbars. The different sample-holder designs developed for these three deposition steps are presented in **Figure 5-13**.

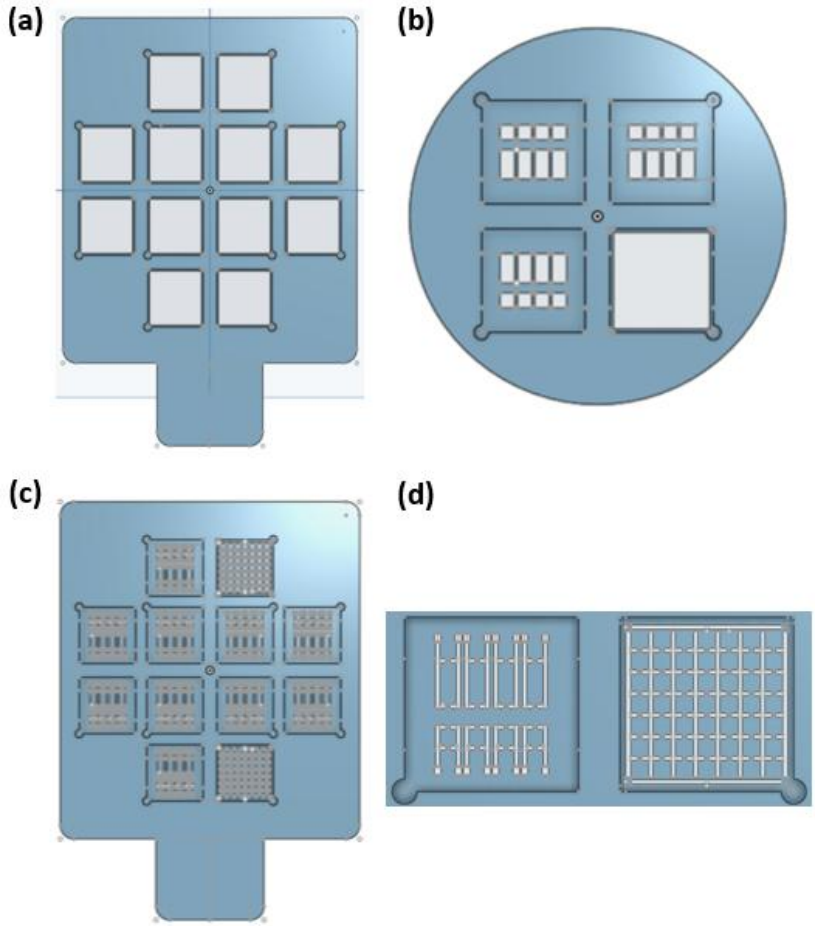

Figure 5-13: *Dedicated sample holders developed for the final fabrication steps of the monolithic OPV/Si tandem cells: (a) sample holder used for thermal evaporation of the 15 nm MoO_3 HTL, (b) sample holder used for deposition of the 120 nm ITO top electrode, (c) sample holder used for thermal evaporation of the 80 nm Ag busbars, and (d) examples of the corresponding Ag busbar geometries, including the fine-mesh design used for the complete tandem devices.*

After deposition of the organic photoactive layer, a 15 nm-thick MoO_3 HTL was deposited by thermal evaporation. A dedicated sample holder was designed for this step, as shown in **Figure 5-13a**. The holder was adapted to the dimensions of the 21.8 × 21.8 mm² IBC cells and enabled their reproducible positioning inside the thermal evaporator. Once placed in the holder, the cells could be exposed over the required surface, allowing the MoO_3 layer to be deposited over the complete device area. The deposition procedure was thus maintained consistent with that established for the reference OPV devices, while adapting the sample handling to the IBC substrate geometry. Following the MoO_3 deposition, the samples were transferred to ELORPRINTEC for deposition of the semi-transparent ITO top electrode. A second dedicated sample holder was developed for this deposition step (**Figure 5-13b**). Different device geometries were defined on each IBC substrates, including 3 × 3 mm² and 3 × 6 mm² devices. The holder comprised four sample positions. Three positions were primarily used for the fabrication of these small-area test structures, whereas one position allowed the

ITO to be deposited over the entire IBC cell surface. A 120 nm-thick ITO layer was deposited by RF magnetron sputtering. This configuration therefore enabled both preliminary small-area structures and full-area devices to be fabricated using the same deposition process, with the latter configuration providing a route toward a complete tandem device covering the 21.8 × 21.8 mm² silicon bottom cell. The final processing step consisted of the deposition of the Ag busbars. After ITO deposition, the cells were placed in a third dedicated sample holder designed for thermal evaporation of the metallic layer (**Figure 5-13c**). An 80 nm-thick Ag layer was deposited onto the predefined non-photoactive regions of the devices. Although the busbar approach had already been developed for the semi-transparent OPV devices presented in **Chapter 4**, the geometry was adapted here to the specific requirements of the tandem architecture. In particular, small electrical contact pads were introduced outside the active device area to facilitate the positioning of the measurement probes, as illustrated in **Figure 5-13d**. This configuration provided accessible electrical contact points while avoiding direct probing of the photoactive region of the tandem device. As for the ITO deposition, two positions of the Ag sample holder were reserved for the fabrication of complete tandem devices. For these devices, the Ag busbars were designed as a fine mesh rather than as fully continuous metallic electrodes (**Figure 5-13d**). The mesh geometry was selected to provide a suitable trade-off between lateral electrical conductivity and optical transmission. The metallic network improves the lateral current collection of the semi-transparent ITO electrode while limiting the fraction of incident light blocked by the Ag layer, thereby preserving the optical transmission required for the tandem architecture.

Overall, the complete OPV stack was therefore fabricated directly on the 21.8 × 21.8 mm² IBC silicon bottom cells. The previously validated spin-coating procedures were applied to the ZnO ETL and organic photoactive layer, while dedicated sample holders were developed for the subsequent MoO_3, ITO, and Ag deposition steps. The combination of small-area test structures and dedicated full-area positions enabled the different technological aspects of the tandem fabrication to be investigated while providing a direct route toward complete devices covering the full IBC cell area. The overall process leading to the final monolithic device is summarized in **Figure 5-14**. The schematic provides an overview of the successive processing steps and the different facilities involved, from the fabrication of the IBC silicon bottom cell to the finalization of the monolithic OPV/Si tandem device.

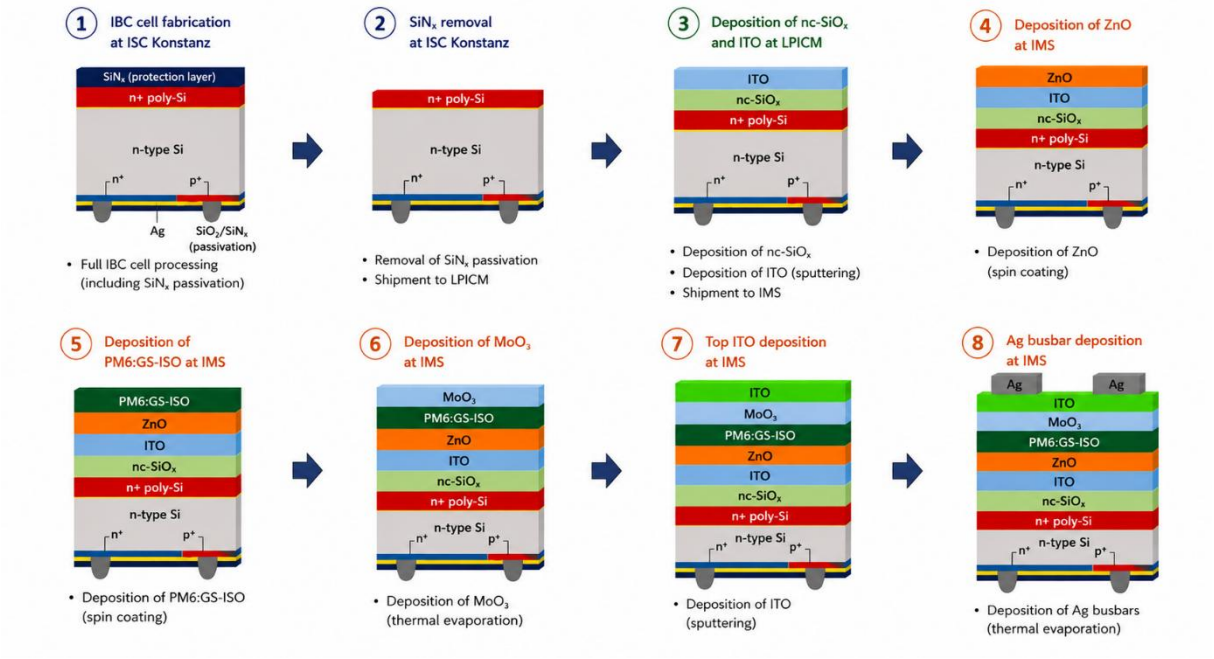

Figure 5-14: *Schematic workflow for the fabrication of the monolithic OPV/Si tandem cell.*

5.4.2 Electrical validation of the Si bottom cell after OPV deposition

Before attempting the complete 3T characterization, it is essential to verify that the deposition of the organic stack does not alter the electrical operation of the Si bottom cell. To this end, *J-V* measurements were performed after deposition of two different organic photoactive blends, PM6:GS-ISO and PTQ10:FCC-Cl, by contacting only the rear n- and p-type electrodes of the IBC cell, while leaving the organic top electrode electrically floating. Under these conditions, the deposited organic stack acts solely as a wavelength-selective optical filter positioned above the Si device. Consequently, the measured PV response originates exclusively from the filtered Si bottom cell.

Figure 5-15 presents the corresponding *J-V* characteristics together with the extracted PV parameters (**Table 5-5**).

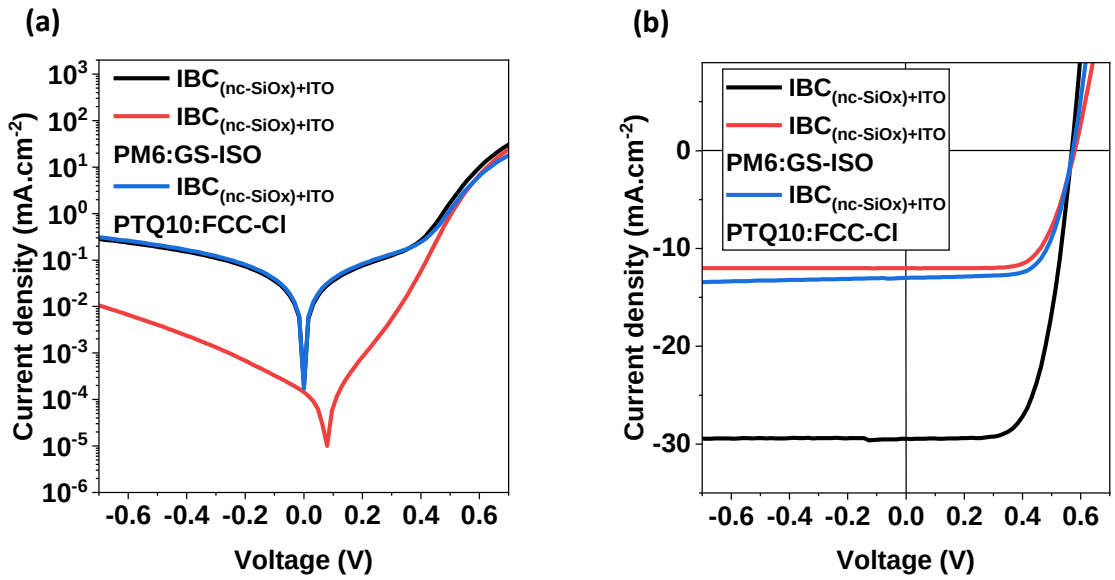

Figure 5-15: *J-V characteristics of $IBC_{(nc\text{-}SiOx)+ITO}$, $IBC_{(nc\text{-}SiOx)+ITO}$ with a PM6:GS-ISO stack, and $IBC_{(nc\text{-}SiOx)+ITO}$ with a PTQ10:FCC-Cl stack: (a) in the dark and (b) under AM1.5G.*

Device	PCE (%)	J_{SC} (mA.cm^{-2})	V_{OC} (V)	FF
$IBC_{(nc\text{-}SiOx)}$ + ITO	11.0	29.5	0.57	0.65
$IBC_{(nc\text{-}SiOx)}$ + ITO PM6:GS-ISO	4.7	12.0	0.58	0.65
$IBC_{(nc\text{-}SiOx)}$ + ITO PTQ10:FCC-Cl	5.2	13.0	0.57	0.70

Table 5-5: *PV parameters of the passivated Gen2 IBC silicon bottom cell before and after deposition of the PM6:GS-ISO and PTQ10:FCC-Cl organic photovoltaic stacks.*

As expected, the J_{SC} decreases significantly compared with the bare $IBC_{(nc\text{-}SiOx)+ITO}$ bottom cell, decreasing from 29.5 mA.cm^{-2} to 12.0 mA.cm^{-2} and 13 mA.cm^{-2} after deposition of the PM6:GS-ISO and PTQ10:FCC-Cl stacks, respectively. This reduction results from the absorption of a fraction of the incident solar spectrum by the organic layers before it reaches the Si absorber. Both the V_{OC} and the FF remain nearly unchanged compared to $IBC_{(nc\text{-}SiOx)+ITO}$, indicating that the fabrication process does not deteriorate the electrical quality of the Si bottom cell. Since the organic stack mainly modifies the optical flux incident on the Si absorber without affecting its junction properties, the reduction in current can be attributed to optical filtering rather than to electrical degradation.[229] These measurements therefore validate both the technological compatibility of the fabrication process and the expected optical behavior of the hybrid structure. The next step was therefore to characterize the complete device in the three-terminal configuration. However, the full 3T characterization was ultimately limited by the mechanical contacting configuration of the available probe station, as discussed below.

5.4.3 Principle of the three-terminal electrical characterization

Once the proper operation of the filtered Si bottom cell had been verified, the final step consisted in electrically characterizing the complete monolithic 3T tandem device. Unlike conventional 2T tandem solar cells, in which the two sub-cells are connected in series and therefore constrained to carry the same current, the 3T architecture allows each PV junction to be measured independently.[78] The Si bottom cell is characterized through the rear n and p contacts, whereas the OPV contribution is obtained by measuring between the rear n contact of the Si cell and the p contact on the transparent top electrode of the organic device. Under this measurement configuration, the extracted current corresponds to the photogenerated holes collected at the organic top electrode together with the electrons transferred through the conductive interfacial layer toward the Si bottom cell. Consequently, the total tandem power can be reconstructed by summing the independently measured power contributions of the filtered Si bottom cell and the organic top cell. This independent electrical extraction represents one of the major advantages of the 3T tandem architecture over conventional monolithic 2T devices.

5.4.4 Electrical validation of the OPV top cell and limitations

Following the electrical validation of the Si bottom cell after deposition of the organic stack, the next objective was to experimentally extract the contribution of the organic top cell in the complete monolithic 3T OPV/Si tandem device. The measurements were performed using the intended OPV-contribution configuration, in which the n-type rear electrode of the IBC cell and the p-type electrode of the organic top cell are contacted independently.

However, the first analysis of the measured current densities revealed an inconsistency. When the active areas of the organic devices were directly used to calculate the current density, values as high as approximately 330 $mA \cdot cm^{-2}$ for the 3 × 3 mm^2 devices and 110 $mA \cdot cm^{-2}$ for the 3 × 6 mm^2 devices were obtained. These values are clearly incompatible with the expected photovoltaic response of the devices. To obtain physically meaningful current densities, the active area was therefore recalculated using the dimensions of the IBC silicon bottom cell. The resulting *J-V* characteristics and photovoltaic parameters are presented in **Figure 5-16** and Table **5-6**.

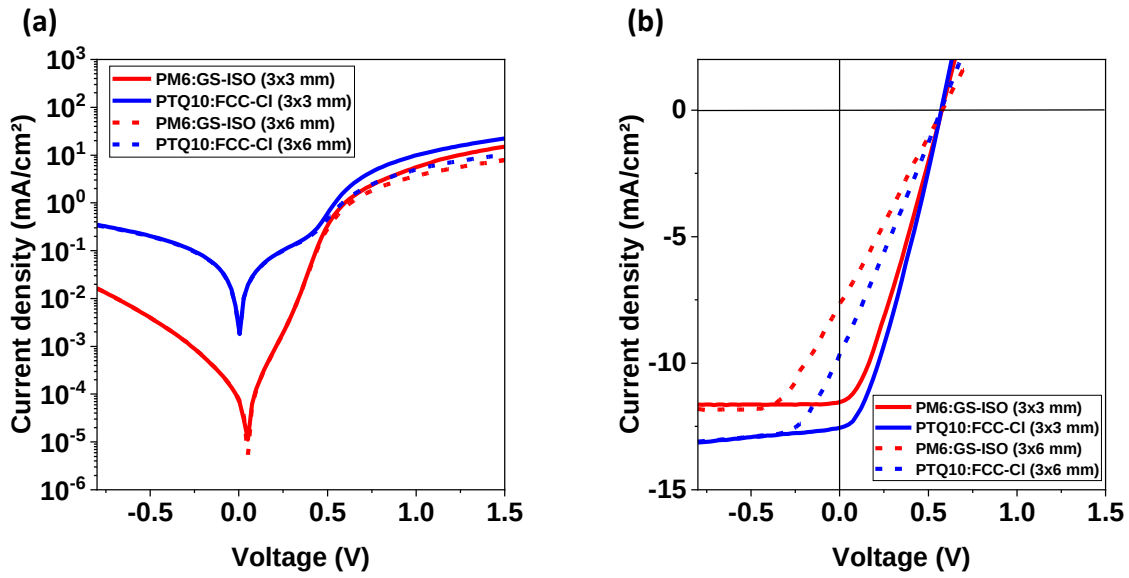

Figure 5-16: *J-V characteristics measured in the intended OPV-contribution configuration, with electrical contacts between the rear n-type IBC electrode and the front p-type electrode of the organic top cell: (a) in the dark and (b) under AM1.5G illumination, for PM6:GS-ISO and PTQ10:FCC-Cl devices with 3 × 3 mm² and 3 × 6 mm² geometries.*

Device	Area (mm²)	PCE (%)	J_{SC} (mA.cm^{-2})	V_{OC} (V)	FF
PM6:GS-ISO	3 x 3	2.1	11.5	0.58	0.32
	3 x 6	1.1	7.6	0.58	0.26
PTQ10:FCC-Cl	3 x 3	2.4	12.6	0.57	0.34
	3 x 6	1.4	9.6	0.57	0.26

Table 5-6: *PV parameters obtained from the electrical measurements performed in the intended OPV-contribution configuration.*

This area correction leads to values consistent with those previously obtained for the filtered Si bottom cell. For the PM6:GS-ISO stack, for example, the corrected measurement gives a V_{OC} of 0.58 V and a J_{SC} of 11.5 mA·cm^{-2}, compared with 0.58 V and 12.0 mA·cm^{-2}, respectively, for the filtered Si bottom cell. A similar agreement is observed for the PTQ10:FCC-Cl stack, with V_{OC} values of 0.57 V and J_{SC} values of 12.6 and 13.0 mA·cm^{-2}, respectively. These similarities suggest that the measured response does not originate primarily from the organic top cell. A first hypothesis was that the sharp probe used for the measurement could mechanically penetrate the organic stack and directly contact the underlying Si layer. However, this interpretation alone does not fully explain the observed diode-like J-V characteristics. If the probe were to contact the n$^+$-doped front side of the IBC cell while the second probe contacted the n-type rear electrode, the measurement would effectively connect two n-type regions of the silicon device and would therefore be expected

to result predominantly in resistive rather than photovoltaic behaviour. Such a behaviour is not observed experimentally.

An alternative hypothesis is therefore related to the electrical selectivity of the interfacial ITO/ZnO layer. In the ideal 3T configuration, the Si bottom cell is first characterized independently by contacting its p- and n-type rear electrodes. For the OPV contribution, the desired electrical path consists of collecting the holes generated in the OPV through its top p-type electrode, while the electrons are collected through the n-type rear electrode of the IBC cell. This configuration requires the intermediate interface to prevent the collection of photogenerated holes from the Si bottom cell at the front-side electrode. We hypothesize that the ITO/ZnO interface used in the present architecture does not provide sufficient hole-blocking selectivity. Consequently, holes generated in the IBC silicon cell may reach the front-side electrode and be collected by the probe, while the n-type rear electrode collects the corresponding electrons. The measured current would then contain, or even be dominated by, the photovoltaic contribution of the Si bottom cell rather than that of the OPV top cell. This interpretation is consistent with the close agreement between the measured response and that of the filtered Si bottom cell. However, this mechanism remains a hypothesis, as the exact electrical path established during the measurement could not be directly verified. Future work should therefore focus on improving the electrical selectivity of the interfacial stack. Further optimization of the ITO/ZnO stack may also be required to ensure efficient hole blocking from the Si bottom cell. Such developments would enable reliable independent characterization of both sub-cells and, ultimately, experimental validation of the complete 3T tandem operation.

Key Point 5.4: Experimental implementation of the monolithic 3-terminal OPV/Si tandem cell.

- **The Gen2 IBC Si bottom cells retained stable PV performance after transportation from LPICM to IMS.**
- **The monolithic OPV/Si tandem cells were fabricated by depositing OPV stack onto the ITO-coated Gen2 IBC Si bottom cells, using both the PM6:GS-ISO and PTQ10:FCC-Cl active layer blends.**
- ***J-V* measurements of the filtered Si bottom cell confirm that the deposition of the organic stack does not degrade the electrical properties of the IBC Si cell, with the observed reduction in current arising solely from the optical filtering of the light by the organic layers.**
- **The intended electrical extraction of the OPV contribution was not achieved. This behavior may originate from insufficient hole-blocking selectivity of the ITO/ZnO interface, allowing photogenerated holes from the IBC to contribute to the measured current.**

5.5. Lateral multijunction OPV/Si solar cells based on the RAINBOW concept

Although the previous sections focused on the monolithic integration of OPV and Si sub-cells, an alternative tandem strategy was also investigated during this thesis. Originally developed by the ICMAB (Institute of Materials Science of Barcelona) team, the RAINBOW concept explores spectral splitting through a laterally distributed architecture rather than relying on vertical integration, thereby addressing the same objective from a fundamentally different perspective.

5.5.1 Concept and motivation

Conventional tandem solar cells primarily use vertically stacked sub-cells to broaden the spectral absorption range, minimize thermalization, and overcome the efficiency limitations of single-junction devices (**Figure 5-17a**).[67] While this method has proven highly effective, it inherently imposes strict constraints on current matching, interconnection layers, optical management, and manufacturing compatibility between dissimilar materials.[78] These challenges are particularly pronounced in OPV/Si hybrid tandems, where mismatches in optical and electrical properties can significantly impair device performance and scalability.

An alternative strategy to overcome these limitations is the spectral splitting geometry.[230] This approach consists of spectrally separating the incident solar spectrum and redirecting the fractions to different non-vertically stacked sub-cells, as shown in **Figure 5-17b**.[231] This strategy has demonstrated promising performance across a wide range of PV systems, including high-efficiency III-V multijunction devices,[232] hybrid inorganic PSC tandems,[233] as well as Si-based thermal absorbers.[234] While the physical separation of sub-cells simplifies fabrication and electrical interconnection, practical implementations remain technically challenging. Conventional configurations typically place the sub-cells at 90° with respect to each other and use a dichroic mirror positioned at 45° to spectrally redistribute the incident sunlight. Such an arrangement leads to a bulky and impractical device geometry, which becomes increasingly complex as the number of junctions increases.[230]

In this work, an alternative beam-splitting architecture based on a dispersive optical element (such as a prism or a diffraction-based structure) is investigated. This element spectrally splits the incident sunlight into its constituent wavelengths (**Figure 5-17c**). Each spectral band is then directed toward a dedicated PV sub-cell operating close to its optimal bandgap, thereby reducing thermalization losses and enhancing overall PCE.

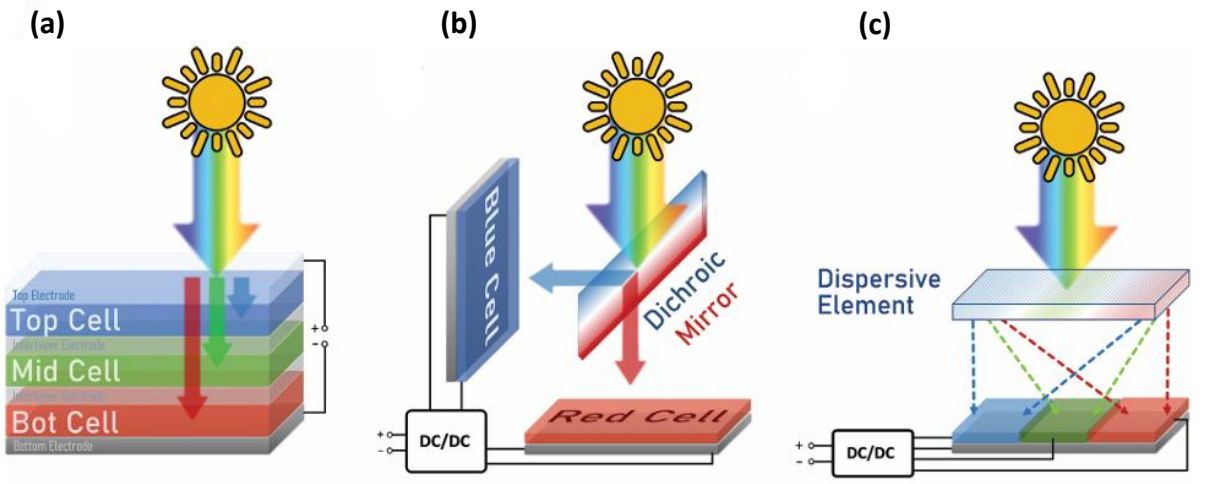

Figure 5-17: *(a) Stacked, series connected multijunction configuration. (b) Solar spectral splitting tandem configuration with a dichroic mirror as the light-redirecting optical element. (c) RAINBOW multijunction configuration with a dispersive element that performs the spectral splitting. Reproduced with permission from M. Gilbert-Roca.* [231]

This method, referred to as the RAINBOW approach, enables a monolithic in-plane manufacturing approach. Moreover, the lateral distribution of each sub-cell allows for the straightforward implementation of electrically independent contacts, eliminating the need for current or voltage matching on a device level.[235,236] Finally, a RAINBOW device requires approximately the same amount of electrode, active, transport-layer and substrate materials as a conventional single-junction device, making it an attractive architecture from a manufacturing perspective.

OPV materials and, more generally, solution-processable materials are particularly suitable for RAINBOW-based lateral multijunction systems. Indeed, they offer a unique degree of freedom: their bandgaps can be tuned through molecular design, they can be deposited as well-defined lateral stripes, and they are compatible with continuous roll-to-roll processing. When combined with high-efficiency Si bottom cells, especially IBC architectures, OPV/Si lateral tandems can leverage both the strong visible absorption of organic semiconductors and the superior near-infrared response of Si. Recent studies have demonstrated the feasibility of lateral multijunction OSC based on the RAINBOW concept, highlighting both the optical advantages of spectral splitting and the resulting improvements in PV performance.[141,231] The RAINBOW approach therefore aims not only to enhance absolute efficiency but also to establish a scalable architecture capable of exploiting the modularity and versatility of such materials, while circumventing the structural and electrical constraints inherent to vertical tandems.

In this context, this section presents on the implementation of lateral multijunction devices based on the RAINBOW concept within the innovative framework of OPV/Si tandem solar cell development. The following subsections detail the operating principles, optical design considerations, simulation results, and experimental validation of this architecture, thereby highlighting its potential as a viable and scalable alternative to conventional vertical

tandem configurations. The experimental results obtained during this thesis served as inputs for the numerical simulations performed by Francesc Xavier Capella Guardià, from the research group of Prof. Mariano Campoy-Quiles. The experimental validation of the laterally integrated multijunction architecture was subsequently carried out at ICMAB during an international research stay.

5.5.2 Modeling and performance prediction of RAINBOW architectures

a) Modeling principles and assumptions

To simulate the behavior of the two sub-cells considered in this study, the solar spectrum is divided into two complementary parts, with a tunable dividing wavelength (λ_{div}). The part containing the shorter wavelengths is called "blue fraction", and the other part containing the larger wavelengths is then called "red fraction". These fractions are directed to each of the two sub-cells, which are consequently named blue and red cells, respectively (**Figure 5-18**). The overall performance of a RAINBOW device strongly depends on the choice of λ_{div}. To determine this parameter, λ_{div} is swept across the solar spectrum, systematically varying the relative size of the blue and red fractions, in order to evaluate the RAINBOW performance under various spectral splitting conditions and material combinations.

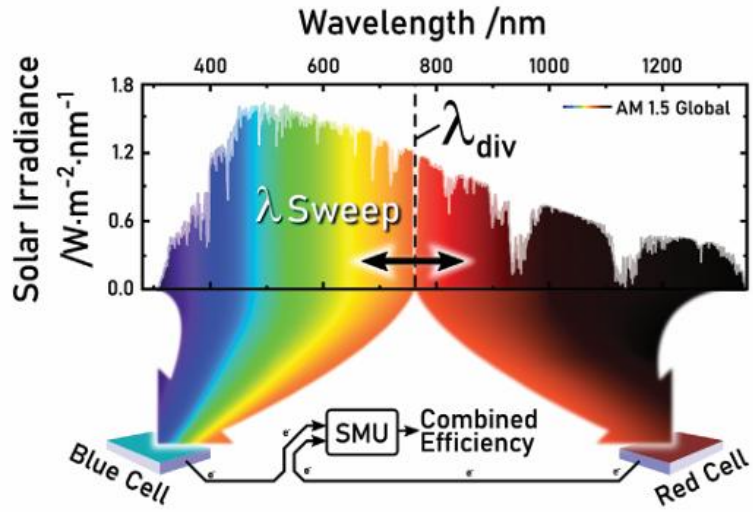

Figure 5-18: *Schematic representation of a two sub-cell RAINBOW measurement, where the solar spectrum is divided into two complementary parts by a dividing wavelength, which is swept across the spectrum to evaluate the optimal value for any given RAINBOW material combination. Reproduced with permission from M. Gilbert-Roca.*[231]

As a first-order approximation of the RAINBOW device efficiency, the J_{SC} is calculated by integrating the product of the measured EQE and the incident solar spectral irradiance, according to **Equation 5-1**, where EQE(λ) is the experimental EQE curve, $E_{e,\lambda}(\lambda)$ is the solar spectral irradiance, $\varepsilon_{ph}(\lambda)$ is the photon energy and q_e is the electron electric charge. By replacing the full solar spectrum in **Equation 5-1** with either the red or blue spectral fraction

at each dividing wavelength ($E_{e,\lambda(red)}(\lambda, \lambda_{div})$ and $E_{e,\lambda(blue)}(\lambda, \lambda_{div})$), **Equation 5-2** and **Equation 5-3** are obtained, from which the respective J_{SC} values are calculated, for each λ_{div}.

$$J_{SC} = \int_0^{\infty} \frac{E_{e,\lambda}(\lambda)}{\varepsilon_{ph}(\lambda)} EQE(\lambda) q_e d\lambda \quad \textbf{(5-1)}$$

$$J_{SC(blue)}(\lambda_{div}) = \int_0^{\infty} \frac{E_{e,\lambda(blue)}(\lambda,\lambda_{div})}{\varepsilon_{ph}(\lambda)} EQE(\lambda) q_e d\lambda \quad \textbf{(5-2)}$$

$$J_{SC(red)}(\lambda_{div}) = \int_0^{\infty} \frac{E_{e,\lambda(red)}(\lambda,\lambda_{div})}{\varepsilon_{ph}(\lambda)} EQE(\lambda) q_e d\lambda \quad \textbf{(5-3)}$$

The resulting partial J_{SC} values are subsequently combined with the V_{OC} and the FF of each sub-cell (measured independently under AM1.5G conditions) to estimate their partial efficiencies, as shown in **Equation 5-4** and **Equation 5-5**.

$$PCE_{(blue)}(\lambda_{div}) = \frac{J_{SC(blue)}(\lambda_{div}) FF_{(blue)} V_{OC(blue)}}{E_{e,\lambda}} \quad \textbf{(5-4)}$$

$$PCE_{(red)}(\lambda_{div}) = \frac{J_{SC(red)}(\lambda_{div}) FF_{(red)} V_{OC(red)}}{E_{e,\lambda}} \quad \textbf{(5-5)}$$

This model therefore yields partial J_{SC} and PCE values for each sub-cell and at each dividing wavelength. The parameters for each sub-cell can then be summed to obtain the combined RAINBOW PCE, as shown in **Figure 5-19**.

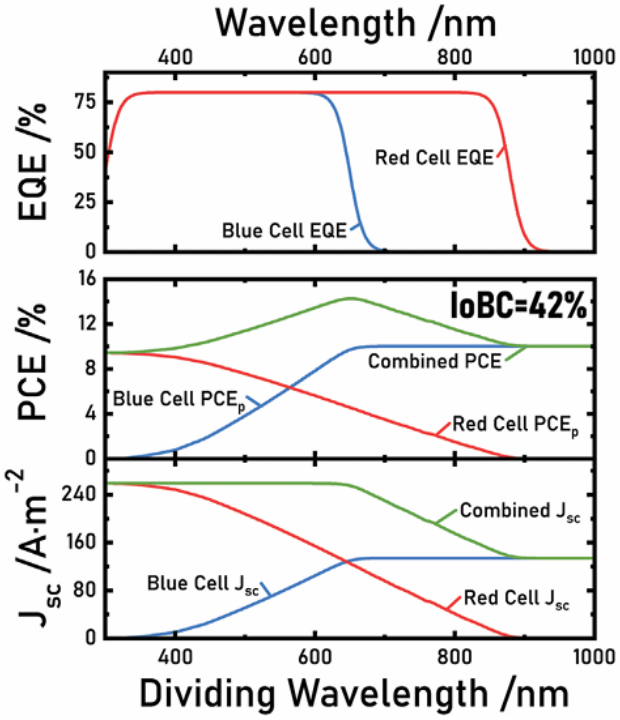

Figure 5-19: *RAINBOW combination performance graph, with ideal EQE curves for each individual sub-cell (top), and the partial and combined PCE (middle) and J_{SC} (bottom) curves as a function of the dividing wavelength. Reproduced with permission from M. Gilbert-Roca.*[231]

The theoretical model relies on the assumption that the sub-cells are electrically independent (in this case, a 4T device). Moreover, the model requires that $E_{e,\lambda(red)} + E_{e,\lambda(blue)} = E_{e,\lambda}$, which allows J_{SC} and PCE to be treated as additive quantities, leading to **Equation 5-6** and **Equation 5-7**.

$$J_{SC(comb)} = J_{SC(red)} + J_{SC(blue)} \quad \textbf{(5-6)}$$

$$PCE_{(comb)} = PCE_{(red)} + PCE_{(blue)} \quad \textbf{(5-7)}$$

An important parameter denoted as $PCE_{(comb,max)}$, can then be introduced. It corresponds to the maximum PCE over the full wavelength range. Relative to this value, a figure of merit, hereafter referred to as the "increase-over-best-cell" (IoBC), is introduced to quantify the relative gain in PCE of a given multijunction combination compared to its best-performing single-junction sub-cell (**Equation 5-8**).[237]

$$IoBC = \frac{PCE_{comb,max} - PCE_{\max(best-sub-cell)}}{PCE_{\max(best-sub-cell)}} \times 100 \quad \textbf{(5-8)}$$

Overall, this model provides a rapid and practical method for evaluating the performance of potential RAINBOW devices using only standard *J-V* and EQE measurements. It therefore enables efficient screening of multijunction material combinations prior to the fabrication of either lateral RAINBOW devices or conventional vertical tandem cells.

b) Simulation of OPV/Si RAINBOW lateral multijunction devices

The model described above was subsequently applied to several OPV/Si material combinations in order to evaluate the potential performance of RAINBOW lateral multijunction devices and identify the most promising architectures prior to experimental validation. Two WBG organic blends, PM6:GS-ISO (labelled "w/o" in **Chapter 3**) and PM6:GS-ISO with F8T2 (F8T2-0.2%wt, as optimized in **Chapter 3**) and two LBG flat IBC-Si cells, IBC-Gen1 and IBC-Gen2 were selected for this study. For the IBC-Si cells, the SiO_2 and SiN_x protective layers used for the Gen1 and Gen2 cells, respectively, were retained (**Figure 5-1**). This choice is specific to the RAINBOW concept, which relies on laterally interconnected sub-cells rather than a monolithic multijunction architecture and therefore does not require the removal of the Si protective layers for the integration of the organic sub-cells. Maintaining these layers also allows the best-performing Si cells to be considered without any additional surface treatment or processing step. Using these four sub-cells, high performance OSC and IBC devices were characterized, and their *J-V* and EQE curves served as inputs to the simulation model (**Figure 5-20 and Figure 5-21**). All measurements were performed under a xenon (Xe) solar simulator reproducing the AM1.5G spectrum.

The first simulations consider PM6:GS-ISO and F8T2-0.2%wt as "blue cells", respectively, and IBC-Gen1 as the "red cell" (**Figure 5-21**). These combinations yield $PCE_{(comb,max)}$ values of 13.8 % and 15.1 %, with high IoBC of 20.0 % and 31.6 %, for λ_{div} at 675

and 685 nm, respectively. In general, the primary factor governing the absolute RAINBOW efficiency is the performance of the individual sub-cells, since the combined efficiency directly depends on their respective PCE. In the case of multijunction combinations of PM6:GS-ISO + IBC-Gen1 and F8T2-0.2%wt + IBC-Gen1, both the OSC and the IBC-Gen1 device exhibit moderate efficiencies, which limits the achievable combined PCE. Conversely, the high IoBC values demonstrate the excellent spectral complementarity between the EQE responses of the two sub-cells. Maximizing IoBC requires the two sub-cells to exhibit complementary spectral responses, while jointly covering a broad fraction of the solar spectrum.

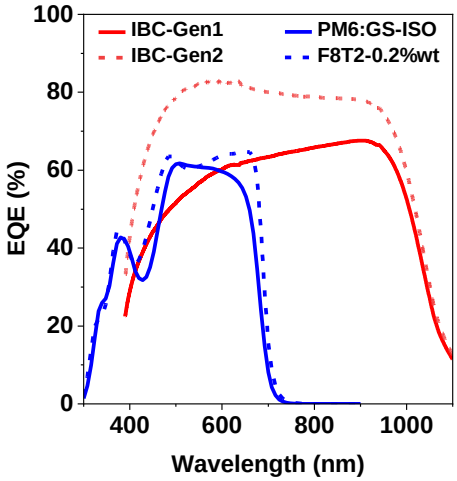

Figure 5-20: *Experimental EQE for "blue cells": PM6:GS-ISO (full blue line) and F8T2-0.2%wt (dashed blue line) measured in IMS; and "red cells": IBC-Gen1 (full red line) and IBC-Gen2 (dashed red line) measured in GeePs.*

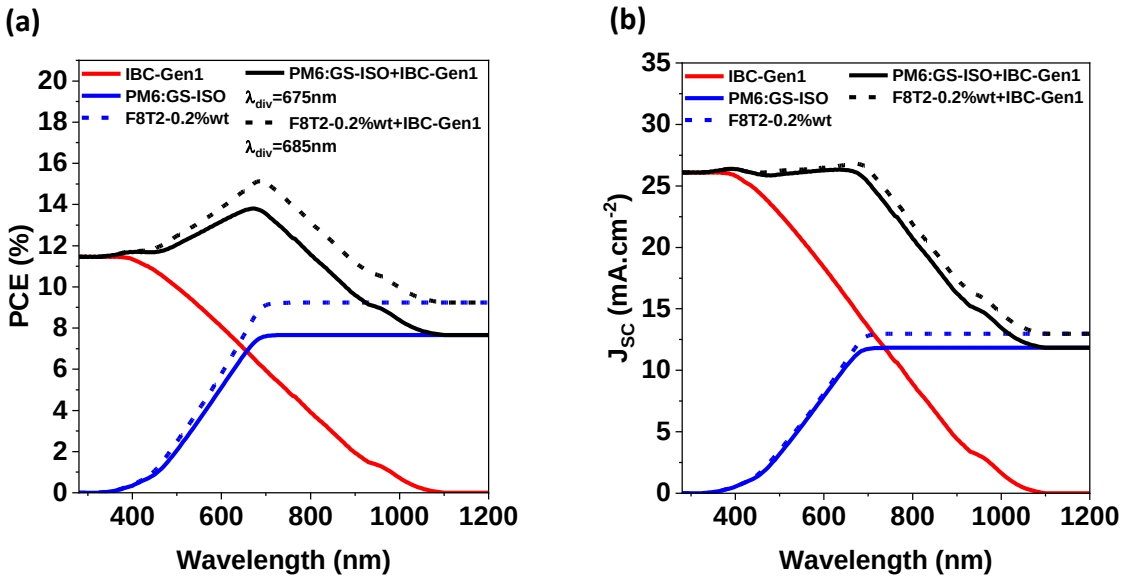

Figure 5-21: *Simulated (a) PCE and (b) J_{SC} for "blue cells": PM6:GS-ISO (full blue line) and F8T2-0.2%wt (dashed blue line); "red cell": IBC-Gen1 (full red line); and lateral multijunction involving PM6:GS-ISO + IBC-Gen1 (full black line) and F8T2-0.2%wt + IBC-Gen1 (dashed black line).*

The same analysis was subsequently performed on organic sub-cells, PM6:GS-ISO and F8T2-0.2 wt% ("blue cells"), in combination with IBC-Gen2 as the "red cell" (**Figure 5-22**). As anticipated, the multijunction simulations yield higher $PCE_{(comb,max)}$ values of 15.3 % and 16.5 %, but lower IoBC values of 13.0 % and 22.6 % for λ_{div} values of 665 nm and 685 nm, respectively. The higher $PCE_{(comb,max)}$ can be attributed to the superior individual performance of the IBC-Gen2 alone. However, the reduced IoBC highlights a fundamental requirement of the RAINBOW concept, namely the need for appropriate EQE matching between sub-cells. In a RAINBOW configuration, each sub-cell should operate close to its bandgap, within the spectral region where it exhibits its strongest absorption. If a significant spectral overlap exists between the blue and red EQE curves, as is the case over a broad wavelength range for IBC-Gen2 and the two organic sub-cells (**Figure 5-20**), the EQE of the OSC should ideally be comparable to, or higher than, to that of the IBC cell. Otherwise, an unavoidable trade-off arises between improved V_{OC} and reduced J_{SC}, which ultimately limits the benefit of spectral splitting. Because this condition is not satisfied in the present case, with the maximum EQE of the OSC reaching approximatively 60 % at 600 nm, while it exceeds 80 % for the IBC cell at the same wavelength, the relative gain achieved through spectral splitting remains limited, resulting in lower IoBC values than with IBC-Gen1.

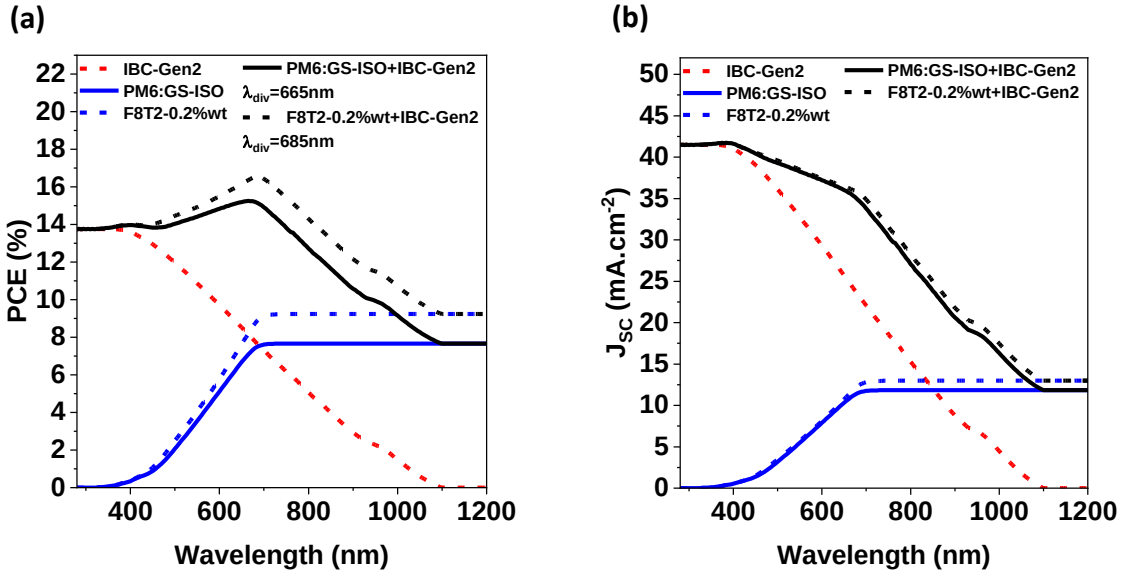

Figure 5-22: *Simulated (a) PCE and (b) J_{SC} for "blue cells": PM6:GS-ISO (full blue line) and F8T2-0.2%wt (dashed blue line); "red cell": IBC-Gen2 (dashed red line); and RAINBOW multijunction combinations involving PM6:GS-ISO + IBC-Gen2 (full black line) and F8T2-0.2%wt + IBC-Gen2 (dashed black line).*

OSC alone	PCE (%)	IBC Cell alone	PCE (%)	RAINBOW Multijunction	$PCE_{(comb,max)}$ (%)	IoBC (%)	λ_{div} (nm)
PM6:GS-ISO	7.7	**IBC-Gen1**	11.5	**PM6:GS-ISO + IBC-Gen1**	13.8	20.0	675
F8T2-0.2%wt	9.2		11.5	**F8T2-0.2%wt + IBC-Gen1**	15.1	31.6	685
PM6:GS-ISO	7.7	**IBC-Gen2**	13.5	**PM6:GS-ISO + IBC-Gen2**	15.3	13.0	665
F8T2-0.2%wt	9.2		13.5	**F8T2-0.2%wt + IBC-Gen2**	16.5	22.6	685

Table 5-7: *Experimental PCE values of the OSC and Si sub-cells measured under AM1.5G, together with the simulated $PCE_{(comb,max)}$, IoBC, and optimal dividing wavelength of the corresponding RAINBOW multijunction devices.*

Overall, these simulations demonstrate that the RAINBOW concept can significantly improve the efficiency of OPV/Si multijunction devices when the spectral responses of the individual sub-cells are sufficiently efficient and well balanced. While spectral complementarity can further enhance the benefit of spectral splitting by allowing each sub-cell to efficiently harvest different regions of the solar spectrum, high and comparable EQE values over the same spectral range can also lead to significant efficiency gains, even in the presence of substantial spectral overlap. They also highlight that maximizing the absolute efficiency of each sub-cell does not necessarily maximize the benefit provided by spectral splitting, particularly for the organic sub-cell, for which the spectral response can be tailored to complement the broad absorption range of Si. In contrast, for the Si sub-cell, maintaining a high photovoltaic performance remains essential given its broad spectral response extending up to approximately 1100 nm. This emphasizes the importance of jointly considering the individual device performance and the spectral response of the organic sub-cell when optimizing the RAINBOW architecture.

5.5.3 Experimental validation of the RAINBOW concept

a) Experimental principle and Spectrum-on-Demand setup

To validate the simulation model experimentally, each sub-cell is illuminated with a well-defined spectral fraction, and its PV performance is measured as a function of λ_{div}. This procedure is repeated over a series of λ_{div} values, thereby enabling a direct experimental reconstruction of the RAINBOW performance curves predicted by the model. The setup

employed to verify these simulations is capable of generating customized illumination spectra that are spatially homogeneous and can be dynamically modified with high accuracy (**Figure 5-23**).[238]

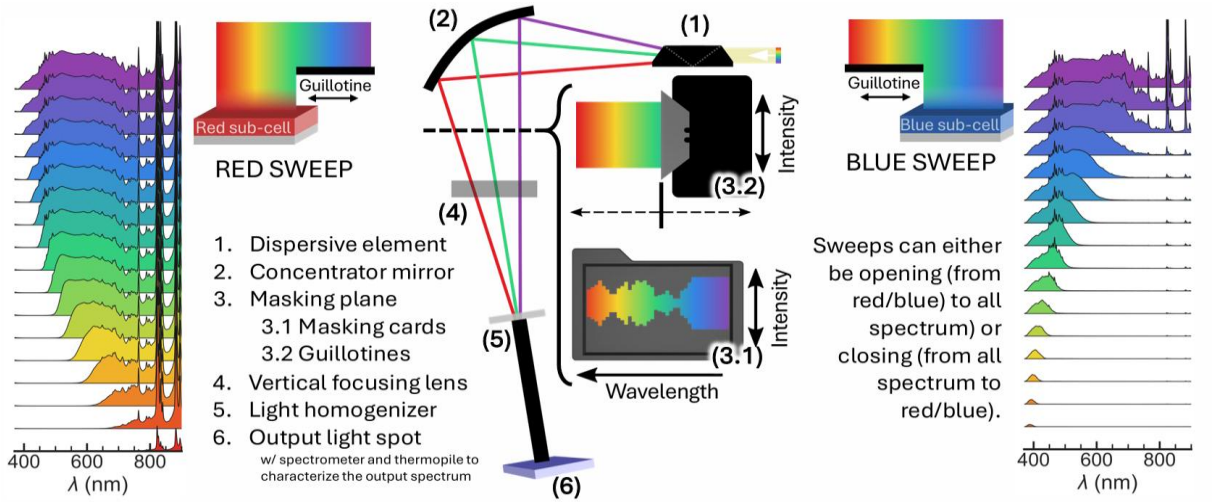

Figure 5-23: *Schematic drawing of the setup for spectrum on demand light source (SOLS) depicting its operation principle (realized by Francesc Xavier Capella Guardià).*[238]

The operating principle is based on a three-step process. First, the incident light is spatially dispersed into its individual wavelength components using a dispersive optical element. Next, the separated spectral components are selectively filtered by a dynamically controlled mask, implemented here using two motorized guillotine blades that block predefined wavelength ranges. Importantly, the instrument is not limited to producing simple spectral fractions of the solar spectrum, it can deliver fully customized spectral profiles through masks that select wavelengths ranges and their relative intensities, always within the limits imposed by the original light source. Finally, the remaining spectral components are recombined to form a spatially uniform illumination spot. This configuration enables the generation of user-defined illumination spectra on demand from a single light source, referred to as the Spectrum-On-Demand Light Source (SOLS).[238] As a result, any conventional solar simulator lamp can be transformed into a RAINBOW characterization platform, thereby enabling an experimental reproduction of the simulated RAINBOW operating conditions, particularly continuous sweeps of λ_{div} while simultaneously monitoring the PV parameters of each sub-cell.

b) Applications to OPV/Si RAINBOW lateral multijunction devices

Before validating the RAINBOW principle, it is essential to compare the PV performance obtained using both conventional Xe solar simulator and SOLS setup, from ICMAB, under full-spectrum illumination. The PV parameters of all investigated cells, measured with both setups, are summarized in **Table 5-8**.

Cell	Simulator	PCE (%)	V_{OC} (V)	J_{SC} (mA.cm^{-2})	FF
PM6:GS-ISO	**Xe**	7.7	1.13	11.8	0.57
	SOLS	8.3	1.21	10.7	0.64
F8T2-0.2%wt	**Xe**	9.2	1.16	13.0	0.61
	SOLS	8.8	1.21	11.3	0.65
IBC-Gen1	**Xe**	11.5	0.61	26.1	0.72
	SOLS	12.0	0.60	28.0	0.71
IBC-Gen2	**Xe**	13.5	0.65	41.5	0.51
	SOLS	16.2	0.64	41.4	0.61

Table 5-8: *PV parameters of PM6:GS-ISO and F8T2-0.2%wt and IBC-Gen1 and IBC-Gen2 for Xe and SOLS simulators.*

The data presented in **Table 5-8** indicate that the PV parameters measured under the conventional Xe simulator and the SOLS setup are of the same order of magnitude, although noticeable differences are observed for some devices. The differences in J_{SC} can partly be related to variations in incident light intensity, spectral distribution, and calibration between the two illumination systems. However, the variations observed in V_{OC} and FF are more difficult to explain based on these factors alone, and the origin of these differences cannot be unambiguously determined from the available measurements. Nevertheless, the overall consistency of the measured PV parameters supports the reliability of the SOLS setup for the purpose of the present study. Consequently, the PV parameters measured using the SOLS setup were used as inputs for the RAINBOW model in order to determine the experimental performance of OPV/Si lateral multijunction devices, as illustrated in **Figure 5-24, Figure 5-25** and summarized in **Table 5-9**.

The first experimental evaluation considers PM6:GS-ISO and F8T2-0.2 wt% as "blue cells" in combination with IBC-Gen1 as the "red cell". These experimental evaluated RAINBOW configurations exhibit $PCE_{(comb,max)}$ values of 14.4 % and 14.8 %, respectively, together with IoBC values of 20.0 % and 23.5 %, for λ_{div} values of 680 nm and 670 nm. These results confirm the trends predicted by the simulations, demonstrating that spectrally complementary sub-cells can yield a substantial efficiency gain over the best single-junction device, even when the absolute efficiency of the Si sub-cell is moderate.

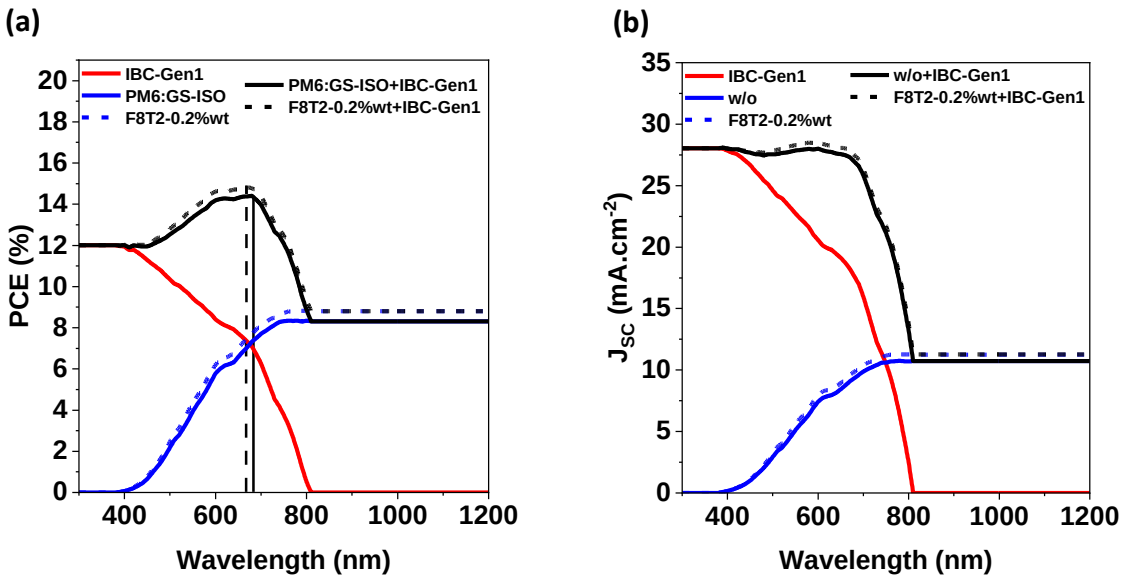

Figure 5-24: *Experimental (a) PCE and (b) J_{SC} for "blue cells": PM6:GS-ISO (full blue line) and F8T2-0.2%wt (dashed blue line); "red cell": IBC-Gen1 (full red line); and RAINBOW multijunction combinations involving PM6:GS-ISO + IBC-Gen1 (full black line) and F8T2-0.2%wt + IBC-Gen1 (dashed black line).*

The same procedure was subsequently applied for PM6:GS-ISO and F8T2-0.2 wt% as "blue cells" combined with IBC-Gen2 as the "red cell". As anticipated, the resulting RAINBOW devices exhibit higher $PCE_{(comb,max)}$ values of 17.4 % and 17.7 %, reflecting the superior performance of the IBC-Gen2 sub-cell (**Figure 5-25**). However, the corresponding IoBC values are reduced to 7.0 % and 9.2 %, respectively, with both optimal λ_{div} values located at 620 nm. This behavior is in excellent agreement with the simulation results and illustrates the trade-off between maximizing absolute efficiency and maximizing the relative gain provided by spectral splitting.

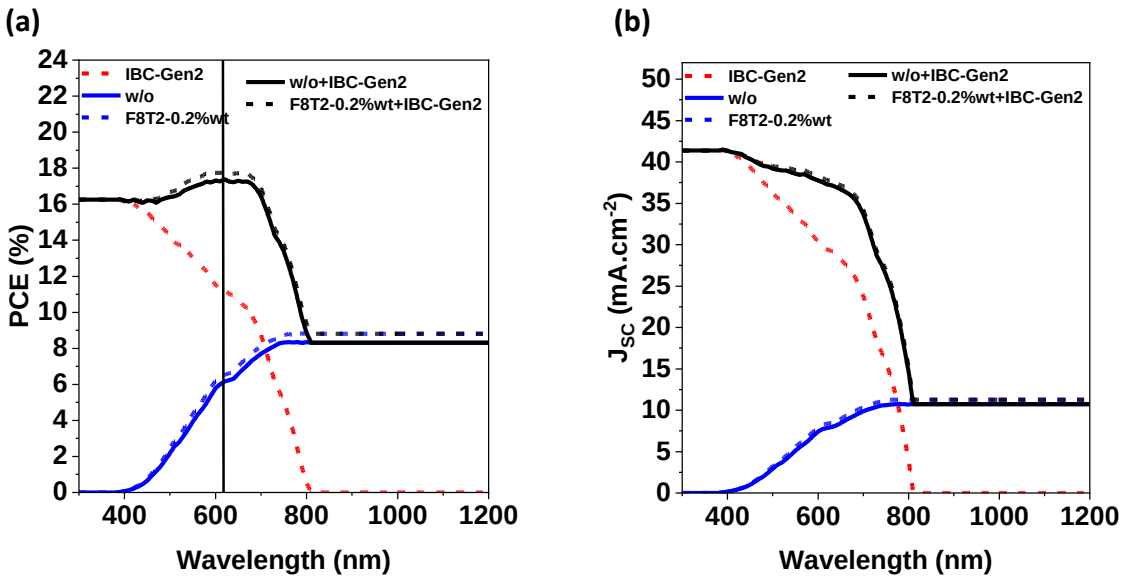

Figure 5-25: *Experimental (a) PCE and (b) J_{SC} for "blue cells": PM6:GS-ISO (full blue line) and F8T2-0.2%wt (dashed blue line); "red cell": IBC-Gen2 (dashed red line); and RAINBOW multijunction combinations involving PM6:GS-ISO + IBC-Gen2 (full black line) and F8T2-0.2%wt + IBC-Gen2 (dashed black line).*

OSC alone	PCE (%)	IBC Cell alone	PCE (%)	RAINBOW Multijunction	$PCE_{(comb,max)}$ (%)	IoBC (%)	λ_{div} (nm)
PM6:GS-ISO	8.3	**IBC-Gen1**	12.0	**PM6:GS-ISO + IBC-Gen1**	14.4	20.0	680
F8T2-0.2%wt	8.8		12.0	**F8T2-0.2%wt + IBC-Gen1**	14.8	23.5	670
PM6:GS-ISO	8.3	**IBC-Gen2**	16.2	**PM6:GS-ISO + IBC-Gen2**	17.4	7.0	620
F8T2-0.2%wt	8.8		16.2	**F8T2-0.2%wt + IBC-Gen2**	17.7	9.2	620

Table 5-9: *Experimental PCE values of the OSC and Si sub-cells measured with SOLS spectrum together with the reconstructed RAINBOW $PCE_{(comb,max)}$, IoBC and optimal λ_{div} values.*

To further validate the model, a direct comparison between the simulated and experimentally reconstructed RAINBOW performance is presented in **Figure 5-26**, focusing on the $PCE_{(comb,max)}$ and IoBC figures of merit. The comparison is performed for the four OPV/Si

combinations investigated using PM6:GS-ISO or F8T2-0.2 wt% as "blue cells" and IBC-Gen1 or IBC-Gen2 as "red cells".

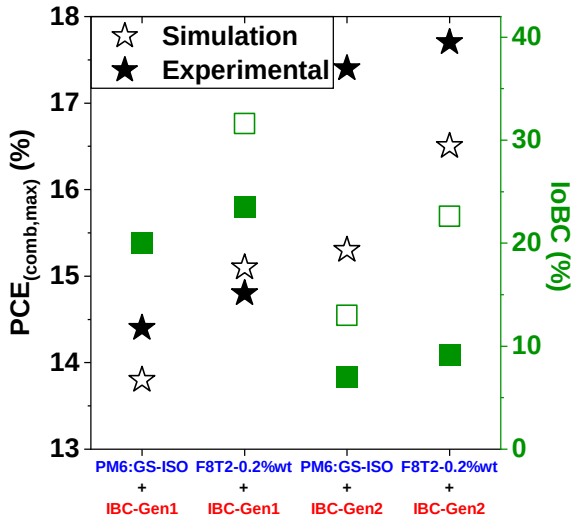

Figure 5-26: *Comparison between $PCE_{(comb,max)}$ and IoBC obtained from simulation and experiment for different OPV/Si lateral multijunctions: PM6:GS-ISO + IBC-Gen1, F8T2-0.2%wt + IBC-Gen1, PM6:GS-ISO + IBC-Gen2 and F8T2-0.2%wt + IBC-Gen2.*

Overall, the simulations reproduce the main trends observed experimentally. In particular, the higher absolute efficiency obtained with IBC-Gen2 compared with IBC-Gen1 is reproduced, as well as the lower IoBC obtained when combining the organic sub-cells with IBC-Gen2. However, noticeable quantitative differences are observed between the simulated and experimental values, particularly for IoBC, and the agreement should therefore not be considered quantitative in all cases. Several factors may contribute to these differences. First, the input parameters used for the simulations and the experimental RAINBOW measurements were obtained under different illumination conditions. The *J-V* and EQE characteristics used as inputs to the model were measured under a conventional Xe solar simulator, whereas the experimental RAINBOW measurements were performed using the SOLS developed within the project. As discussed previously, the PV parameters obtained with the two illumination systems are generally of the same order of magnitude, although noticeable differences can occur depending on the device. For the IBC-Gen2 cell, for instance, the measured PCE increases from 13.5 % under Xe simulator, to 16.2 % under the SOLS illumination system, highlighting the sensitivity of the measured PV performance to the illumination conditions. In the model, J_{SC} is calculated from the experimentally measured EQE, whereas experimentally, J_{SC} is directly measured under the SOLS illumination system. Differences in spectral distribution, incident light intensity, calibration, and optical alignment between the two systems can therefore contribute to the observed deviations. Such effects are expected to be particularly relevant for J_{SC} and, consequently, for the reconstructed RAINBOW performance. The differences are also reflected in the optimal λ_{div}. While the simulated and experimental

λ_{div} values are relatively close for the IBC-Gen1 combinations, a larger shift is observed for the IBC-Gen2 configurations, for which the experimental optimum is located at 620 nm compared with 665 and 685 nm in the simulations, for PM6:GS-ISO and F8T2-0.2wt%, respectively. This shift further indicates that the differences between the two approaches cannot be reduced to a simple scaling of the photovoltaic parameters and may result from the combined effects of the spectral response, illumination conditions, and experimental variability.

Despite these limitations, the model correctly reproduces the relative behavior of the different material combinations and provides a useful estimation of their expected RAINBOW performance. The comparison therefore supports the use of the model as a screening tool for identifying promising OPV/Si combinations, while the observed quantitative deviations emphasize that experimental validation remains necessary to accurately assess the performance of fabricated RAINBOW devices.

Equation 5-9 introduces an additional comparative parameter, denoted as IoSC (Increase over Silicon Cell). This figure of merit is particularly relevant in the context of this thesis, whose primary objective is not merely to demonstrate the superiority of a multijunction device over any given sub-cell, but rather to quantify the benefit of adding an organic top cell to a Si-based device**.**

$$IoSC = \frac{PCE_{(comb,\max)} - PCE_{Si-cell}}{PCE_{Si-cell}} \times 100 \qquad \textbf{(5-9)}$$

Figure 5-27 further illustrates this parameter by comparing the initial PCE of the Si red cell with the $PCE_{(comb,max)}$ of the corresponding OPV/Si RAINBOW lateral multijunction for each combination. For the material combinations investigated here, the integration of the organic sub-cell results in an increase in the maximum combined efficiency compared with the initial Si cell efficiency.

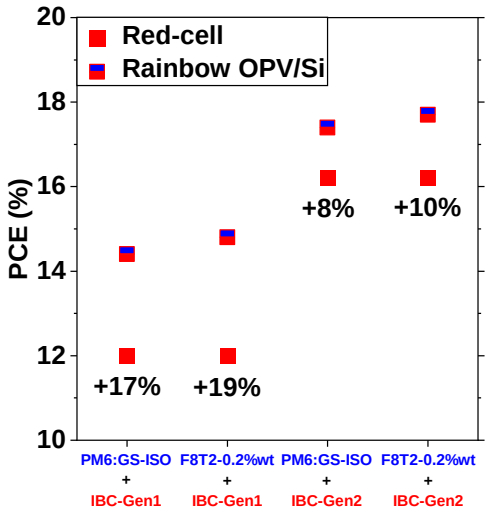

Figure 5-27: *PCE comparison between "red cells": IBC-Gen1 and IBC-Gen2; and OPV/Si lateral multijunctions: PM6:GS-ISO + IBC-Gen1, F8T2-0.2%wt + IBC-Gen1, PM6:GS-ISO + IBC-Gen2 and F8T2-0.2%wt + IBC-Gen2.*

However, the magnitude of this gain varies significantly depending on the performance and spectral response of the two sub-cells. At the same time, the results indicate that achieving a substantial efficiency gain requires not only a suitable spectral response, but also high photovoltaic performance of the individual sub-cells. In particular, for a highly efficient Si sub-cell, the organic sub-cell must combine a high PCE with a sufficiently high and appropriate EQE to provide a significant additional contribution. Therefore, the optimization of RAINBOW devices should consider both the development of high-performance sub-cells and their spectral compatibility.

Key Point 5.5: Lateral multijunction OPV/Si solar cells based on the RAINBOW concept.

- **The RAINBOW concept uses spectral splitting to independently direct different wavelength ranges toward complementary OPV and Si sub-cells, eliminating current-matching constraints while providing a scalable alternative to conventional vertical tandem architectures.**
- **The predictive model indicates that the RAINBOW architecture can achieve a maximum combined PCE of up to 16.5 % with an IoBC of up to 22.6 %, highlighting the importance of spectral complementarity between the OPV and Si sub-cells.**
- **Experimental validation using the SOLS confirmed the model predictions, achieving a maximum combined PCE of 17.7 % and demonstrating efficiency gains of up to 9.2 % over the best individual sub-cell.**

5.6. Conclusion of Chapter 5

In this chapter, the technological route toward hybrid OPV/Si tandem solar cells was successfully established. First, Gen2 IBC Si bottom cells specifically developed for tandem integration were introduced and validated. A transparent conductive interfacial architecture based on ITO was then demonstrated to be fully compatible with both the Si bottom cell and the OPV stack, while remaining compatible with the fabrication workflow implemented within the ORGANIST project. Building upon these developments, the complete fabrication protocol of a monolithic 3T OPV/Si tandem device was successfully established, including the adaptation of the deposition processes to the IBC cell geometry through dedicated sample holders. The electrical characterization of the fabricated tandem devices was then investigated in the intended 3T configuration. However, the measured response was found to be consistent with that of the Si bottom cell filtered by the organic stack, suggesting that the mechanical probes penetrated through the organic layers and established electrical contact with the Si surface rather than reliably contacting the OPV electrode. Consequently, the contribution of the organic top cell could not be independently extracted and the total 3T

tandem power could not be reconstructed. This limitation therefore concerns the hole blocking strategy rather than the fabrication of the tandem architecture itself. Although the electrical characterization of the device could not yet be finalized, the successful fabrication of the hybrid architecture together with the validation of the filtered Si bottom cell demonstrate the feasibility of the proposed integration strategy.

Finally, the RAINBOW concept was investigated as an alternative tandem architecture based on spectral splitting. Numerical simulations and experimental validation demonstrated that combining spectrally complementary OPV and Si sub-cells can significantly enhance the overall PV performance while avoiding the electrical constraints associated with conventional vertically stacked tandem devices.

Overall, this chapter demonstrates two complementary strategies toward high-efficiency hybrid OPV/Si multijunction solar cells, namely monolithic 3T integration and lateral spectral-splitting architectures. While the monolithic approach enabled the complete fabrication of the hybrid architecture and its individual technological components, the RAINBOW approach provided experimental evidence of the potential efficiency gains achievable through spectral splitting.

Chapter 6
Conclusion and Outlook

6.1. Conclusion

The increasing global demand for electricity, together with the urgent need to reduce greenhouse gas emissions, has reinforced the importance of developing PV technologies capable of delivering higher PCE while remaining compatible with large-scale industrial deployment. Although c-Si has established itself as the dominant PV technology thanks to its outstanding stability, technological maturity and certified efficiencies exceeding 27 %, it is now approaching the practical limits of single-junction solar energy conversion. In this context, tandem PV architectures have emerged as one of the most promising routes for surpassing the Shockley-Queisser limit by combining absorber materials with complementary bandgaps. Among the various candidates investigated for the fabrication of the top subcell, OPV constitute a particularly attractive solution owing to their tunable absorption spectrum, low-temperature processing and compatibility with lightweight and semi-transparent device architectures. Combined with high-efficiency IBC Si solar cells, they offer a promising pathway towards the realization of high-performance tandem PV devices. Within this context, the objective of this thesis was not limited to improving the efficiency of a single OSC. Instead, it aimed at developing the different technological building blocks required for the realization of a monolithically integrated 3T OPV/Si tandem solar cell. This objective required addressing several scientific and technological challenges extending from the optimization of the WBG organic absorber to the development of transparent electrodes compatible with fragile organic semiconductors, before ultimately investigating the integration of the semi-transparent organic top cell with high-efficiency Si bottom cells. Throughout this work, each development step was conceived as part of a global strategy directed towards the fabrication of a complete tandem device rather than as an isolated optimization.

The first stage of this work focused on the development of a WBG OSC suitable for tandem applications. Since the performance of the top subcell directly determines both its own PV conversion and the fraction of the solar spectrum transmitted towards the Si bottom cell, particular attention was devoted to the optimization of the organic solar cell with the PM6:GS-ISO blend. A systematic investigation of thermal annealing conditions, solvent engineering and conjugated solid additives was carried out in order to optimize the morphology of the photoactive layer while limiting non-radiative recombination losses. This optimization resulted in WBG OSC exhibiting PCE approaching 10 % together with V_{OC} close to 1.20 V, demonstrating that the PM6:GS-ISO system constitutes a suitable active layer for semi-transparent tandem applications. Beyond the PV performances themselves, this study established a robust processing route that served as the foundation for all subsequent developments presented throughout this manuscript.

Once the active layer had been optimized, the next challenge consisted in replacing the conventional opaque metallic electrode by a transparent conductive electrode capable of simultaneously ensuring efficient charge extraction and sufficient optical transmission towards the Si bottom cell. This aspect constitutes one of the major technological bottlenecks in the development of ST-OSC, since the transparent electrode must satisfy electrical, optical

and processing requirements that are often mutually contradictory. Rather than restricting the study to a single material, three complementary transparent electrode strategies were therefore investigated successively, each providing valuable insights into the limitations and opportunities associated with transparent contacts for tandem PV applications. The first approach explored OMO multilayer electrodes based on the MoO_3/Ag/MoO_3 architecture. Thanks to the outstanding electrical conductivity of the ultrathin silver layer, these multilayers exhibited excellent electrical conductivity while simultaneously benefiting from optical interference effects introduced by the surrounding oxide layers. A systematic optimization of the Ag thickness highlighted the critical role of multilayer optical engineering in controlling the spectral transmission of the electrode. However, despite these excellent electrical performances, the *AVT* of the optimized OMO structures remained insufficient for the targeted OPV/Si tandem configuration. The unavoidable parasitic absorption and reflection associated with the metallic layer reduced the amount of light transmitted towards the Si bottom cell, thereby limiting their relevance for tandem applications. The second transparent electrode strategy investigated in this work relied on Ag-NWs networks, which have emerged as one of the most promising alternatives to conventional TCO owing to their excellent intrinsic optoelectronic properties and compatibility with solution processing. The first developments focused on screen-printed Ag-NWs electrodes, a deposition technique particularly attractive for large-area manufacturing because of its simplicity, scalability and compatibility with industrial printing processes. The commercial Ag-NWs ink exhibited excellent optoelectronic performances, combining an *AVT* exceeding 90 % with a R_{sheet} fully compatible with ST-OSC. However, the relatively limited spatial resolution associated with the screen-printing process proved incompatible with the fine electrode geometries required for laboratory-scale PV devices. Although highly promising from an industrial perspective, this approach therefore highlighted the need for a deposition technique offering improved pattern definition while preserving the favourable optoelectronic properties of the NWs network. To overcome these limitations, the deposition process was subsequently transferred to spin coating, allowing a precise control of the NWs surface density and film homogeneity. A systematic investigation of the spin-coating parameters demonstrated the strong correlation between NWs surface coverage, R_{sheet} and optical transmission, leading to the identification of an optimum compromise between electrical conductivity and transparency. This study further confirmed that the performance of Ag-NWs electrodes is governed not only by the intrinsic properties of the NWs themselves but also by the morphology of the percolating network, which directly determines both charge transport and light transmission. The optimized spin-coated electrodes exhibited optoelectronic performances comparable to those obtained by screen printing while providing a significantly more homogeneous morphology suitable for device fabrication. Following the optimization of the Ag-NWs deposition, a laser patterning strategy was developed to define electrically isolated transparent electrodes. The systematic optimization of the laser parameters demonstrated that complete lateral electrical isolation of the NWs network could be achieved while minimizing visible damage to the surrounding layers. Nevertheless, despite the successful

electrical interruption of the Ag-NWs electrode, all fabricated PV devices systematically exhibited electrical short circuits. This unexpected result demonstrated that electrical isolation of the transparent electrode alone is insufficient to guarantee proper device operation and revealed the high sensitivity of the complete multilayer architecture to laser-induced modifications. In view of the respective advantages and limitations identified for OMO and Ag-NWs electrodes, room-temperature RF-sputtered ITO was finally selected as the most suitable transparent electrode for the remainder of this work. Unlike OMO electrodes, whose transparency remained insufficient for tandem applications, or Ag-NWs networks, whose integration was limited by patterning-related issues, sputtered ITO offered the most balanced compromise between optical transparency, electrical conductivity, process reproducibility and compatibility with the targeted tandem architecture. A comprehensive optimization of the sputtering conditions, including the oxygen partial pressure, working pressure, RF power density and film thickness, demonstrated that high-quality ITO films could be deposited at room temperature despite the absence of any thermal post-treatment. The optimized electrodes exhibited a R_{sheet} of approximately 53 $\Omega \cdot sq^{-1}$ together with an *AVT* of 87 %, values fully compatible with the fabrication of ST-OSC while preserving the integrity of the underlying organic layers. These results establish room-temperature sputtered ITO as the most mature transparent electrode technology developed throughout this thesis and the cornerstone upon which the subsequent stages of tandem integration were built.

The transparent ITO electrode developed throughout this work was subsequently integrated into complete ST-OSC. Particular attention was devoted to preserving the electrical performance of the optimized PM6 active layer while ensuring efficient charge extraction through the transparent top contact. Since RF magnetron sputtering is generally regarded as a potentially damaging process for organic semiconductors, the development of a suitable interfacial layer proved to be a critical step. In this respect, the introduction of a thin MoO_3 layer successfully fulfilled a dual function. Besides acting as an efficient hole-transporting material, it also provided effective protection of the underlying organic stack against plasma-induced damage during the sputtering process. The combination of the optimized room-temperature ITO deposition and the MoO_3 interfacial layer resulted in ST-OSC exhibiting PCE approaching 6 %, while maintaining high V_{OC} and good optical transparency. These results demonstrate that transparent electrodes deposited by sputtering can be successfully integrated into high-performance OPV devices, provided that appropriate interface engineering is implemented. Beyond the PM6:GS-ISO system that constituted the main focus of this thesis, the transferability of the developed transparent electrode strategy was also investigated using alternative OPV technologies. The successful fabrication of semi-transparent devices based on different active layer systems demonstrated that the optimized sputtering process is not restricted to a single material combination but instead constitutes a versatile platform applicable to a broader range of OPV architectures.

Having established a reliable semi-transparent organic top cell, the final objective consisted in evaluating its compatibility with high-efficiency c-Si bottom cells. Before transferring the complete architecture to the IBC bottom cells, the compatibility of the

selected ITO interfacial layer with the organic photovoltaic stack was systematically investigated on heavily doped Si(n^+) substrates. A preliminary comparison between ITO and AZO using P3HT:PCBM demonstrated that both TCO-based architectures were compatible with the OPV deposition process, while the slightly higher photovoltaic performance obtained with ITO supported its selection for the subsequent integration steps. The selected Si(n^+)/ITO architecture was then validated with the PM6:GS-ISO system developed throughout this thesis. Despite a reduction in PCE compared with reference devices fabricated on glass/ITO, the preservation of a clear photovoltaic response confirmed that the targeted WBG organic stack could be successfully processed on the Si-based interfacial architecture. These results provided the necessary process validation before transferring the architecture to complete IBC Si bottom cells.

The optical and electrical characterizations of the IBC, performed after integration demonstrated that the monolithically integrated OSC transmitted a significant fraction of the incident solar spectrum towards the IBC Si bottom cell while preserving its characteristic photovoltaic behavior. Although a reduction in the J_{SC} was naturally observed owing to the absorption occurring within the organic top cell, the J_{SC} decreased from 29.5 mA.cm^{-2} for the bare IBC-Gen2 cell to 12.0 and 13.0 mA.cm^{-2} after integration of the PM6:GS-ISO and PTQ10:FCC-Cl stacks, respectively. Importantly, the V_{OC} and FF remained comparable. These results indicate that the reduction in photocurrent primarily originates from optical filtering by the organic stack rather than from a significant degradation of the Si electrical properties. The Si devices maintained their characteristic diode behavior and no significant degradation associated with the fabrication of the semi-transparent organic stack was identified. These results therefore validate the compatibility between the two subcells and constitute an essential milestone towards the realization of a monolithically integrated OPV/Si tandem device. The complete integration process was also successfully transferred to the 21.8 × 21.8 mm² IBC cells, with dedicated sample holders developed for the successive deposition of the organic stack, MoO_3, ITO and Ag busbars. This adaptation enabled the use of the deposition protocols established on laboratory-scale OPV devices while accommodating the specific geometry and contacting requirements of the IBC cells. Beyond the simple demonstration of optical compatibility, this work also addressed one of the major challenges associated with monolithic tandem PV, namely the development of an appropriate interconnection strategy between the organic and Si subcells. In this context, the 3T architecture investigated throughout this thesis offers an attractive alternative to conventional 2T tandem devices by relaxing the stringent current-matching constraint while preserving the compactness of a monolithic structure. Although the monolithic 3T structure was successfully fabricated, the contribution of the OPV subcell could not be selectively measured. The measured V_{OC} and J_{SC} were instead very close to those obtained for the Si bottom cell filtered by the organic stack, indicating that the measured response was not representative of the OPV subcell alone. One possible explanation is related to the charge selectivity of the interfacial ITO/ZnO layer. Indeed, its charge selectivity may not be sufficient in the monolithic 3T architecture to prevent photogenerated holes from the Si bottom cell from contributing to the front-side contact.

Consequently, the measured response may contain a significant contribution from the Si bottom cell, preventing the selective extraction of the OPV contribution. This interpretation remains a hypothesis, as the exact electrical pathways involved in the 3T measurement could not be directly verified. Nevertheless, the successful fabrication and integration of the different components demonstrate the feasibility of the proposed monolithic architecture and highlight the charge selectivity of the interfacial stack as a key issue for achieving selective electrical extraction in the 3T configuration.

Finally, this work used the RAINBOW concept, which aims to exploit the complementary advantages of different PV technologies, notably OPV and c-Si, through innovative lateral multijunction architectures. Throughout this thesis, the development of a monolithically integrated OPV/Si tandem device highlighted the numerous technological challenges associated with such an approach, including the fabrication of ST-OSC, the development of suitable transparent electrodes, interface engineering, and the integration and characterization of the complete 3T architecture. In parallel, the RAINBOW concept proposes an alternative strategy that circumvents many of these fabrication constraints by combining independently optimized PV devices within lateral multijunction configurations based on spectral splitting. This approach enables the rapid evaluation and optimization of hybrid OPV/Si associations without requiring the complex monolithic integration process. Within the framework of the project, several lateral OPV/Si multijunction architectures were experimentally demonstrated, yielding a maximum combined PCE of 17.7 % with IoBC of 9.2 %. These encouraging results confirm the potential of hybrid OPV/Si PV systems while providing valuable guidelines for the future development of fully integrated monolithic tandem architectures.

Overall, this thesis demonstrates that the successful realization of an OPV/Si tandem solar cell cannot rely on the optimization of a single component but instead requires the simultaneous development of interconnected technological building blocks spanning materials engineering, transparent electrode design, interface optimization and device integration. By adopting this comprehensive approach, this work not only provides practical solutions to several key technological challenges but also establishes a coherent experimental framework upon which future developments towards high-efficiency monolithic 3T terminal tandem solar cells can be built. More broadly, the results demonstrate that the main technological barriers to monolithic OPV/Si integration can be addressed through the coordinated optimization of the organic absorber, transparent electrode, interfacial layer and Si integration process, while also highlighting the electrical and technological challenges that remain before fully optimized 3T tandem operation can be achieved.

6.2. Outlook

The work presented throughout this thesis has demonstrated the feasibility of developing the main technological building blocks required for the realization of monolithic 3T OPV/Si tandem solar cells. Nevertheless, several scientific and technological challenges remain before this concept can reach its full potential. The future development of hybrid

OPV/Si tandem PV will rely not only on incremental improvements of each individual component but also on the simultaneous optimization of materials, interfaces and device architectures. The following perspectives therefore outline the main research directions that naturally emerge from the results obtained during this work.

A first avenue for future research concerns the continued development of WBG absorbers specifically designed for semi-transparent tandem applications. Although the PM6:GS-ISO system investigated throughout this thesis proved to be an excellent candidate, combining PCE approaching 10 % with V_{OC} close to 1.20 V, the field of OPV is evolving at an exceptionally rapid pace. In recent years, newly developed WBG donor and NFA materials have enabled certified efficiencies exceeding 19 % in single-junction OSC, with bandgaps of approximately equals to 1.5 eV, while maintaining V_{OC} over 1.0 V.[239] Future tandem devices could benefit from the integration of these next-generation materials, provided that their optical properties remain compatible with the spectral requirements imposed by the Si bottom cell. However, improving the efficiency of the organic top cell alone will not necessarily translate into higher tandem performances. Unlike conventional single-junction devices, ST-OSC require a careful balance between electrical conversion and optical transmission. Future active-layer systems should therefore be designed not only to maximize charge generation and minimize non-radiative recombination losses, but also to selectively absorb the high-energy part of the solar spectrum while transmitting near-infrared photons towards the c-Si bottom cell. In this respect, molecular design strategies enabling precise control of the absorption profile, together with advanced morphology engineering approaches, are expected to play a central role in the next generation of WBG organic absorbers.[219]

The second major challenge concerns the transparent electrode, which remains one of the key limiting components for semi-transparent OPV. Throughout this thesis, four complementary transparent electrode approaches were investigated, each exhibiting specific advantages and limitations. Although room-temperature RF-sputtered ITO ultimately emerged as the most suitable solution for the targeted tandem architecture, none of the investigated electrodes can yet be regarded as an ideal transparent contact. Consequently, the continued development of transparent electrodes remains a major research direction for future OPV/Si tandem solar cells. The room-temperature sputtering process developed during this work already demonstrated that TCO can be deposited directly onto sensitive organic semiconductors without significantly degrading device performance. Nevertheless, additional improvements remain possible. Further optimization of the plasma conditions could reduce the Rsheet while maintaining high *AVT*, thereby improving both charge collection and optical transmission. Alternative TCO, including hydrogenated indium oxide (IO:H),[240] indium zinc oxide (IZO)[241] or aluminium-doped zinc oxide (AZO),[242] also represent promising candidates that could combine lower free-carrier absorption with improved electrical conductivity. Beyond the choice of material itself, future investigations should focus on understanding the relationships between sputtering conditions, film microstructure and plasma-induced damage, with the objective of further extending the compatibility of PVD techniques with increasingly fragile organic semiconductors. Although sputtered ITO emerged as the most

suitable transparent electrode within the scope of this work, the search for the ideal transparent contact remains an open challenge. Each of the electrode technologies investigated throughout this thesis highlighted a different aspect of the complex compromise between electrical conductivity, optical transparency, process compatibility and device integration. Consequently, future developments should not necessarily focus on replacing ITO, but rather on identifying whether and how the strengths of the different approaches explored in this work. The OMO architecture remains particularly attractive owing to its outstanding electrical properties and its ability to efficiently collect photogenerated charges. Future work should therefore focus on increasing its optical transparency while preserving its excellent conductivity. This could be achieved through the optimization of the dielectric layers, the investigation of alternative high-refractive-index materials, or the replacement of silver by thinner or less absorbing metallic layers. More advanced optical modeling could also provide valuable guidelines for tailoring the interference effects within the multilayer and maximizing the light transmitted towards the Si bottom cell. Such developments could eventually enable OMO electrodes to satisfy the stringent optical requirements imposed by semi-transparent OPV/Si tandem devices. Ag-NWs networks also remain a highly promising technology despite the limitations encountered during this thesis. Their exceptional combination of low R_{sheet}, high optical transparency and compatibility with solution processing makes them attractive candidates for future large-area and flexible PV modules. However, the systematic occurrence of electrical short circuits following laser patterning clearly demonstrated that the successful integration of Ag-NWs extends beyond the optimization of the transparent electrode itself. Future investigations should therefore aim at understanding the physical origin of these residual conductive pathways using advanced cross-sectional electron microscopy and electrical failure analysis. Alternative electrode patterning strategies, including mechanical scribing, selective chemical etching, ultrashort-pulse laser processing or direct printed patterning, could also be explored to eliminate thermal damage while maintaining the advantages of solution-processed transparent electrodes. Overcoming these challenges would considerably broaden the range of transparent electrodes available for future tandem PV technologies.

Beyond the transparent electrode itself, interface engineering is expected to play an increasingly important role in the development of ST-OSC. The protective function demonstrated by the thin MoO_3 interfacial layer confirms that appropriate interface design can simultaneously improve charge extraction and preserve the integrity of the underlying organic layers during sputtering deposition. Nevertheless, further improvements remain possible. Alternative transition metal oxides, self-assembled monolayers or hybrid interfacial materials could provide improved energy level alignment while offering enhanced protection against plasma-induced damage. In parallel, a better understanding of the degradation mechanisms occurring at buried interfaces will be essential for improving both the operational stability and the long-term reliability of ST-OSC. In particular, combining spectroscopic, structural and electrical characterization techniques could help distinguish between chemical degradation, morphological modifications and electrically active defects generated during

electrode deposition. Such an understanding would provide a more rational basis for the design of protective interlayers and deposition processes.

The interfacial architecture developed between the Si bottom cell and the organic top cell also offers several opportunities for further optimization. The preliminary results obtained on Si(n^+) demonstrated that both ITO- and AZO-based architectures can support the deposition of the OPV stack, while the subsequent validation with PM6:GS-ISO confirmed the suitability of the Si/ITO interface for the targeted organic absorber. Future work should therefore investigate this interface from the perspective of the complete tandem device, with particular attention to the optical and electrical losses introduced by the TCO and ZnO layers. Optimization of the TCO thickness, carrier concentration and optical properties, together with improved control of the ZnO morphology and interfacial energetics, could further increase the transmission of photons towards the Si absorber while minimizing resistive losses. In addition, the charge selectivity of the interfacial layer should be specifically investigated in the context of the 3T architecture. The results obtained in this thesis suggest that the ITO-based interfacial stack may not provide sufficient charge selectivity to enable the independant extraction of the OPV contribution. Future work should therefore aim at identifying transparent conductive materials and interfacial architectures combining high optical transparency and electrical conductivity with suitable energy-level alignment to promote electron transport from the organic subcell while suppressing the contribution of photogenerated holes from the Si bottom cell. Importantly, this issue is not specific to the OPV system investigated in this thesis. More generally, the charge selectivity of the interfacial layer is expected to be a critical consideration for monolithic 3T architectures combining an IBC Si bottom cell with any WBG top-cell technology. Regardless of the nature of the WBG absorber, the interfacial stack must simultaneously provide efficient charge transport from the top cell and prevent unwanted carrier extraction from the Si bottom cell. Therefore, the development of selective transparent interfacial contacts could represent a key enabling step for the broader development of monolithic 3T tandem solar cells.

The next major milestone naturally concerns the realization of a fully optimized monolithic 3T OPV/Si tandem solar cell. While this thesis demonstrated the compatibility between the semi-transparent organic top cell and IBC Si devices, several challenges remain before the full potential of this architecture can be exploited. Future work should focus on establishing a sufficiently selective electrical pathway between the two subcells, while minimizing optical losses throughout the complete multilayer stack and reducing parasitic resistive losses associated with the monolithic integration process. A key objective will therefore be to develop an interfacial architecture enabling efficient electron transport from the OPV subcell towards the n-type Si contact while suppressing hole transport from the Si bottom cell towards the front-side electrode. Such selective charge transport is essential to enable the independent electrical extraction of the two subcells and, ultimately, the reconstruction of the total 3T tandem power. In this context, numerical simulations could provide valuable guidance for the rational design of the interfacial stack. By combining optical and electrical modeling with the electronic properties of candidate TCO and interfacial

materials, it should be possible to screen materials according to their energy-level alignment, carrier selectivity, optical transmission and electrical conductivity. Such an approach could help identify transparent conductive materials and interfacial architectures offering a more favourable balance between electron transport from the OPV subcell and hole blocking at the Si interface than the ITO-based architecture investigated in this thesis. In addition, optical simulations combined with experimental investigations could be employed to optimize the thickness of each functional layer and maximize the complementary absorption of the two PV technologies. Such a global optimization strategy, considering the tandem device as a single integrated system rather than two independent subcells, is expected to provide the largest improvements in overall PV performance.

Beyond the electrical selectivity of the interfacial layer, future studies should also investigate the complete energy-loss of the 3T architecture. Quantifying the contributions of parasitic absorption, reflection, imperfect charge extraction and resistive losses would make it possible to identify the most limiting components of the integrated device. In this respect, coupling optical and electrical modeling with experimentally measured EQE and *J-V* characteristics could provide a direct framework for guiding the optimization of both subcells and their interfaces. Such an approach would be particularly relevant for determining the optimum spectral response of the organic top cell, rather than optimizing its standalone efficiency independently of the Si bottom cell.

Finally, the developments achieved throughout this thesis also contribute to a new vision extending beyond monolithic tandem integration. As demonstrated within the framework of the RAINBOW concept, the realization of a fully integrated OPV/Si tandem device requires numerous successive fabrication, integration and characterization steps, making the rapid evaluation of new material combinations particularly time-consuming. To overcome these limitations, the RAINBOW concept proposes an alternative research strategy based on lateral multijunction architectures, in which independently optimized PV devices are associated through spectral splitting rather than vertical monolithic stacking. Such an approach provides a versatile experimental platform for rapidly assessing the complementarity between different PV technologies without requiring the complete fabrication of a monolithic tandem device. Within the project, several lateral OPV/Si associations have already demonstrated a maximum combined PCE of 17.7 %, with an IoBC of 9.2 %, thereby confirming the considerable potential of hybrid PV systems. More importantly, this methodology represents a powerful screening tool that enables the rapid exploration of numerous multijunction combinations, including OPV/OPV, OPV/Si, PSC/OPV, PSC/Si, and potentially other emerging PV technologies. By allowing each subcell technology to be independently optimized before evaluating their spectral complementarity, the RAINBOW concept can accelerate the identification of the most promising material associations while providing valuable guidelines for the future development of fully integrated monolithic tandem devices.

Overall, the results presented throughout this thesis demonstrate that the development of high-performance OPV/Si tandem solar cells relies on the convergence of

advances in organic semiconductor design, transparent electrode engineering, Si/OPV interfacial architecture, and device integration. Although several scientific and technological challenges remain, the rapid progress achieved in OPV and multijunction cells over the past decade strongly suggests that hybrid OPV/Si tandem PV is evolving from a proof-of-concept technology towards a realistic solution for next-generation PV energy conversion. By establishing robust processing methodologies and identifying the key technological bottlenecks that still need to be overcome, from the optimization of the WBG organic absorber and transparent electrode to the validation of the Si/ITO interfacial architecture, the identification of charge-selectivity limitations in the 3T configuration, and the integration of IBC Si bottom cells, this work provides a solid foundation upon which future developments towards efficient monolithic 3T OPV/Si tandem solar cells can be built.

Glossary

PV	Photovoltaic
NREL	National Renewable Energy Laboratory
c-Si	Mono-Crystalline Silicon
mc-Si	Multi-Crystalline Silicon
GaAs	Gallium Arsenide
CIGS	Copper Indium Gallium diselenide
CdTe	Cadmium Telluride
CdS	Cadmium Sulphide
a-Si:H	Hydrogenated Amorphous Silicon
PECVD	Plasma-Enhanced Chemical Vapor Deposition
CVD	Chemical Vapor Deposition
OSC	Organic Solar Cells
PSC	Perovskite Solar Cells
QD	Quantum Dots Solar Cells
DSSC	Dye-Sensitized Solar Cells
PCE	Power Conversion Efficiency
SQ	Shockley-Queisser
AM1.5G	Air Mass 1.5 Global
LCOE	Levelized Cost Of Electricity
OPV	Organic Photovoltaic
OPV/Si	Organic on Silicon Tandem Cell
2/3/4T	Two/Three/Four-Terminal configuration
ANR	French National Research Agency
ST-OSC	Semi-Transparent Organic Solar Cell
PE	Photoelectric
eV	Electron Volt
E_V	Valence Band Energy
E_C	Conduction Band Energy
E_g	Electronic Bandgap
CZ	Czochralski
V_{OC}	Open-Circuit Voltage
PERC	Passivated Emitter and Rear Cell

TOPCon	Tunnel Oxide Passivated Contact
SHJ	Silicon Heterojunction with Intrinsic Thin Layer
IBC	Interdigitated Back Contact
J_{SC}	Short-Circuit Current
FF	Fill Factor
TCO	Transparent Conductive Oxides
D_{it}	Interface Trap Density
SRV	Surface Recombination Velocity
ARC	Antireflective Coating
Al_2O_3	Aluminum Oxide
SiO_x	Silicon Oxide
SiN_x	Silicon Nitride
HOMO	Highest Occupied Molecular Orbital
LUMO	Lowest Unoccupied Molecular Orbital
$E_{g,opt}$	Optical Bandgap
λ_{Edge}	Cutoff Wavelength
h	Planck's Constant
c	Speed of Light
E_b	Binding Energy
BHJ	Bulk Heterojunction
CT	Charge-Transfer
μ_e	Electron Mobility
μ_h	Hole Mobility
HTL	Hole Transport Layer
ETL	Electron Transport Layer
TCL	Transparent Conductive Layer
PAL	Photoactive Layer
PCBM	[6,6]-phenyl-C_{61}-butyric acid methyl ester
NFA	Non-Fullerene Acceptor
LBG	Low Bandgap
PL	Photoluminescence
EL	Electroluminescence

TAS	Transient Absorption Spectroscopy
WBG	Wide Bandgap
PVD	Physical Vapor Deposition
Ag	Silver
MoO_3	Molybdenum Trioxide
Ar^+	Argon ions
RF	Radiofrequency
ITO	Indium Tin Oxide
J-V	Current-Voltage measurement
θ	Solar zenith angle
R_{SH}	Shunt Resistance
R_S	Series Resistance
J_0	Saturation current density
n	Diode ideality factor
q	Elementary charge
k	Boltzmann constant
T	Temperature
J_{MPP}	Current Density at the Maximum Power Point
V_{MPP}	Voltage at the Maximum Power Point
P_{MPP}	Power Density at the Maximum Power Point
P_{IN}	Incident illumination Power
R_{sheet}	Sheet Resistance
SCLC	Space-Charge-Limited-Current
n_0	Equilibrium free carrier concentration
L	Active layer thickness
V_{TF}	Trap-Filled Limit Voltage
ε_0	Vacuum permittivity
ε_r	Relative dielectric constant
TPV	Transient Photovoltage
LED	Light-Emitting Diode
τ_{fast}	Fast decay component

τ_{slow}	Slow decay component
α	Indicator of extraction losses
ISOS	International Summit on Organic Solar Cells
ISOS-D	Aging under dark storage
ISOS-L	Aging under atmospheric Exposure
ISOS-T	Aging under thermal Stress
ISOS-L/O	Aging under continuous Illumination
T_{80}	Time required to reach 80 % of its initial PCE
T_{50}	Time required to reach 50 % of its initial PCE
SEM	Scanning Electron Microscopy
W	Tungsten
SE	Secondary Electrons
BSE	Backscattered Electrons
AFM	Atomic Force Microscopy
RMS	Root-Mean-Square
γ_{SV}	Solid-Vapor surface energy
γ_{SL}	Solid-Liquid surface energy
γ_{LV}	Liquid-Vapor surface energy
$A(\lambda)$	Absorbance
$I_0(\lambda)$	Incident light Intensity
$I(\lambda)$	Transmitted Intensity
$\alpha(\lambda)$	Absorption coefficient
EQE	External Quantum Efficiency
N_E	Number of collected charge carriers
N_{Ph}	Number of incident photons
$\phi_{Ph}^{AM\ 1.5G}$	Photon flux of the reference AM 1.5G spectrum
I_{Ph}	Photocurrent
GIWAXS	Grazing Incidence Wide-Angle X-ray Scattering
PBDB-T-2F	Poly[(2,6-(4,8-bis(5-(2-ethylhexyl)-4-fluorothiophen-2-yl)-benzo[1,2-b:4,5-b']dithiophene))-alt-(5,5-(1',3'-di-2-thienyl-5',7'-bis(2-ethylhexyl)benzo[1',2'-c:4',5'-c']dithiophene-4,8-dione))]

ZnO	Zinc Oxide
Ca	Calcium
Al	Aluminum
SBOB	Selective Band-Offset Barrier
PTFE	Polytetrafluoroethylene
D:A Ratio	Donor-to-Acceptor Ratio
FWHM	Full Width at Half Maximum
$\mathbf{D_{avg}}$	Average grain size
$\mathbf{\sigma_{rms}}$	Root-Mean-Square roughness
DIO	1,8-diiodooctane
F8T2	Poly[(9,9-dioctylfluorenyl-2,7-diyl)-co-(2,2'-bithiophene-5,5'-diyl)]
IP	In-Plane
OOP	Out-Of-Plane
$\mathbf{I_{light}}$	Light Intensity
P	Dissociation Probability
γ	Bimolecular recombination rate coefficient
$\mathbf{N_C}$	Effective density of states
G	Photogeneration rate
IoT	Internet of Things
IOPV	Indoor OPV
FL	Fluorescent Lamps
CCT	Correlated Color Temperature
lx	Lux
BIPV	Building-Integrated Photovoltaics
AVT	Average Visible Transmittance
$\mathbf{AT_{300\text{-}1000nm}}$	Average Transmittance over the 300-1000nm range
$\mathbf{T(\lambda)}$	Film transmittance
$\mathbf{V(\lambda)}$	Photopic luminous efficiency
OMO	Oxide-Metal-Oxide
Ag-NWs	Silver Nanowires
$\mathbf{T_{max}}$	Maximum visible transparency
$\mathbf{C_{NWs}}$	Nanowires surface coverage

R_C	Contact Resistance
φ	Surface power density
p	Working pressure
Ar/O_2	Argon-to-oxygen flow ratio
t	Thickness
LPICM	Laboratoire de Physique des Interfaces et Couches Minces
T_{avg}	Transmittance over the absorption range of the active material
FOM	Figure of Merit
ICMAB	Institut de Ciència de Materials de Barcelona
ISC Konstanz	International Solar Energy Research Center Konstanz
GeePs	Laboratoire de Génie Electrique de Paris
IBC-Gen1	First-Generation IBC
FSF	Front Surface Field
IBC-Gen2	Second-Generation IBC
a-Si:H/nc-SiO_x	Hydrogenated Amorphous Silicon/Nanocrystalline Silicon Oxide
AZO	Aluminum-doped Zinc Oxide
λ_{div}	Dividing wavelength
$E_{e,\lambda}(\lambda)$	Solar spectral irradiance
$\varepsilon_{ph}(\lambda)$	Photon energy
q_e	Electron electric charge
IoBC	Increase over Best Cell
Xe	Xenon
SOLS	Spectrum On Demand Light Source
IoSC	Increase over Silicon Cell
ITO:H	Hydrogenated Indium Tin Oxide
IZO	Indium Zinc Oxide
AZO	Aluminum-doped Zinc Oxide

References

[1] "Energy Institute - Statistical Review of World Energy (2025) – with major processing by Our World in Data," (2025).

[2] "World Electricity Generation," (2025).

[3] Nrel, *NREL Best Research-Cell Efficiencies Chart* (1976).

[4] T. Béjat, N. Gazbour, A. Boulanger, R. Monna, R. Varache, J. François, W. Favre, C. Roux, A. Derrier, and E. Voroshazi, "Design for the environment: SHJ module with ultra-low carbon footprint," Progress in Photovoltaics: Research and Applications **33**(1), 184–199 (2025).

[5] H. Nishiwaki, K. Uchihashi, K. Takaoka, M. Nakagawa, H. Inoue, A. Takeoka, S. Tsuda, and M. Ohnishi, "Development of an ultralight, flexible a-Si solar cell submodule," Solar Energy Materials and Solar Cells **37**(3–4), 295–306 (1995).

[6] N. Shah, A.A. Shah, P.K. Leung, S. Khan, K. Sun, X. Zhu, and Q. Liao, "A Review of Third Generation Solar Cells," Processes **11**(6), (2023).

[7] X. Zhao, and N.-G. Park, "Stability Issues on Perovskite Solar Cells," Photonics **2**(4), 1139–1151 (2015).

[8] M.A. Green, E.D. Dunlop, M. Yoshita, N. Kopidakis, K. Bothe, G. Siefer, D. Hinken, M. Rauer, J. Hohl-Ebinger, and X. Hao, "Solar cell efficiency tables (Version 64)," Progress in Photovoltaics: Research and Applications **32**(7), 425–441 (2024).

[9] A. Richter, M. Hermle, and S.W. Glunz, "Reassessment of the Limiting Efficiency for Crystalline Silicon Solar Cells," IEEE J. Photovolt. **3**(4), 1184–1191 (2013).

[10] L. Wang, N. Wang, X. Wu, B. Liu, Q. Liu, B. Li, D. Zhang, N. Kalasariya, Y. Zhang, X. Yan, J. Wang, P. Zheng, J. Yang, H. Jin, C. Wang, L. Qian, B. Yang, Y. Wang, X. Cheng, T. Song, M. Stolterfoht, X.C. Zeng, X. Zhang, M. Xu, Y. Bai, F. Xu, C. Zhou, and Z. Zhu, "Highly Efficient Monolithic Perovskite/TOPCon Silicon Tandem Solar Cells Enabled by 'Halide Locking,'" Advanced Materials **37**(7), (2025).

[11] M. Kaltenbrunner, M.S. White, E.D. Głowacki, T. Sekitani, T. Someya, N.S. Sariciftci, and S. Bauer, "Ultrathin and lightweight organic solar cells with high flexibility," Nat. Commun. **3**(1), 770 (2012).

[12] B. Lee, L. Lahann, Y. Li, and S.R. Forrest, "Cost estimates of production scale semitransparent organic photovoltaic modules for building integrated photovoltaics," Sustain. Energy Fuels **4**(11), 5765–5772 (2020).

[13] R. Zeng, F. Han, W. Zhong, M. Zhang, S. Tan, Y. Lin, J. Deng, G. Zhou, L. Kan, L. Zhu, X. Gao, J. Zhu, W. Zhao, S. Xu, X. Xue, B. Hao, Z. Zhou, X. Wu, C. Wang, Z. Fink, Z. Tang, H. Jing, T.P. Russell, Y. Zhang, and F. Liu, "Lowering Toxicity of Solvent in Organic Solar Cells Manufacturing for 20% Efficiency," Advanced Materials **37**(28), (2025).

[14] Edmond Becquerel, "On electric effects under the influence of solar radiation," Compt. Rend. **9**, 561 (1839).

[15] H. Hertz, “Ueber sehr schnelle electrische Schwingungen,” Ann. Phys. **267**(7), 421–448 (1887).

[16] Albert Einstein, “Über einem die Erzeugung und Verwandlung des Lichtes betreffenden heuristischen Gesichtspunkt,” Ann. Phys. **4**, 132–148 (1905).

[17] S.. Amelinckx, *Electron Microscopy : Principles and Fundamentals* (VCH, 1997).

[18] A.S. Al-Ezzi, and M.N.M. Ansari, “Photovoltaic Solar Cells: A Review,” Applied System Innovation **5**(4), 67 (2022).

[19] E. Płaczek-Popko, “Top PV market solar cells 2016,” Opto-Electronics Review **25**(2), 55–64 (2017).

[20] S. Binetti, M. Acciarri, A. Le Donne, M. Morgano, and Y. Jestin, “Key Success Factors and Future Perspective of Silicon-Based Solar Cells,” International Journal of Photoenergy **2013**, 1–6 (2013).

[21] Q. Wang, K. Guo, S. Gu, W. Huang, H. Peng, W. Wu, and J. Ding, “Electrical Performance, Loss Analysis, and Efficiency Potential of Industrial-Type PERC, TOPCon, and SHJ Solar Cells: A Comparative Study,” Progress in Photovoltaics: Research and Applications **32**(12), 889–903 (2024).

[22] S. Foroushani, A. Wintzer, F.-M. Kiessling, and K. Dadzis, “Heating efficiency and energy saving potential of Czochralski crystal growth furnaces,” J. Cryst. Growth **662**, 128106 (2025).

[23] L. Méndez, E. Forniés, D. Garrain, A.P. Vázquez, A. Souto, and T. Vlasenko, “Upgraded Metallurgical Grade Silicon for solar electricity production: a comparative Life Cycle Assessment,” (2021).

[24] PERC cell Efficiency Achieves 24.5%, Trinasolar, 2022.

[25] JinkoSolar achieves world record efficiency of 27.02% for TOPCon solar cell, PV Magazine, 2025.

[26] Trina Solar hits a new 27.08% record for HJT solar cell, PV Magazine, 2024.

[27] N. Chen, A. Ebong, Y. Zhang, E.B. Stokes, M. Yasin, and T. Schmitz, "*Understanding and development of cost-effective industrial aluminum back surface field (Al-BSF) silicon solar cells*", Doctoral dissertation, (2015).

[28] IBC Solar Cells: Definition, Benefits, vs. Similar Techs, Solar Magazine, 2022.

[29] C. Ballif, F.-J. Haug, M. Boccard, P.J. Verlinden, and G. Hahn, “Status and perspectives of crystalline silicon photovoltaics in research and industry,” Nat. Rev. Mater. **7**(8), 597–616 (2022).

[30] T.G. Allen, J. Bullock, X. Yang, A. Javey, and S. De Wolf, “Passivating contacts for crystalline silicon solar cells,” Nat. Energy **4**(11), 914–928 (2019).

[31] Longi revendique le record mondial d'efficacité pour les cellules solaires en silicium, PV Magazine, 2025.

[32] A. Froitzheim, R. Stangl, L. Elstner, M. Schmidt, and W. Fuhs, “Interface recombination in amorphous/crystalline silicon solar cells, a simulation study,” in *Conference Record of the Twenty-Ninth IEEE Photovoltaic Specialists Conference, 2002.*, (IEEE, n.d.), pp. 1238–1241.

[33] J.G. Fossum, R.P. Mertens, D.S. Lee, and J.F. Nijs, “Carrier recombination and lifetime in highly doped silicon,” Solid. State. Electron. **26**(6), 569–576 (1983).

[34] A. Zaban, M. Greenshtein, and J. Bisquert, “Determination of the Electron Lifetime in Nanocrystalline Dye Solar Cells by Open-Circuit Voltage Decay Measurements,” ChemPhysChem **4**(8), 859–864 (2003).

[35] M.Z. Rahman, and S.I. Khan, “Advances in surface passivation of c-Si solar cells,” Mater. Renew. Sustain. Energy **1**(1), 1 (2012).

[36] M. Lu, S. Bowden, U. Das, and R. Birkmire, “Interdigitated back contact silicon heterojunction solar cell and the effect of front surface passivation,” Appl. Phys. Lett. **91**(6), (2007).

[37] N.E.I. Boukortt, S. Patanè, and F. Bouhjar, “Design, Optimization and Characterisation of IBC c-Si (n) Solar Cell,” Silicon **12**(2), 365–372 (2020).

[38] Z. Shu, U. Das, J. Allen, R. Birkmire, and S. Hegedus, “Experimental and simulated analysis of front versus all-back-contact silicon heterojunction solar cells: effect of interface and doped a-Si:H layer defects,” Progress in Photovoltaics: Research and Applications **23**(1), 78–93 (2015).

[39] R. Müller, C. Reichel, X. Yang, A. Richter, J. Benick, and M. Hermle, “Impact of the homogeneous junction breakdown in IBC solar cells on the passivation quality of Al2O3 and SiO2: degradation and regeneration behavior,” Energy Procedia **124**, 365–370 (2017).

[40] A.J. Heeger, S. Kivelson, J.R. Schrieffer, and W.-P. Su, “Solitons in conducting polymers,” Rev. Mod. Phys. **60**(3), 781–850 (1988).

[41] J. Frenkel, “On the Transformation of light into Heat in Solids. I,” Physical Review **37**(1), 17–44 (1931).

[42] C.M. Proctor, M. Kuik, and T.-Q. Nguyen, “Charge carrier recombination in organic solar cells,” Prog. Polym. Sci. **38**(12), 1941–1960 (2013).

[43] J.D. Servaites, M.A. Ratner, and T.J. Marks, “Organic solar cells: A new look at traditional models,” Energy Environ. Sci. **4**(11), 4410 (2011).

[44] S.M. Menke, and R.J. Holmes, “Exciton diffusion in organic photovoltaic cells,” Energy Environ. Sci. **7**(2), 499–512 (2014).

[45] J.-T. Shieh, C.-H. Liu, H.-F. Meng, S.-R. Tseng, Y.-C. Chao, and S.-F. Horng, “The effect of carrier mobility in organic solar cells,” J. Appl. Phys. **107**(8), (2010).

[46] Y. Wang, H. Bai, and X. Zhan, “Comparison of conventional and inverted structures in fullerene-free organic solar cells,” Journal of Energy Chemistry **24**(6), 744–749 (2015).

[47] K. Wang, C. Liu, T. Meng, C. Yi, and X. Gong, “Inverted organic photovoltaic cells,” Chem. Soc. Rev. **45**(10), 2937–2975 (2016).

[48] D. Han, and S. Yoo, “The stability of normal vs. inverted organic solar cells under highly damp conditions: Comparison with the same interfacial layers,” Solar Energy Materials and Solar Cells **128**, 41–47 (2014).

[49] C.W. Tang, “Two-layer organic photovoltaic cell,” Appl. Phys. Lett. **48**(2), 183–185 (1986).

[50] G. Yu, J. Gao, J.C. Hummelen, F. Wudl, and A.J. Heeger, “Polymer Photovoltaic Cells: Enhanced Efficiencies via a Network of Internal Donor-Acceptor Heterojunctions,” Science (1979). **270**(5243), 1789–1791 (1995).

[51] S. Li, L. Ye, W. Zhao, S. Zhang, S. Mukherjee, H. Ade, and J. Hou, “Energy-Level Modulation of Small-Molecule Electron Acceptors to Achieve over 12% Efficiency in Polymer Solar Cells,” Advanced Materials **28**(42), 9423–9429 (2016).

[52] C.B. Nielsen, S. Holliday, H.-Y. Chen, S.J. Cryer, and I. McCulloch, “Non-Fullerene Electron Acceptors for Use in Organic Solar Cells,” Acc. Chem. Res. **48**(11), 2803–2812 (2015).

[53] J. Song, L. Zhu, C. Li, J. Xu, H. Wu, X. Zhang, Y. Zhang, Z. Tang, F. Liu, and Y. Sun, “High-efficiency organic solar cells with low voltage loss induced by solvent additive strategy,” Matter **4**(7), 2542–2552 (2021).

[54] R. Ma, T. Liu, Z. Luo, Q. Guo, Y. Xiao, Y. Chen, X. Li, S. Luo, X. Lu, M. Zhang, Y. Li, and H. Yan, “Improving open-circuit voltage by a chlorinated polymer donor endows binary organic solar cells efficiencies over 17%,” Sci. China Chem. **63**(3), 325–330 (2020).

[55] Q. An, F. Zhang, J. Zhang, W. Tang, Z. Deng, and B. Hu, “Versatile ternary organic solar cells: a critical review,” Energy Environ. Sci. **9**(2), 281–322 (2016).

[56] S.H.K. Paleti, S. Hultmark, J. Han, Y. Wen, H. Xu, S. Chen, E. Järsvall, I. Jalan, D.R. Villalva, A. Sharma, Jafar.I. Khan, E. Moons, R. Li, L. Yu, J. Gorenflot, F. Laquai, C. Müller, and D. Baran, “Hexanary blends: a strategy towards thermally stable organic photovoltaics,” Nat. Commun. **14**(1), 4608 (2023).

[57] C. Chen, L. Wang, W. Xia, K. Qiu, C. Guo, Z. Gan, J. Zhou, Y. Sun, D. Liu, W. Li, and T. Wang, “Molecular interaction induced dual fibrils towards organic solar cells with certified efficiency over 20%,” Nat. Commun. **15**(1), 6865 (2024).

[58] M.R. Lilliedal, A.J. Medford, M. V. Madsen, K. Norrman, and F.C. Krebs, “The effect of post-processing treatments on inflection points in current–voltage curves of roll-to-roll processed polymer photovoltaics,” Solar Energy Materials and Solar Cells **94**(12), 2018–2031 (2010).

[59] P. Peumans, A. Yakimov, and S.R. Forrest, “Small molecular weight organic thin-film photodetectors and solar cells,” J. Appl. Phys. **93**(7), 3693–3723 (2003).

[60] Y. Firdaus, V.M. Le Corre, S. Karuthedath, W. Liu, A. Markina, W. Huang, S. Chattopadhyay, M.M. Nahid, M.I. Nugraha, Y. Lin, A. Seitkhan, A. Basu, W. Zhang, I. McCulloch, H. Ade, J.

Labram, F. Laquai, D. Andrienko, L.J.A. Koster, and T.D. Anthopoulos, “Long-range exciton diffusion in molecular non-fullerene acceptors,” Nat. Commun. **11**(1), 5220 (2020).

[61] G. Lakhwani, A. Rao, and R.H. Friend, “Bimolecular Recombination in Organic Photovoltaics,” Annu. Rev. Phys. Chem. **65**(1), 557–581 (2014).

[62] S. Zeiske, O.J. Sandberg, N. Zarrabi, W. Li, P. Meredith, and A. Armin, “Direct observation of trap-assisted recombination in organic photovoltaic devices,” Nat. Commun. **12**(1), 3603 (2021).

[63] S. Rühle, “Tabulated values of the Shockley–Queisser limit for single junction solar cells,” Solar Energy **130**, 139–147 (2016).

[64] J. Chen, and N. Park, “Causes and Solutions of Recombination in Perovskite Solar Cells,” Advanced Materials **31**(47), (2019).

[65] L.C. Hirst, and N.J. Ekins-Daukes, “Fundamental losses in solar cells,” Progress in Photovoltaics: Research and Applications **19**(3), 286–293 (2011).

[66] Z. Jia, S. Qin, L. Meng, Q. Ma, I. Angunawela, J. Zhang, X. Li, Y. He, W. Lai, N. Li, H. Ade, C.J. Brabec, and Y. Li, “High performance tandem organic solar cells via a strongly infrared-absorbing narrow bandgap acceptor,” Nat. Commun. **12**(1), 178 (2021).

[67] J. Wang, Z. Zheng, P. Bi, Z. Chen, Y. Wang, X. Liu, S. Zhang, X. Hao, M. Zhang, Y. Li, and J. Hou, “Tandem organic solar cells with 20.6% efficiency enabled by reduced voltage losses,” Natl. Sci. Rev. **10**(6), (2023).

[68] Z. Zheng, J. Wang, P. Bi, J. Ren, Y. Wang, Y. Yang, X. Liu, S. Zhang, and J. Hou, “Tandem Organic Solar Cell with 20.2% Efficiency,” Joule **6**(1), 171–184 (2022).

[69] G. Giliberti, M. Cagnoni, and F. Cappelluti, “Monolithic 3-terminal perovskite/silicon HBT-based tandem compatible with both-side contact silicon cells: a theoretical study,” EPJ Photovoltaics **14**, 37 (2023).

[70] H. Laval, A. Holmes, M.A. Marcus, B. Watts, G. Bonfante, M. Schmutz, E. Deniau, R. Szymanski, C. Lartigau-Dagron, X. Xu, J.M. Cairney, K. Hirakawa, F. Awai, T. Kubo, G. Wantz, A. Bousquet, N.P. Holmes, and S. Chambon, “Toward High Efficiency Water Processed Organic Photovoltaics: Controlling the Nanoparticle Morphology with Surface Energies,” Adv. Energy Mater. **13**(26), (2023).

[71] Q. Fan, W. Su, S. Chen, W. Kim, X. Chen, B. Lee, T. Liu, U.A. Méndez-Romero, R. Ma, T. Yang, W. Zhuang, Y. Li, Y. Li, T.S. Kim, L. Hou, C. Yang, H. Yan, D. Yu, and E. Wang, “Mechanically Robust All-Polymer Solar Cells from Narrow Band Gap Acceptors with Hetero-Bridging Atoms,” Joule **4**(3), 658–672 (2020).

[72] J. Hou, O. Inganäs, R.H. Friend, and F. Gao, “Organic solar cells based on non-fullerene acceptors,” Nat. Mater. **17**(2), 119–128 (2018).

[73] Y. Wang, J. Lee, X. Hou, C. Labanti, J. Yan, E. Mazzolini, A. Parhar, J. Nelson, J. Kim, and Z. Li, "Recent Progress and Challenges toward Highly Stable Nonfullerene Acceptor-Based Organic Solar Cells," Adv. Energy Mater. **11**(5), (2021).

[74] H. Kim, M. Shin, and Y. Kim, "Distinct Annealing Temperature in Polymer:Fullerene:Polymer Ternary Blend Solar Cells," The Journal of Physical Chemistry C **113**(4), 1620–1623 (2009).

[75] P.G.V. Sampaio, M.O.A. González, P. Oliveira Ferreira, P. Cunha Jácome Vidal, J.P.P. Pereira, H.R. Ferreira, and P.C. Oprime, "Overview of printing and coating techniques in the production of organic photovoltaic cells," Int. J. Energy Res. **44**(13), 9912–9931 (2020).

[76] D. Zhao, C. Chen, C. Wang, M.M. Junda, Z. Song, C.R. Grice, Y. Yu, C. Li, B. Subedi, N.J. Podraza, X. Zhao, G. Fang, R.-G. Xiong, K. Zhu, and Y. Yan, "Efficient two-terminal all-perovskite tandem solar cells enabled by high-quality low-bandgap absorber layers," Nat. Energy **3**(12), 1093–1100 (2018).

[77] D. Zhang, M. Najafi, V. Zardetto, M. Dörenkämper, X. Zhou, S. Veenstra, L.J. Geerligs, T. Aernouts, and R. Andriessen, "High efficiency 4-terminal perovskite/c-Si tandem cells," Solar Energy Materials and Solar Cells **188**, 1–5 (2018).

[78] Z. Djebbour, W. El-Huni, A. Migan Dubois, and J. Kleider, "Bandgap engineered smart three-terminal solar cell: New perspectives towards very high efficiencies in the silicon world," Progress in Photovoltaics: Research and Applications **27**(4), 306–315 (2019).

[79] Z. Jia, X. Guo, X. Yin, M. Sun, J. Qiao, X. Jiang, X. Wang, Y. Wang, Z. Dong, Z. Shi, C.-H. Kuan, J. Hu, Q. Zhou, X. Jia, J. Chen, Z. Wei, S. Liu, H. Liang, N. Li, L.K. Lee, R. Guo, S. V. Roth, P. Müller-Buschbaum, X. Hao, X. Du, and Y. Hou, "Efficient near-infrared harvesting in perovskite–organic tandem solar cells," Nature **643**(8070), 104–110 (2025).

[80] J. Troughton, S. Neubert, N. Gasparini, D.R. Villalva, J. Bertrandie, A. Seitkhan, S.H.K. Paleti, A. Sharma, M. De Bastiani, E. Aydin, T.D. Anthopoulos, S. De Wolf, R. Schlatmann, and D. Baran, "Efficient Hybrid Amorphous Silicon/Organic Tandem Solar Cells Enabled by Near-Infrared Absorbing Nonfullerene Acceptors," Adv. Energy Mater. **11**(23), (2021).

[81] H.J. Park, S.H. Park, S.W. Lee, Y. Kang, D. Kim, H.J. Son, and H.S. Lee, "Novel Polymer-Based Organic/c-Si Monolithic Tandem Solar Cell: Enhanced Efficiency using Interlayer and Transparent Top Electrode Engineering," Macromol. Rapid Commun. **42**(17), (2021).

[82] G. Srinivasan, N. Gopalakrishnan, Y.S. Yu, R. Kesavamoorthy, and J. Kumar, "Influence of post-deposition annealing on the structural and optical properties of ZnO thin films prepared by sol–gel and spin-coating method," Superlattices Microstruct. **43**(2), 112–119 (2008).

[83] D. Li, W.Y. Lai, F. Feng, and W. Huang, "Post-Treatment of Screen-Printed Silver Nanowire Networks for Highly Conductive Flexible Transparent Films," Adv. Mater. Interfaces **8**(13), (2021).

[84] Nasa, and Casi, *General Disclaimer*.

[85] G.S. Kinsey, "Solar cell efficiency divergence due to operating spectrum variation," Solar Energy **217**, 49–57 (2021).

[86] B. Qi, and J. Wang, “Fill factor in organic solar cells,” Physical Chemistry Chemical Physics **15**(23), 8972 (2013).

[87] A. Khodr, Development and Characterization of Indoor Photovoltaics Cells Based on Non-Fullerene Acceptors for Industrial Inkjet Printing, Aix-Marseille, 2024.

[88] E.A. Duijnstee, J.M. Ball, V.M. Le Corre, L.J.A. Koster, H.J. Snaith, and J. Lim, “Toward Understanding Space-Charge Limited Current Measurements on Metal Halide Perovskites,” ACS Energy Lett. **5**(2), 376–384 (2020).

[89] P. Schilinsky, C. Waldauf, and C.J. Brabec, “Recombination and loss analysis in polythiophene based bulk heterojunction photodetectors,” Appl. Phys. Lett. **81**(20), 3885–3887 (2002).

[90] C.M. Proctor, and T.-Q. Nguyen, “Effect of leakage current and shunt resistance on the light intensity dependence of organic solar cells,” Appl. Phys. Lett. **106**(8), (2015).

[91] A. Mohammed, and A. Abdullah, "Scanning electron microscopy (SEM): A review", Proceedings of the 2018 international conference on hydraulics and pneumatics, (2018).

[92] Y. Xiao, and X. Lu, “Morphology of organic photovoltaic non-fullerene acceptors investigated by grazing incidence X-ray scattering techniques,” Mater. Today Nano **5**, 100030 (2019).

[93] Z. Qiu, Z. Xu, N. Li, N. Zhou, Y. Chen, X. Wan, J. Liu, N. Li, X. Hao, P. Bi, Q. Chen, B. Cao, and H. Zhou, “Monolithic perovskite/Si tandem solar cells exceeding 22% efficiency via optimizing top cell absorber,” Nano Energy **53**, 798–807 (2018).

[94] J.P. Connolly, K. Ahanogbe, J.-P.P. Kleider, J. Alvarez, H. Kanda, M.K. Nazeeruddin, V. Mihailetchi, P. Baranek, M. Vogt, R. Santbergen, K. Ahanobge, J.P. Kleider, V. Mihailetchi, P. Baranek, and O. Isabella, *Photovoltaic Solar Energy Conference and Exhibition (EU PVSEC 2020)* (2020).

[95] P. Bi, S. Zhang, J. Ren, Z. Chen, Z. Zheng, Y. Cui, J. Wang, S. Wang, T. Zhang, J. Li, Y. Xu, J. Qin, C. An, W. Ma, X. Hao, and J. Hou, “A High-Performance Nonfused Wide-Bandgap Acceptor for Versatile Photovoltaic Applications,” Advanced Materials **34**(5), (2022).

[96] T. Huang, S. Geng, D. Wang, Y. Zhang, N. Weng, X. Li, Q. Liao, Z. Zhang, J. Lu, and J. Zhang, “18.63% Efficiency of Ternary Organic Solar Cells Achieved via Nonhalogenated Solvent and Hot Spin-Coating Process,” Adv. Funct. Mater. **34**(27), (2024).

[97] M.-E. Gueunier-Farret, S. Chambon, L. Hirsch, L. Vignau, G. Wantz, J. Capdevila, J. Alvarez, J. Connolly, J.-P. Kleider, P. Roca i Cabarrocas, P. Pattanasattayavong, and S. Waiprasoet, “Steps Towards the Development of Organic/Silicon Tandem Solar Cells in a 3-Terminal Design,” in *Spring Meeting of the European Materials Research Society (E-MRS)*, (2024).

[98] Z. Xu, L. Chen, G. Yang, C. Huang, J. Hou, Y. Wu, G. Li, C. Hsu, and Y. Yang, “Vertical Phase Separation in Poly(3-hexylthiophene): Fullerene Derivative Blends and its Advantage for Inverted Structure Solar Cells,” Adv. Funct. Mater. **19**(8), 1227–1234 (2009).

[99] Q. Li, L.-M. Wang, S. Liu, L. Guo, S. Dong, G. Ma, Z. Cao, X. Zhan, X. Gu, T. Zhu, Y.-P. Cai, and F. Huang, “Vertical Composition Distribution and Crystallinity Regulations Enable High-

Performance Polymer Solar Cells with >17% Efficiency," ACS Energy Lett. **5**(11), 3637–3646 (2020).

[100] W.-H. Baek, H. Yang, T.-S. Yoon, C.J. Kang, H.H. Lee, and Y.-S. Kim, "Effect of P3HT:PCBM concentration in solvent on performances of organic solar cells," Solar Energy Materials and Solar Cells **93**(8), 1263–1267 (2009).

[101] W. Ma, G. Yang, K. Jiang, J.H. Carpenter, Y. Wu, X. Meng, T. McAfee, J. Zhao, C. Zhu, C. Wang, H. Ade, and H. Yan, "Influence of Processing Parameters and Molecular Weight on the Morphology and Properties of High-Performance PffBT4T-2OD:PC $_{71}$ BM Organic Solar Cells," Adv. Energy Mater. **5**(23), (2015).

[102] X. Guo, M. Zhang, J. Tan, S. Zhang, L. Huo, W. Hu, Y. Li, and J. Hou, "Influence of D/A Ratio on Photovoltaic Performance of a Highly Efficient Polymer Solar Cell System," Advanced Materials **24**(48), 6536–6541 (2012).

[103] A. Karki, J. Vollbrecht, A.J. Gillett, S.S. Xiao, Y. Yang, Z. Peng, N. Schopp, A.L. Dixon, S. Yoon, M. Schrock, H. Ade, G.N.M. Reddy, R.H. Friend, and T.-Q. Nguyen, "The role of bulk and interfacial morphology in charge generation, recombination, and extraction in non-fullerene acceptor organic solar cells," Energy Environ. Sci. **13**(10), 3679–3692 (2020).

[104] Z. Wang, K. Gao, Y. Kan, M. Zhang, C. Qiu, L. Zhu, Z. Zhao, X. Peng, W. Feng, Z. Qian, X. Gu, A.K.-Y. Jen, B.Z. Tang, Y. Cao, Y. Zhang, and F. Liu, "The coupling and competition of crystallization and phase separation, correlating thermodynamics and kinetics in OPV morphology and performances," Nat. Commun. **12**(1), 332 (2021).

[105] F.C. Spano, "The Spectral Signatures of Frenkel Polarons in H- and J-Aggregates," Acc. Chem. Res. **43**(3), 429–439 (2010).

[106] L. Zhao, H. Ji, S. Li, Q. Shi, C. Zhu, W. Wang, and D. Huang, "The charge dynamics of PBDB-TF:IT-4F based non-fullerene organic solar cells with 1,8-diiodooctane additive," Appl. Surf. Sci. **569**, 151120 (2021).

[107] J.M. Szarko, B.S. Rolczynski, S.J. Lou, T. Xu, J. Strzalka, T.J. Marks, L. Yu, and L.X. Chen, "Photovoltaic Function and Exciton/Charge Transfer Dynamics in a Highly Efficient Semiconducting Copolymer," Adv. Funct. Mater. **24**(1), 10–26 (2014).

[108] H. Saeki, O. Kurimoto, H. Nakaoka, M. Misaki, D. Kuzuhara, H. Yamada, K. Ishida, and Y. Ueda, "Effect of crystallinity in small molecular weight organic heterojunction solar cells," J. Mater. Chem. C Mater. **2**(27), 5357 (2014).

[109] B. Arredondo, J. Carlos Pérez-Martínez, L. Muñoz-Díaz, M. del C. López-González, D. Martín-Martín, G. del Pozo, E. Hernández-Balaguera, B. Romero, J. Lamminaho, V. Turkovic, and M. Madsen, "Influence of solvent additive on the performance and aging behavior of non-fullerene organic solar cells," Solar Energy **232**, 120–127 (2022).

[110] Q. He, W. Sheng, M. Zhang, G. Xu, P. Zhu, H. Zhang, Z. Yao, F. Gao, F. Liu, X. Liao, and Y. Chen, "Revealing Morphology Evolution in Highly Efficient Bulk Heterojunction and Pseudo-Planar Heterojunction Solar Cells by Additives Treatment," Adv. Energy Mater. **11**(7), (2021).

[111] X. Ma, F. Zhang, Q. An, Q. Sun, M. Zhang, and J. Zhang, "Dramatically Boosted Efficiency of Small Molecule Solar Cells by Synergistically Optimizing Molecular Aggregation and Crystallinity," ACS Sustain. Chem. Eng. **5**(2), 1982–1989 (2017).

[112] W. Kim, J.K. Kim, E. Kim, T.K. Ahn, D.H. Wang, and J.H. Park, "Conflicted Effects of a Solvent Additive on PTB7:PC $_{71}$ BM Bulk Heterojunction Solar Cells," The Journal of Physical Chemistry C **119**(11), 5954–5961 (2015).

[113] L. Li, L. Xiao, H. Qin, K. Gao, J. Peng, Y. Cao, F. Liu, T.P. Russell, and X. Peng, "High-Efficiency Small Molecule-Based Bulk-Heterojunction Solar Cells Enhanced by Additive Annealing," ACS Appl. Mater. Interfaces **7**(38), 21495–21502 (2015).

[114] A.K.K. Kyaw, D.H. Wang, C. Luo, Y. Cao, T. Nguyen, G.C. Bazan, and A.J. Heeger, "Effects of Solvent Additives on Morphology, Charge Generation, Transport, and Recombination in Solution-Processed Small-Molecule Solar Cells," Adv. Energy Mater. **4**(7), (2014).

[115] R. Szymanski, R. Henry, S. Stuard, U. Vongsaysy, S. Courtel, L. Vellutini, M. Bertrand, H. Ade, S. Chambon, and G. Wantz, "Balanced Charge Transport Optimizes Industry-Relevant Ternary Polymer Solar Cells," Solar RRL **4**(11), (2020).

[116] Y.-F. Ma, Y. Zhang, and H.-L. Zhang, "Solid additives in organic solar cells: progress and perspectives," J. Mater. Chem. C Mater. **10**(7), 2364–2374 (2022).

[117] J. HUANG, C. YANG, Z. HO, D. KEKUDA, M. WU, F. CHIEN, P. CHEN, C. CHU, and K. HO, "Annealing effect of polymer bulk heterojunction solar cells based on polyfluorene and fullerene blend," Org. Electron. **10**(1), 27–33 (2009).

[118] H. Benten, T. Nishida, D. Mori, H. Ohkita, and S. Ito, "Ternary Blend of Conjugated Polymers for Broadening the Absorption Bandwidth of Polymer Solar Cells," Journal of Photopolymer Science and Technology **29**(4), 537–540 (2016).

[119] Y. Deng, X. Feng, D. Yang, C. Yi, and X. Qiu, *Pi Stacking in Lignosulfonates* (2012).

[120] L. Zhu, M. Zhang, G. Zhou, T. Hao, J. Xu, J. Wang, C. Qiu, N. Prine, J. Ali, W. Feng, X. Gu, Z. Ma, Z. Tang, H. Zhu, L. Ying, Y. Zhang, and F. Liu, "Efficient Organic Solar Cell with 16.88% Efficiency Enabled by Refined Acceptor Crystallization and Morphology with Improved Charge Transfer and Transport Properties," Adv. Energy Mater. **10**(18), (2020).

[121] N.T. Shewmon, D.L. Watkins, J.F. Galindo, R.B. Zerdan, J. Chen, J. Keum, A.E. Roitberg, J. Xue, and R.K. Castellano, "Enhancement in Organic Photovoltaic Efficiency through the Synergistic Interplay of Molecular Donor Hydrogen Bonding and π-Stacking," Adv. Funct. Mater. **25**(32), 5166–5177 (2015).

[122] Y. Wang, T. Hasegawa, H. Matsumoto, and T. Michinobu, "Significant Improvement of Unipolar n-Type Transistor Performances by Manipulating the Coplanar Backbone Conformation of Electron-Deficient Polymers via Hydrogen Bonding," J. Am. Chem. Soc. **141**(8), 3566–3575 (2019).

[123] Y. Lin, M.I. Nugraha, Y. Firdaus, A.D. Scaccabarozzi, F. Aniés, A.-H. Emwas, E. Yengel, X. Zheng, J. Liu, W. Wahyudi, E. Yarali, H. Faber, O.M. Bakr, L. Tsetseris, M. Heeney, and T.D.

Anthopoulos, “A Simple n-Dopant Derived from Diquat Boosts the Efficiency of Organic Solar Cells to 18.3%,” ACS Energy Lett. **5**(12), 3663–3671 (2020).

[124] M. Kielar, T. Hamid, M. Wiemer, F. Windels, L. Hirsch, P. Sah, and A.K. Pandey, “Light Detection in Open-Circuit Voltage Mode of Organic Photodetectors,” Adv. Funct. Mater. **30**(9), (2020).

[125] D. Liu, Y. Zhang, L. Zhan, T.-K. Lau, H. Yin, P.W.K. Fong, S.K. So, S. Zhang, X. Lu, J. Hou, H. Chen, W.-Y. Wong, and G. Li, “Design of wide-bandgap polymers with deeper ionization potential enables efficient ternary non-fullerene polymer solar cells with 13% efficiency,” J. Mater. Chem. A Mater. **7**(23), 14153–14162 (2019).

[126] T. Hahn, S. Tscheuschner, F. Kahle, M. Reichenberger, S. Athanasopoulos, C. Saller, G.C. Bazan, T. Nguyen, P. Strohriegl, H. Bässler, and A. Köhler, “Monomolecular and Bimolecular Recombination of Electron–Hole Pairs at the Interface of a Bilayer Organic Solar Cell,” Adv. Funct. Mater. **27**(1), (2017).

[127] P.W.M. Blom, M.J.M. de Jong, and J.J.M. Vleggaar, “Electron and hole transport in poly(*p* -phenylene vinylene) devices,” Appl. Phys. Lett. **68**(23), 3308–3310 (1996).

[128] S. Shao, M. Abdu-Aguye, T.S. Sherkar, H. Fang, S. Adjokatse, G. ten Brink, B.J. Kooi, L.J.A. Koster, and M.A. Loi, “The Effect of the Microstructure on Trap-Assisted Recombination and Light Soaking Phenomenon in Hybrid Perovskite Solar Cells,” Adv. Funct. Mater. **26**(44), 8094–8102 (2016).

[129] Y. Chen, S. Wu, X. Li, M. Liu, Z. Chen, P. Zhang, and S. Li, “Efficient and stable low-cost perovskite solar cells enabled by using surface passivated carbon as the counter electrode,” J. Mater. Chem. C Mater. **10**(4), 1270–1275 (2022).

[130] C. Xu, S. Zhang, W. Fan, F. Cheng, H. Sun, Z. Kang, and Y. Zhang, “Pushing the Limit of Open-Circuit Voltage Deficit via Modifying Buried Interface in $CsPbI_3$ Perovskite Solar Cells,” Advanced Materials **35**(7), (2023).

[131] G. Bernardo, T. Lopes, D.G. Lidzey, and A. Mendes, “Progress in Upscaling Organic Photovoltaic Devices,” Adv. Energy Mater. **11**(23), (2021).

[132] S.C. Mukhopadhyay, and N.K. Suryadevara, “Internet of Things: Challenges and Opportunities,” (2014), pp. 1–17.

[133] J. Russo, W. Ray, and M.S. Litz, “Low light illumination study on commercially available homojunction photovoltaic cells,” Appl. Energy **191**, 10–21 (2017).

[134] T. Zhang, C. An, Y. Xu, P. Bi, Z. Chen, J. Wang, N. Yang, Y. Yang, B. Xu, H. Yao, X. Hao, S. Zhang, and J. Hou, “A Medium-Bandgap Nonfullerene Acceptor Enabling Organic Photovoltaic Cells with 30% Efficiency under Indoor Artificial Light,” Advanced Materials **34**(43), (2022).

[135] G. Kumar, and F.-C. Chen, “A review on recent progress in organic photovoltaic devices for indoor applications,” J. Phys. D Appl. Phys. **56**(35), 353001 (2023).

[136] S. Yang, Z. Hsieh, M.L. Keshtov, G.D. Sharma, and F. Chen, “Toward High-Performance Polymer Photovoltaic Devices for Low-Power Indoor Applications,” Solar RRL **1**(12), (2017).

[137] X. Xu, W. Liu, X. Luo, H. Chen, Q. Wei, J. Yuan, and Y. Zou, “An Overview of High-Performance Indoor Organic Photovoltaics,” ChemSusChem **14**(17), 3428–3448 (2021).

[138] G.K. Grandhi, G. Koutsourakis, J.C. Blakesley, F. De Rossi, F. Brunetti, S. Öz, A. Sinicropi, M.L. Parisi, T.M. Brown, M.J. Carnie, R.L.Z. Hoye, and P. Vivo, “Promises and challenges of indoor photovoltaics,” Nature Reviews Clean Technology **1**(2), 132–147 (2025).

[139] C. Xie, X. Li, J. Tong, Y. Gu, and Y. Shen, “Effects of white light-emitting diode (LED) light exposure with different Correlated Color Temperatures (CCTs) on human lens epithelial cells in culture,” Photochem. Photobiol. **90**(4), 853–859 (2014).

[140] D. Müller, E. Jiang, P. Rivas-Lazaro, C. Baretzky, G. Loukeris, S. Bogati, S. Paetel, S.J.C. Irvine, O. Oklobia, S. Jones, D. Lamb, A. Richter, G. Siefer, D. Lackner, H. Helmers, C. Teixeira, D. Forgács, M. Freitag, D. Bradford, Z. Shen, B. Zimmermann, and U. Würfel, “Indoor Photovoltaics for the Internet-of-Things - A Comparison of State-of-the-Art Devices from Different Photovoltaic Technologies,” ACS Appl. Energy Mater. **6**(20), 10404–10414 (2023).

[141] J. Capdevila, S. Waiprasoet, F.X. Capella Guardià, C. Ruiz Herrero, L. Hirsch, M. Campoy-Quiles, G. Wantz, P. Pattanasattayavong, S. Chambon, and M.E. Gueunier-Farret, “Wide bandgap organic solar cells with improved photovoltaic performance via solid additive integration,” J. Mater. Chem. C Mater. **13**(35), 18450–18462 (2025).

[142] M. Wu, C. Kuo, L. Jhuang, P. Chen, Y. Lai, and F. Chen, “Photovoltaics: Bandgap Engineering Enhances the Performance of Mixed-Cation Perovskite Materials for Indoor Photovoltaic Applications (Adv. Energy Mater. 37/2019),” Adv. Energy Mater. **9**(37), (2019).

[143] T. Wang, J. Fang, H. Zhang, C. Tian, Y. Wang, Z. Fu, W. Zou, D. Deng, X. Hao, C. He, J. Zhang, and Z. Wei, “Scalable semitransparent organic solar cells with robust film thickness tolerance for building-integrated photovoltaics,” Nat. Commun. **17**(1), 2916 (2026).

[144] C. Xu, Y. Chen, Z. Zhao, B. Yang, J. Suo, K. Ba, A. Tarasov, Y. Wu, X. Lian, M. Luo, Y. Zhan, Y. Chen, J. Gao, X. Mo, W.C.H. Choy, J. Wang, H. Zhang, and J. Chu, “Semi-transparent photovoltaics,” Energy Environ. Sci. **18**(5), 2095–2135 (2025).

[145] C. Sheng, Y. Shi, Y. Li, W. Wang, W. Zhou, C. Chen, N. Zhang, J. Ran, E. Stathatos, and B. Yang, “Semi-Transparent Colored Solar Cells for Agrivoltaics Ecosystem Applications,” Adv. Sustain. Syst. **9**(5), (2025).

[146] D.C. Lim, J.H. Jeong, K. Hong, S. Nho, J. Lee, Q.V. Hoang, S.K. Lee, K. Pyo, D. Lee, and S. Cho, “Semi-transparent plastic solar cell based on oxide-metal-oxide multilayer electrodes,” Progress in Photovoltaics: Research and Applications **26**(3), 188–195 (2018).

[147] S. Wageh, M. Raïssi, T. Berthelot, A.A. Al-Ghamdi, A.M. Abusorrah, W. Boukhili, and O.A. Al-Hartomy, “Silver Nanowires Digital Printing for Inverted Flexible Semi-Transparent Solar Cells,” Adv. Eng. Mater. **23**(4), (2021).

[148] H. Schmidt, H. Flügge, T. Winkler, T. Bülow, T. Riedl, and W. Kowalsky, "Efficient semitransparent inverted organic solar cells with indium tin oxide top electrode," Appl. Phys. Lett. **94**(24), (2009).

[149] J. Han, C. Sung, C. Shin, Y. Kim, and T.-Y. Kim, "Optimization of oxide materials in oxide-metal-oxide(OMO) electrodes for flexible electrochromic devices," Solar Energy Materials and Solar Cells **249**, 112035 (2023).

[150] M. Girtan, and B. Negulescu, "A review on oxide/metal/oxide thin films on flexible substrates as electrodes for organic and perovskite solar cells," Optical Materials: X **13**, 100122 (2022).

[151] E. Annabi Milani, M. Piralaee, D. Raeyani, and A. Asgari, "High-performance semi-transparent organic solar cells for window applications using MoO3/Ag/MoO3 transparent anodes," Solar Energy Materials and Solar Cells **276**, 113066 (2024).

[152] F.-J. Du, J.-J. Yu, J.-G. Liu, and L. Wang, "Influences of Ar Flow-Rate and Sublimation Temperature on the Sublimation Product of Analytical Reagent MoO3," Molecules **30**(13), 2751 (2025).

[153] W. Greenbank, L. Hirsch, G. Wantz, and S. Chambon, "Interfacial thermal degradation in inverted organic solar cells," Appl. Phys. Lett. **107**(26), (2015).

[154] D.C. Lim, J.H. Jeong, K. Hong, S. Nho, J. Lee, Q.V. Hoang, S.K. Lee, K. Pyo, D. Lee, and S. Cho, "Semi-transparent plastic solar cell based on oxide-metal-oxide multilayer electrodes," Progress in Photovoltaics: Research and Applications **26**(3), 188–195 (2018).

[155] X. Guo, X. Liu, F. Lin, H. Li, Y. Fan, and N. Zhang, "Highly Conductive Transparent Organic Electrodes with Multilayer Structures for Rigid and Flexible Optoelectronics," Sci. Rep. **5**(1), 10569 (2015).

[156] J. Lv, F. Lai, L. Lin, Y. Lin, Z. Huang, and R. Chen, "Thermal stability of Ag films in air prepared by thermal evaporation," Appl. Surf. Sci. **253**(17), 7036–7040 (2007).

[157] J. Capdevila, "Synthèse et Caractérisation de Couches Minces de VO2 Dopé au Chrome en Tant que Nouveau Matériau D'électrode Dans les Batteries Li-Ion", Master's thesis, (2023).

[158] Z. Wang, C. Zhang, R. Gao, D. Chen, S. Tang, J. Zhang, D. Wang, X. Lu, and Y. Hao, "Improvement of transparent silver thin film anodes for organic solar cells with a decreased percolation threshold of silver," Solar Energy Materials and Solar Cells **127**, 193–200 (2014).

[159] V.E. Babicheva, "Optical Processes behind Plasmonic Applications," Nanomaterials **13**(7), 1270 (2023).

[160]*Thin-Film Optical Filters, Fifth Edition* (CRC Press, 2017).

[161] N. Sharma, N.M. Nair, G. Nagasarvari, D. Ray, and P. Swaminathan, "A review of silver nanowire-based composites for flexible electronic applications," Flexible and Printed Electronics **7**(1), (2022).

[162] S. Coskun, E. Selen Ates, and H. Emrah Unalan, “Optimization of silver nanowire networks for polymer light emitting diode electrodes,” Nanotechnology **24**(12), (2013).

[163] Y. Jia, A.J. Zheng, T.F.M. Chang, M. Sone, and W.T. Chiu, “Highly functional Ag nanowires/PDMS transparent conductive films enabled by thermal-assisted multilayer coating for flexible electronic devices,” Surf. Coat. Technol. **526**, (2026).

[164] S. De, T.M. Higgins, P.E. Lyons, E.M. Doherty, P.N. Nirmalraj, W.J. Blau, J.J. Boland, and J.N. Coleman, “Silver Nanowire Networks as Flexible, Transparent, Conducting Films: Extremely High DC to Optical Conductivity Ratios,” ACS Nano **3**(7), 1767–1774 (2009).

[165] J. Krantz, T. Stubhan, M. Richter, S. Spallek, I. Litzov, G.J. Matt, E. Spiecker, and C.J. Brabec, “Spray-Coated Silver Nanowires as Top Electrode Layer in Semitransparent P3HT:PCBM-Based Organic Solar Cell Devices,” Adv. Funct. Mater. **23**(13), 1711–1717 (2013).

[166] G. Ji, Y. Wang, Q. Luo, K. Han, M. Xie, L. Zhang, N. Wu, J. Lin, S. Xiao, Y.-Q. Li, L.-Q. Luo, and C.-Q. Ma, “Fully Coated Semitransparent Organic Solar Cells with a Doctor-Blade-Coated Composite Anode Buffer Layer of Phosphomolybdic Acid and PEDOT:PSS and a Spray-Coated Silver Nanowire Top Electrode,” ACS Appl. Mater. Interfaces **10**(1), 943–954 (2018).

[167] W. Li, S. Yang, and A. Shamim, “Screen printing of silver nanowires: balancing conductivity with transparency while maintaining flexibility and stretchability,” Npj Flexible Electronics **3**(1), 13 (2019).

[168] H. Jang, D. Kim, H. Tak, J. Nam, and T. Kim, “Ultra-mechanically stable and transparent conductive electrodes using transferred grid of Ag nanowires on flexible substrate,” Current Applied Physics **16**(1), 24–30 (2016).

[169] B. Ha, and S. Jo, “Hybrid Ag nanowire transparent conductive electrodes with randomly oriented and grid-patterned Ag nanowire networks,” Sci. Rep. **7**(1), 11614 (2017).

[170] T.Y. Goh, S.N. Basah, H. Yazid, M.J. Aziz Safar, and F.S. Ahmad Saad, “Performance analysis of image thresholding: Otsu technique,” Measurement **114**, 298–307 (2018).

[171] A.T. Bellew, H.G. Manning, C. Gomes da Rocha, M.S. Ferreira, and J.J. Boland, “Resistance of Single Ag Nanowire Junctions and Their Role in the Conductivity of Nanowire Networks,” ACS Nano **9**(11), 11422–11429 (2015).

[172] F. Selzer, C. Floresca, D. Kneppe, L. Bormann, C. Sachse, N. Weiß, A. Eychmüller, A. Amassian, L. Müller-Meskamp, and K. Leo, “Electrical limit of silver nanowire electrodes: Direct measurement of the nanowire junction resistance,” Appl. Phys. Lett. **108**(16), (2016).

[173] S. De, T.M. Higgins, P.E. Lyons, E.M. Doherty, P.N. Nirmalraj, W.J. Blau, J.J. Boland, and J.N. Coleman, “Silver Nanowire Networks as Flexible, Transparent, Conducting Films: Extremely High DC to Optical Conductivity Ratios,” ACS Nano **3**(7), 1767–1774 (2009).

[174] W.M. Steen, and J. Mazumder, “Background to Laser Design and General Applications,” in *Laser Material Processing*, (Springer London, London, 2010), pp. 11–78.

[175] M.E.T. Molares, A.G. Balogh, T.W. Cornelius, R. Neumann, and C. Trautmann, “Fragmentation of nanowires driven by Rayleigh instability,” Appl. Phys. Lett. **85**(22), 5337–5339 (2004).

[176] C.A. Hartnett, I. Seric, K. Mahady, L. Kondic, S. Afkhami, J.D. Fowlkes, and P.D. Rack, “Exploiting the Marangoni Effect to Initiate Instabilities and Direct the Assembly of Liquid Metal Filaments,” Langmuir **33**(33), 8123–8128 (2017).

[177] D. Bäuerle, *Laser Processing and Chemistry* (Springer Berlin Heidelberg, Berlin, Heidelberg, 2011).

[178] P. Kubis, N. Li, T. Stubhan, F. Machui, G.J. Matt, M.M. Voigt, and C.J. Brabec, “Patterning of organic photovoltaic modules by ultrafast laser,” Progress in Photovoltaics: Research and Applications **23**(2), 238–246 (2015).

[179] W. Tress, “Organic Solar Cells,” (2014), pp. 67–214.

[180] S. Röttinger, B. Schwarz, S. Schäfer, R. Gauch, B. Zimmermann, and U. Würfel, “Laser patterning of vacuum processed small molecular weight organic photovoltaics,” Solar Energy Materials and Solar Cells **154**, 35–41 (2016).

[181] T. Söderström, F. -J. Haug, X. Niquille, and C. Ballif, “TCOs for nip thin film silicon solar cells,” Progress in Photovoltaics: Research and Applications **17**(3), 165–176 (2009).

[182] C.G. Granqvist, “Transparent conductors as solar energy materials: A panoramic review,” Solar Energy Materials and Solar Cells **91**(17), 1529–1598 (2007).

[183] K. Ellmer, “Past achievements and future challenges in the development of optically transparent electrodes,” Nat. Photonics **6**(12), 809–817 (2012).

[184] D.S. Ginley, and J.D. Perkins, “Transparent Conductors,” in *Handbook of Transparent Conductors*, (Springer US, Boston, MA, 2011), pp. 1–25.

[185] R.R. Kabulov, A. Kutlimratov, A.S. Saidov, M.U. Khajiev, and Kh.N. Juraev, “ITO Films Deposited on Silicon by CVD Method,” Surface Engineering and Applied Electrochemistry **61**(2), 148–153 (2025).

[186] Y. Feng, L. Zhang, H. Chen, L. Zhang, X. Guo, X. Liu, and S. Guo, “Effects of Sn doping content on the structure, morphology, optical and electrical properties of ITO thin films prepared by microwave-assisted spray pyrolysis,” RSC Adv. **16**(8), 7538–7548 (2026).

[187] J.H. Kim, K.A. Jeon, G.H. Kim, and S.Y. Lee, “Electrical, structural, and optical properties of ITO thin films prepared at room temperature by pulsed laser deposition,” Appl. Surf. Sci. **252**(13), 4834–4837 (2006).

[188] M. Nicolescu, M. Anastasescu, J.M. Calderon-Moreno, A.V. Maraloiu, V.S. Teodorescu, S. Preda, L. Predoana, M. Zaharescu, and M. Gartner, “Optical, microstructural and vibrational properties of sol–gel ITO films,” Opt. Mater. (Amst). **114**, 110999 (2021).

[189] J.T. Leonard, D.A. Cohen, B.P. Yonkee, R.M. Farrell, S.P. DenBaars, J.S. Speck, and S. Nakamura, “Smooth e-beam-deposited tin-doped indium oxide for III-nitride vertical-cavity surface-emitting laser intracavity contacts,” J. Appl. Phys. **118**(14), (2015).

[190] F. Kurdesau, G. Khripunov, A.F. da Cunha, M. Kaelin, and A.N. Tiwari, “Comparative study of ITO layers deposited by DC and RF magnetron sputtering at room temperature,” J. Non. Cryst. Solids **352**(9–20), 1466–1470 (2006).

[191] R. Karthikeyan, C.T. Cherian, and R.P. Fernandes, “Review: RF magnetron sputtering, a promising synthesis route for scalable production of thin-film batteries,” J. Mater. Sci. **60**(21), 8569–8601 (2025).

[192] K. Ellmer, “Magnetron sputtering of transparent conductive zinc oxide: relation between the sputtering parameters and the electronic properties,” J. Phys. D Appl. Phys. **33**(4), R17–R32 (2000).

[193] I. Hamberg, and C.G. Granqvist, “Evaporated Sn-doped In2O3 films: Basic optical properties and applications to energy-efficient windows,” J. Appl. Phys. **60**(11), R123–R160 (1986).

[194] K. Ellmer, “Past achievements and future challenges in the development of optically transparent electrodes,” Nat. Photonics **6**(12), 809–817 (2012).

[195] G. Frank, and H. Köstlin, “Electrical properties and defect model of tin-doped indium oxide layers,” Applied Physics A Solids and Surfaces **27**(4), 197–206 (1982).

[196] D.S. Ginley, editor , *Handbook of Transparent Conductors* (Springer US, Boston, MA, 2011).

[197] P.J. Kelly, and R.D. Arnell, “Magnetron sputtering: a review of recent developments and applications,” Vacuum **56**(3), 159–172 (2000).

[198] H. Kim, C.M. Gilmore, A. Piqué, J.S. Horwitz, H. Mattoussi, H. Murata, Z.H. Kafafi, and D.B. Chrisey, “Electrical, optical, and structural properties of indium–tin–oxide thin films for organic light-emitting devices,” J. Appl. Phys. **86**(11), 6451–6461 (1999).

[199] F.C. Krebs, “Fabrication and processing of polymer solar cells: A review of printing and coating techniques,” Solar Energy Materials and Solar Cells **93**(4), 394–412 (2009).

[200] S.M. Rossnagel, “Thin film deposition with physical vapor deposition and related technologies,” Journal of Vacuum Science & Technology A: Vacuum, Surfaces, and Films **21**(5), S74–S87 (2003).

[201] M. Jørgensen, K. Norrman, and F.C. Krebs, “Stability/degradation of polymer solar cells,” Solar Energy Materials and Solar Cells **92**(7), 686–714 (2008).

[202] S.H. Reddy, F. Di Giacomo, F. Matteocci, L.A. Castriotta, and A. Di Carlo, “Holistic Approach toward a Damage-Less Sputtered Indium Tin Oxide Barrier Layer for High-Stability Inverted Perovskite Solar Cells and Modules,” ACS Appl. Mater. Interfaces **14**(45), 51438–51448 (2022).

[203] J. Liu, Y. Wu, Z. Zhao, S. Wu, X. Tang, J. Wang, B. Mehmood, S. Yue, S. Qu, Z. Wang, K. Liu, and X. Liu, “Reducing damage of sputtering and improving conductivity of transparent

electrodes for efficient semi-transparent perovskite solar cells," J. Phys. D Appl. Phys. **56**(36), 365101 (2023).

[204] J. Txintxurreta, E. G-Berasategui, R. Ortiz, O. Hernández, L. Mendizábal, and J. Barriga, "Indium Tin Oxide Thin Film Deposition by Magnetron Sputtering at Room Temperature for the Manufacturing of Efficient Transparent Heaters," Coatings **11**(1), 92 (2021).

[205] J.A. Thornton, "Influence of apparatus geometry and deposition conditions on the structure and topography of thick sputtered coatings," Journal of Vacuum Science and Technology **11**(4), 666–670 (1974).

[206] Y.S. Jung, "Spectroscopic ellipsometry studies on the optical constants of indium tin oxide films deposited under various sputtering conditions," Thin Solid Films **467**(1–2), 36–42 (2004).

[207] A.P. Amalathas, and M.M. Alkaisi, "Effects of film thickness and sputtering power on properties of ITO thin films deposited by RF magnetron sputtering without oxygen," Journal of Materials Science: Materials in Electronics **27**(10), 11064–11071 (2016).

[208] D.B. Fraser, and H.D. Cook, "Highly Conductive, Transparent Films of Sputtered In[sub 2−x]Sn[sub x]O[sub 3−y]," J. Electrochem. Soc. **119**(10), 1368 (1972).

[209] G. Haacke, "New figure of merit for transparent conductors," J. Appl. Phys. **47**(9), 4086–4089 (1976).

[210] I.R. Cisneros-Contreras, A.L. Muñoz-Rosas, and A. Rodríguez-Gómez, "Resolution improvement in Haacke's figure of merit for transparent conductive films," Results Phys. **15**, 102695 (2019).

[211] I. Hancox, K. V. Chauhan, P. Sullivan, R.A. Hatton, A. Moshar, C.P.A. Mulcahy, and T.S. Jones, "Increased efficiency of small molecule photovoltaic cells by insertion of a MoO_3 hole-extracting layer," Energy Environ. Sci. **3**(1), 107–110 (2010).

[212] Y. Li, J. Wang, C. Yan, S. Zhang, N. Cui, Y. Liu, G. Li, and P. Cheng, "Optical and electrical losses in semitransparent organic photovoltaics," Joule **8**(2), 527–541 (2024).

[213] J. Gilot, M.M. Wienk, and R.A.J. Janssen, "Double and triple junction polymer solar cells processed from solution," Appl. Phys. Lett. **90**(14), (2007).

[214] M.W. Rowell, and M.D. McGehee, "Transparent electrode requirements for thin film solar cell modules," Energy Environ. Sci. **4**(1), 131–134 (2011).

[215] J. Kettle, V. Stoichkov, D. Kumar, M. Corazza, S.A. Gevorgyan, and F.C. Krebs, "Using ISOS consensus test protocols for development of quantitative life test models in ageing of organic solar cells," Solar Energy Materials and Solar Cells **167**, 53–59 (2017).

[216] B. Walker, H. Choi, and J.Y. Kim, "Interfacial engineering for highly efficient organic solar cells," Current Applied Physics **17**(3), 370–391 (2017).

[217] R.A. Street, M. Schoendorf, A. Roy, and J.H. Lee, "Interface state recombination in organic solar cells," Phys. Rev. B Condens. Matter Mater. Phys. **81**(20), (2010).

[218] F.X. Capella-Guardià, J.S. Müller, M.A. Saeed, X. Rodríguez-Martínez, M. Casademont-Viñas, A. Harillo-Baños, J. Martín, J. Nelson, A.R. Goñi, and M. Campoy-Quiles, “Exploring the Potential of Ternary Blending for Two and Three-Junction RAINBOW Solar Cells,” (2026).

[219] M. Martín-Ruiz, P. Pinyol-Castillo, X. Rodríguez-Martínez, J. Martín, I. Burgués-Ceballos, and M. Campoy-Quiles, “Increasing polymer molecular weight enables low-donor-content, efficient and scalable semi-transparent organic solar cells,” J. Mater. Chem. A Mater. **14**(22), 13688–13706 (2026).

[220] H. Dinesh, and J.M. Pearce, “The potential of agrivoltaic systems,” Renewable and Sustainable Energy Reviews **54**, 299–308 (2016).

[221] J. Wang, M. Zhang, J. Lin, Z. Zheng, L. Zhu, P. Bi, H. Liang, X. Guo, J. Wu, Y. Wang, L. Yu, J. Li, J. Lv, X. Liu, F. Liu, J. Hou, and Y. Li, “An asymmetric wide-bandgap acceptor simultaneously enabling highly efficient single-junction and tandem organic solar cells,” Energy Environ. Sci. **15**(4), 1585–1593 (2022).

[222] J. Capdevila, S. Chambon, and M.E. Gueunier-Farret, “Damage-free sputtered ITO top electrode for semi-transparent organic solar cells: Protective and electronic role of the MoO3 transport layer,” Appl. Phys. Lett. **128**(20), (2026).

[223] Y. Li, X. Huang, H.K.M. Sheriff, and S.R. Forrest, “Semitransparent organic photovoltaics for building-integrated photovoltaic applications,” Nat. Rev. Mater. **8**(3), 186–201 (2022).

[224] L.K. Markov, A.S. Pavluchenko, and I.P. Smirnova, “Technique for the Formation of Antireflection Coatings Based on ITO Films,” Semiconductors **53**(2), 172–179 (2019).

[225] J. Zheng, W. Duan, Y. Guo, Z.C. Zhao, H. Yi, F.-J. Ma, L. Granados Caro, C. Yi, J. Bing, S. Tang, J. Qu, K.C. Fong, X. Cui, Y. Zhu, L. Yang, A. Lambertz, M. Arafat Mahmud, H. Chen, C. Liao, G. Wang, M. Jankovec, C. Xu, A. Uddin, J.M. Cairney, S. Bremner, S. Huang, K. Ding, D.R. McKenzie, and A.W.Y. Ho-Baillie, “Efficient monolithic perovskite–Si tandem solar cells enabled by an ultra-thin indium tin oxide interlayer,” Energy Environ. Sci. **16**(3), 1223–1233 (2023).

[226] M.T. Dang, L. Hirsch, and G. Wantz, “P3HT:PCBM, Best Seller in Polymer Photovoltaic Research,” Advanced Materials **23**(31), 3597–3602 (2011).

[227] W.R. Good, “A comparison of contact angle interpretations,” J. Colloid Interface Sci. **44**(1), 63–71 (1973).

[228] N.C. Giebink, G.P. Wiederrecht, M.R. Wasielewski, and S.R. Forrest, “Ideal diode equation for organic heterojunctions. I. Derivation and application,” Phys. Rev. B **82**(15), 155305 (2010).

[229] K.O. Brinkmann, P. Wang, F. Lang, W. Li, X. Guo, F. Zimmermann, S. Olthof, D. Neher, Y. Hou, M. Stolterfoht, T. Wang, A.B. Djurišić, and T. Riedl, “Perovskite–organic tandem solar cells,” Nat. Rev. Mater. **9**(3), 202–217 (2024).

[230] A. Mokri, and M. Emziane, "Beam-splitting versus tandem cell approaches for converting the solar spectrum into electricity: A comparative study.", International Renewable Energy Congress, (2010).

[231] M. Gibert-Roca, M. Casademont-Viñas, Q. Liu, K. Vandewal, A.R. Goñi, and M. Campoy-Quiles, “RAINBOW Organic Solar Cells: Implementing Spectral Splitting in Lateral Multi-Junction Architectures,” Advanced Materials **36**(20), (2024).

[232] M.A. Smith, S. Sinharoy, V.G. Weizer, O. Khan, A. Pal, E.B. Clark, D.M. Wilt, D.A. Scheiman, and N. Mardesich, “Solar cells for NASA RAINBOW concentrator,” in *Conference Record of the Twenty-Eighth IEEE Photovoltaic Specialists Conference - 2000 (Cat. No.00CH37036)*, (IEEE, n.d.), pp. 1139–1141.

[233] H. Uzu, M. Ichikawa, M. Hino, K. Nakano, T. Meguro, J.L. Hernández, H.-S. Kim, N.-G. Park, and K. Yamamoto, “High efficiency solar cells combining a perovskite and a silicon heterojunction solar cells via an optical splitting system,” Appl. Phys. Lett. **106**(1), (2015).

[234] S. Jiang, P. Hu, S. Mo, and Z. Chen, “Optical modeling for a two-stage parabolic trough concentrating photovoltaic/thermal system using spectral beam splitting technology,” Solar Energy Materials and Solar Cells **94**(10), 1686–1696 (2010).

[235] F.I. Mime, Md.R. Islam, E. Hossain, I.M. Mehedi, and Md.T. Hasan, “Design and Performance Analysis of Tandem Organic Solar Cells: Effect of Cell Parameter,” IEEE Access **9**, 40665–40680 (2021).

[236] I. Etxebarria, J. Ajuria, and R. Pacios, “Solution-processable polymeric solar cells: A review on materials, strategies and cell architectures to overcome 10%,” Org. Electron. **19**, 34–60 (2015).

[237] S.D. Vorndran, S. Ayala, Y. Wu, J.M. Russo, R.K. Kostuk, J.T. Friedlein, S.E. Shaheen, and C.K. Luscombe, “Holographic spectral beamsplitting for increased organic photovoltaic conversion efficiency,” edited by Z.H. Kafafi, P.A. Lane, and I.D.W. Samuel, (2014), p. 918423.

[238] M. Casademont-Viñas, M. Gibert-Roca, M. Campoy-Quiles, and A.R. Goñi, “Spectrum on demand light source (SOLS) for advanced photovoltaic characterization,” Review of Scientific Instruments **94**(10), (2023).

[239] R. Xu, Y. Jiang, F. Liu, G. Ran, K. Liu, W. Zhang, and X. Zhu, “High Open-Circuit Voltage Organic Solar Cells with 19.2% Efficiency Enabled by Synergistic Side-Chain Engineering,” Advanced Materials **36**(26), (2024).

[240] A.W.S. Budhi, Hydrogenated Indium Oxide (IO:H) for Thin Film Solar Cell, Doctoral dissertation, (2016).

[241] H.-J. Kim, K.-W. Seo, Y.-J. Noh, S.-I. Na, A. Sohn, D.-W. Kim, and H.-K. Kim, “Work function and interface control of amorphous IZO electrodes by MoO3 layer grading for organic solar cells,” Solar Energy Materials and Solar Cells **141**, 194–202 (2015).

[242] Z. Yin, S. Mei, P. Gu, H.-Q. Wang, and W. Song, “Efficient organic solar cells with superior stability based on PM6:BTP-eC9 blend and AZO/Al cathode,” IScience **24**(9), 103027 (2021).

Publications and Presentations

Publications in international peer-reviewed journals:

- **J. Capdevila**, S. Chambon, M.E. Gueunier-Farret, "Damage-free sputtered ITO top electrode for semi-transparent organic solar cells: Protective and electronic role of the MoO_3 transport layer", Applied Physics Letters, **128**, 203302 (2026), 10.1063/5.0321090.

- **J. Capdevila**, S. Waiprasoet, FXC. Guardià, CR. Herrero, L. Hirsch, M. Campoy-Quiles, G. Wantz, P. Pattanasattayavong, S. Chambon and M.E. Gueunier-Farret, "Wide bandgap organic solar cells with improved photovoltaic performance via solid additive integration", Journal of Materials Chemistry C, **13** (35), 18450-18462 (2025), 10.1039/d5tc02260f.

Oral Presentation:

- **J. Capdevila**, S. Chambon, M.E. Gueunier-Farret, "Sputtered ITO top electrode for semi-transparent organic solar cells", 18th International Symposium on Flexible Organic Electronics, Thessaloniki, Greece (2025).

- **J. Capdevila**, S. Waiprasoet, C. Dindault, G. Wantz, P. Pattanasattayavong, S. Chambon, M.E. Gueunier-Farret, "Development of wide bandgap organic solar cells and their integration in organic/silicon tandem cells", Emerging Solar Energy Materials & Applications, Porquerolles, France (2024).

- M.E. Gueunier-Farret, S. Chambon, L. Hirsch, L. Vignau, G. Wantz, **J. Capdevila**, J. Alvarez, J.P. Connolly, J-P. Kleider, P. Roca i Cabarrocas, P. Pattanasattayavong, S. Waiprasoet, "Steps towards the development of organic/silicon tandem solar cells in a 3-terminal design", Spring Meeting of the European Materials Research Society, Strasbourg, France (2024).

Poster Presentation:

- **J. Capdevila**, F.X. Capella-Guardià, M. Campoy-Quiles, J.P. Connoly, A. Hossein-Habibi, L. Hirsch, J.P. Kleider, P. Roca i Cabarrocas, G. Wantz, S. Chambon, M.E. Gueunier-Farret, "Organic/silicon tandem solar cells: Advances of the ORGANIST project", Journées Nationales du Photovoltaïque, Strasbourg, France (2025).

- F.X. Capella-Guardià, **J. Capdevila**, M. Casademont-Viñas, S. Chambon, A.R. Goñi, M.E. Gueunier-Farret, M. Campoy-Quiles, "Multijunction RAINBOW solar cells using all organic and organic-silicon sub-cells, European Conference on Optics for Solar Energy, Berlin, Germany (2025).

- **J. Capdevila**, S. Waiprasoet, C. Dindault, L. Hirsch, G. Wantz, S. Chambon, P. Pattanasattayavong, M.E. Gueunier-Farret, "Development of wide bandgap organic solar cells for an integration in organic/silicon tandem cells", Journée de l'École Doctorale, Bordeaux, France (2025).

- **J. Capdevila**, S. Waiprasoet, S. Chambon, G. Wantz, L. Hirsch, P. Pattanasattayavong, M.E. Gueunier-Farret, Physics of Solar Cells: From Basic Principles to High Performance, Les Houches, France (2024).

- S. Waiprasoet, **J. Capdevila**, G. Wantz, S. Chambon, L. Hirsch, P. Pattanasattayavong, M.E. Gueunier-Farret, "Development of wide bandgap organic solar cells for an integration in organic/silicon tandem cells, Journées Nationales du Photovoltaïque, Dourdan, France (2023).

Titre : Fabrication, caractérisation et modélisation de cellules photovoltaïques tandem organique/silicium en configuration 3 terminaux.

Résumé : Le photovoltaïque est aujourd'hui une technologie mature, largement dominée par le silicium cristallin (c-Si), qui représente plus de 98 % du marché mondial. Les performances de cette technologie approchent désormais leur limite théorique Auger de 29,4 %, les meilleurs dispositifs atteignant des rendements de 27,9 % en laboratoire. Les architectures multijonctions constituent aujourd'hui la voie la plus prometteuse pour dépasser cette limite en réduisant les pertes par thermalisation grâce à l'association de matériaux de bandes interdites complémentaires. Parmi elles, les cellules tandem à base de silicium suscitent un intérêt croissant pour les applications terrestres. L'association d'une cellule silicium, dont la fabrication est mature industriellement, à une cellule à grand gap (pérovskite, CIGS...) permet de repousser la limite de rendement des cellules simples, avec des records dépassant 33 %. Les progrès récents du photovoltaïque organique (OPV), dont les cellules de laboratoire atteignent 20 % de rendement, ainsi que les propriétés des semi-conducteurs organiques (diversité des matériaux, largeur de bande interdite ajustable, forts coefficients d'absorption et procédés de fabrication à faible coût), rendent cette filière particulièrement attractive pour une association tandem avec le silicium. C'est dans ce contexte, et dans le cadre du projet ANR ORGANIST, que s'inscrit cette thèse. Son objectif est de développer les briques technologiques nécessaires à la réalisation d'une cellule tandem associant une cellule OPV semi-transparente à large bande interdite à une cellule en silicium cristallin à contacts interdigités en face arrière (IBC, Interdigitated Back Contacts). L'architecture trois terminaux (3T) a été retenue car elle s'affranchit des contraintes d'adaptation des courants et de l'utilisation de jonctions tunnel imposées par les configurations classiques à deux terminaux. Les premiers travaux ont porté sur le développement de la cellule organique à large bande interdite (« cellule top ») basée sur l'hétérojonction PM6:GS-ISO. L'optimisation des procédés de fabrication, combinant traitements thermiques, ingénierie des solvants et additifs solides conjugués, a permis d'améliorer la cristallinité de la couche active, ses propriétés optiques et de limiter les recombinaisons, conduisant à des rendements de 10 % pour une tension en circuit ouvert (V_{OC}) de 1,20 V. La seconde partie de la thèse est consacrée au développement d'une électrode transparente en oxyde d'indium-étain (ITO), déposée par pulvérisation cathodique à température ambiante et associée à une couche de MoO_3 assurant la protection des couches organiques et le transport des trous. L'optimisation des paramètres de dépôt a permis d'obtenir des cellules organiques semi-transparentes présentant des rendements proches de 6 % pour des V_{OC} supérieurs à 1,1 V. Ces développements ont conduit aux premières études d'intégration d'une cellule organique semi-transparente avec une cellule silicium IBC en architecture 3T. L'étude des interfaces a démontré le potentiel de l'ITO pulvérisé comme couche d'interconnexion grâce à sa forte transparence, sa faible résistance électrique et sa compatibilité avec les technologies organique et silicium. Enfin, un concept baptisé RAINBOW, développé en collaboration avec l'ICMAB-CSIC de Barcelone, a été proposé afin de relier expérimentation et modélisation pour l'étude d'architectures multijonctions organique/silicium latérales. Les simulations prédisent des rendements pouvant atteindre 18

% (pour une cellule Si d'environ 16 %), confirmant le potentiel de ces associations et guidant le développement de futures générations de cellules tandem organique/silicium à haut rendement.

Mots-clés : Photovoltaïque, Organique, Silicium.

Title: Fabrication, characterization and modeling of organic/silicon tandem photovoltaic cells in 3-terminal configuration

Abstract: Photovoltaics is now a mature technology, largely dominated by crystalline silicon (c-Si), which accounts for more than 98 % of the global market. The performance of this technology is now approaching its theoretical Auger efficiency limit of 29.4 %, with the best devices achieving conversion efficiencies of 27.9 % (lab cells). Multijunction architectures currently represent the most promising route to surpass this limit by reducing thermalization losses through the combination of materials with complementary bandgaps. Among these, silicon-based tandem solar cells have attracted increasing interest for terrestrial applications. Combining a silicon bottom cell, using a well-established industrial process, with a wide-bandgap top cell (e.g., perovskite or CIGS) extends the efficiency limit of single-junction devices, with record efficiencies now exceeding 33 %. At the same time, recent advances in organic photovoltaics (OPV), with laboratory cells reaching efficiencies up to 20 %, together with the unique properties of organic semiconductors (including their wide range of available materials, tunable bandgaps, high optical absorption coefficients, and compatibility with low-cost fabrication processes), make this technology an attractive candidate for tandem integration with silicon. Within this context, and as part of the ANR ORGANIST project, this thesis aims to develop the key technological building blocks required to realize a tandem solar cell combining a wide-bandgap semi-transparent OPV top cell with an interdigitated back-contact (IBC) crystalline silicon bottom cell. A three-terminal (3T) architecture was selected because it eliminates the current-matching constraints and the need for tunnel junctions inherent to conventional two-terminal tandem devices. The first part of this work focuses on the development of the wide-bandgap organic top cell based on the PM6:GS-ISO bulk heterojunction. Optimization of the fabrication process, combining thermal treatments, solvent engineering, and conjugated solid additives, improved the crystallinity of the active layer, enhanced its optical properties, and reduced recombination losses, leading to power conversion efficiencies of 10 % with an open-circuit voltage (V_{OC}) of 1.20 V. The second part of the thesis addresses the development of a transparent top electrode based on indium tin oxide (ITO), deposited at room-temperature by magnetron sputtering and combined with a MoO_3 layer providing both protection of the organic layer and efficient hole transport. Optimization of the deposition parameters enabled the fabrication of semi-transparent organic solar cells with efficiencies close to 6 % and V_{OC} values exceeding 1.1 V. These developments enabled the first integration studies of a semi-transparent organic solar cell with an IBC silicon solar cell in a 3T architecture. Interface investigations demonstrated the

potential of sputtered ITO as an interconnection layer owing to its high optical transparency, low electrical resistance, and compatibility with both organic and silicon photovoltaic technologies. Finally, a concept named RAINBOW, developed in collaboration with ICMAB-CSIC (Barcelona), was introduced to make the link between experimental results and modeling for the investigation of lateral organic/silicon multijunction architectures. Simulations predict efficiencies of up to 18 % (for a silicon cell efficiency of approximately 16 %), confirming the potential of these hybrid structures and providing valuable guidance for the development of future generations of high-efficiency organic/silicon tandem solar cells.

Keywords: Photovoltaic, Organic, Silicon.

Unité de Recherche

Laboratoire de l'Intégration du Matériau au Système (IMS), UMR CNRS 5218, 351 Cours de la Libération, 33405 Talence, France.